2012

Quantitative differences between lightning and non-lightning convective rainfall events as observed with dual-polarimetric radar and MSG satellite data

Retha Matthee

QUANTITATIVE DIFFERENCES BETWEEN LIGHTNING AND NON–LIGHTNING CONVECTIVE RAINFALL EVENTS AS OBSERVED WITH DUAL–POLARIMETRIC RADAR AND MSG SATELLITE DATA

by

RETHA MATTHEE

A THESIS

Submitted in partial fulfillment of the requirements
for the degree of Master of Science
in
The Department of Atmospheric Science
to
The School of Graduate Studies
of
The University of Alabama in Huntsville

HUNTSVILLE, ALABAMA

2012

In presenting this thesis in partial fulfillment of the requirements for a master's degree from The University of Alabama in Huntsville, I agree that the Library of this University shall make it freely available for inspection. I further agree that permission for extensive copying for scholarly purposes may be granted by my advisor or, in his/her absence, by the Chair of the Department or the Dean of the School of Graduate Studies. It is also understood that due recognition shall be given to me and to The University of Alabama in Huntsville in any scholarly use which may be made of any material in this thesis.

05/07/2012

Retha Matthee Date

THESIS APPROVAL FORM

Submitted by Retha Matthee in partial fulfillment of the requirements for the degree of Master of Science in Atmospheric Science and accepted on behalf of the Faculty of the School of Graduate Studies by the thesis committee.

We, the undersigned members of the Graduate Faculty of The University of Alabama in Huntsville, certify that we have advised and/or supervised the candidate on the work described in this thesis. We further certify that we have reviewed the thesis manuscript and approve it in partial fulfillment of the requirements for the degree of Master of Science in Atmospheric Science.

John R. Mecikalski 5/7/12 Committee Chair

(Date)

Lawrence D. Carey 5/17/2012

Richard T. Pierrehumbert 5/17/2012

_____

_____

Sundar A. Christopher Department Chair

_____ College Dean

Rhonda Kay Hoede 5/18/12 Graduate Dean

ABSTRACT
The School of Graduate Studies
The University of Alabama in Huntsville

Degree Master of Science College/Dept. Atmospheric Science .
Name of Candidate Retha Matthee .
Title Quantitative Differences Between Lightning and Non–Lightning Convective Rainfall Events As Observed with Dual–Polarimetric Radar and MSG Satellite Data

In order to increase understanding on the physical relationships between lightning and non–lightning convective storms, dual–polarimetric Doppler radar and lightning observations from the NASA African Monsoon Multidisciplinary Analyses campaign were statistically analyzed in concert with infrared interest fields from the Meteosat Second Generation (MSG) satellite. The horizontal reflectivity (Z_H), differential reflectivity (Z_{DR}), correlation, as well as MSG fields, showed that for 33 lightning and 30 non–lightning storms, the lightning storms on average had larger maximum Z_H values, elevated modes, a tilted structure below and vertical alignment above the melting level for both Z_H and Z_{DR}, and mostly negative Z_{DR} values above and positive below the melting level. These features are not as prominent (if observed) for the non–lightning storms. Finally, the lightning storms had stronger updraft strengths, deeper clouds, and had more cloud–top glaciation occurring at earlier times as compared to the non–lightning storms.

Abstract Approval: Committee Chair John R. Mecikalski

Department Chair Sundar. A.C.

Graduate Dean Rhonda Kay Sheede 5/18/12

ACKNOWLEDGEMENTS

First, I would like to thank my advisor, Dr. J. R. Mecikalski, for his guidance, patience, support and feedback in completing this thesis as well as for sponsoring me throughout this period. I am also thankful to Dr. L. D. Carey and Dr. P. M. Bitzer for being willing to serve on my committee and for providing me with guidance, feedback and support. I would like to acknowledge the Global Hydrology Resource Center (GHRC) at the Global Hydrology and Climate Center, Huntsville, Alabama, for making the radar and lightning data available and EUMETSAT, Germany, for making the MSG satellite data available for this research.

Additionally, I would like to thank Jonathan Fairman, Xuanli Li, Elise Schultz and Stephanie Mullins for their help with learning some of the software and programming skills needed to complete this work. This research was supported by the National Research Foundation Grant 0813603. Most importantly, I thank my Mother, Sister and Brother for allowing me to move across the world to pursue my dreams, and for supporting me unconditionally through this process. I dedicate this thesis to my loving Mother, Engela Matthee, without whom this thesis would never have been possible.

TABLE OF CONTENTS

LIST OF FIGURES

LIST OF TABLES

CHAPTER 1

INTRODUCTION

The forecasting of cloud–to–ground (CG) lightning is extremely important and is one of the leading causes of convective weather–related deaths around the world. In order to increase understanding on the relationships between lightning and non–lightning producing convective storms, radar and lightning observations from the National Aeronautics and Space Administration (NASA) African Monsoon Multidisciplinary Analyses (NAMMA) campaign were analyzed in concert with satellite data. Figure 1.1 shows the domain of NAMMA (in red), with the boundaries being approximately 30 ° North to –5 ° South and –50 ° West to 10 ° East. However, the research presented here was for a much smaller domain, and included roughly 13 ° to 16 ° North and 15.5 ° to 18.5 ° West. Although the NAMMA campaign had its main focus on improving knowledge and understanding of the West African Monsoon and its variability, African easterly waves (AEWs), examining the formation and evolution of tropical hurricanes, as well as examining the composition and structure of the Saharan air layer, and more (Redelsperger *et al.*, 2006; Jenkins & Pratt, 2008; Ferreira

et al., 2009; Arnault & Roux, 2009; Reale *et al.*, 2009; Ross & Krishnamurti, 2009; Zipser *et al.*, 2009; Cifelli *et al.*, 2010; Zawislak & Zipser, 2010), the focus of this research was on the relationships between lightning and non–lightning producing convective storms over the Equatorial Africa region. An important reason for using the NAMMA data was the fact that a multitude of instruments were used during this campaign, including two dual–polarimetric radars (placed in different locations), cloud particle imagers, a cloud and aerosol precipitation spectrometer, diode laser hygrometer, and many more, as well as the fact that this research was done over Equatorial Africa, which is an area where very little research has been done in the past. Although only the radar data from these instruments were used in this research, the wide range of data was helpful and one could be selective in terms of which data to use.

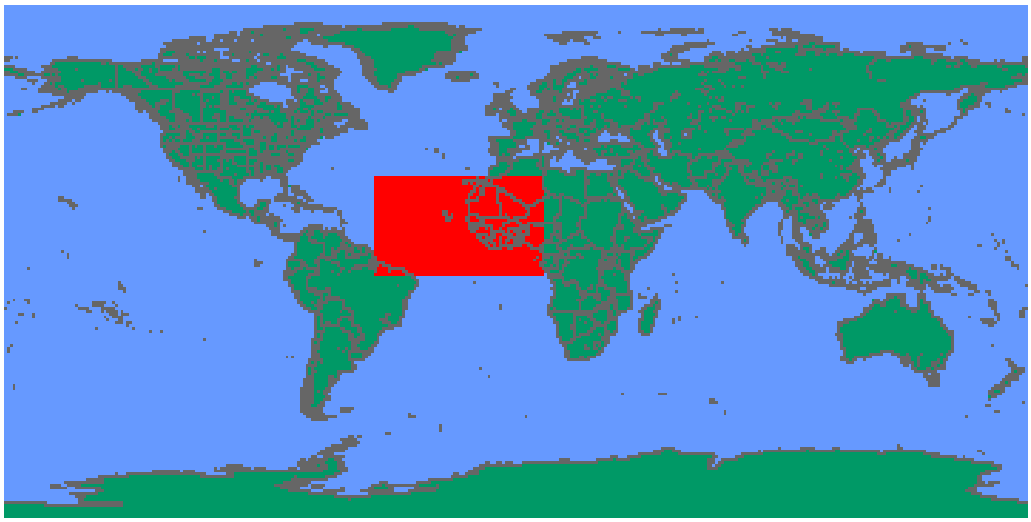

Figure 1.1: Domain of NAMMA in red; the boundaries are approximately 30 ° North to –5 ° South and –50 ° West to 10 ° East.

Many studies have been performed on convective storms using either radar (Hondl & Eilts, 1994; Carey & Rutledge, 1996; Vivekanandan *et al.*, 1999; Carey & Rutledge, 2000; Carey *et al.*, 2003; Vincent *et al.*, 2003; Lund *et al.*, 2009) or satellite

(Leap, 1986; Donovan *et al.*, 2008; Harris *et al.*, 2010; Mecikalski *et al*., 2010a,b; Mecikalski *et al*., 2011) and lightning data, yet the combined use of these three datasets together with the fact that the research was done over Equatorial Africa is unique. This research is technically similar to that done with the Tropical Rainfall Measuring Mission (TRMM) sensor suite, yet the distinctive aspects are co–analyzed ground–based dual–polarimetric radar observations and geostationary satellite multi–spectral infrared observations over Equatorial Africa. Some of the relevant TRMM–related research includes showing that convective systems over tropical continents typically have higher cloud–top reflectivity values, with stronger ice scattering and greater supercooled water contents aloft, and thus, also more lightning, as compared to convective systems over oceans (Boccippio *et al*., 2000; Petersen & Rutledge, 2001; Toracinta *et al*., 2002; Cecil *et al*., 2005; Petersen *et al*., 2005; Pessi & Businger, 2009).

The main motivation for this research was to increase understanding of the relationships between lightning and non–lightning producing storms by analyzing the time–evolution of cloud–top infrared geostationary satellite fields, ground–based dual–polarimetric radar, and lightning fields. These fields were analyzed in concert to describe physical attributes of growing cumulus clouds, including water and ice mass production, updraft strength, cloud depth and cloud–top glaciation. Pessi & Businger (2009) found that heights of radar echo tops show strong correlation to lightning rates. These echo tops can also be related to cloud–top temperatures; colder temperatures will therefore correlate to increased lightning rates (Toracinta *et al*., 2002). Cecil & Zipser (2002) stated that lightning storms with colder brightness temperatures (T_B) tend to have larger reflectivities in the mixed–phase region of these storms. In addition, ice scattering

from the top of deep convective clouds, with cloud–top heights located above the freezing level (–40 °C) will lead to lower T_B values (Vivekanandan *et al.,* 1991).

Developing a clear understanding of all of water and ice mass production, updraft strength, cloud depth and cloud–top glaciation using the combination of satellite, radar and lightning data becomes valuable for diagnosing storm intensity (important for aviation), for short–term prediction of rainfall and convective storm attributes (e.g., lightning, hail), and for climate–based studies. Use of dual–polarimetric data is particularly relevant at the time of this study given the ongoing upgrade of the U.S. National Weather Service Weather Surveillance Radar–1988 Doppler (WSR–88D) systems that will possess these capabilities. Use of multi–spectral data from Meteosat Second Generation (MSG) is important given the forthcoming GOES–R/–S sensors over North America, whereas use of lightning data together with infrared observations helps prepare the science community for the Geostationary Lightning Mapper on GOES–R, and the pending Lightning Imager on the Meteosat Third Generation satellite that will cover a large portion of the Eastern Hemisphere. Another main outcome of this study is to enhance predictability and identification of CG lightning initiation events by quantifying dual–polarimetric radar patterns in conjunction with defining MSG interest field thresholds.

For this study, the radar, satellite and lightning data sets were co–located in time and space, then the time–evolution of 33 lightning producing and 30 non–lightning producing convective storms were analyzed as clouds grew from the cumulus to cumulonimbus cloud scale. As the clouds evolved, various dual–polarimetric fields, as well as the satellite infrared fields were used to characterize hydrometeor fields and to

help understand the changing microphysical structure within the clouds, noting that some clouds went on to produce substantial lightning while others produced no lightning. The various aspects of the research, instruments used, and the results of the analysis, will be discussed in detail in the following chapters.

CHAPTER 2

BACKGROUND AND MOTIVATION

As mentioned earlier, various research has been done on convective storms using either satellite or radar data in combination with lightning data. Here, these three datasets were *combined* to increase understanding on the relationships between lightning– and non–lightning producing storms by analyzing the time–evolution of infrared satellite fields, ground–based dual–polarimetric radar fields and lightning fields.

The domain of the research presented here was roughly 13 ° to 16 ° North and 15.5 ° to 18.5 ° West, which is located over the western parts of West Africa, with the central point being the location of the NASA Polarimetric Doppler Weather Radar (NPOL), located in Kawsara, Senegal, with the period of analysis being August and September 2006. This region is influenced by the Saharan Air Layer (SAL), which is a warm, well–mixed dry and dusty air mass that advects westward and southwestward from the Sahara Desert and is most dominant during June – September (Jenkins & Pratt, 2008; Jenkins *et al*., 2008; Reale *et al*., 2009). Some research has shown that the SAL has an influence on the development of convective storms and lightning on the large–scale environment from West Africa to the western tropical North Atlantic

(Jenkins & Pratt, 2008; Jenkins *et al*., 2008; Reale *et al*., 2009; Zipser *et al*., 2009). Levi & Rosenfeld (1996); Rosenfeld & Nirel (1996); DeMont *et al*. (2003); Koren *et al*. (2005) and Khain *et al*., (2005) performed studies on the impact of aerosols and dust particles on convective storms and the effects these have on cloud condensation nuclei (CCN) and ice nuclei (IN). It was found that dust storms (such as those that occur frequently over the Saharan desert), are a good source of CCN and IN, which subsequently lead to the creation of smaller droplets, which are lifted to subfreezing temperatures, and drive stronger up– and downdrafts, as well as lead to cloud–top glaciation (Levi & Rosenfeld, 1996; Rosenfeld & Nirel, 1996; DeMott *et al*., 2003; Khain *et al*., 2005; Zipser *et al*., 2009). This dust, as well as other sources, has been shown to lead to an increased amount of CG lightning (Jenkins & Pratt, 2008). These CCN and IN are extremely important in the formation of rain, ice crystals and graupel through various processes. Small droplets form by condensing on CCN, after which accretion occurs, consisting of coalescence and riming (Rogers & Yau, 1989; Zeng *et al*., 2001).

Coalescence is the collection of cloud water by larger drops as these drops fall downward due to gravitational sorting. Thus the larger drops will fall through the cloud, collide with smaller droplets and if these two stick together (i.e., do not rebound), the larger drop will grow even larger (Rogers & Yau, 1989; Zeng *et al*., 2001). Accretion occurs when supercooled droplets (droplets that occur in the mixed phase region between 0 °C and –40 °C without being frozen) are captured by an ice particle or crystal. If these supercooled droplets freeze immediately when they are captured, it is called riming, and will lead to the formation of graupel or rimed ice crystals (Rogers & Yau, 1989; Zeng *et al*., 2001). If the freezing of the supercooled droplets onto the ice crystal is not

immediate, then denser structures are created, resulting in hail (Rogers & Yau, 1989). Aggregation occurs when two or more ice crystals merge together to form one, larger ice crystal (Rogers & Yau, 1989). In addition, water vapor can deposit on IN and form an ice particle, which then grows by diffusion from water droplets. These supercooled water droplets, graupel and ice are important for the electrification of convective clouds.

Currently, there are two main theories of electrification in clouds, namely inductive charging and non–inductive charging (NIC), with the majority of research indicating that the dominant charging method is NIC (and more specifically, the graupel–ice rebound NIC method) (Takahashi, 1978; Saunders *et al*., 1991; Rutledge *et al*., 1992; Saunders, 1993; MacGorman & Rust, 1998; Rakov & Uman, 2003; Deierling *et al*., 2005; Steiger *et al*., 2007; Deierling, *et al*., 2008; Poelman, 2010). NIC does not require the presence of a pre–existing electric field (which is the case with the inductive charging method), with the graupel–ice NIC method requiring the collision and separation of precipitation particles (graupel) and cloud particles (ice) in the presence of supercooled liquid water, which occurs in the mixed–phase region. Figure 2.1 shows a schematic representation of this mechanism. It is in this mixed–phase region where strong updrafts occur (although updrafts also occur in other regions of a storm), which leads to ice particles being lofted higher in the cloud, while larger, heavier graupel particles move downward due to gravitational sorting, which effectively, leads to the ice and graupel particles colliding and rebounding (Rutledge *et al*., 1992; Carey & Rutledge, 1996; MacGorman & Rust, 1998; Rakov & Uman, 2003; Deierling *et al*., 2005). Laboratory experiments have shown that when the temperature within the cloud is below a critical value (known as the reversal temperature, T_R), the falling graupel particles

obtain a negative charge and the ice crystals obtain a positive charge after charge separation has occurred (Takahashi, 1978; Jayaratne *et al*., 1983; MacGorman & Rust, 1998; Rakov & Uman, 2003). However, when the temperature is above T_R the falling graupel will become positively charged and the ice crystals will become negatively charged, as can be seen in Figure 2.1. This critical T_R was found to be between –10 °C and –20 °C, which is located roughly at 6 km vertical height within a cloud, although for the storms analyzed here, this is between 6.2 km and 8 km. The amount of charge that is then transferred per collision depends on the size of the ice crystals and the fall speeds of the graupel (Takahashi, 1978; Saunders *et al*., 1991; MacGorman & Rust, 1998; Rakov & Uman, 2003).

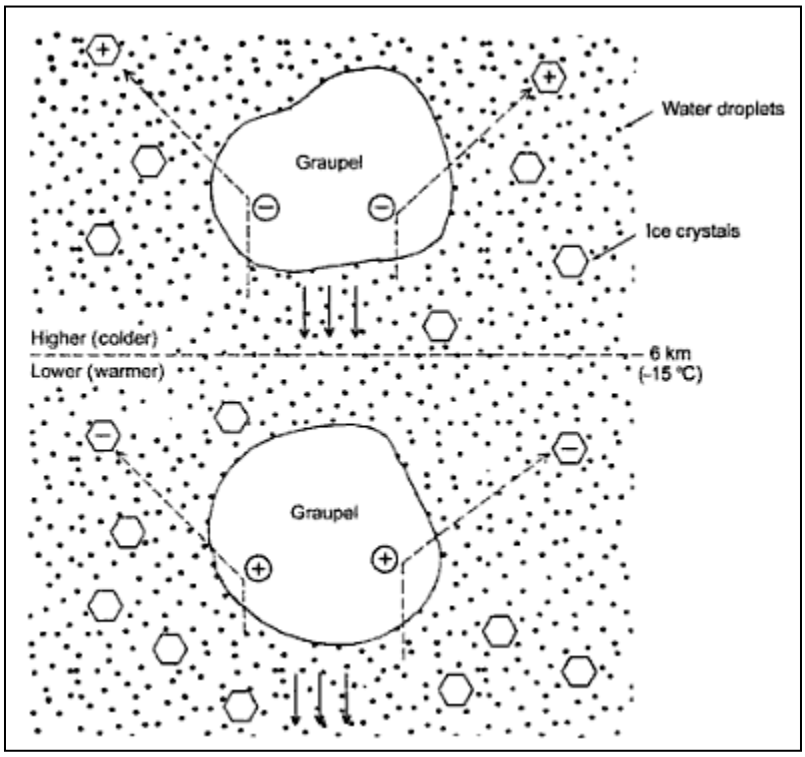

Figure 2.1: Charge transfer by collision in the graupel–ice mechanism of NIC cloud electrification. Here it is assumed that the reversal temperature, T_R, is –15 °C at a height of 6 km (from Rakov & Uman, 2003).

It is due to these charging mechanisms and processes involving hydrometeors that one typically observes a tripole charge structure in thunderstorms, although some evidence exist that the charge structure can be more complicated, for example in a mesoscale convective systems (MCSs), there can be up to 6 or more charge layers (Stolzenburg, *et al*., 1998). The tripole charge structure is a vertically separated charged region, consisting of a net positive charge near the top of the cloud (called the main positive charge, MPC), a main negative charge (MNC) region below this, and a smaller, positive charge region (called the lower positive charge (LPC)) at the bottom of the cloud (MacGorman & Rust, 1998; Poelman, 2010). It has been found that the LPC region is roughly located around 0 °C, the MNC region is located between –5 °C and –15 °C and the MPC region is at –20 °C, with a charge of approximately +12 Coulomb (C), –40 C and +40 C, respectively (Krehbiel, 1986; MacGorman & Rust, 1998). Figure 2.2 shows this graphically, but it should be noted that this tripole structure is not always evident in storms, with an inverted tripole structure, a dipole structure, as well as additional charging regions, also being observed in some storms, as mentioned earlier. As charge builds in these regions, inter–cloud (IC) and CG lightning might occur after a certain magnitude is reached.

Much research has been done with radar and satellite data in order to obtain some sort of relationship between these data (Meischner *et al*., 1991; Strabala *et al*., 1994; Ackerman, 1996; Carey & Rutledge, 1996; Schmetz, *et al*., 1997; Tong *et al*., 1998; Carey & Rutledge, 2000; Carey *et al*., 2003; Setvák *et al*, 2003; Vincent *et al*., 2003; Mecikalski & Bedka, 2006; Steiger *et al*., 2007; Lund *et al*., 2009; Williams *et al*., 2009; Harris *et al*., 2010; Mecikalski *et al*., 2010a,b; to name but a few). Previous studies have

shown that dual–polarimetric variables provide important information on the size, shape, thermodynamic phase as well as the orientation of hydrometeors in order to distinguish water drops, graupel, hail and ice crystals, and these variables can be used to locate areas of possible lightning occurrence (Doviak & Zrnić, 1993; Hondl & Eilts, 1994; Carey & Rutledge, 1996; Carey & Rutledge, 2000; Straka *et al*., 2000; Bringi & Chandrasekar, 2001; Cifelli, *et al*., 2002; Carey *et al*., 2003; Vincent *et al*., 2003; Wang & Carey, 2005; Lund *et al*., 2009). Dual polarimetric variables of horizontal reflectivity (Z_H), differential reflectivity (Z_{DR}), correlation (ρ_{HV}), and difference reflectivity (Z_{DP}) are often used to distinguish and categorize hydrometeor types. This is due to the fact that rain drops have a different shape and dielectric constant than ice crystals and small or large hail; in particular ice has a lower dielectric constant than water (Doviak & Zrnić, 1993; Bringi & Chandrasekar, 2001). Together with the dielectric constant differences, the shapes of these particles also differ, which leads to varying values of the above–mentioned radar polarimetric variables being obtained per hydrometeor type. Raindrops (larger than about 1 mm in diameter) closely approximate oblate, non–spherical particles, with the oblateness increasing with increasing size of the drop and thus their horizontal dimensions are larger than their vertical dimensions (Balakrishnan & Zrnić, 1990; Carey & Rutledge, 1996; Tong *et al*., 1998). On the other hand, small hail appears spherically symmetric and tumbles as it falls; hence their horizontal and vertical dimensions appear roughly equal (Carey & Rutledge, 1996; Tong *et al*., 1998). However, sometimes large hailstones can be oblate, with their vertical dimensions being larger than their horizontal dimensions (Carey & Rutledge, 1996). Ice crystals also tumble as they fall and can sometimes be seen as spherical as well.

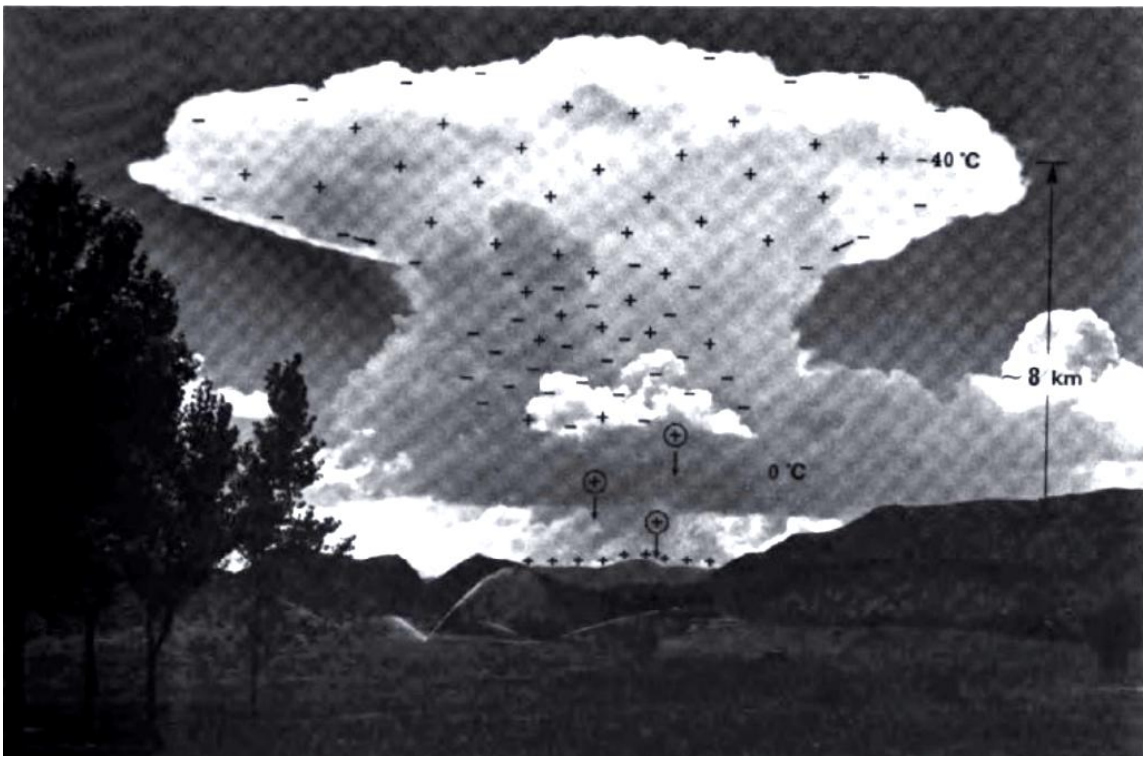

Figure 2.2: An isolated thunderstorm over Langmuir Laboratory in central New Mexico and a rudimentary picture of how electric charge appears to be distributed inside and around the thundercloud, as inferred from in–cloud and remote observations (Krehbiel, 1986).

Because Z_{DR} is related to the decibel difference between Z_H and vertical reflectivity (Z_V), Z_{DR} will vary for raindrops, ice crystals and graupel due to these hydrometeors having varying horizontal and vertical dimensions (Doviak & Zrnić, 1993; Yuter & Houze, 1995; Carey & Rutledge, 1996; Vivekanandan *et al*., 1999; and Bringi & Chandrasekar, 2001). Z_H is the sixth moment of the particle size distribution (when the particle is small compared to the wavelength used); therefore the larger the hydrometeors, the larger the Z_H values will be. In addition, ρ_{HV} is the correlation coefficient of the horizontal and vertical back scattered power and will also vary depending on the horizontal and vertical dimensions of the hydrometeors (Doviak & Zrnić, 1993; Vivekanandan *et al*., 1999). Low ρ_{HV} values (< 0.85) indicate the presence of

non–hydrometeors (such as insects) that have a larger vertical dimension than horizontal dimension. Large values of ρ_{HV} (~ 1.0) indicate fairly uniform sized and shaped particles, such as small rain drops, graupel and hail. Also, Balakrishnan & Zrnić (1990) and Zrnić *et al*. (1993) showed that lowered ρ_{HV} values are observed in regions where mixed–phase hydrometeors are present due to the distribution of shapes, sizes and phase shifts varying for these hydrometeors. In addition, substantial negative Z_{DR} values (roughly –1.0 dB) in a region of high Z_H values is caused by hailstones that are larger than about 2 cm in diameters (Balakrishnan & Zrnić, 1990). Therefore, the combination of varying oblateness of hydrometeors for the same particle size distribution (small droplets versus large drops, ice crystals, supercooled drops, graupel and hail), lower dielectric constants of ice particles (including hail and graupel), possible canting, and variations in vertical and horizontal dimensions for certain hydrometeors, make it possible to distinguish water droplets, large drops, ice crystals and graupel/hail.

From the previous discussion, Z_H will have higher values for hail and graupel (usually ≥ 40 dBZ), $-1.0 \leq Z_{DR} \leq 0.5$ dB, and ρ_{HV} values ≥ 0.95. This is due to hail and graupel being roughly spherical as well as the dielectric constant of ice being lower than for water. Z_H for rain could vary between 10 dBZ (small drops) to roughly 40 dBZ (and higher for large drops), Z_{DR} values greater than about 0.5 dB, with larger values as the drop size increases, and ρ_{HV} values > 0.97 (Balakrishnan & Zrnić, 1990; Meischner *et al*., 1991; Doviak & Zrnić, 1993; Yuter & Houze, 1995; Carey & Rutledge, 1996; Vivekanandan *et al*., 1999; Straka *et al*., 2000; Bringi & Chandrasekar, 2001; Zeng *et al*., 2001). Ice particles will also have Z_{DR} values roughly around 0 dB and sometimes marginally higher at low Z_H values. In addition, it has been found that narrow columnar

regions of positive Z_{DR} values ≥ 1 dB that extends above the 0 °C isotherm, known as the Z_{DR} column, could be supercooled rain drops that are lofted upwards in the cloud due to strong updrafts (Meischner *et al*., 1991; Doviak & Zrnić, 1993; Yuter & Houze, 1995; Straka *et al*., 2000; Bringi & Chandrasekar, 2001; Zeng *et al*., 2001, Rowe, 2011).

Using dual–polarimetric radar data, Carey & Rutledge (1996) found that the occurrence of ice particles, graupel and hail were well correlated to the occurrence of IC and CG lightning. Also, the maximum volume of low–level graupel was well correlated with CG flash rate; and hail rates lagged the peak CG rate by two to six minutes (Carey & Rutledge, 1996). Carey & Rutledge (2000) showed that mixed–phase ice mass and rainfall are strongly correlated to lightning and that ground locations of CG flashes clustered beneath radar–inferred mixed–phase ice mass maxima. Further, increased updraft strength inferred from radar variables directly resulted in more ice mass aloft, and thus more lightning (Carey & Rutledge, 2000). These updraft strengths can also be obtained from satellite T_B's. In addition, it was found that the occurrence of more ice in the mixed–phase region, as well as the merging of different convective cells into one larger cell, will lead to an increased production of lightning (Carey & Rutledge, 2000; Carey *et al*., 2003; Lund *et al*., 2009). Lund *et al*. (2009) states that lightning initiation occurred in two regions: (1) Above a local reflectivity maximum (35 dBZ – 47.5 dBZ) and (2) Near the top of a Z_{DR} column with relatively low ρ_{HV} values. These two regions often consist of graupel and hail (Bruning *et al*., 2007; Lund *et al*., 2009).

Besides the importance of radar polarimetric variables when separating various precipitation particles, information from satellites, such as cloud–top temperature, inferred updraft strength, cloud–top glaciation, and other parameters, are also important.

These and can help distinguish storms that have large amounts of ice and thus may develop into lightning–producing convective storms versus convective storms that will not produce lightning. Rosenfeld *et al*. (2008) and Mecikalski *et al*. (2011) studied retrieved fields from the MSG Spinning Enhanced Visible and Infrared Imager (SEVIRI) to obtain information on cloud optical thickness (τ), cloud–top particle effective radius (r_e) and cloud–top pressure (p_c) to understand the physical attributes of growing cumulus clouds. Other research includes obtaining various cloud–top properties of growing cumulus clouds prior to the onset of rainfall and so–called convective initiation (which is defined as the first occurrence of a $\geq$ 35 dBZ radar reflectivity echo at the –10 °C level) by using both MSG, Geostationary Operational Environmental Satellite (GOES) and the Moderate–Resolution Imaging Spectrometer (MODIS) infrared (IR) and visible (VIS) channel information (Strabala *et al*., 1994; Ackerman, 1996; Schmetz *et al*., 1997; Setvák *et al*., 2003; Mecikalski & Bedka, 2006; Mecikalski *et al*., 2008; Rosenfeld *et al*., 2008; Harris *et al*., 2010; Mecikalski *et al*., 2010a,b). These studies have defined satellite "interest fields" that can be used in various ways to obtain important information on updraft strength, glaciation, cloud depth, cloud–type and vigor. Due to the fact that the research presented in this study uses information from the MSG SEVIRI instrument, most, but not all, of the following information and background will be focused on this instrument.

The main dataset for the satellite part of this research is calibrated Level–1.5 IR channels collected at a 3 km sampling distance from the SEVIRI instrument on the MSG (specifically *Meteosat–8*) satellite, which is a geostationary satellite located over the equator at 0 ° latitude (Schmetz *et al*., 2002). It has a 15–minute repeat cycle, consisting

of 12 spectral channels, including eight IR channels, two VIS channels, one near–infrared (NIR) channel, two water vapor (WV) channels and one high–resolution visible channel (HRV) (Schmetz *et al*., 2002; Mecikalski *et al*., 2010a). All of the channels, except one, have a 3 km sampling distance at nadir (and thus one pixel is 3 x 3 km in dimension); the HRV channel has a 1 km sampling distance at nadir. Table 2.1 shows the various channels from SEVIRI, each channel's central wavelength, and whether the channel is an absorption or "window" channel (Schmetz *et al*., 2002). Because the MSG SEVIRI channels cover a variety of wavelengths, each with its own weighting function, various cloud properties can be obtained using these channels, which are important for convective storm research. However, only some of the IR channels were used in this research; therefore the remainder of this chapter will mostly be focused on the IR channels only.

Figure 2.3 shows the clear–sky per–channel SEVIRI thermal IR weighting functions as a function of altitude (EUMETSAT, 2007). Weighting functions are for SEVIRI's subsatellite point over the equator. The 3.9 μm channel is used primarily for low cloud and fog detection (yet, 3.9 μm reflectance is important for estimating r_e at cloud–top, Lindsey *et al*., 2006), with the 6.2 μm and 7.3 μm channels being most sensitive to the water vapor content in the upper– and mid–troposphere (6.2 μm and 7.3 μm, respectively) (Lee *et al*., 1997; Schmetz *et al*., 2002; Otkin *et al*., 2009). The 8.7 μm channel is a window channel, which provides quantitative information on thin cirrus clouds, is used to discriminate between ice and water clouds; the 9.7 μm channel is an ozone channel, which is used to monitor ozone patterns, but can also be used to

observe features along the tropopause and within the lower stratosphere (Schmetz *et al*., 2002; Otkin *et al*., 2009).

Table 2.1: Spectral channel characteristics of SEVIRI providing the approximate central wavelength of the channels and whether it is an absorption or window channel (Adapted from Schmetz *et al*., 2002).

Channel Number	**Central Spectral Band (μm)**	**Channel**	**Main gaseous absorber or window**
Channel 1	0.6	VIS	Window
Channel 2	0.8	VIS	Window
Channel 3	1.6	NIR	Window
Channel 4	3.9	IR	Window
Channel 5	6.2	WV	Water Vapor
Channel 6	7.3	WV	Water Vapor
Channel 7	8.7	IR	Window
Channel 8	9.7	IR	Ozone
Channel 9	10.8	IR	Window
Channel 10	12.0	IR	Window
Channel 11	13.4	IR	Carbon Dioxide
Channel 12	Broadband (about 0.4 – 1.1)	HRV	Window/Water vapor

The 10.8 μm and 12.0 μm channels are window and split window channels, respectively and are used to observe cloud–top temperatures and sea and land surface areas (Schmetz *et al*., 2002; Otkin *et al*., 2009). The 13.4 μm channel, which is the carbon dioxide absorption channel, is used for reducing cirrus contamination and in–cloud height assignment studies (Schmetz *et al*., 2002; Otkin *et al*., 2009). Due to the characteristics of each channel, it is possible to create satellite "interest fields" for cumulus cloud monitoring in order to obtain indicators of cumulus cloud–top temperature change rates, updraft strength estimates, and cloud–top glaciation, as well as general

information on cumulus clouds, such as their texture (Strabala *et al*., 1994; Ackerman, 1996; Schmetz *et al*., 1997; Setvák *et al*., 2003; Mecikalski & Bedka, 2006; Mecikalski *et al*., 2008; Harris *et al*., 2010; Mecikalski *et al*., 2010a,b).

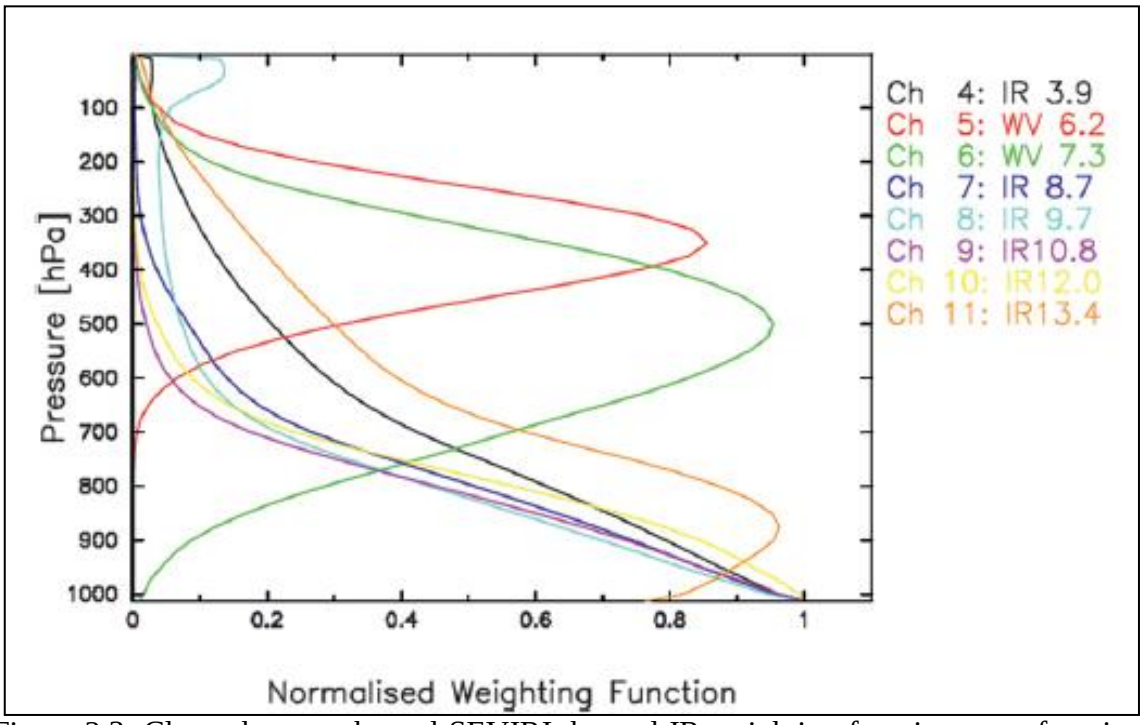

Figure 2.3: Clear–sky per–channel SEVIRI thermal IR weighting functions as a function of altitude (EUMETSAT, 2007). Weighting functions are for SEVIRI's sub–satellite point over the equator.

These interest fields are developed directly from T_B for the various IR channels, which for this study are the 6.2 μm, 7.3 μm, 8.7 μm, 10.8 μm and 12.0 μm channels. Table 2.2 shows the 10 interest fields used here that are calculated from the five IR channels. These interest fields were created on the premise that as cumulus clouds grow, T_B values associated with each channel (and corresponding weighting function) will change over time (Strabala *et al*., 1994; Mecikalski & Bedka, 2006; Mecikalski *et al*., 2008; Harris *et al*., 2010; Mecikalski *et al*., 2010a,b). When channel differences are

used, differences that approach zero or change signs provide meaning for identifying important physical attributes, such as the occurrence of ice at the top of the cloud (Strabala *et al*., 1994). This is especially true for the 6.2 μm and 7.3 μm channels, as these two have similar shaped weighting functions and are both sensitive to the water vapor content in the upper– and mid–troposphere (6.2 μm and 7.3 μm, respectively). Channel differences, such as 6.2 μm – 7.3 μm, are then used to estimate whether a cloud has grown to a given altitude; values are that approximating zero indicate a continuously growing and deepening cumulus cloud (Mecikalski *et al*., 2010a). The time trends, such as the 15 minute 6.2 μm – 7.3 μm, provide an indication of updraft strength of a convective cloud by inferring the rate of deepening of the cloud, and hence, the updraft velocity (Adler *et al*., 1985; Mecikalski *et al*., 2010a). Therefore, 15 minute and 30 minute time trends of 6.2 μm – 7.3 μm should be negative when convective clouds are present, implying that the T_B difference between the two channels is becoming smaller over time (Mecikalski *et al*., 2010a). The same reasoning can be used with the other channel differences and time trends, but with varying results (i.e., some will increase and possibly become positive, while others will decrease and become more negative). More will be said in Chapter 3 on how the IR interest fields in Table 2.2 are used in this study.

These satellite interest fields, as well as dual–polarimetric radar variables, will be used in combination with lightning data to increase understanding of the relationships between lightning– and non–lightning producing storms. The specific data and methodology used in this research will be discussed in more detail in the subsequent chapters, followed with average results from both lightning and non–lightning producing storms.

Table 2.2: Interest fields used in this research that indicate updraft strength, glaciation and cloud depth (adapted from Mecikalski *et al*., 2010a).

Channel differencing and time trends	**Category**
15 minute 6.2 μm – 7.3 μm	Updraft strength
30 minute 6.2 μm – 7.3 μm	Updraft strength
15 minute 10.8 μm	Updraft strength
30 minute 10.8 μm	Updraft strength
6.2 μm – 7.3 μm	Cloud depth
6.2 μm – 10.8 μm	Cloud depth
8.7 μm – 10.8 μm	Cloud–top glaciation
15 minute 8.7 μm – 10.8 μm	Cloud–top glaciation
(8.7 μm – 10.8 μm) – (10.8 μm – 12.0 μm)	Cloud–top glaciation
15 minute (8.7 μm – 10.8 μm) – (10.8 μm – 12.0 μm)	Cloud–top glaciation

CHAPTER 3

DATA AND METHODOLOGY

Observations from the NPOL radar which is an S–band radar located at Kawsara, Senegal in West Africa are used in this research in conjunction with Very Low Frequency (VLF) Arrival Time Difference (ATD) lightning data obtained from the United Kingdom Meteorological Office (UKMO), which records mostly only strong CG lightning as well as MSG SEVIRI satellite interest fields as described in Chapter 2. These datasets are utilized to evaluate and describe the physical attributes of growing cumulus and cumulonimbus clouds, including water and ice mass production, updraft strength, cloud depth and cloud–top glaciation between lightning and non–lightning convective storms. In this chapter, the various instruments, as well as the methods used in the research, will be discussed. For the research presented, 33 lightning and 30 non–lightning storms were analyzed.

3.1. "T–time" for lightning and non–lightning storms:

In order to compare the lightning producing and non–lightning convective storms, a "t–time" must be obtained for all the convective storms used, from which

a backward and forward time trend can be obtained for all storms. For the lightning storms, the t–time is defined as the radar time when the first lightning flash occurred, i.e., if the first flash occurred at 1435, then this flash falls into the 1430 radar time; the lightning t–time then is 1430. Once a t–time is established for a given storm, the storm's evolution is then divided into 15–minute intervals, from t–45 through t+30 for both the lightning and non–lightning storms for radar and from t–75 through t+30 for the satellite data.

The t–time for the non–lightning storms is more complicated to obtain, as there is no obvious reference point (compared to the first CG lightning as the reference point of the lightning storms). Therefore various Z_H intensity–based tests were performed on the lightning producing storms to obtain a t–time for the non–lightning storms, including, but not limited to, (1) obtaining the frequency of maximum reflectivity at any height between 0.5 km and 10 km at times t–45 through t+30, (2) using the frequency of maximum reflectivity at 1.5 km for all times, (3) the frequency of maximum area of all reflectivity values above 10 dBZ for all times, (4) the frequency of maximum area of all reflectivity values above 35 dBZ for all times, and (5) the frequency of maximum volume of all reflectivity values above 35 dBZ for all times. After performing these various tests, the 35 dBZ reflectivity threshold was utilized given that this value is seen as the reflectivity value where "convective initiation" is defined to occur (Browning & Atlas, 1965; Marshall & Radhakant, 1978; Wilson *et al*., 1992; Mueller *et al*., 2003; Mecikalski & Bedka, 2006; Mecikalski *et al*., 2008; Harrison *et al*., 2009; Mecikalski *et al*., 2010a,b). Thus, after much analysis, it is found that using the maximum volume of reflectivity values above 35 dBZ had the highest frequency of occurrence within the 33 lightning

event dataset, with 24.24 % obtained at t+15 for the lightning producing storms. Therefore, this parameter is used as t+15 for all non–lightning storms in this research, and thus the 15 minutes before this maximum volume above 35 dBZ was reached is the "t–time".

3.2. NPOL Radar Data:

The NPOL radar is an S–band dual–polarimetric radar located at 14.65654 ° North and 17.09803 ° West, in Kawsara, Senegal, West Africa (see Figure 3.1). The radar operated nearly continuously between 19 August 2006 and 30 September 2006, however, only 15 days were useable for the research done here. Full volume scans were produced every 15 minutes, and either 270 km or 150 km long range scans were available. In addition, real time products such as plan position indicator (PPI) scans of reflectivities and velocities, and near–real time products, including range height indicator (RHI) graphs and other polarimetric products were also available. During each 15–minute repeat cycle, a 1–tilt (0.8 °) surveillance scan (270 km range) and one 19 tilt volume scan (150 km range) were collected. Two scanning strategies were employed, namely "near" and "far". The near scanning strategy consisted of 19 angles which included 0.8 °, 1.5 °, 3.2 °, 5.5 °, 7.9 °, 10.3 °, 12.7 °, 15.1 °, 17.6 °, 20.0 °, 22.6 °, 25.1 °, 27.8 °, 30.5 °, 33.2 °, 36.1 °, 39.1 °, 44.0 ° and 49.0 °. The far scanning strategy also consisted of 19 angles, which include 0.7 °, 1.4 °, 1.8 °, 2.3 °, 3.4 °, 4.5 °, 5.7 °, 6.9 °, 8.2 °, 9.6 °, 11.3 °, 13.0 °, 15.0 °, 17.2 °, 19.8 °, 22.5 °, 26.5 °, 29.5 ° and 33.0 °. The volume scan setup for both scanning strategies comprised of an azimuthal resolution of 1.4 °, a pulse width of 0.8, and horizontal and vertical polarization. The maximum range

of the radar was 150 km, and the unambiguous range before folding occurs was 157.8 km. Various polarimetric fields were collected during the NAMMA campaign, but only Z_H, Z_{DR}, and ρ_{HV} were used in this research, with Z_{DP} being calculated from Z_{DR} and Z_H.

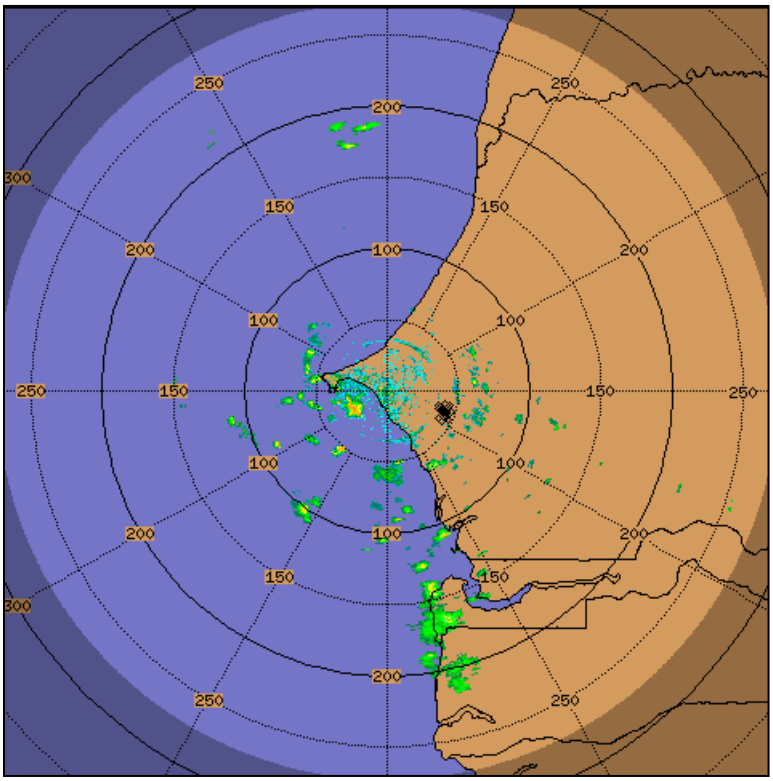

Figure 3.1: Image showing the NPOL radar location (middle of cross) and range during NAMMA 2006. The distances shown in the image are in km's.

Quality control procedures were implemented as part of NAMMA post–processing throughout the period that the data were recorded, with various filters being incorporated in the process. The filters included a range dependent correlation test, which examined the ρ_{HV} of each range gate. Therefore certain ρ_{HV} threshold values were set to reduce the chance of precipitation being removed due to attenuation. If data passed this range dependent correlation test without being removed, then it was passed through a

minimum reflectivity filter, where all reflectivity values below 0.0 dBZ were removed. After this second test, the data went through a range dependent parameter filter, where radar echoes with low ρ_{hv} values, low reflectivity values and near zero velocities were removed. These filters formed part of the first pass of the quality control process. The second pass of the quality control process included more filters, which consisted of examining the vertical extent of the echo; values are removed if the reflectivity at any range gate is only seen in the first sweep with a ρ_{hv} value of less than 0.8. After this filter, ground clutter was removed (though not all of it was removed, as will be seen later in this chapter) by removing ρ_{hv} values of less than 0.3. Backlobes were then removed from the data via the final filter, a neighbor test, which examined the spatial distribution of bins surrounding the analysis bin and removing data where four or less of the surrounding range gates contained reflectivity values. In addition to these filters, calibration of Z_H and Z_{DR} values were also completed by comparing these fields to the TRMM precipitation radar. This showed that the NPOL Z_H values were biased low, with a value of –2 dB, and therefore a +2 dB correction factor was added to the NPOL data.

Initially, the Z_{DR} field had a fluctuation in bias due to bad correction offsets, bad noise samples and unexpected power failures (Kucera, 2006). Thus, various corrections were made to the NPOL Z_{DR} to yield final bias of 0.0 dB being reached (however, a later study showed that these variables were still biased after these corrections were made). These corrections are not made clear in the NPOL documentation. It is very important to note that although all these filters were applied to the NPOL radar data before the data were used in the research presented, a lot of clutter and backlobe echoes were still

present, which had to be manually removed (this is discussed in the following chapters, Kucera, 2006).

For this study, care was taken to only use data from the far scanning strategy in order to keep the analysis more consistent and comparable. Prior to any analysis, raw data from NPOL were converted to universal format (UF) and then converted to Doppler Radar Data Exchange (DORADE) format sweep files (in order to use the radar data in the National Center for Atmospheric Research (NCAR)'s SoloII software, Lee *et al*., 1994). Clear air radar echoes from dust, salt, insects and other particles, and backlobe echoes where then manually removed at each elevation for all times used for Z_H, Z_{DR} and ρ_{HV} using the SoloII software (Figure 3.2). After the removal of the clutter, the data were gridded using REORDER (an NCAR software package, Oye *et al*., 1995) to a common Cartesian grid of 100 km x 100 km x 15 km and 130 km x 130 km x 15 km using the Cressman weighting inverse distance scheme with a radius of influence of 0.5 km (the varying horizontal dimensions were due to some storms either developing or moving further away from the radar and therefore the horizontal dimensions were increased for these storm days). The horizontal resolution for both grids was 1 km and the vertical resolution was 0.5 km. The origin of the Cartesian grid was the location of the NPOL radar. The gridded data were then used in the NCAR's Custom Editing and Display of Reduced Information in Cartesian space (CEDRIC, Mohr *et al*., 1986) software; the output from this package is in netCDF format (Rew & Davis, 1990), where after the netCDF files were read, formatted and displayed using the Interactive Data Language (IDL, Gumley, 2002).

As the clouds evolved, dual–polarimetric fields of Z_H, Z_{DR} and ρ_{HV} were analyzed to help understand the changing microphysical structure within the clouds. Using the same methods as presented in Doviak & Zrnić (1993), Carey & Rutledge (1996), Carey & Rutledge (2000), Cifelli *et al*. (2002) and Vincent *et al*. (2003), a combination of dual polarimetric variables (as mentioned previously) were used to accurately obtain hail and graupel, mixed–phase, and reflectivity volumes above certain reflectivity and temperature thresholds.

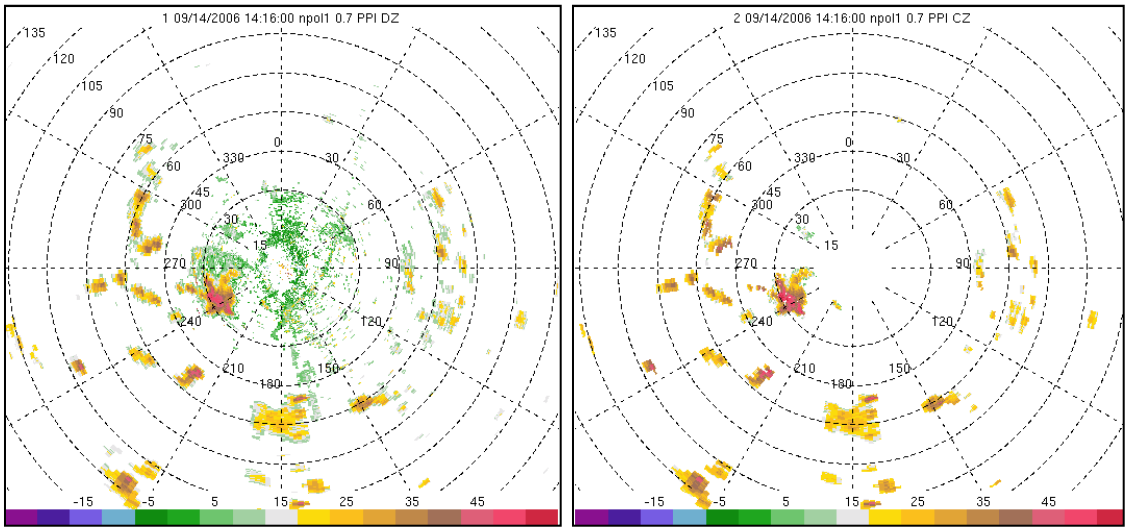

Figure 3.2: Z_H for 20060914 at 1416 at 0.7 ° elevation. The image on the left is before clutter and backlobes were removed and the image on the right is after clutter and backlobes were manually removed.

3.2.1. Contoured Frequency by Altitude Diagrams (CFADs):

Un–normalized contoured frequency by altitude diagrams (CFADs) were produced for the Z_H, Z_{DR} and ρ_{HV} variables for each of the 33 lightning and 30 non–lightning convective storms from t–45 through t+30. These diagrams display the statistical distributions of storm properties and have been used by various other researchers (Yuter & Houze, 1995; Zeng *et al*., 2001; Lang *et al*., 2003; Cifelli *et al*.,

2004; Wang & Carey, 2005; Rogers *et al*., 2007; Cecil, 2011). Basically, CFADs display the frequency distribution of a chosen variable at each selected height. Because the temporal evolution of the storms used here is important, it was decided to display the various polarimetric radar variables in CFADs, as other studies have shown this to be a convenient tool for time evolution–type research (Wang & Carey, 2005; Cecil, 2011). The CFADs developed here were calculated according to Yuter & Houze (1995), except that the CFADs presented here were not normalized with respect to the bin size at each level, which helped convey more information and made it easier to analyze.

The radar variables are binned within a constant vertical level increment, and a histogram is then calculated at each reflectivity bin from data at each height. The total number of points in the entire data set are then calculated (i.e. for Z_H values, these are all the values between 10 dBZ and 60 dBZ), with the histogram at each reflectivity bin and vertical level then being divided by the total number of data points, but *not dividing by the bin size per vertical height*. The result is then multiplied with 100 to present the fraction as a percentage value. For the research done here, the Z_H bin size was set to 5 dBZ from 10 dBZ to 60 dBZ, Z_{DR} was set at 0.5 dB from –3 dB to +3 dB and ρ_{HV} was set to 0.02, from 0.8 to 1.0. All of these have a vertical resolution of 0.5 km.

3.2.2. Rain Line, Rain and Ice Masses:

In addition to the above–mentioned dual–polarimetric variables, Z_{DP}, the difference reflectivity between Z_H and Z_V (with only Z_H > 35 dBZ being used), was calculated in order to obtain the fraction of ice in rain/ice mixtures (Meischner *et al*., 1991; Aydin & Giridhar, 1992; Doviak & Zrnić, 1993; Carey & Rutledge, 1996; Tong *et*

al., 1998; Carey & Rutledge, 2000; Cifelli *et al*. 2002; Wang *et al*., 2007). Although the simultaneous use of Z_{DR} and Z_H are good indicators of pure rain and pure ice, it is not a good indicator of mixed–phase precipitation (Carey & Rutledge, 1996). The equation to calculate Z_{DP} is defined as

$$Z_{DP} = 10\log_{10}\left(Z_H - Z_V\right) \cdot \tag{3.1}$$

Z_V is obtained from Z_{DR}, defined as

$$Z_{DR} = 10\log_{10}\left(\frac{Z_H}{Z_V}\right). \tag{3.2}$$

Both Z_H and Z_V are in linear units (mm^6/m^3) and Z_{DP} is in dB. It should be noted that only horizontal reflectivities where $Z_H > Z_V$ can be used to calculate Z_{DP}, as it leads to only oblate hydrometeors being used (Carey & Rutledge, 1996; Tong *et al*., 1998; Carey & Rutledge, 2000; Cifelli *et al*. 2002; Wang *et al*., 2007).

From equation (3.2) the "rain line" was then obtained, which is an approximate line, with some scatter, that separates pure rain hydrometeors from mixed–phase hydrometeors (Carey & Rutledge, 1996; Tong *et al*., 1998; Carey & Rutledge, 2000). The line is obtained by using a "robust" least absolute deviation technique (which is less sensitive to outliers than using a least squares fit) from all the remaining data points ($Z_H > Z_V$ and $Z_H > 35$ dBZ). The Z_{DP} equation has the following form:

$$Z_{DP} = a*Z_H - b \tag{3.3}$$

and was only calculated at 1 km height. Although rain particles fall on both sides of the line, defined by (3.3), only particles that fall below the rain line are considered in the rest of the analysis as particles falling above the rain line will have $Z_H >> Z_V$, indicative of large water hydrometeors (the rain line method is used to obtain mixed–phase hydrometeors). It should be noted that the above limits results in many of the precipitation particles not being used in the calculation of Z_{DP} and the rain line, i.e., only reflectivity values of 35 dBZ and higher, as well as the fact that Z_H must be greater than Z_V for all the remaining precipitation particles will be used. This will be seen more clearly in the non–lightning events, where very few data points remain after these limits were applied to the data, because the non–lightning storms did not produce as many high–reflectivity values as the lightning–producing storms.

Because there is scatter about the rain line, the standard deviation (σ) from the line is calculated, and then all particles that fall within 2σ below the line are delineated as being pure rain particles. This is because at 1.0 km, most particles should be rain particles, as the temperature was approximately 15 °C and warmer at this height. The remaining particles that fall below the 2σ line (and thus possess a lower Z_{DP} for the same Z_H values) are then defined as being mixed–phase particles (Doviak & Zrnić, 1993; Carey & Rutledge, 1996; Carey & Rutledge, 2000; Cifelli *et al*. 2002). Figure 3.3 is a scatter plot of Z_{DP} versus Z_H (rain line) for NPOL at 1.0 km for one lightning (14 September 2006) and one non–lightning storm (on 14 September 2006). The solid blue line is the robust least absolute deviation line to the NPOL data; the solid green line indicates the best fit line for simulated gamma raindrop size distributions from Golestani *et al*. (1989) and the solid red line is the least–squares best fit line to the Colorado State

University (CSU)–University of Chicago–Illinois State Water Survey (CHILL) (CSU–CHILL) data from Carey & Rutledge (1996). The image on the left is the rain line obtained for a lightning producing storm and the image on the right is the rain line for a non–lightning storm. Clearly there are many more data points for the lightning producing storm (156) as compared to the non–lightning storm (22). This is because the non–lightning storms, on average, having fewer Z_H values > 35 dBZ as compared to the lightning producing storms, which is one of the limits introduced when calculating the rain line. Also, it is clear that there is more scatter at lower Z_H values than at high Z_H values for both lightning and non–lightning storms.

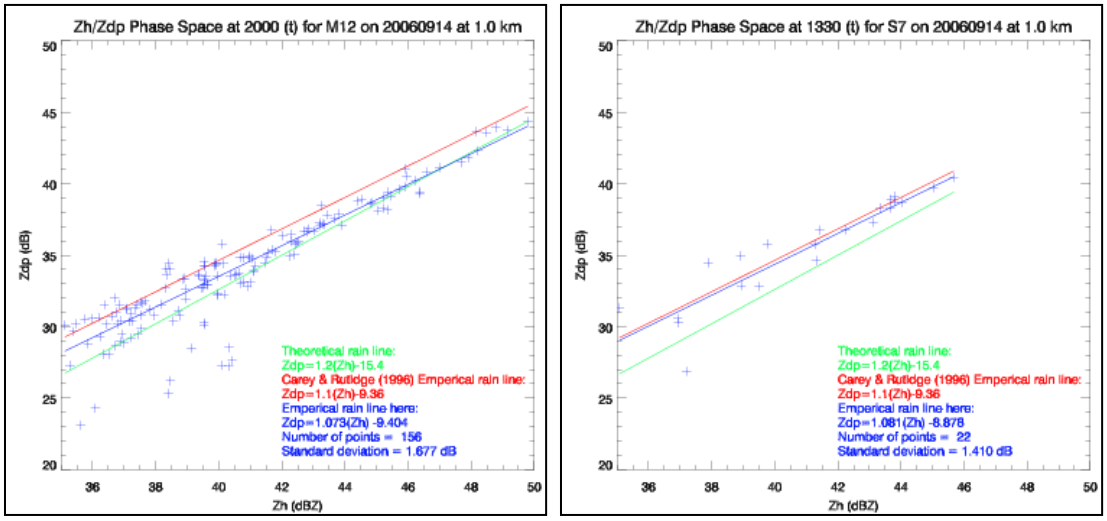

Figure 3.3: Scatter plot of Z_{DP} versus Z_H (rain line) for NPOL at 1.0 km. The solid blue line is the least–squares best fit line to the NPOL data. The solid green line indicates the best fit line for simulated gamma raindrop size distributions from Golestani *et al*. (1989) and the solid red line is the least–squares best fit line to the CSU–CHILL data from Carey & Rutledge (1996). The image on the left is the rain line obtained for a lightning producing storm on 14 September 2006, and the image on the right is the rain line for a non–lightning storm on 14 September 2006.

The other limiting factor of the rain line is that all values used to calculate Z_{DP} must have a higher Z_H than a Z_V. This was done in order to only use oblate particles (Carey & Rutledge, 1996; Tong *et al*., 1998; Carey & Rutledge, 2000; Cifelli *et al*. 2002; Wang *et al*., 2007), as noted previously. The rain line was obtained at time t (the "t–time") for all the lightning producing storms and for most of the non–lightning storms. Four of the non–lightning storms have a rain line that was obtained at t+15, because there were not enough data points left after the above limits were applied to produce a rain line at time t. However, these non–lightning rain lines are still applicable and comparable to the rain lines that would have been obtained at time t if there were enough data points available.

From the mixed–phase hydrometeors that were determined from the rain line calculations, one can estimate the fraction of water and ice present in the convective storm. In particular, f_R, the reflectivity weighted fraction of rain, is given by

$$f_R = \frac{Z_{HR}}{Z_H} \quad . \tag{3.4}$$

Z_{HR} is the reflectivity values for all pure rain hydrometeors and Z_H is the horizontal reflectivity for all hydrometeors (water and ice). Using f_R, it is easy to find the fraction of ice using

$$f_I = 1 - f_R \tag{3.5}$$

where f_I is the reflectivity weighted fraction of ice. It is important to note that this ice fraction does not refer to the fraction of ice volume or mass in the mixed phase region, but rather refers to the fraction of the Z_H signal in a volume that has high reflectivity values due to the scattering of ice particles (Tong *et al*., 1998).

Finally, the graupel/ice mass (M_i), and water mass (M_w) that occurs for Z_H above 35 dBZ are calculated in order to investigate whether the size of these volumes can in any way be used to infer the possible occurrence of CG lightning. This is done by using

$$M_w = 3.44x10^{-3}(Z_{HR})^{(4/7)} \ (gm^{-3}) \tag{3.6}$$

and

$$M_i = 1000\pi\rho_i N_0^{\frac{3}{7}}\left(5.28x10^{-18}\frac{Z_{HI}}{720}\right)^{4/7} (gm^{-3}) \tag{3.7}$$

where Z_{HI} is in mm^6/m^3 and is the horizontal reflectivity of the ice particles in the mixed phase, ρ_i is 917 kgm^{-3} and is the density of ice, and N_0 is $4x10^6$ m^{-4} and is the intercept parameter of an assumed inverse exponential distribution for ice (Marshall & Palmer, 1948; Carey & Rutledge, 2000). From these equations, the total mass of water and ice for all times between t–45 and t+30 for all heights between 0 °C and –40 °C, is estimated, which is the region where mixed–phase precipitation occurs, for the lightning and non–lightning storms (Doviak & Zrnić, 1993; Carey & Rutledge, 1996; Carey & Rutledge, 2000; Bringi & Chandrasekar, 2001).

It should be noted here that additional statistical analyses were performed on the dual–polarimetric radar variables to verify whether the data from the lightning and non–lightning storms were statistically different. The statistical methods as well as the results obtained from the analyses used, will be discussed in more detail in chapter 7.

3.3. MSG Satellite Interest Fields:

As mentioned earlier, much research has been done showing that satellite channel differencing and time trends are important in obtaining information about developing convective clouds. In addition to the description provided with respect to the 6.2 μm and 7.3 μm channels above that describe cloud depth and updrafts (when time trends are considered of this channel difference), other MSG channels can be used to deduce cloud top glaciation, which is particularly relevant for this study given the correlation between cloud ice volumes, the charging process and lightning. Cloud–top temperatures and cooling rates from the 10.8 μm channel are more easily related to cloud processes (depth and updraft strength; Roberts & Rutledge, 2003), whereas understanding how to estimate glaciation from IR data requires some discussion.

Estimating cloud–top glaciation from IR data can be accomplished because ice and water having varying real and imaginary portions of their index of refractions (Strabala *et al*., 1994; Baum *et al*., 2000). Therefore, the magnitude of the imaginary index of refraction will be approximately the same for water and ice between 8.5 μm and 10 μm, but will be substantially different between 10 μm and 13 μm, with more absorption taking place in ice clouds between 10 μm and 13 μm than in water clouds of

equal water content (Strabala *et al*., 1994; Baum *et al*., 2000). This increased absorption in ice clouds will lead to lower T_B values for these clouds as compared to water clouds.

The 8.7 – 10.8 μm channel difference is positive if there are cold/ice clouds present, while near–zero and negative T_B values indicate clear–sky regions (Strabala *et al*., 1994). In addition, due to more absorption taking place in ice clouds between 10 μm and 13 μm than in water clouds, the 10.8 – 12.0 μm channel difference will have larger T_B values here than for the 8.7 – 10 μm channel difference in water clouds, and ice clouds will have a lower 10.8 – 12.0 μm T_B values than the 8.7 – 10 μm T_B values. Due to this, water clouds will have a negative "tri–spectral" (8.7 μm – 10.8 μm) – (10.8 μm – 12.0 μm) T_B value whereas ice clouds will have a positive tri–spectral T_B value (Strabala *et al*., 1994, Baum *et al*., 2000).

As discussed above, the 6.2 μm MSG channel will observe the clear sky emitted water vapor at approximately 300 hPa to 400 hPa, with a T_B related to the temperature and moisture in that layer, whereas the surface or low clouds will not be sensed by the satellite, as the radiation emitted by these features are absorbed in the atmosphere (Ackerman, 1996). On the other hand, due to absorption by atmospheric gases being weak at 10.8 μm, the clear sky T_B values obtained here as mostly from the surface (and a small layer above the surface). Thus the 10.8 μm T_B value will be warmer than the 6.2 μm T_B value for the same scene, which will lead to the 6.2 – 10.8 μm T_B interest field having negative values in clear sky conditions, with > –5 K T_B values typically being obtained when cold clouds (i.e. cirrus) are present (Ackerman, 1996).

Due to these variations between cloud and water clouds, various critical values have been obtained from satellite channel differences, to approximately show when ice

clouds start to develop, i.e., glaciation. These critical values are shown in Table 3.1 for the MSG interest fields used here that indicate updraft strength, glaciation and cloud depth (as seen in Table 2.2), as well as the critical values that indicate the occurrence of ice clouds (adapted from Strabala *et al*., 1994; Ackerman, 1996; Baum *et al*., 2000; Mecikalski *et al*., 2010a). It should be noted here however, that some of these values were obtained using satellites other than MSG, but with mainly the same spectral fields.

Table 3.1: MSG interest fields used here that indicate updraft strength, glaciation and cloud depth, as well as the critical values that indicate the occurrence of ice clouds (adapted from Strabala *et al*., 1994; Ackerman, 1996; Baum *et al*., 2000; Mecikalski *et al*., 2010a).

Channel differencing and time trends	**Category**	**Critical value**
15 minute 6.2 μm – 7.3 μm	Updraft strength	Positive trends
30 minute 6.2 μm – 7.3 μm	Updraft strength	Positive trends
15 minute 10.8 μm	Updraft strength	< –4 °C
30 minute 10.8 μm	Updraft strength	< 15 min 10.8 μm
6.2 μm – 7.3 μm	Cloud depth	Differences toward 0 °C
6.2 μm – 10.8 μm	Cloud depth	From –30 °C to –10 °C
8.7 μm – 10.8 μm	Cloud–top glaciation	> 0 °C
15 minute 8.7 μm – 10.8 μm	Cloud–top glaciation	> 0 °C
(8.7 μm – 10.8 μm) – (10.8 μm – 12.0 μm)	Cloud–top glaciation	Becoming > 0 °C
15 minute (8.7 μm – 10.8 μm) – (10.8 μm – 12.0 μm)	Cloud–top glaciation	Positive trends

As such, the above–mentioned IR channels from the MSG SEVIRI sensor suite were used to obtain information on cloud–top glaciation, updraft strength and cloud depth (Table 3.1) for the 33 lightning and 30 non–lightning storms during August and September 2006. Using the IR 6.2 μm (channel 5), 7.3 μm (channel 6), 8.7 μm (channel

7), 10.8 μm (channel 9) and 12.0 μm (channel 10), which includes window channels as well as the two water vapor channels, satellite interest fields were obtained by using the Man computer Interactive Data Access System (McIDAS–X, version 2010) software package.

Figure 3.4 shows the five channels used, indicating the location of a lightning (circled in red) and non–lightning (circled in green) storm that occurred on 14 September 2006, with the NPOL radar image as reference. In this figure one can easily see the brightness differences between the two storms, with the lightning producing storm trivially appearing much brighter (i.e., colder T_B's) than the non–lightning storm in all five of the channels (and therefore the lightning storm had colder T_B values). Similar features were seen throughout most of the analysis done here. However, it should be noted that these two storms were in different times of their lifecycles, which will also influence the brightness and T_B values obtain for both.

The MSG satellite data were co–located with the NPOL radar and lightning data to analyze the lightning and non–lightning storms, involving some level of subjective comparison and selection. These data have a temporal resolution of 15 minutes, thus the storms were tracked from 75 minutes before "t" time (i.e. t – 75) to 30 minutes after t (t + 30) for every storm, and a horizontal resolution of 3 x 3 km resolution per pixel at nadir. The storms were subjectively tracked by referring to the NPOL radar and the obtained lightning locations. Once the storm locations were acquired, the 10.8 μm channel was used as the "primary locator" of the data, due to the fact that one can easily observe the main updraft location of a storm by obtaining the coldest pixel. Therefore, the T_B data were first obtained for the 10.8 μm channel over the entire region of the storm

[which varied from 3 x 3 pixels (and thus 9 x 9 km area), to 11 x 11 pixels (33 x 33 km area)], and then the exact same area was analyzed in the other four channels used. The coldest 3 pixels from the 10.8 μm were obtained for each time frame, and then averaged, in order to smooth the data which helped reduce noise caused by cloud–pixel special mismatches (i.e., round clouds observed by rectangular pixels; a cloud cut in portions by multiple pixels). The locations of these three coldest pixels in 10.8 μm were then used for the remaining four channels, with their values also being averaged to obtain a single value per time frame for each of the five channels. These T_B values were then used to calculate the ten interest fields, as seen in Tables 2.2 and 3.1, by differencing the various channels and obtaining 15–minute time–trends of these channel differences.

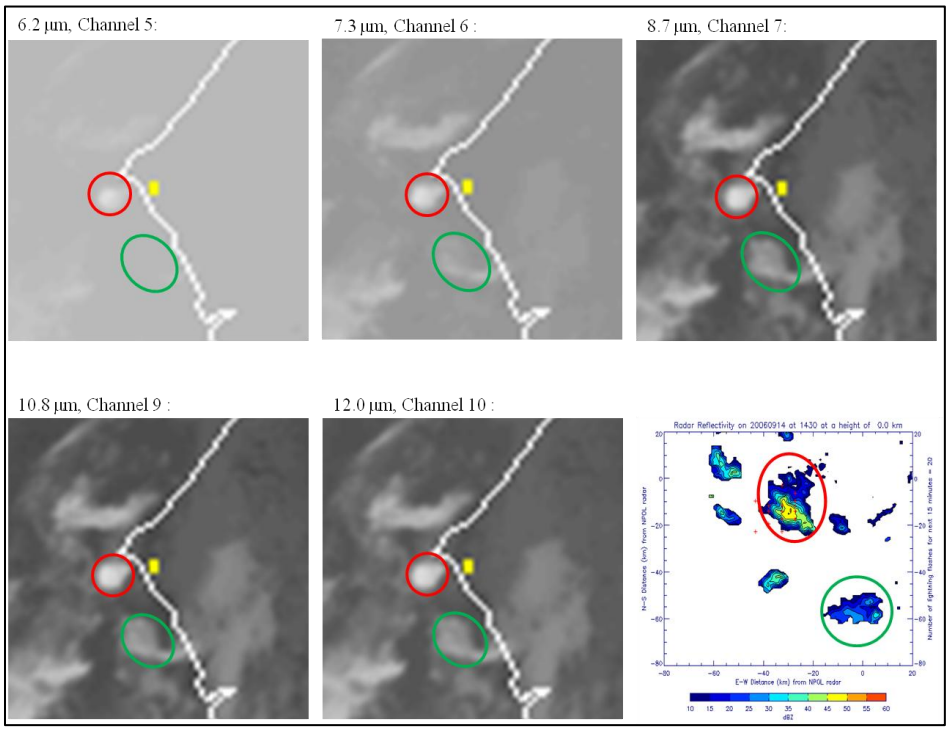

Figure 3.4: The five MSG channels used, indicating the location of a lightning (circled in red) and non–lightning (circled in green) producing storm that occurred on 14 September 2006, with the NPOL radar image as reference. The yellow rectangle indicates the location of the NPOL radar.

3.4. ATD Lightning Data:

Lightning data are utilized for delineating lightning from non–lightning events in this research. Specifically, VLF ATD lightning data, obtained from the UKMO are used. These data cover the area from 35 ° North to 5 ° South and 30 ° East to 75 ° West, however the observations used here only covered an area enclosing roughly 13 ° to 16 ° North and 15.5 ° to 18.5 ° West, which is the approximate region spanned by the NPOL radar. This lightning network is a ground–based detection system that observes the vertical component of the electromagnetic field generated by CG lightning discharges at a frequency around 10 kHz (Keogh *et al*., 2006; De Leonibus *et al*., 2007; Gaffard, *et al*., 2008). The network consists of seven remote stations, with one central control station in the UK. Figure 3.5 shows the locations of all eight stations (in blue), which include Iceland, Lerwick, Exeter, Cambone, Norderney, Korppoo, Gibraltar and Cyprus, as well the location of the NPOL radar during NAMMA (in red).

This lightning network operates at very low frequencies (10 kHz to 14 kHz), where the electromagnetic pulses from the return stroke of a CG flash can propagate over very large distances (due to low atmospheric attenuation) in the Earth–ionosphere waveguide. Therefore lightning from a large area of Earth can be detected using this method (Keogh *et al*., 2006; De Leonibus *et al*., 2007; Gaffard, *et al*., 2008). If the lightning stroke were strong enough to be detected by four stations, then the control station records the waveforms from all of the stations. Using a correlation technique, the ATD's between the waveforms are calculated. The location of the CG stroke is obtained by the intersection (loci) of hyperbolae inferred from the ATD's between each of the outstation pairs. For the lightning stroke to be used, at least four stations need to record

the flash waveform and therefore it is possible to fix the location of the stroke on the ground. The accurate recording of the ATD for each stroke is very important, as it influences the location accuracy (LA) of the stroke, with the time accuracy being approximately 0.1 μs, which is achieved by a rubidium oscillator. The processing of the data takes roughly 30 seconds and the stroke locations are displayed every five minutes (Lee, 1986; Lee, 1990; Roger *et al*., 2004; Keogh *et al*., 2006; De Leonibus *et al*., 2007; Gaffard, *et al*., 2008).

The LA and detection efficiency (DE) of the CG flashes recorded by the network vary tremendously over the domain covered by the network. The closer the lightning is to the various stations, the better the LA and DE will be, and vice versa. The LA is roughly 5 km in the UK, 20 km in Europe, 40 km inside a 3 000 km radius from the UK and 100 km at the perimeters of the network (De Leonibus *et al*., 2007). The location of the NPOL radar is approximately 2 000 km from the closest lightning station, indicating that the LA will only be approximately 40 km. In addition, the DE also varies, with 70 % – 90 % in the winter and 20 % – 90 % in the summer for the UK and Europe and 10 % – 70 % (throughout the year) for the Eastern parts of Europe. For Africa, the DE can vary from 80 % in North Africa to 0 % in South Africa, and 20% in South America (Keogh *et al*., 2006; De Leonibus *et al*., 2007). However, the DE for Africa could be as low as roughly 20 % to 30 % on average (WMO, 2006). Therefore, because the NPOL radar is located approximately 2 000 km from the closest station (Gibraltar, refer to Figure 3.5) and 3 500 km from Exeter and Cambone, the LA at NPOL is only approximately 40 km and the DE could be anywhere from 20 % to 60 %. This will have an impact on the results presented in chapters 5 and 6, and are discussed in more detail in

chapter 4. Another noteworthy point is that the ATD network only detects very strong CG strokes, meaning that the DE values above might be decreased even more over the NAMMA domain, as IC flashes occur much more frequently than CG flashes, and many of the weaker CG strokes not being recorded for the area of interest.

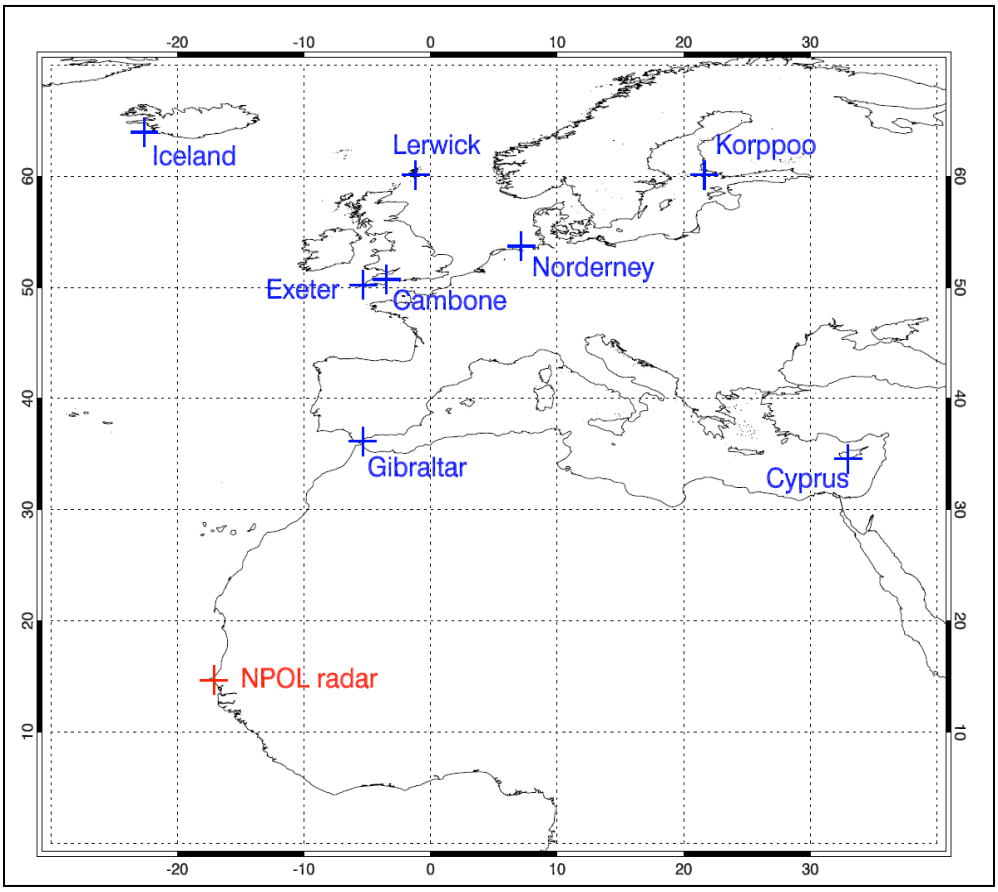

Figure 3.5: The locations of all eight ATD VLF lightning stations (in blue), which include Iceland, Lerwick, Exeter, Cambone, Norderney, Korppoo, Gibraltar and Cyprus, as well the location of the NPOL radar (in red) during NAMMA.

The location of the CG strokes are disseminated in latitude and longitude coordinates, which is converted to Cartesian coordinates in order to match the lightning with the radar data. This is done for all the lightning strokes that occurred within a

200 km radius of the radar. The lightning locations were then overlaid on the radar data to observe which storms produced lightning. Due to the low LA mentioned earlier, a storm is identified as a lightning producing storm when a stroke was located immediately on top of the storm (as seen in from a horizontal plot of the Z_H field), and only strokes that were located within 20 km of the radar echo edge of the storm (when no other storm is closer to at specific stroke) were used as part of that storm. If there were another storm that produced lightning and it was located closer to the lightning than the first storm, then the lightning will be used as part of the closest storm.

CHAPTER 4

ERRORS

As in all research, there are always some random errors, biases and calibration issues that occur with instruments and data. Carey (2007) performed a study in which the obtained NPOL radar data were compared to the National Center for Atmospheric Research (NCAR) S–band Polarimetric (SPOL; NCAR SPOL) radar, the CSU–CHILL radar and the WSR–88D radar (and others). In this study it was found that the NPOL radar has general radar–system issues, including transmitter and receiver chain hardware and/or signal processing problems. This was found by radar variables analyzed for drizzle, as these hydrometeors should have Z_{DR} and ρ_{HV} values of approximately 0 dB and 0.99, respectively for S–band radars. The study revealed that the median values obtained from NPOL data for Z_{DR} and ρ_{HV} in drizzle were 0.9 dB and 0.95, respectively, implying the data obtained from NPOL have a random error of –0.04 for ρ_{HV} and a Z_{DR} bias of 0.46 dB, which could indicate that the data used is of poor quality. However, it should be noted that these values were only obtained from a relatively small sample (< 15 convective events) and thus might not be representative over all storms analyzed

for the research presented here. Furthermore, and particularly relevant to this study, the NPOL radar experienced problems with attenuation when the antenna became wet (i.e., when a storm moved immediately over the radar); Z_H values were roughly 9 dBZ lower as compared to the NEXRAD radar during heavy rain periods (Carey, 2007). This latter problem is handled in this particular study by taking care to not consider any storms that developed or moved close to the radar within ~ 1 hour after a previous storm moved directly overhead of NPOL. The errors in the Z_{DR} and ρ_{HV} fields are taken into account while interpreting the results here, but no error corrections are made in the analysis. Therefore caution should be taken when comparing the results found here to other dual–polarimetric radar studies.

There are a few points that need to be considered when analyzing the results of the satellite data used. For instance, all the storms were tracked backward to t–75 and in most of the storm cases, this meant that the ground was observed because the storms had not yet developed. Therefore it was somewhat difficult to ensure that the correct storm locations were recorded during these times. However, this should not influence the results by much, as the focus was on how the T_B values decreased over time, especially the closer one got to the t–time. In addition, as with all satellites, there are some calibration biases with MSG SEVIRI, summarized in Table 4.1 (EUMETSAT, 2007). As can be seen, all the channels used in this research have a positive bias, although these are relatively small and should not have a big influence on the results presented here due to averaging and time–trends calculated. In addition, these errors are well within the variability that one can expect across a single pixel (i.e. a pixel has a resolution of 3 km at nadir; thus has an area of 9 km, with an average value across cloud–tops given for that

one pixel). Furthermore, because time–trends are used, these biases should be eliminated, and channel differences will also remove some of the bias issues. In addition, the satellite viewing angle might also influence some results, with higher viewing angles leading to both the tops and sides of clouds being observed (instead of just cloud–tops) in a given cloud pixel, which may dull pure cloud–top signatures (Mecikalski *et al*., 2010a). However, because the location of this research is centered on 14.65654 ° N, the viewing angle is relatively small and should not influence the results of the cloud–top temperatures by much. Solar angles also influence the results obtained from the satellite fields, especially for the VIS channels, but to a lesser extent for the IR channels (Mecikalski *et al*., 2011). These are more evident early morning and early evening, when the solar viewing angles are low. The storms used here all developed during the day, with most of the storms used having their t–times between 1100 and 1800 UTC, yet a few storms had their t–times before 1100 and after 1800, which will increase the noise in the results. These early morning and early evening storms were unavoidable due to the small sample size of usable storms during NAMMA. Furthermore, errors caused by convective clouds that do not fill the entire 3 x 3 km pixel will lead to problems with the T_B values and thus will lead to artificially higher temperatures if the ground is partially within the scene. This is also why it was decided to use the average of the three coldest pixels for each storm time frame of the t–75 to t+30 period, which helps smooth the data and lead to fewer large errors.

In addition to the above–mentioned possible errors, there were also concerns with the ATD VLF lightning network. As mentioned earlier, the DE over the area of interest was as low as 20 % to 30 % on average, and the LA is only roughly 40 km and therefore

only the strongest CG strokes are recorded (WMO, 2006; De Leonibus *et al*., 2007). These values might lead to some of the storms that were labeled as non–lightning, actually falling into the lightning producing category. Due to the large LA values, some of the lightning locations might be off by up to 40 km, which means that a CG stroke might be inaccurately placed with one storm instead of an adjacent storm. Therefore, as mentioned earlier, a storm was seen as a lightning producing storm when a stroke was located immediately on top of the storm, and only strokes that were located within 20 km of the edge of the detectable echo (when no other storm is closer to the stroke) were used for the specific storm. If there were another storm that produced lightning and it was located closer to the lightning than the other storm, then the lightning will be used as part of the closest storm. These limits will help decrease these errors. However, due to all these errors, it was decided to do statistical analyses on the data as well, in order to verify that the lightning and non–lightning storms are indeed significantly different. These statistics will be discussed in more detail in chapter 7.

Table 4.1: Overview of requirements and results of radiometric accuracy for MSG–2, cold channels (adapted from EUMETSAT, 2007).

Channel (μm)	**Manufacturer Blackbody Calculation Uncertainty estimate (K)**	**Bias of Satellites (K)**
IR 6.2	0.73	0.04
IR 7.3	0.73	0.28
IR 8.7	0.80	0.16
IR 10.8	0.94	0.11
IR 12.0	0.93	0.23

CHAPTER 5

SINGLE STORM LIGHTNING AND NON–LIGHTNING RESULTS

In this chapter, the results from one lightning and one non–lightning storm will be discussed to provide some context for the average results that will be seen in Chapter 6. This will be done by showing the analysis of the dual–polarimetric radar and MSG satellite interest fields, together with vertical cross sections of the dual–polarimetric radar fields. These are important to distinguish the occurrence of ice/graupel and water hydrometeors.

The lightning and non–lightning storms that were chosen both occurred on 14 September 2006; M1 did not producing any lightning and M3 produced 23 flashes (30 strokes) between time t and t+30 (with more flashes recorded after this time). The t–time for M1 occurred at 1300 UTC and for M3 the t–time was at 1415 UTC (please refer to Appendix A for sounding images on this day as well as for all other storm days). The reason for choosing to show these two storms is that they occur on the same day and have roughly the same area; M1 has an area of approximately 30 x 20 km and M3 has an area of roughly 20 x 25.

Figure 5.1 displays the horizontal cross section of radar Z_H images of the lightning storm, M3 (left) and the non–lightning storm, M1 (right), both taken at a height of 1.5 km above ground level at the respective t–times (1415 UTC for M3 and 1300 UTC for M1). Note the different axes for both images. The red crosses in M3 indicate the location of each lightning flash, totaling 7 flashes within the time period from 1415 UTC to 1430 UTC. Clearly both storms had almost the same areal dimensions, but not evident in this Figure (but will be shown later) is that at time t, the lightning storm had a cloud–top height of approximately 15 km while the non–lightning storm only has a cloud–top height of near 11 km. Also, both storms had Z_H values of around 45 dBZ, although the area constituting these reflectivity values varies between the two storms; the lightning storm has a much larger area covered by > 45 dBZ than the non–lightning storm.

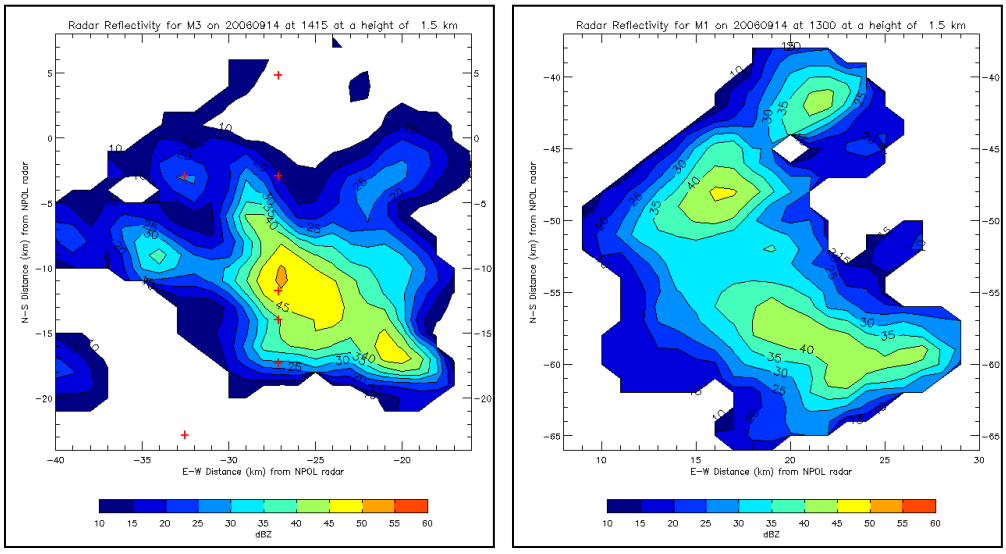

Figure 5.1: A horizontal cross section of radar Z_H images of the lightning storm, M3 (left) and the non–lightning storm, M1 (right), both taken at a height of 1.5 km above ground level at the respective t–times (1415 UTC for M3 and 1300 UTC for M1). Note the different axes for both images. The red crosses in M3 indicate the location of each lightning flash, totaling 7 flashes within the next 15 minutes.

It is important to note though that most of the non–lightning storms were smaller in dimension and reached lower maximum cloud–top heights than M1. Approximately half of the lightning storms reached the same size and maximum cloud–top height (due to the height limitation of 15 km introduced in the data) and higher, as seen for M3, yet the number of lightning flashes for the lightning storms varied from 2 flashes to more than 30 flashes in the 30 minutes after time t. Therefore it is clear that there are large variations in these storms, making it very difficult to obtain a lightning and non–lightning storm that are completely representative of the average results, as well as being comparable to each other. The remainder of this chapter will follow approximately the same layout as the previous chapter, with the un–normalized CFADs for each radar variable and the MSG interest fields being discussed separately; however, here the individual rain lines that were obtained will also be discussed.

5.1. Vertical cross sections of Z_H, Z_{DR} and ρ_{HV}:

As stated, vertical cross sections of the various dual–polarimetric radar variables will be shown to provide some context for the average un–normalized CFADs that will be shown in Chapter 6. Also, Z_H will have higher values for hail and graupel (usually $\geq$ 35 dBZ); Z_{DR} values will be around 0 dB and lower (negative), and ρ_{HV} values $\geq$ 0.95. Z_H for rain could vary between 10 dBZ (small drops) to roughly 40 dBZ (and higher for large drops); Z_{DR} values will be greater than about 0.5 dB, with larger values as the drop size increases, and ρ_{HV} values will be > 0.97. Ice particles will also have $Z_H \geq$ 10 dBZ, Z_{DR} values around 0 dB and ρ_{HV} values > 0.97. Therefore, there is a lot of overlap in the dual–polarimetric values, which is why a combination of vertical cross sections is

important to show for the above variables. It is important to remember here that the NPOL radar had random errors, which lead to Z_{DR} errors of +0.46 dB and ρ_{HV} errors of –0.04. This will be seen clearly in the un–normalized CFADs, with the mode of these radar variables being shifted to left for the ρ_{HV} values and shifted to the right for the Z_{DR} values.

Figure 5.2 shows the results for the vertical cross sections of the lightning storm, M3 (left column) and the non–lightning storm, M1 (right column) at t–45. For storm M3, the plots are as follow: Z_H (top left); Z_{DR} (middle, left) and ρ_{HV} (bottom, left) and for storm M1 the plots are Z_H (top right); Z_{DR} (middle, right) and ρ_{HV} (bottom, right). Note the different x–axis ranges for the lightning (22 km range) and non–lightning (18 km range) storms and both storms have a y–axis range of 0 km to 15 km. For the lightning storm (left column), reflectivity values of up to 40 dBZ is reached at the ground, with values of $\geq$ 10 dBZ being reached to –10 °C. The lightning storm has high reflectivity values of $\geq$ 35 dBZ close to the ground in combination with Z_{DR} values > 0 dB below the melting layer (0 °C). This is indicative of water drops with varying sizes in this region. In addition, the low ρ_{HV} values (< 0.94) below the melting layer also indicates that these drops vary in size, but are mostly small and medium–sized drops. The non–lightning storm has much lower reflectivity values at t–45; a maximum of 35 dBZ is reached at the ground. In addition, there are no Z_H values above the melting level, and thus all these particles are water drops. This is confirmed by the mostly positive Z_{DR} values of up to 1.5 dB in this region. The large spread of the ρ_{HV} values for the non–lightning storm also indicates that there are a variety of drop sizes present at this time, with smaller drops being more evident here.

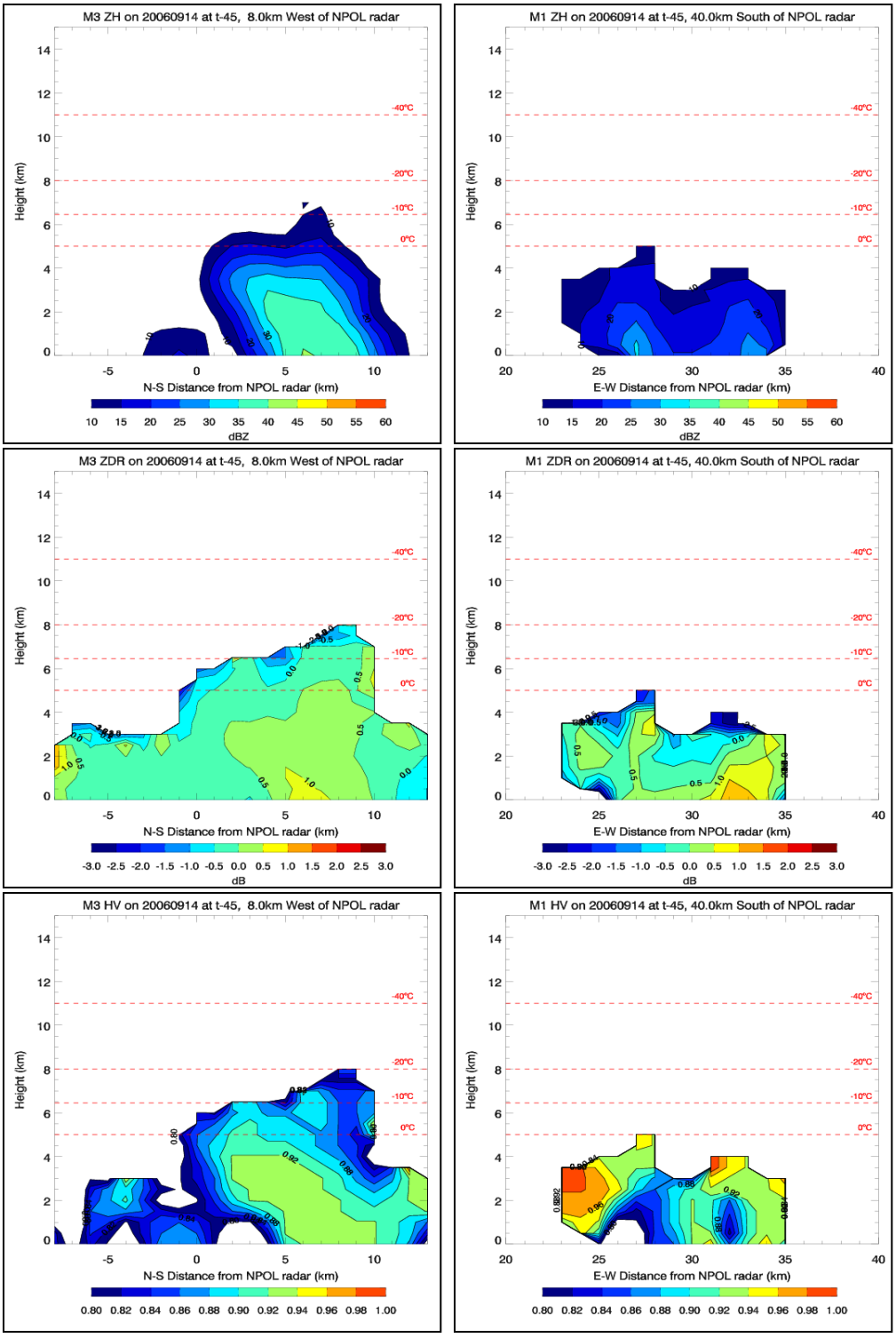

Figure 5.2: Vertical cross sections of the lightning storm, M3 (left column) and the non–lightning storm, M1 (right column) at t–45. For storm M3, the plots are as follow: Z_H (top left); Z_{DR} (middle, left) and ρ_{HV} (bottom, left) and storm M1 the plots are Z_H (top right); Z_{DR} (middle, right) and ρ_{HV} (bottom, right).

In Figure 5.3, which shows the results for the vertical cross sections of the lightning storm, M3 (left column) and the non–lightning storm, M1 (right column) at t–30 (the explanation of the plots are the same as in Figure 5.2), it is clear that both storms are growing in intensity and vertical height. The lightning storm has Z_H values of $\geq$ 40 dBZ for a larger area close to the ground, indicating that the drops are increasing in size. Smaller Z_H values between 10 dBZ and 30 dBZ are also seen to 8 km (–20 °C) indicating that these drops are smaller with some being frozen. This is confirmed by the Z_{DR} plot (middle, left) which shows mostly positive Z_{DR} values below the melting level. Between 5 km and 8 km, the Z_{DR} values are lowered and point to the hydrometeors being either smaller water drops or frozen drops in this layer. Due to the Z_H values being below 35 dBZ in the layer above 5 km (and thus colder temperatures), there is no large hail or graupel present at this time, however smaller graupel and hail might be possible, as seen by the lower Z_{DR} values. From the 0.92 to 0.94 ρ_{HV} values (Figure 5.3; bottom, left) in the same region that high reflectivity values ($\geq$ 35 dBZ) and 0.5 dB to 1.5 dB Z_{DR} values were observed, one can see that medium and larger sized water drops are present in this region. This could also indicate the melting of smaller graupel and hail particles.

The Z_H values for the non–lightning storm (Figure 5.3; top, left) also reach to 40 dBZ, however values $\geq$ 35 dBZ only reach 2.5 km. This, together with the higher Z_{DR} values of $\geq$ 0.5 dB shows that there are medium–sized drops located in this region. Also, low reflectivity values ($\leq$ 15 dBZ) and low Z_{DR} values of $\leq$ –0.5 dB are only seen to 6.5 km, therefore the non–lightning storm mostly consists of small water drops in this region, with some very small frozen drops. Finally, the ρ_{HV} values of 0.94 in the same

region as the higher Z_H and Z_{DR} values close to the ground confirms that the drops are not very small and have horizontal and vertical dimensions that are close to each other.

At t–15 (Figure 5.4), the lightning storm (left column) now has Z_H values reaching ≥ 45 dBZ, Z_{DR} values ≥ 0.5 dB and ρ_{HV} values from 0.90 to 0.94 to 5.5 km. The combination of these variables signifies the presence of larger drops and melting graupel and small hail below 5 km. The Z_H values ≥ 25 dBZ, Z_{DR} values between –1.0 dB and 1.5 dB and ρ_{HV} between 0.84 and 0.94 indicate that ice particles, graupel, hail and larger drops are present up to –20 °C. The lower Z_H values of 10 dBZ to 20 dBZ seen at colder than –40 °C, with negative Z_{DR} values indicate the presence of ice crystals at the top of the cloud.

The non–lightning storm (right column) has Z_H values between 30 dBZ and 45 dBZ at t–15, Z_{DR} values ≥ 0.5 dB and ρ_{HV} values ≥ 0.92 below 5 km; all pointing to the occurrence of medium and large–sized water drops being present. Above 5 km, Z_H values vary between 10 dBZ and 30 dBZ, Z_{DR} values are between –1.0 dB and 0.5 dB and ρ_{HV} values are mostly ≥ 0.86. This shows that the non–lightning storm has a variety of drop sizes present above 5 km, with small frozen drops also being present at this time. Therefore, one can see that the lightning storm has many more frozen drops, graupel and hail present in the mixed–phase region, with ice crystals at the top of the cloud as compared to the non–lightning storm. In addition, the lightning storm also has a large range of drop sizes present throughout the cloud, which is important for coalescence and riming to occur. Finally, although this cannot be seen by the NPOL radar due to the wavelength of operation (10 cm), supercooled drops will also be present in the lightning storm, which is important for electrification and CG lightning to occur.

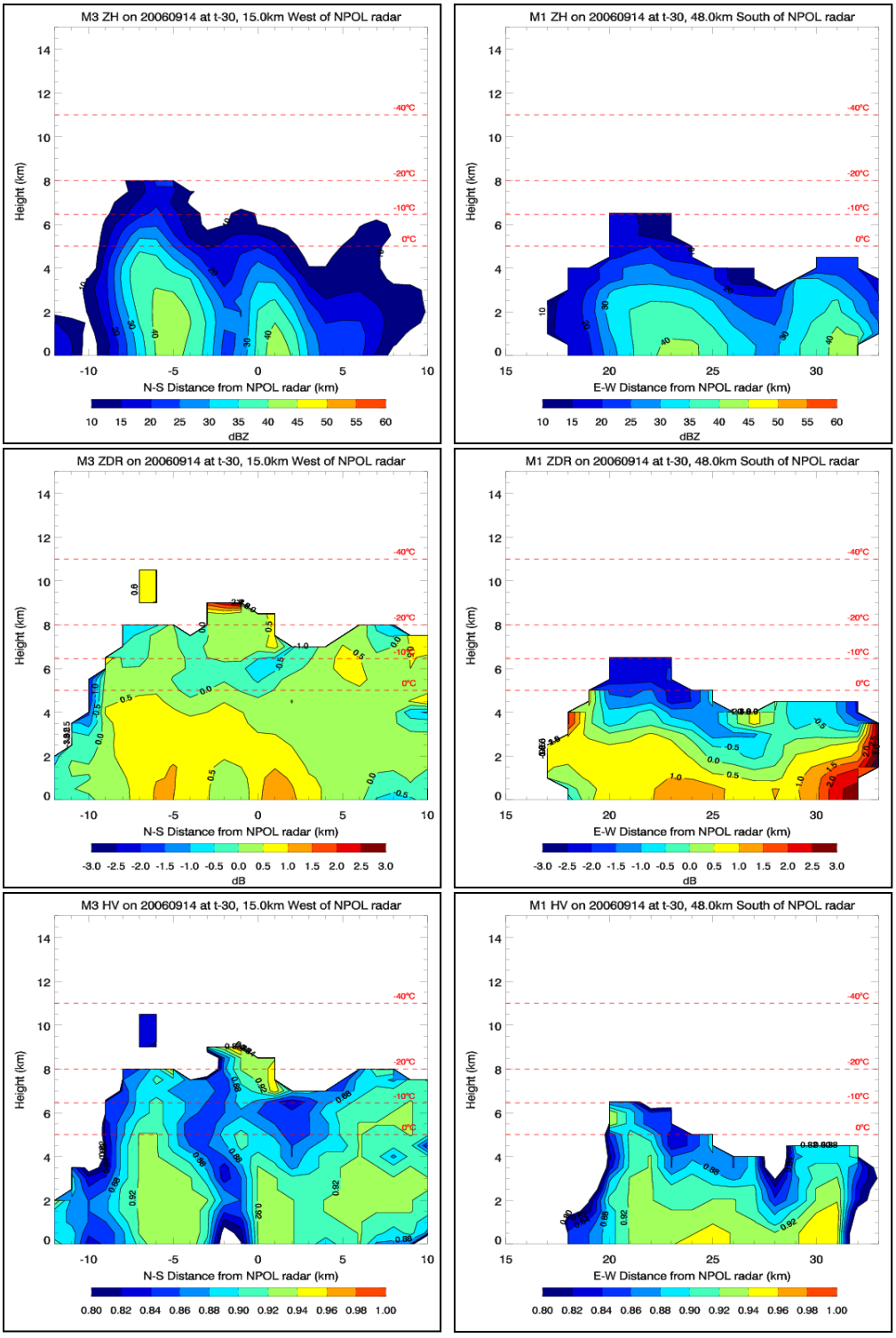

Figure 5.3: Vertical cross sections of the lightning storm, M3 (left column) and the non–lightning storm, M1 (right column) at t–30. For storm M3, the plots are as follow: Z_H (top left); Z_{DR} (middle, left) and ρ_{HV} (bottom, left) and for storm M1 the plots are Z_H (top right); Z_{DR} (middle, right) and ρ_{HV} (bottom, right).

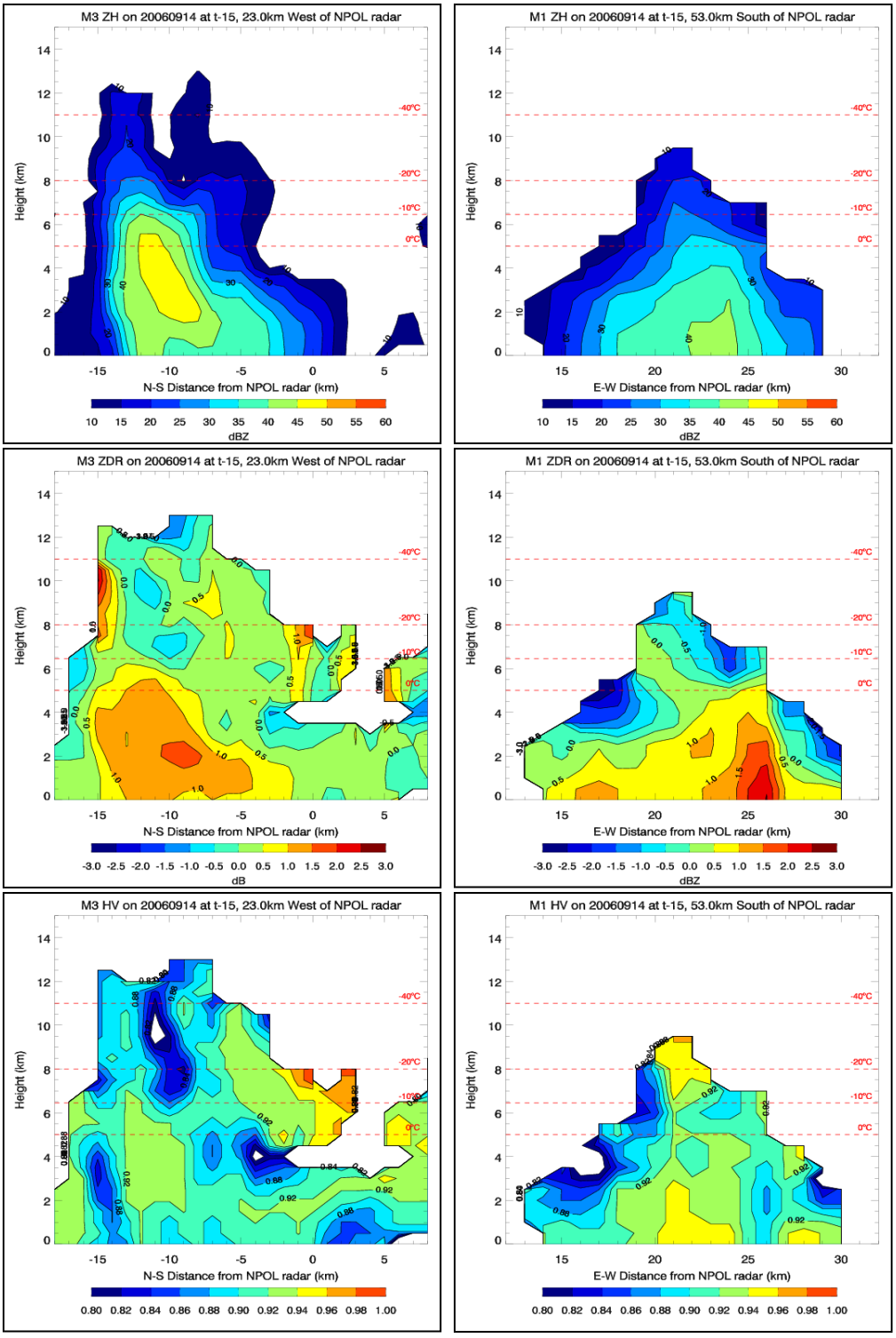

Figure 5.4: Vertical cross sections of the lightning storm, M3 (left column) and the non–lightning storm, M1 (right column) at t–15. For storm M3, the plots are as follow: Z_H (top left); Z_{DR} (middle, left) and ρ_{HV} (bottom, left) and for storm M1 the plots are Z_H (top right); Z_{DR} (middle, right) and ρ_{HV} (bottom, right).

At time t (Figure 5.5) the lightning storm (left column) has a column of Z_H values $\geq$ 30 dBZ and Z_{DR} between 0 dB and 0.5 dB occurring to 14 km. At this height, all particles are frozen and the Z_H and Z_{DR} values confirm this. In the mixed–phase, however, Z_H values up to 45 dBZ are seen and Z_{DR} values vary between –0.5 dB and 1.0 dB, indicating the presence of graupel, hail, frozen drops, as well as smaller and medium–sized water drops in this region, especially for the columnar region of higher reflectivities. This is also confirmed by the columnar region of ρ_{HV} values between 0.9 and 0.94. Due to this, it is clear that the hydrometeors needed for charging and electrification to occur to the point of CG lightning occurring, is present, which is confirmed by the presence of CG lightning within 15 minutes after time t.

The non–lightning storm (Figure 5.5, right column) has Z_H values reaching 45 dBZ and only positive Z_{DR} values reaching 2.0 dB below the melting layer. This, in combination with ρ_{HV} values < 0.96 indicate that medium to large water drops are present in this region, with melting hail or graupel not being present, due to the lower Z_H values. If melting graupel or hail were present, larger Z_H values would have been present, as was the case with the lightning storm. Also, Z_H values between 10 dBZ and 30 dBZ are only seen to 11 km, which is much lower in terms of reflectivity values and maximum height than was observed for the lightning storm. However, negative Z_{DR} values (as well as positive Z_{DR} values) are present in this region, which indicate that some frozen drops and water drops of varying sizes occur in the mixed–phase region. Nevertheless, even with these particles being present, and although some charging is possible, it was not enough for CG lightning to be observed in this storm.

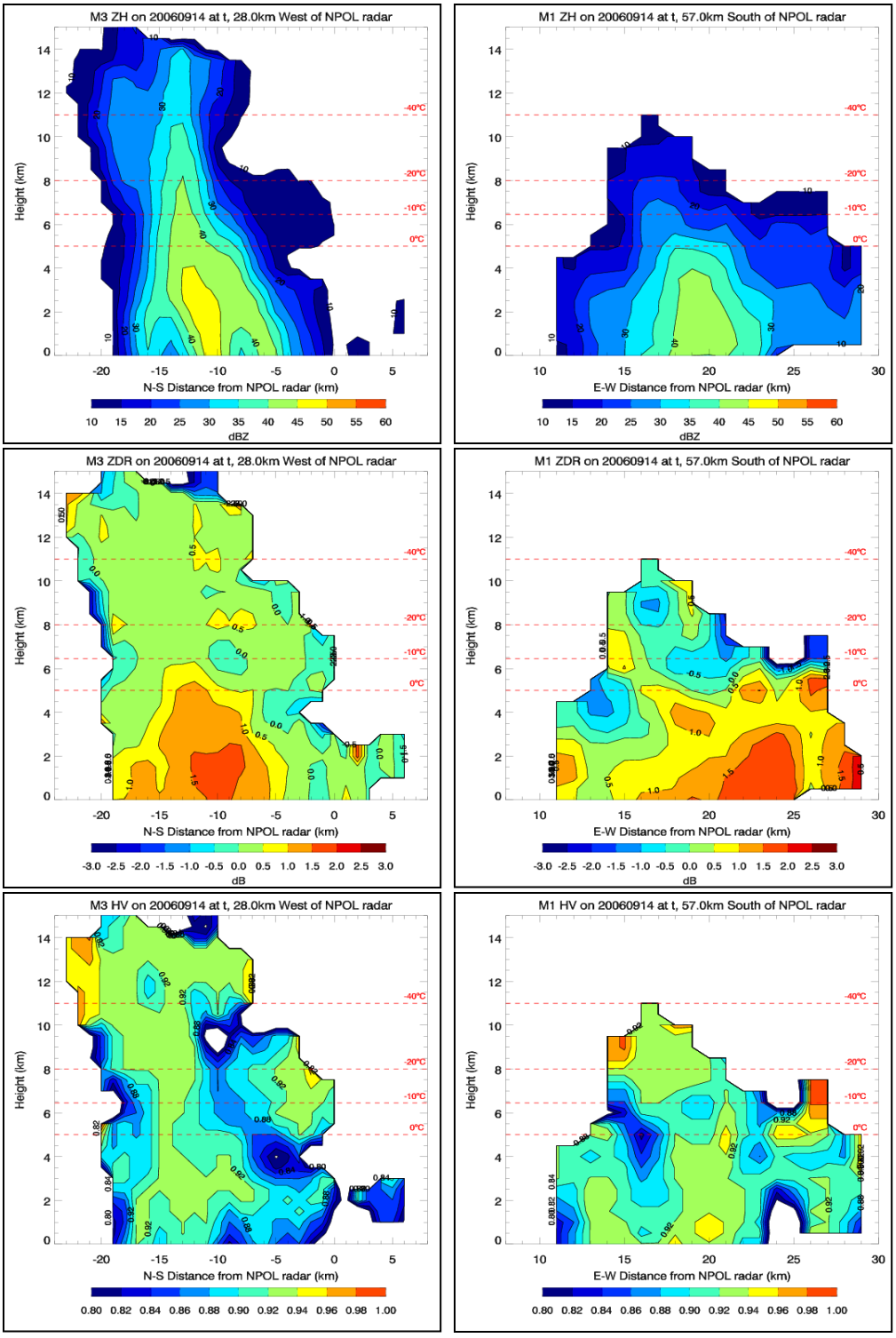

Figure 5.5: Vertical cross sections of the lightning storm, M3 (left column) and the non–lightning storm, M1 (right column) at time t. For storm M3, the plots are as follow: Z_H (top left); Z_{DR} (middle, left) and ρ_{HV} (bottom, left) and for storm M1 the plots are Z_H (top right); Z_{DR} (middle, right) and ρ_{HV} (bottom, right).

At t+15 (Figure 5.6) the lightning storm (left column) has an area of large Z_H values (to 45 dBZ); larger than was seen at time t, denoting that more melting graupel and hail is present below the melting layer than was observed earlier. This is evident by the large positive Z_{DR} values of up to 2 dB and ρ_{HV} values > 0.90 for the same region as the high Z_H values. Furthermore, Z_H values between 10 dBZ and 40 dBZ are present in the mixed–layer; Z_{DR} values of mostly 0 dB to 1 dB and ρ_{HV} values around 0.9 and 0.92 are seen for this region. This indicates that there is a variety of drop sizes present, together with varying sizes of graupel and hail. The lightning storm also has Z_H values to 30 dBZ present up to 15 km. At this height, all particles are frozen, and therefore the storm has an abundance of ice crystals present for electrification to occur (the ice crystals will reached the mixed–layer due to down drafts).

Much lower Z_H values are seen for the non–lightning storm at t+15 (Figure 5.6, right column) as compared to the lightning storm at the same time. This means that smaller drops as well as fewer melting graupel and hail (that are also much smaller) are present in the non–lightning storm below the melting layer. This is confirmed by Z_H values only reaching 40 dBZ, Z_{DR} values varying between 0 dB and 1.5 dB and ρ_{HV} values being ≥ 0.90. Above the melting layer, the Z_H values vary between 10 dBZ at 10 km and 40 dBZ at 5 km. Although the larger Z_H values could indicate the presence of small graupel and hail, these particles do not occur frequently, as can be seen by the varying Z_{DR} values of mostly between 0 dB and 1 dB and ρ_{HV} values being mostly ≥ 0.90. Therefore, as was the case at time t, although small graupel and hail is possible, especially at around 5 km to 6 km, these particles did not occur enough to lead to sufficient charging and electrification to occur to lead to the presence of CG lightning.

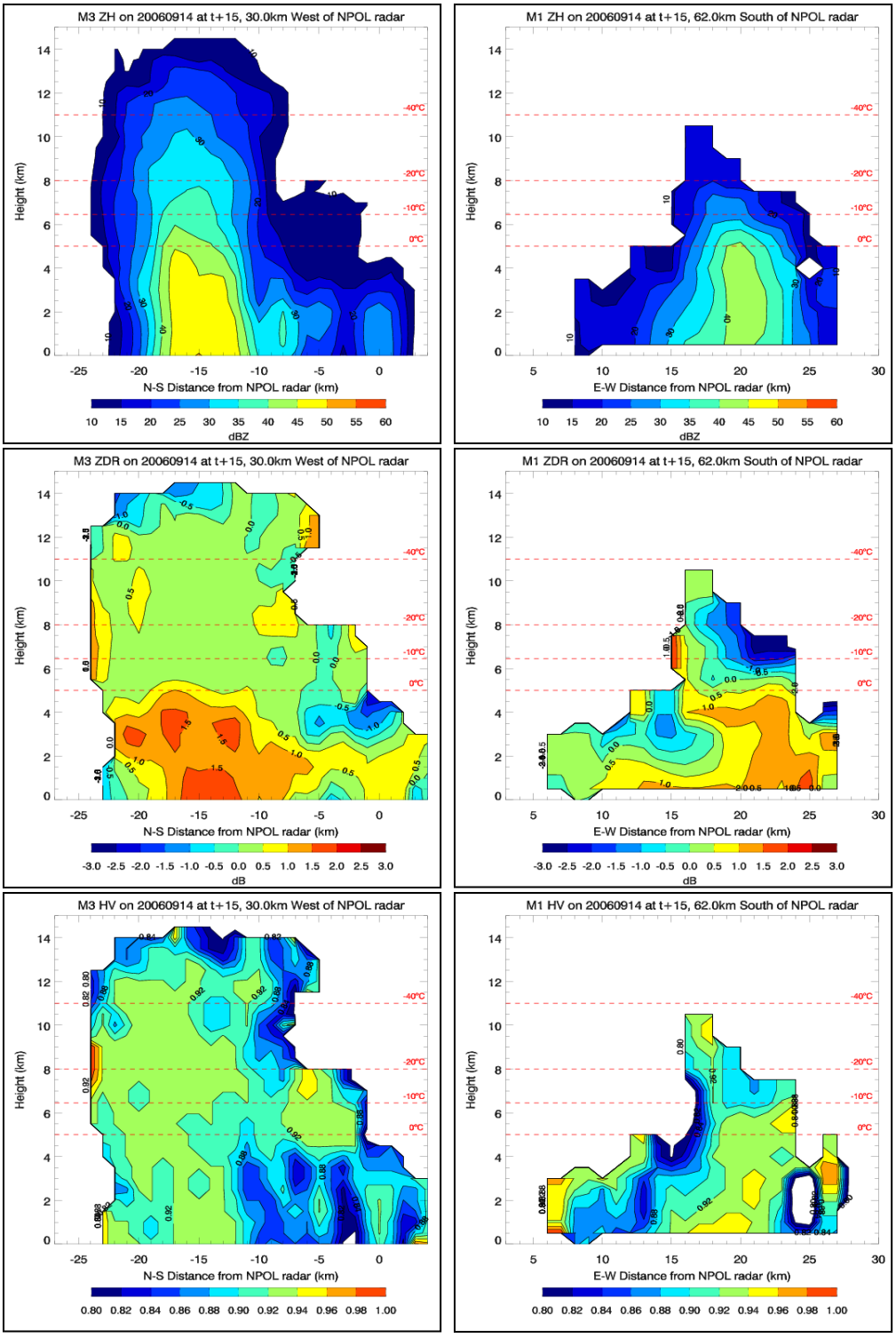

Figure 5.6: Vertical cross sections of the lightning storm, M3 (left column) and the non–lightning storm, M1 (right column) at t+15. For storm M3, the plots are as follow: Z_H (top left); Z_{DR} (middle, left) and ρ_{HV} (bottom, left) and for storm M1 the plots are Z_H (top right); Z_{DR} (middle, right) and ρ_{HV} (bottom, right).

At t+30 (Figure 5.7), the lightning storm (left column) still consist of high reflectivity values of ≥ 50 dBZ below the melting layer; Z_{DR} values mostly ≥ 0.5 dB and ρ_{HV} values ≥ 0.90. This is all indicative of melting graupel and hail, as well as large water drops occurring in this region. In the mixed–phase layer, the Z_H values vary between 10 dBZ and 40 dBZ at 5 km, with Z_{DR} values being between 0 dB and 0.5 dB. This, together with ρ_{HV} values mostly ≥ 0.90 shows the presence of graupel, hail, as well as medium–sized water drops in this region. Ice crystals are also present at 15 km, however the amount of ice crystals is decreased as compared to t+15, as can be seen by the smaller area of Z_H values above 11 km.

The non–lightning storm is dissipating as can be seen by the lower Z_H values and lower maximum height reached at t+30 (Figure 5.7, right column). Only a small area of the storm has Z_H values higher than 30 dBZ, with most of this area having Z_{DR} values ≥ 0 dB. This, in combination of varying ρ_{HV} values indicate that the storm now consists mostly of smaller and medium–sized drops below 5 km. There are some particles between 5 km and 8 km, with Z_H values between 10 dBZ and 30 dBZ, Z_{DR} values mostly between –1 dB and 0.5 dB and ρ_{HV} values mostly between 0.9 and 0.94. This shows that there are some small graupel and hail present in the mixed–phase region, however, most of the hydrometeors in this region is smaller water drops.

From this analysis, it is clear that the lightning storm has much more graupel, hail and ice crystals in the mixed–phase region than the non–lightning storm. However, even though the NPOL radar cannot see the supercooled liquid droplets, the lightning storm also consisted of these hydrometeors, as is clear by the presence of CG lightning for this storm.

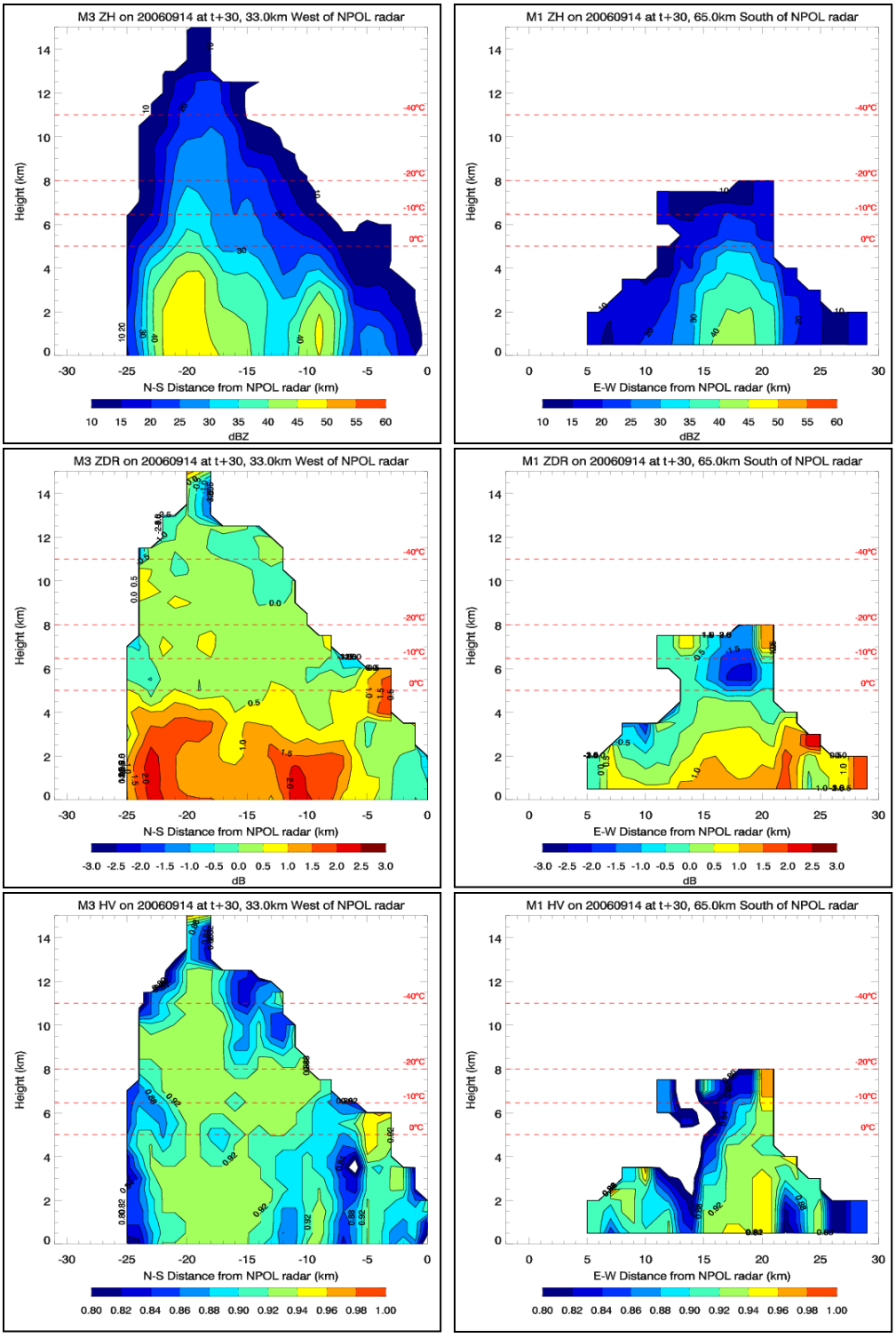

Figure 5.7: Vertical cross sections of the lightning storm, M3 (left column) and the non–lightning storm, M1 (right column) at t+30. For storm M3, the plots are as follow: Z_H (top left); Z_{DR} (middle, left) and ρ_{HV} (bottom, left) and for storm M1 the plots are Z_H (top right); Z_{DR} (middle, right) and ρ_{HV} (bottom, right).

5.2. Z_H, Z_{DR} and ρ_{HV} CFADs:

Figure 5.8 through 5.13 are the un–normalized Z_H (also called CZ in the plots) CFADs for the lightning storm, M3 (left) and the non–lightning storm, M1 (right) for all times from t–45 (Figure 5.8) to t+30 (Figure 5.13). As mentioned earlier, the CFADs presented here were not normalized with the bin size at each level and therefore their units are % dBZ^{-1}. Even at t–45 (Figure 5.8) one can see that there are differences between the lightning and non–lightning producing storms. The lightning storm has Z_H values of at least 1 % dBZ^{-1} up to 9 km, where the non–lightning storm only has Z_H values up to roughly 6.5 km. The lightning storm has values up to 42 dBZ at 1 % dBZ^{-1} to a height of approximately 3 km, with 30 dBZ values being observed to a height of 5 km. The mode seems to be located between 0 km and 9 km, with 10 dBZ to 25 dBZ being reached here at ≥ 15 % dBZ^{-1}. The non–lightning storm only has Z_H values up to 40 dBZ and 43 dBZ at 1 % dBZ^{-1} between 0 km and 2 km, which are lower as compared to the lightning storm. Although the maximum height of the storm top is lower than for the lightning storm, the mode is located between 0 km and 5.5 km with 10 dBZ to 20 dBZ being reached at ≥ 15 % dBZ^{-1}, however, values of up to 30 dBZ are obtained between 0 km and 2.5 km at ≥ 15 % dBZ^{-1}. The non–lightning storm also has a protrusion that is evident at around 5.5 km, with up to 30 dBZ being reached here at 1 % dBZ^{-1}.

At t–30 (Figure 5.9), the lightning storm now reached 11 km with Z_H values of to 45 dBZ being reached between 0 km and 3.5 km at ≥ 1 % dBZ^{-1}. It is clear that larger water drops and possible graupel and hail are already present in this storm. The mode now consists of values ranging from 10 dBZ to 27 dBZ between 0 km and 2.5 km and

from 10 dBZ to 20 dBZ between 4 km and 9 km, both at ≥ 15 % dBZ^{-1}. This indicates that there are many small drops located in the mixed phase region, which is important for the growth of the larger drops, as well as for the creation of supercooled droplets. These drops could be lofted to colder temperatures, where freezing might not occur immediately, leading to supercooled drops forming. Also worth mentioning is the presence of a small tilt in the reflectivity mode below 5 km, with a vertical alignment above this level, although this tilt is not very noticeable (as was seen for the average lightning storm results). The non–lightning storm also increased in height, with 7.5 km being reached at t–30. Z_H values of up to 45 dBZ are reached at ≥ 1 % dBZ^{-1}, although this only occurs below 1.5 km. Here, the mode is tilted throughout the cloud, with it varying from 15 dBZ to 35 dBZ below 3 km and between roughly 10 dBZ to 23 dBZ between 3 km and 7.5 km, all at ≥ 15 % dBZ^{-1}. A higher occurrence of larger Z_H values is observed for the non–lightning storm as compared to the lightning storm, especially below 5 km. This suggests the presence of many small to medium–sized drops, possibly not as large as in the lightning storm located below 5 km at this time, however, above 5 km the precipitation particles are small and probably all in the liquid phase.

Figure 5.10 displays the CFADs for the lightning storm, M3 (left) and the non–lightning storm, M1 (right) at t–15, 15 minutes before the first CG lightning flashes were recorded for the lightning storm. One can see that during t–30 and t–15, there are many changes that occurred for the lightning storm, including another increase in maximum cloud–top height, with 13.5 km being reached. Z_H values of up to 49 dBZ at ≥ 1 % dBZ^{-1} are reached below 5 km, indicating that large raindrops, as well as graupel and hail are definitely present at these heights. The mode now extends from 0 km to

13.5 km, and includes values between 10 dBZ and roughly 20 dBZ at ≥ 15 % dBZ^{-1}, with values between 10 dBZ and 15 dBZ being present at ≥ 30 % dBZ^{-1} above 4 km, indicating that there is a large number of smaller water droplets, as well as supercooled drops and ice crystals present in the mixed–phase region. The spread of ZH variables in the lightning storm is also much broader through the entire cloud as compared to the non–lightning storm at t–15. Also notable is the fact that the mode seems to be divided into two parts, with one extending from the ground to 7.5 km and the other extending from 7.5 km to 13.5 km. In addition, the Z_H values reach up to between 35 dBZ and 47 dBZ in the 5 km to 8 km region, with 25 dBZ to 35 dBZ being reached between 8 km and 11 km. This again indicates that there are a lot of graupel, hail and large water drops, as well as ice crystals present in the mixed–phase region. One can thus see from the plot that the gradients are becoming weaker as the Z_H values reached at higher altitudes increase. Furthermore, the mode is again tilted below the 5 km level, with a vertical alignment above this level, however, this is not as clear as was seen at t–30. This tilt in the more below the 5 km level is indicative of a large number of larger drops being present close to the ground, and a large number of smaller drops as well as some smaller graupel/hail being present close to 5 km. This could therefore show that a warm–rain process is occurring in the non–lightning storm. At t–15, the non–lightning storm also has a maximum cloud–top height at a higher level, with 10 km being reached. The maximum Z_H is now 45 dBZ at ≥ 1 % dBZ^{-1} and is reached up to approximately 3.5 km.

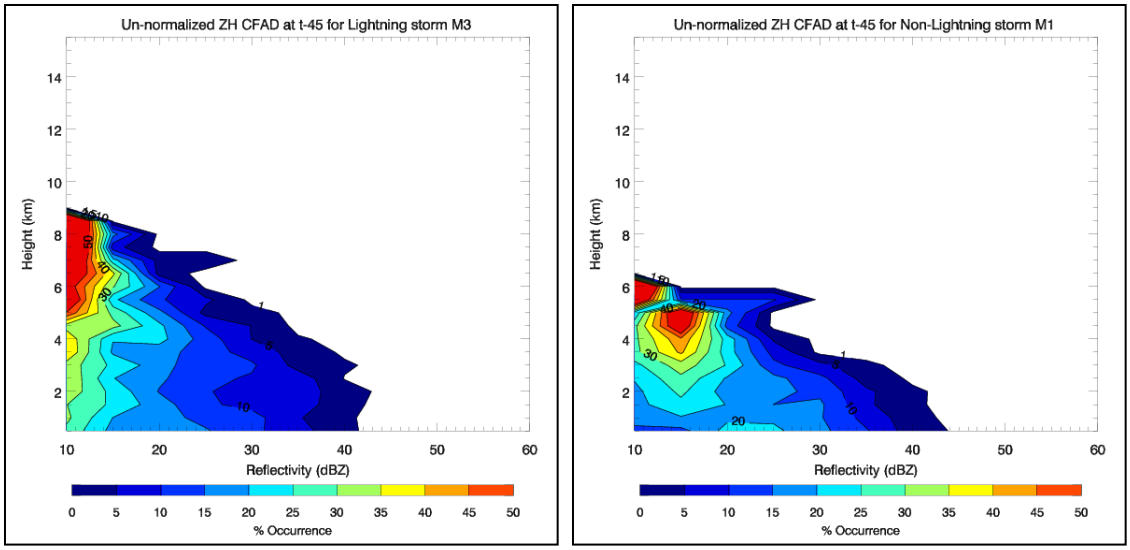

Figure 5.8: Un–normalized Z_H (called ZH in plot) CFADs for the lightning storm, M3 (left) and the non–lightning storm, M1 (right) at t–45.

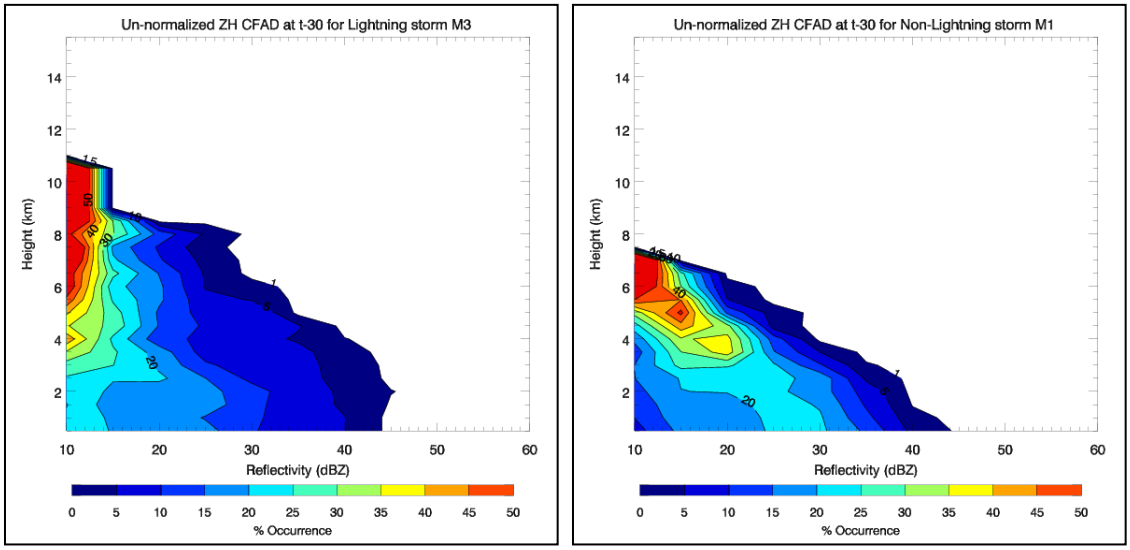

Figure 5.9: Un–normalized Z_H (called ZH in plot) CFADs for the lightning storm, M3 (left) and the non–lightning storm, M1 (right) at t–30.

The non–lightning storm mode is again tilted, with values between 15 dBZ and 30 dBZ being reached below 4 km and 10 dBZ to 20 dBZ being reached between 4 km and 10 km, both at ≥ 15 % dBZ^{-1}. There is a tilt in the mode below 4 km and a vertical alignment above this height. Nevertheless, the Z_H values in the mixed–phase region only reach between 20 dBZ and 40 dBZ at ≥ 1 % dBZ^{-1}, with these Z_H values decreasing

rapidly with height. The gradients of occurrence of Z_H values are much stronger for the non–lightning storm than the lightning storm, which indicates that although some graupel and ice might be present in the mixed–phase region, the amount here is more comparable to the amount of graupel and ice in the lightning storm at anywhere between t–45 and t–30.

Figure 5.11 shows the results for time t, which is the time in which the lightning storm produced 7 CG flashes within the next 15 minutes. There is a big change in the lightning storm from t–15 to t, with the cloud–top height now reaching 15 km, and 50 dBZ being reached up to 5 km at ≥ 1 % dBZ^{-1}. The mode is again divided into two, with the lower mode extending from the ground to 9 km, and the higher mode now occurring between 11 km and 15 km. The lower mode consists of Z_H values from 10 dBZ to roughly 20 dBZ at ≥ 15 % dBZ^{-1}, with the higher mode consisting of values ranging from 0 dBZ to 25 dBZ at ≥ 15 % dBZ^{-1}. Thus, one can see that the two modes both increased in horizontal extent, with both modes also being located at higher altitudes. The mixed–phase region (between 5 km and 11 km) now consist of Z_H values up to at least 40 dBZ at ≥ 1 % dBZ^{-1} again indicating the presence of hail, graupel, ice crystals as well as small to large water drops, thus all the precipitation particles needed for electrification to occur. The gradient of occurrence is now also weaker as compared to t–15, with Z_H values reaching up to 34 dBZ between 11 km and 14 km. The tilt that was visible below the melting level at t–15 is now vertical, thus the entire mode from the ground to 15 km is now vertical in appearance. This same feature, where the entire mode becomes vertical at time t, was seen for the lightning storms.

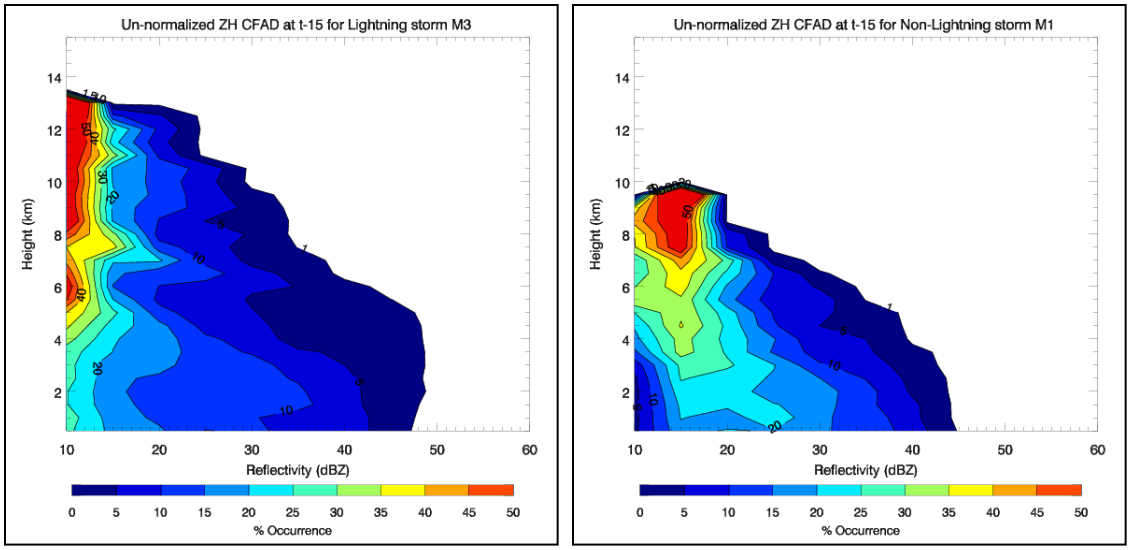

Figure 5.10: Un–normalized Z_H (called ZH in plot) CFADs for the lightning storm, M3 (left) and the non–lightning storm, M1 (right) at t–15.

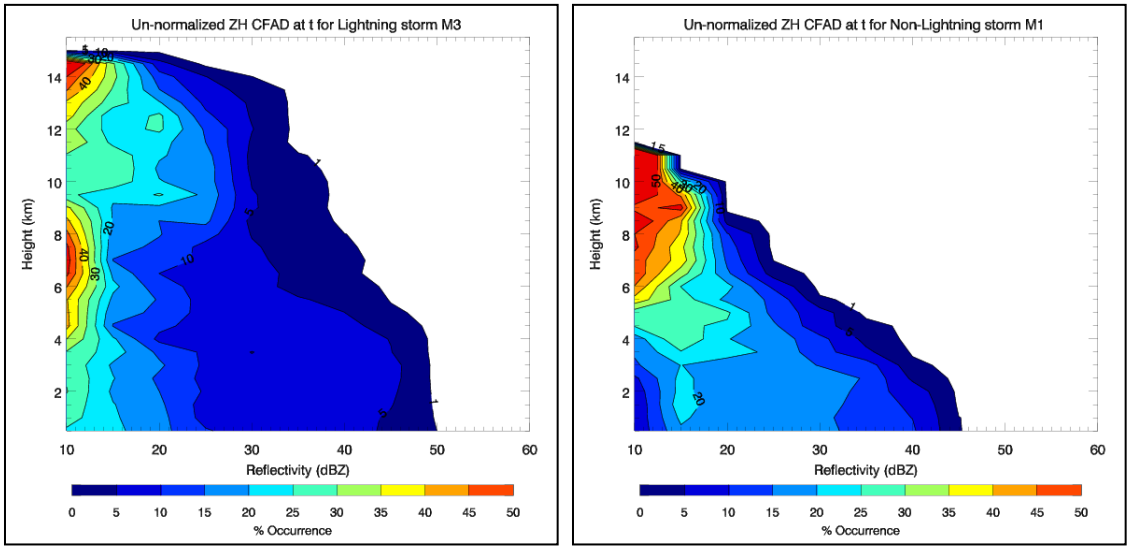

Figure 5.11: Un–normalized Z_H (called ZH in plot) CFADs for the lightning storm, M3 (left) and the non–lightning storm, M1 (right) at time t.

Comparing the lightning storm to the non–lightning storm at time t, one can see that the non–lightning storm is much weaker and smaller in terms of Z_H values and maximum cloud–top height obtained. In fact, the non–lightning storm is now more comparable to the lightning storm at t–30, 30 minutes earlier. At time t, the non–lightning storm only has a cloud–top height of 11.5 km, with Z_H values only

reaching 45 dBZ at ≥ 1 % dBZ^{-1} from the ground to 3 km, which is 3 km lower than was observed for the lightning storm. At 5 km, the maximum Z_H that was obtained is 35 dBZ at ≥ 1 % dBZ^{-1} with only 20 dBZ being reached at 10 km. Here the mode is tilted below the melting level, with values of up to roughly 35 dBZ being reached at ≥ 15 % dBZ^{-1} and above the melting level the mode is vertically aligned with only 20 dBZ being reached at ≥ 15 % dBZ^{-1}. As a result, one can see that the occurrence of large amounts of hail and graupel in the mixed–phase region is unsupported, as the Z_H values obtained in this layer being too low. Therefore, although some electrification is possible at this time, it is not nearly enough to cause the development of CG lightning for the non–lightning storm.

By t+15 (Figure 5.12), the lightning storm has already produced 7 CG flashes; and 16 more CG flashes occurring within the next 15 minutes. Here the lightning storm has the same approximate appearance as at time t, however it seems as though the mixed–phase region collapsed due to lower values of Z_H being reached, with only 30 dBZ to 40 dBZ being obtained here at ≥ 1 % dBZ^{-1}. Nevertheless, Z_H values of up to 50 dBZ are reached below 5 km at ≥ 1 % dBZ^{-1} and up to 30 dBZ is reached between 11 km and 15 km at ≥ 1 % dBZ^{-1}. The mode is again vertically aligned throughout the cloud, and divided into two areas, with the lower mode now being located between 4 km and 9.5 km and the higher mode being located at 10.5 km to 15.0 km, both with values reaching 15 dBZ at ≥ 30 % dBZ^{-1} and values of up to 25 dBZ being reached at ≥ 15 % dBZ^{-1}. The non–lightning storm in contrast seems to have a lower in cloud–top height, reaching only 11 km at t+15. The non–lightning storm at this time is more representative of the lightning storm at t–30, which is 45 minutes earlier, with very little further growth being

observed from time t. Nevertheless, Z_H values of up to 45 dBZ is reached to 5 km at ≥ 1 % dBZ^{-1}, signifying that large water drops, as well as possible melting graupel and hail are present at these heights. The tilt in the mode below the melting level as well as the vertical alignment of the mode above this level is again visible here, with 14 dBZ to 38 dBZ being reached at the ground at ≥ 15 % dBZ^{-1} and 0 dBZ to roughly 20 dBZ being reached between 5 km and 11 km at ≥ 15 % dBZ^{-1}.

Figure 5.13 shows the results obtained at t+30 for the lightning storm (left) and non–lightning storm (right). The lightning storm produced another 5 CG flashes during the next 15 minutes, which is not surprising, as Z_H values of 50 dBZ is reached up to 4 km at ≥ 1 % dBZ^{-1} and 30 dBZ to 40 dBZ is reached between 5 km and 7 km at ≥ 1 % dBZ^{-1}. Also, the lightning storm still has a cloud–top height of 15 km, with 30 dBZ being observed between 7 km and 11 km at ≥ 1 % dBZ^{-1}, representing the occurrence of graupel and small hail, as well as larger drops in the mixed–phase region. Therefore, these precipitation particles have been present in this region for at least 45 minutes, and may explain the additional 11 CG flashes that occurred between t+30 and t+60 (not shown here). The two mode layers that were visible in the previous three figures are no longer visible, with a single mode being located from 0 km to 15 km at ≥ 15 % dBZ^{-1} with Z_H values reaching 20 dBZ throughout the mode. Thus, the percentage of smaller drops are increasing as the percentage of larger drops, graupel and hail are decreasing (due to gravitational sorting), especially in the mixed–phase region. The non–lightning storm is starting to completely collapse at t+30, with the cloud–top height now only reaching 9.5 km, and the maximum Z_H only being 44 dBZ below 2.5 km at ≥ 1 % dBZ^{-1}. The mode is now more vertical in alignment and only reaches a

maximum of 32 dBZ at ground–level at ≥ 15 % dBZ^{-1}, and 22 dBZ above 5 km, also at ≥ 15 % dBZ^{-1}. Only 33 dBZ is reached at 5 km at ≥ 1 % dBZ^{-1}, much less than was obtained at this height at t–+15. However, due to the large percentage of 10 dBZ to 20 dBZ being observed throughout the cloud, it seems as though there are many smaller water drops, and possibly some ice crystals still present in the storm at t+30. It is clear that the lightning storm has passed its mature phase and is now in its dissipating phase, making the initiation of lightning almost impossible.

From the above, one can deduce that the lightning storm had much more smaller drops, larger drops, graupel and/or hail present in the storm throughout its lifetime as compared to the non–lightning storm, which had a maximum cloud–top height of 11 km at time t and t+15 only, as compared to the lightning storm, that reached 15 km from time t onwards. This is also confirmed by the vertical cross sections discussed earlier in this chapter. Also, the lightning storm consistently reached Z_H values of 45 dBZ and higher up to 5 km from t–15 onwards, where the non–lightning storm only displayed this at t+15. Interestingly, the lightning storm had a two–layer mode that was observed from t–15 through t+15, which was not seen in the non–lightning storm, however the non–lightning storm displayed the tilt in the mode below 5 km, which was also seen in the lightning storm, but to a lesser extent. In addition, the lightning storm had Z_H values of at least roughly 30 dBZ between 5 km and 11 km, seen from t–15 through t+15, which was not seen in the non–lightning storm. All of these could explain why the non–lightning storm did not produce any lightning, whereas the lightning storm produced 23 CG flashes from time t to t+15.

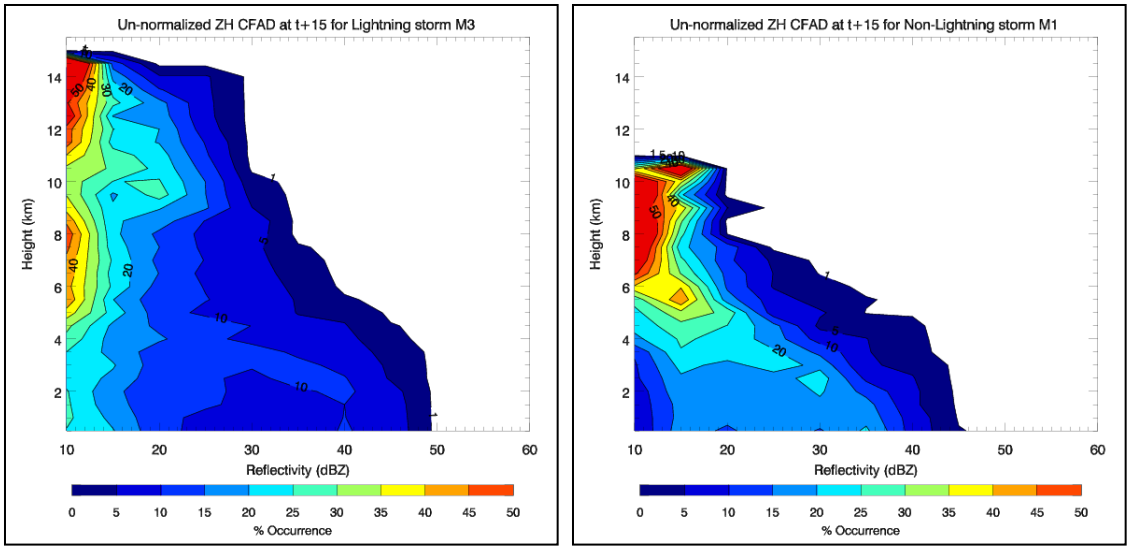

Figure 5.12: Un–normalized Z_H (called ZH in plot) CFADs for the lightning storm, M3 (left) and the non–lightning storm, M1 (right) at t+15.

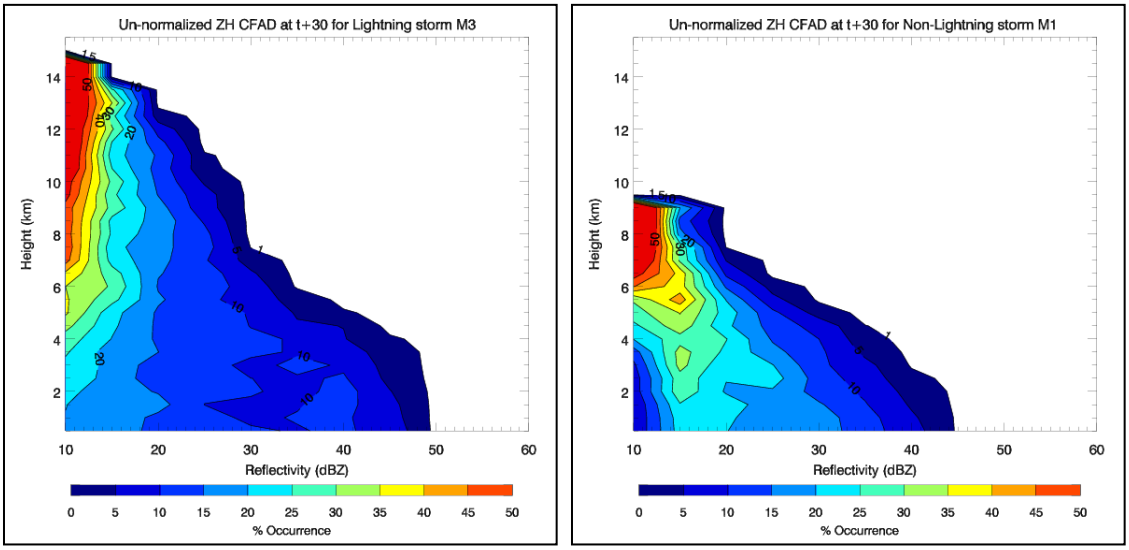

Figure 5.13: Un–normalized Z_H (called ZH in plot) CFADs for the lightning storm, M3 (left) and the non–lightning storm, M1 (right) at t+30.

Figure 5.14 through 5.19 show the un–normalized Z_{DR} (also called DR in plot) CFADs for the lightning storm, M3 (left) and the non–lightning storm, M1 (right) from t–45 through t+30, respectively. At t–45 (Figure 5.14) the lightning storm has its mode centered around 0 dB, with –0.7 dB to 0.9 dB being reached at ≥ 1 % dB^{-1}, especially below the melting level, denoting that there are a variety of precipitation types and sizes

in the cloud, including ice, graupel and/or hail, as well as water drops. There is a protrusion of positive Z_{DR} values located at roughly 5 km to 7 km that extends to 2.3 dB at ≥ 1 % dB^{-1}, which might indicate the presence of supercooled liquid water, due to the fact this occurs in the mixed–phase region. There are also negative Z_{DR} values between –2 dB and –3 dB above 3 km, which could also indicate hail or graupel that have a larger vertical extent than a horizontal extent. The mode of the storm is vertically aligned and seems to be divided into three sections, below 3 km, between 4 km and 6 km and above 7 km, although this feature is not yet that clear.

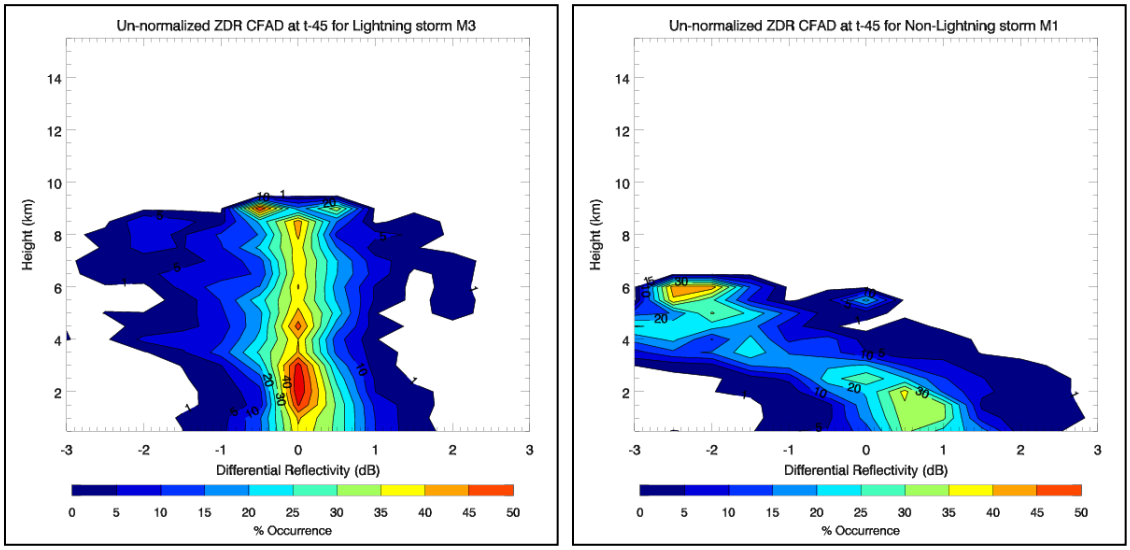

Figure 5.14: Un–normalized Z_{DR} (called ZDR in plot) CFADs for the lightning storm, M3 (left) and the non–lightning storm, M1 (right) at t–45.

The non–lightning storm, in contrast, has a completely different appearance, with the mode being tilted throughout the storm, and all Z_{DR} values from –2.8 dB to 1.6 dB being observed at ≥ 15 % dB^{-1}. In fact, the mode is almost completely positive below 2 km and completely negative above this height. Interestingly, values of up to 2.9 dB are reached below 3 km at ≥ 1 % dB^{-1} and up to –3 dB is reached between 3 km and 6 km at

≥ 1 % dB^{-1} (although these very negative Z_{DR} values could be a radar artifact). The positive values indicate that there is a variety of small to large water drops present in the cloud below the melting layer and the negative values indicate that there might be some small ice possible above 5 km. Over and above the fact that Z_{DR} mode is tilted, it seems as though there may be a two–layer mode, with the first mode being located below 3 km and the second mode being seen above 5 km. Also, the gradient of the Z_{DR} occurrences for the non–lightning storm is much weaker as compared to the gradient of occurrence for the lightning storm.

At t–30 (Figure 5.15), the lightning storm now has its mode located up to 12 km, with values ranging from –0.5 dB to 0.9 dB at ≥ 15 % dB^{-1}. Below 9 km, the mode is mostly –0.6 dB to 0.7 dB and above 9 km the mode is mostly between –0.9 dB and 0.3 dB, indicating that above 9 km the mode is more negative than below, although only by a little. The protrusion of positive Z_{DR} values in the mixed–phase that was seen in t–45 is also seen here, with values up to 2.8 dB being reached between 8.5 km and 10.5 km at ≥ 1 % dB^{-1}, again possibly indicating a column of supercooled liquid water. There are also negative Z_{DR} values occurring between 3 km and 11 km reaching up to –2.5 dB. It appears that the mode here consists of four regions; one below 3 km, one between 3 km and 9 km (both of these falling around 0 dB), one between 9 km and 11 km (consisting of mostly negative Z_{DR} values) and the last one located above 11 km (and also consisting of mostly negative Z_{DR} values).

The non–lightning storm has almost the same appearance at t–30 than was obtained at t–45, with a tilted mode below 5 km and a more vertical mode above this height. The mode also varies in terms of Z_{DR} values that are observed, with values

varying between –0.2 dB and 1.2 dB below 2.5 km, –1.5 dB and 0 dB between 2.5 km and 5 km and finally –1.2 dB to –0.2 dB above 5 km, all at ≥ 15 % dB^{-1}. Therefore, the mode is more complicated than was observed at t–45, and there are positive Z_{DR} values between 1 dB and 2 dB occurring between 4 km and 6 km, with values up to 3 dB being observed below 2 km, both at ≥ 1 % dB^{-1}. Thus, there are a variety of hydrometeor particles present in this storm as seen from the varying Z_{DR} values.

Figure 5.16 shows the un–normalized Z_{DR} CFAD for the lightning storm, M3 (left) and the non–lightning storm, M1 (right) at t–15. At this time, the lightning storm still mostly possess a vertical alignment in the mode, with values between –0.8 dB and 0.6 dB being observed up to a height of 11 km at ≥ 15 % dB^{-1} and mostly negative Z_{DR} values of –1.5 dB to 0 dB occurring above 11 km at ≥ 15 % dB^{-1}. This indicates that many smaller water drops, graupel and/or hail, as well as ice crystals, are present in the storm. There are also two large protrusions of negative Z_{DR} values reaching –2.7 dB at around 4 km and 7 km to 9 km, which could also indicate the presence of graupel, hail and ice crystals. The large positive protrusion seen at t–30 (Figure 5.15) is no longer as visible, however Z_{DR} values of up to 1.8 dB are reached between 0 km and 12 km. The mode is once again consisting of four regions, with the lowest region occurring below 3 km, the second one at 4 km to 8 km, the third at 9 km to 10.5 km and the fourth region being located above 12 km. The first three regions are all centered on 0 dB, but the fourth region has mostly negative Z_{DR} values. The three lower regions seem to be located in the same areas as the tripole charging layer seen in a normal thunderstorm, with the fourth region possibly located in the screening layer and caused by strong updrafts.

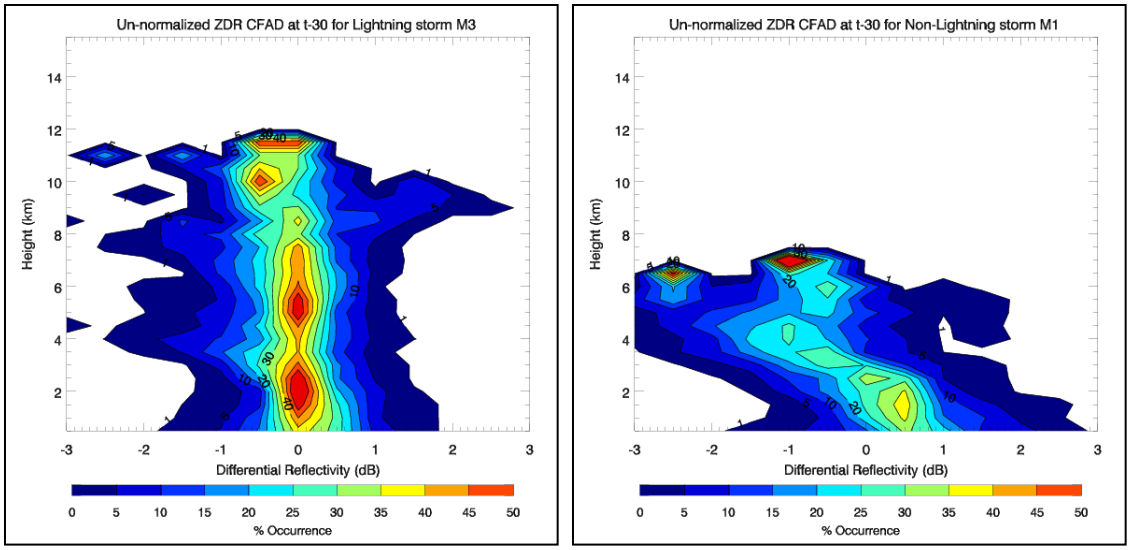

Figure 5.15: Un–normalized Z_{DR} (called ZDR in plot) CFADs for the lightning storm, M3 (left) and the non–lightning storm, M1 (right) at t–30.

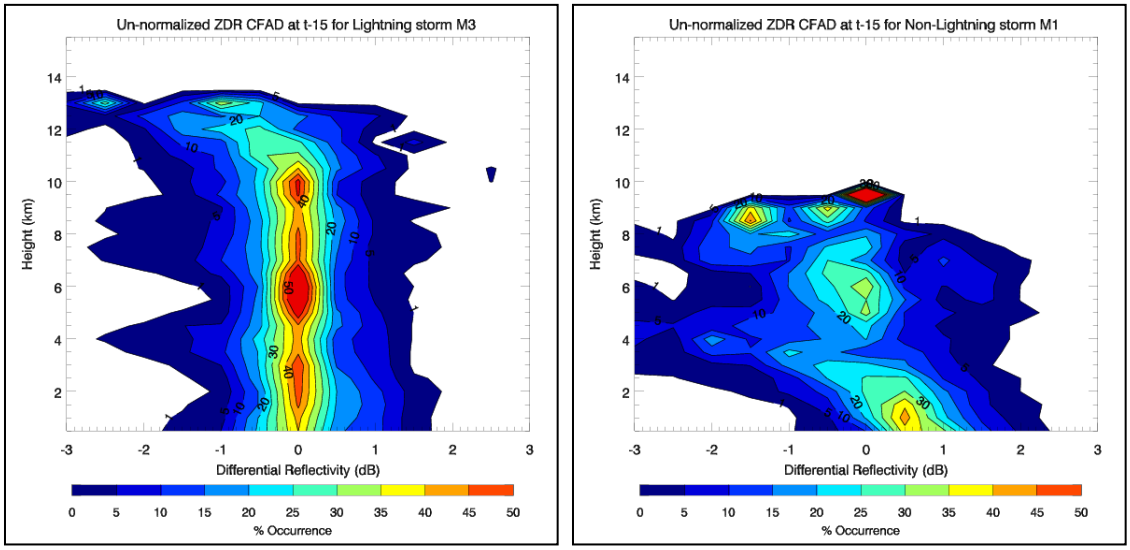

Figure 5.16: Un–normalized Z_{DR} (called ZDR in plot) CFADs for the lightning storm, M3 (left) and the non–lightning storm, M1 (right) at t–15.

The non–lightning storm seen in Figure 5.16 is again very complicated, with up to five mode regions being observed, however, some of these modes, especially the ones at higher altitudes, may be artifacts from the data. The lowest region is seen below 3 km, with Z_{DR} values ranging from –0.6 dB at 3 km to 1.4 dB at the ground (mostly positive), with the occurrence reaching ≥ 15 % dB^{-1}. The second mode region appears to be

located between 4 km and 8 km, with values between –0.6 dB and 0.4 dB (mostly negative) at ≥ 15 % dB^{-1}. The remaining three regions all occur above 8 km and contain Z_{DR} values of –1.8 dB to 0.5 dB, thus also mostly negative. The negative regions might indicate the presence of ice and graupel, especially at temperatures colder than –10 °C, and the positive regions indicate small to larger water drops. There is also a region of higher positive Z_{DR} values located in the mixed–phase region, with values up to 2.3 dB being reached at ≥ 1 % dB^{-1}. This suggests the presence of some supercooled liquid water, but at much lower levels than was observed for the lightning storm. Also worth mentioning is the fact that –3 dB values are reached from 2.5 km to 8.5 km at this time.

At the time of first lightning (Figure 5.17), the lightning and non–lightning storms look vastly different; the lightning storm has a completely vertical mode between 0 km and 14 km and the non–lightning storm again has a much more complicated mode. The Z_{DR} values in the lightning storm mode consists of values ranging from –0.7 dB to roughly 0.7 dB up to 14 km at ≥ 15 % dB^{-1}, thus having an approximately equal number of positive and negative Z_{DR} values, showing that at the time of first lightning, there is about the same amount of smaller drops, larger drops, ice crystals, graupel and possibly hail. Below 4 km, there are positive Z_{DR} values of up to 2.2 dB, which might indicate the presence of larger drops or melting hail and/or graupel at these heights. Furthermore, there are positive Z_{DR} values reaching 1.9 dB between 12 km and 14.5 km, and a small area of 2.2 dB being reached between 6 km and 8 km. It appears that the negative Z_{DR} values obtained between 3.5 km and 11 km are layered, with up to –3 dB being reached (again, this could be due to artifacts from the data). Interestingly, the “fourth” mode region seen at t–15 (Figure 5.16) is present again, but is now located

between 14 km and 15 km, which is once again in the same region that the screening layer will be seen in an electrically active storm (but can also be due to artifacts from the data). The other three mode regions are also still observed, although these regions are now located at different heights: The first region is still located below 3 km, the second region is now smaller and located between 4 km and 6 km, and the third region is now much more elongated and extends from roughly 6 km to 14 km. Finally, the gradients of % dB^{-1} values are now somewhat stronger, especially for values located in the mode region, as compared to the lightning storm at t–15.

The non–lightning storm at time t has a tilted mode throughout the cloud depth, however, a negative tilt below 5 km and a positive tilt above this layer are suggested. Below 3 km, the mode consists of Z_{DR} values ranging from –0.3 dB to 1.5 dB (mostly positive), between 3 km and 8 km the mode consists of roughly –1. dB to 0.3 dB (mostly negative), and above 8 km the mode consists of values between –1 dB and 1 dB, all at ≥ 15 % dB^{-1}. There is also a large area of negative Z_{DR} values reaching –3 dB between 3 km and 9 km at ≥ 1 % dB^{-1}, indicating the presence of ice particles, graupel and possibly hail. Below 6 km, there is a large area of positive Z_{DR} values reaching roughly 2 dB at ≥ 1 % dB^{-1}, which shows that there are larger water drops present at these heights.

Figure 5.18 shows the results for t+15, which is 15 minutes after the first CG lightning was observed. There are only two mode regions here, as the upper mode regions have now merged into one large region, stretching from 3.5 km to 14.5 km. However this large region consists of Z_{DR} values between –0.6 dB and 0.5 dB up to roughly 13 km, with –1.3 dB to 0.5 dB being reached between 13 km and 14.5 km at

≥ 15 % dB^{-1}. The second mode region is located below 4 km, with values ranging from –0.5 dB to 1.2 dB at ≥ 15 % dB^{-1}, which includes an interesting protrusion below the melting layer. There is also a large area below the melting layer that consists of Z_{DR} values up to 2 dB. These two features could indicate a region of larger water drops, or melting hail and graupel, which is highly possible at this time of the storms' life. There is also a much lower occurrence of large negative Z_{DR} values in the mixed–phase region, however, –2 dB is reached at ≥ 1 % dB^{-1} showing that some ice, graupel and hail is still present in the storm. Nevertheless, there are large negative Z_{DR} values between 13 km and 15 km, with positive values of up to 2 dB located at around 13 km, with both occurring at ≥ 1 % dB^{-1}.

The non–lightning storm, as seen at t+15, has a tilted mode below 3 km, with Z_{DR} values between roughly –0.5 dB and 1.3 dB (mostly negative), with another region located between 3 km and 8 km consisting of values ranging between –1.2 dB and 0.5 dB (mostly negative), and a final region between 9 km and 11 km, centered around 0 dB, all at ≥ 15 % dB^{-1}. The occurrence of large negative Z_{DR} values (up to –3 dB) in the mixed–phase region is decreasing, with larger positive Z_{DR} values (up to 2.8 dB) now being observed between 7 km and 9 km, as well as up to 2.5 dB between 1.5 km and 3.5 km. The increase in occurrence of larger positive Z_{DR} values signifies that there is an increase in larger drops in the mixed–phase region and below it with possible melting graupel below the melting layer, and the decrease in negative values signifying the decrease in the amount of ice and graupel being present in the mixed–phase region.

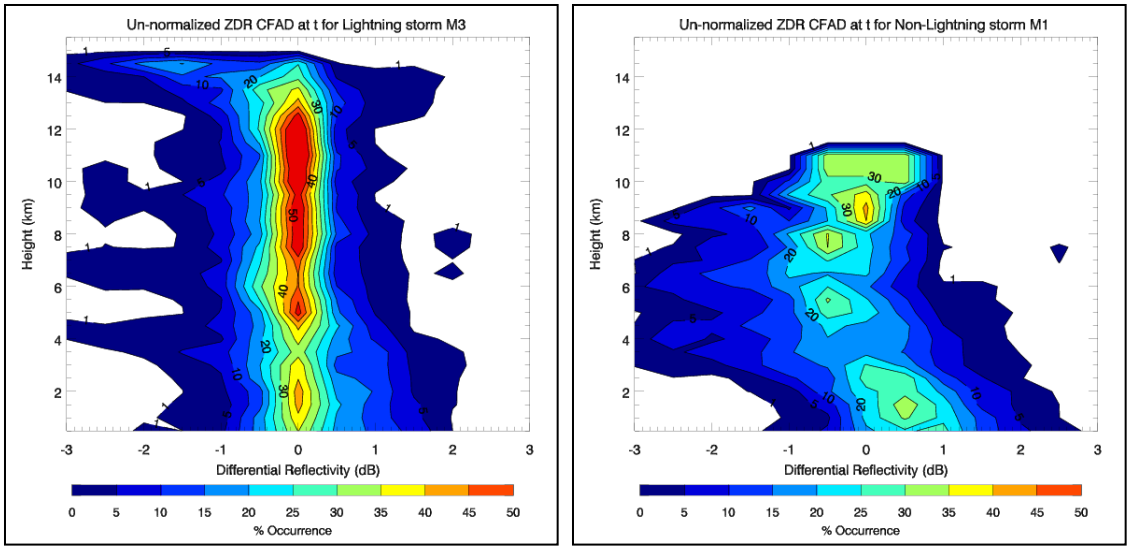

Figure 5.17: Un–normalized Z_{DR} (called ZDR in plot) CFADs for the lightning storm, M3 (left) and the non–lightning storm, M1 (right) at time t.

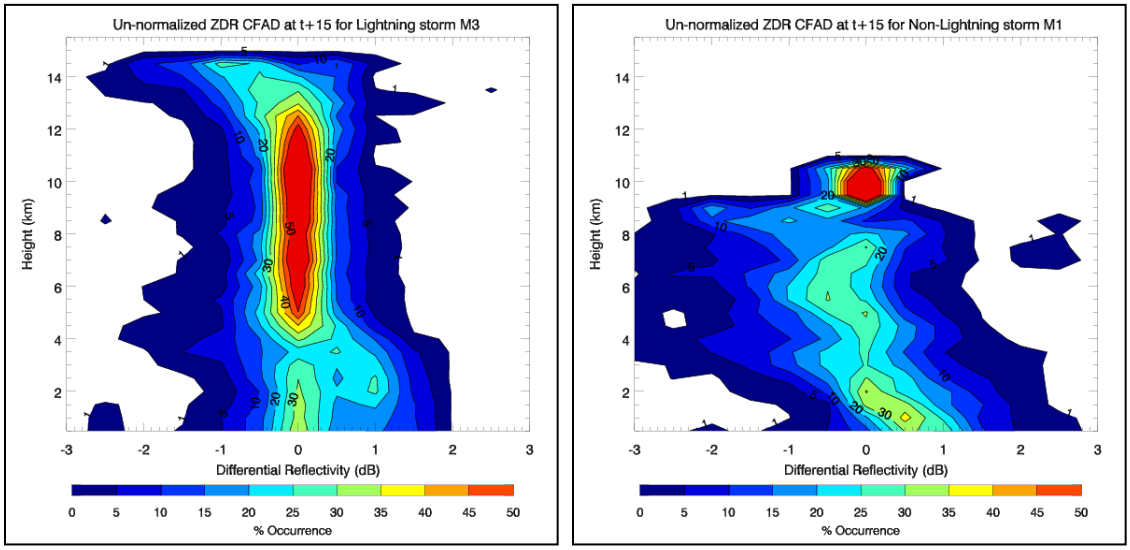

Figure 5.18: Un–normalized Z_{DR} (called ZDR in plot) CFADs for the lightning storm, M3 (left) and the non–lightning storm, M1 (right) at t+15.

At t+30 (Figure 5.19), one can see that the lightning storm looks very similar to the previous figure, with an elongated mode being obtained between 4 km and 13 km and centered around 0 dB at ≥ 15 % dB^{-1}. Below this height, the mode gradient is weaker and includes Z_{DR} values from –0.4 dB to 1.2 dB (and is thus more positive) at ≥ 15 % dB^{-1}, however, above 13 km, the mode consists of values from –1.7 dB to 0.5 dB

(and thus more negative), also at ≥ 15 % dB^{-1}. There is now only one distinct mode region that extends over a larger Z_{DR} range, with ice being present above 13 km and large water drops and melting graupel and hail being present below the melting layer. Z_{DR} values of to –2 dB are also reached at around 5 km as well as around 14 km, indicating ice particles and graupel at these heights, respectively. The non–lightning storm, on the other hand, again has a tilted mode structure, with mostly positive Z_{DR} values (up to 1.4 dB) being reached below 3 km, and mostly negative values (to –1.7 dB) being observed between 3 km and 9.5 km, which is the cloud–top height here, both at ≥ 15 % dB^{-1}. In addition, there is a small occurrence of larger positive Z_{DR} values greater than 1.5 dB located between 7 km and 9 km as well as below the melting level, indicating the presence of larger water drops at these heights.

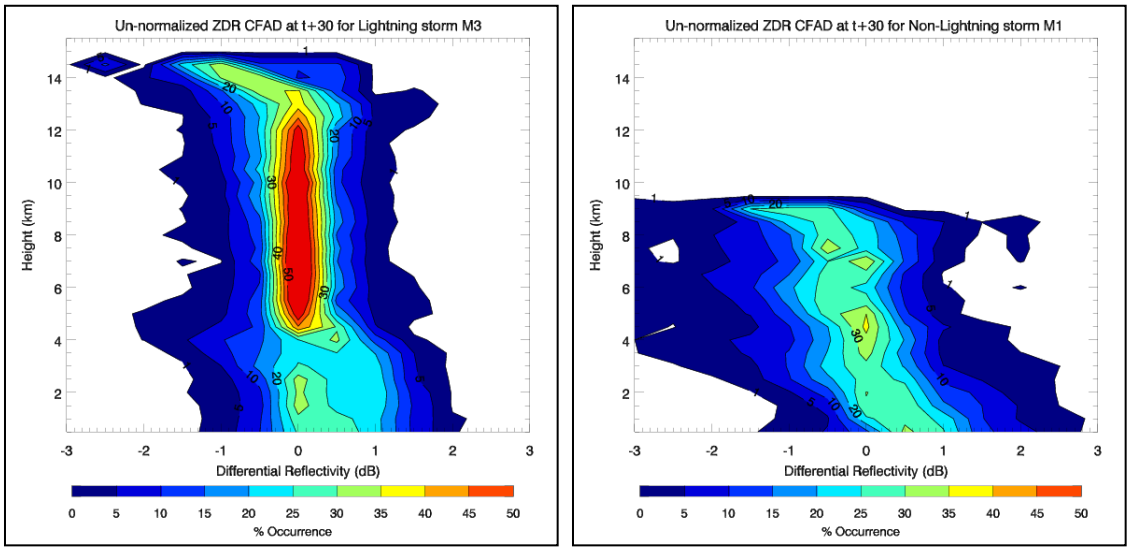

Figure 5.19: Un–normalized Z_{DR} (called ZDR in plot) CFADs for the lightning storm, M3 (left) and the non–lightning storm, M1 (right) at t+30.

From the above Z_{DR} un–normalized CFAD plots (Figure 5.13 through 5.19) and referring to the vertical cross sections shown earlier, it is clear that the lightning storm

has much more graupel and ice particles, as well as supercooled liquid drops and hail in the mixed–phase region than the non–lightning storm. In addition, the mode of the lightning storm is vertically aligned for most of the storms' lifetime, although the Z_{DR} values below 5 km were mostly positive and mostly negative above 5 km up to time t. The non–lightning storm mode was more tilted. Interestingly, the lightning storm mode was separated into various regions, each approximately located at the same heights as the various charging regions found in a lightning storm.

Figure 5.20 through 5.25 show the un–normalized ρ_{HV} (also called RH in plot) CFAD plots for the lightning storm, M3 (left) and the non–lightning storm, M1 (right) from t–45 through t+30. At t–45 (Figure 5.20), the lightning storm consists of all ρ_{HV} values between 0.83 and 0.95 from 0 km to 9 km at ≥ 15 %. Therefore, there is no clear mode, although there is a higher occurrence of 0.88 to 0.93 values below 4 km. There are ρ_{HV} values between 0.95 and 1 at a height ranging from 3 km to 9 km. The non–lightning storm however seems more organized, with the mode being centered on 0.92, and some values of around 0.84 occurring at ≥ 15 %. The non–lightning storm has ρ_{HV} values up to 1 below 6 km.

At t–30 (Figure 5.21), the ρ_{HV} values in the lightning storm seems more organized than at t–45, with a possible mode being located from 0.84 to 0.93 at ≥ 15 %, with the lower region of the mode being centered around 0.92. There is a large region in the mixed–phase region that consists of ρ_{HV} values from 0.9 to 0.94 at ≥ 20 %. The region of ρ_{HV} values of 1 are only located between 5 km and 9 km, although values of 0.80 are reached for the entire storm height. The non–lightning storm has the same approximate features as in t–45, however there now seems to be a tilt in the mode below 5 km, with

the mode being centered on 0.92 below 3 km and ranging from 0.83 to 0.9 between 3 km and 5 km, both at ≥ 15 %. Also, the mode region above the melting layer is again centered on 0.92, with some values here extending to 0.96.

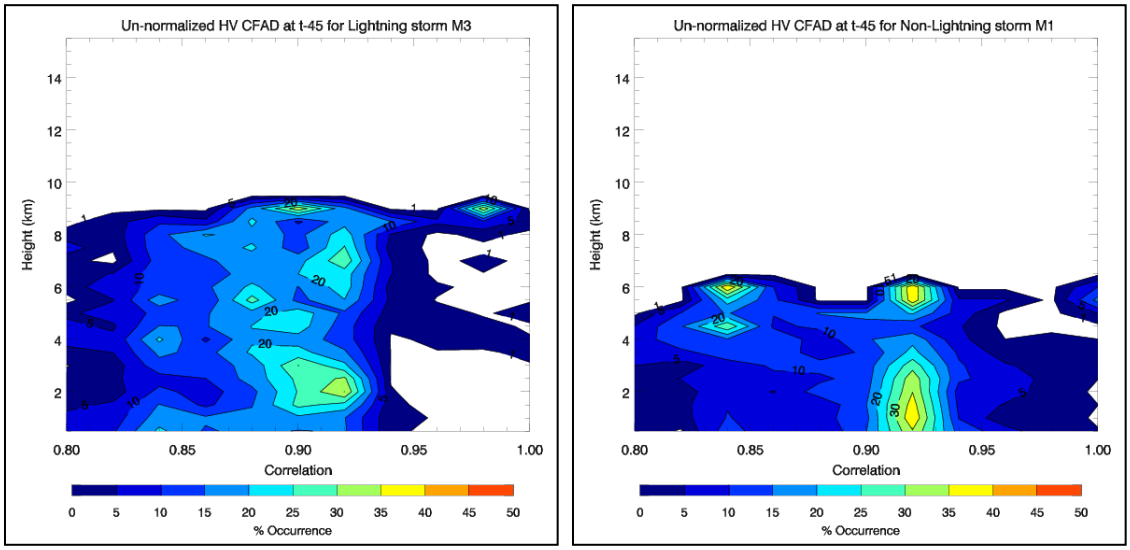

Figure 5.20: Un–normalized ρ_{HV} (called HV in plot) CFADs for the lightning storm, M3 (left) and the non–lightning storm, M1 (right) at t–45.

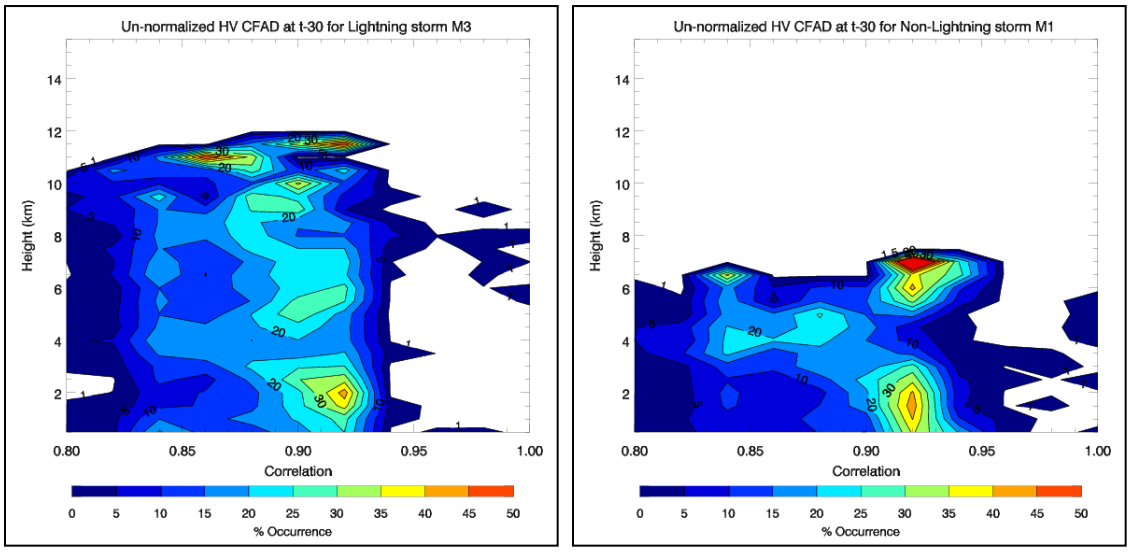

Figure 5.21: Un–normalized ρ_{HV} (called HV in plot) CFADs for the lightning storm, M3 (left) and the non–lightning storm, M1 (right) at t–30.

In Figure 5.22 (t–15) one can see that the lightning storm is now much more organized and looking similar in appearance as the Z_{DR} plots seen earlier. Here the mode is now vertical and centered around 0.92, with up to four regions being observed, with the strongest region being located below 5 km with ρ_{HV} values between 0.88 and 0.93 at ≥ 15 % and 0.92 being reached at ≥ 45 %. At the top of the cloud, the ρ_{HV} values range from 0.82 to 0.97, indicating a range of different sizes and orientations of precipitation particles. Once again, values of 0.8 and 1 are reached throughout the storm height, however these only occur for a small percentage of the time. The non–lightning storm now has three distinct mode regions, with the lowest region being located below 3 km, with ρ_{HV} values between 0.88 and 0.94. The second mode region is located between 3 km and roughly 7 km, with ρ_{HV} values ranging from 0.89 to 0.95 and the final region is located above 8 km, with values from 0.93 to 0.97, all at ≥ 15 %. As was the case with the lightning storm, there are values of 0.8 and 1.0 being reached at low frequency of occurrence throughout the cloud height, although the non–lightning storm has a much lower cloud–top height than the lightning storm at t–15.

At time t (Figure 5.23), the lightning ρ_{HV} values are again vertically aligned, with the mode being centered on 0.92, as was the case with t–15, with ρ_{HV} values ranging between 0.9 and 0.94 at ≥ 15 %. The mode again has different regions, with the two most obvious ones being located below 7 km and above 10 km. At the cloud–top, ρ_{HV} values range from 0.80 to 1.0, indicating that a large variety of sizes and orientations are again present. In fact, these ρ_{HV} values are also found over the entire height of the cloud, however only at low percentages. In the mixed–phase region there are ρ_{HV} values of up to 0.97, with 0.83 also being reached, both at ≥ 5 %.

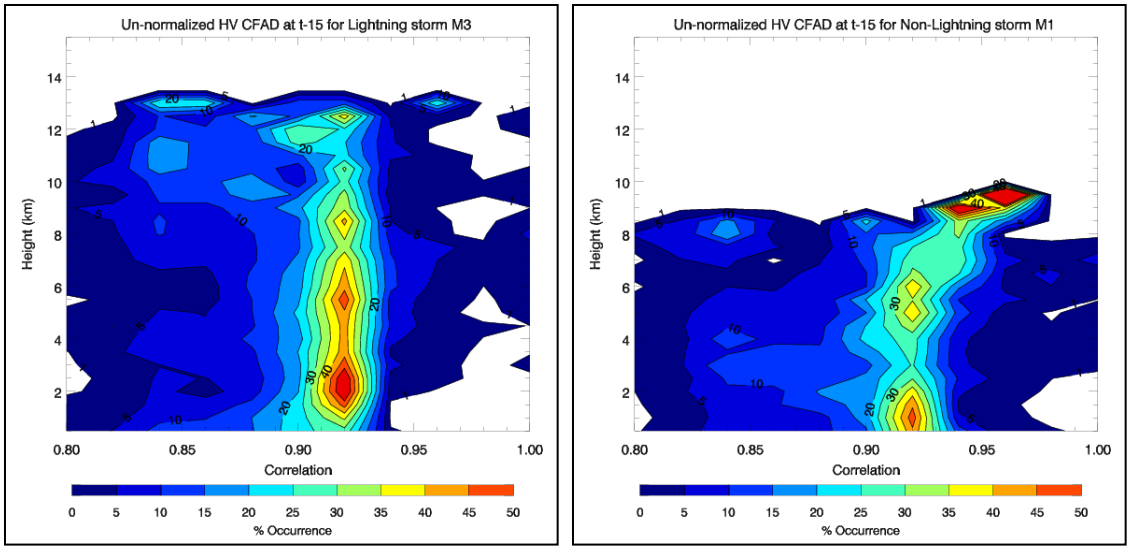

Figure 5.22: Un–normalized ρ_{HV} (called HV in plot) CFADs for the lightning storm, M3 (left) and the non–lightning storm, M1 (right) at t–15.

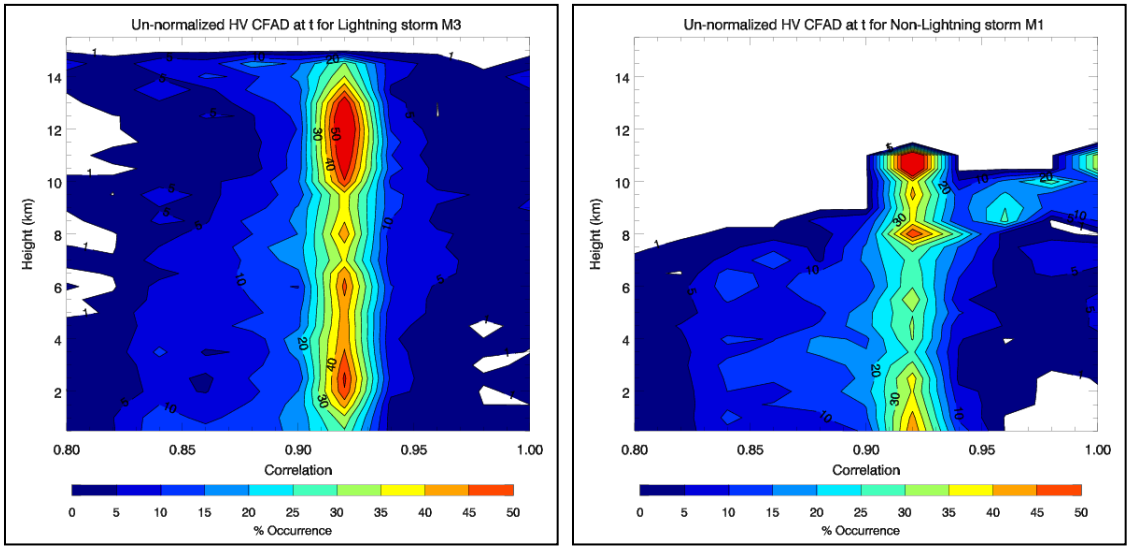

Figure 5.23: Un–normalized ρ_{HV} (called HV in plot) CFADs for the lightning storm, M3 (left) and the non–lightning storm, M1 (right) at time t.

The non–lightning storm mode is now also aligned vertically, with an additional small area (not seen as part of the mode) being located between 0.95 and 1 above 8 km. The mode is again centered on 0.92, with three main regions being observed. These regions include a lower region below 3.5 km, a region between 3.5 and 9 km and a final region above 9.5 km. The cloud–top height only consists of ρ_{HV} values ranging from

0.9 to 0.94, with 0.8 to 0.9 being reached at ≥ 1 % below 9 km and values between 0.94 and 1 being reached below 10.5 km.

Figure 5.24 is for the t+15 timeframe, with the lightning storm mode now consisting of a single mode that extends throughout the mixed–phase layer and higher, again centered around 0.92, and a lower mode located below 5 km, with ρ_{HV} values ranging from 0.88 to 0.93, both at ≥ 15 %. Therefore this lower, weaker mode holds more lower ρ_{HV} values, which indicates that there are more precipitation particles that have vertical and horizontal dimensions that are not equal. There is also an additional mode located at the top of the cloud, with ρ_{HV} values ranging between 0.82 and 0.85, probably indicating some ice crystals or needles. However, ρ_{HV} values ranging from 0.8 to 1 are reached at the cloud–top, as well as through the entire height of the cloud, although only at ≥ 1 %. In contrast, the non–lightning storm at t+15 looks approximately the same as at time t, with the mode being vertically aligned and centered around 0.92 and once again consisting of three main regions: The lowest region is located below 7 km, the second region is located between 8 km and 9 km, and the third region being located above 9.5 km, all having ρ_{HV} values between 0.9 and 0.94 at ≥ 15 %. There is another region, although it does not form part of the mode, located between 8.5 km and 11 km and consisting of ρ_{HV} values between 0.97 and 0.99 at 15 – 20 % (this was also seen at time t).

At t+30 (Figure 5.25), the lightning storm once again has a mode that is vertically aligned and centered around 0.92, with ρ_{HV} values of 0.88 to 0.94 being reached at ≥ 15 %. The mode also has two regions, such as seen at t+15, with the lower region located below 4 km and the higher region located between 4 km and 13 km. However,

there is an area of higher percentage of occurrence located between 13.5 km and 15 km, with ρ_{HV} values ranging from 0.87 to 0.92 at ≥ 15 %. The cloud–top again consists of all ρ_{HV} values (from 0.80 to 1), with these values also occurring over the entire cloud height, but only at ≥ 1 %.

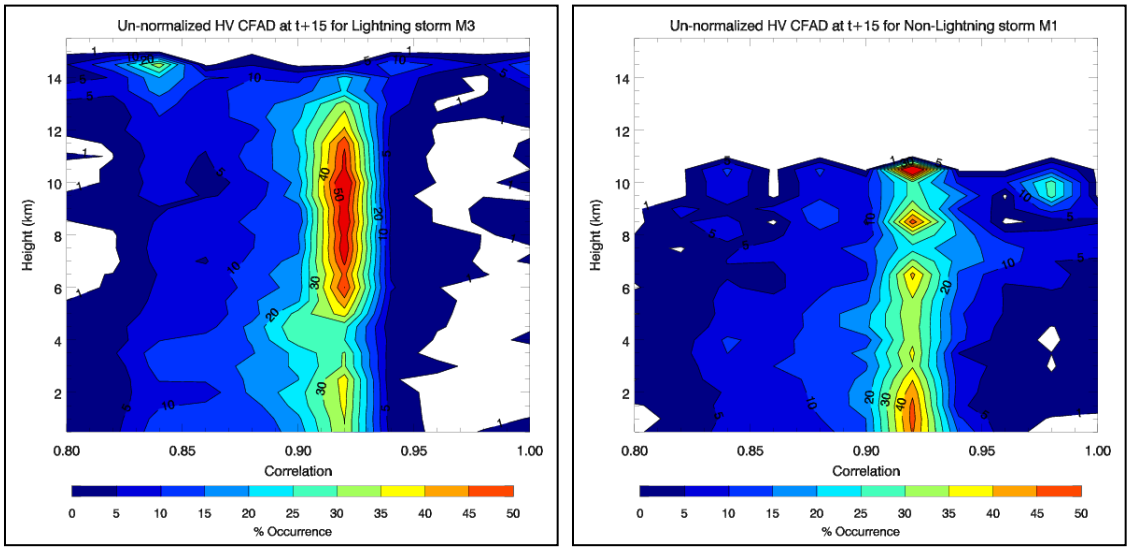

Figure 5.24: Un–normalized ρ_{HV} (called HV in plot) CFADs for the lightning storm, M3 (left) and the non–lightning storm, M1 (right) at t+15.

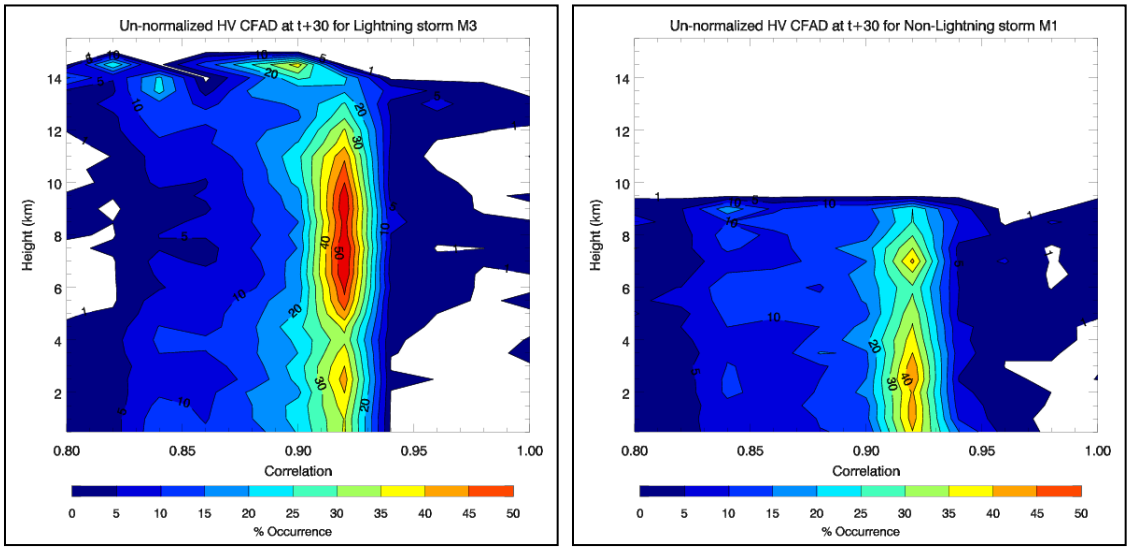

Figure 5.25: Un–normalized ρ_{HV} (called HV in plot) CFADs for the lightning storm, M3 (left) and the non–lightning storm, M1 (right) at t+30.

The non–lightning storm at t+30 again has its mode centered around 0.92, with the mode now consisting of only two regions, one located below 5.5 km and the other above this height. Both of these mode regions contain ρ_{HV} values between 0.90 and 0.94 at ≥ 15 %, with all ρ_{HV} values between 0.8 and 1 being reached throughout the cloud, although at a much lower percentage of occurrence.

From the above un–normalized ρ_{HV} CFAD figures (Figure 5.20 through 5.25) for the lightning and non–lightning storms, one can see that both of these storms have their modes centered around 0.92, however the lightning storm mode has approximately three regions which are located at roughly the same heights as the charging regions in a thunderstorm cloud (as was seen with the Z_{DR} plots as well). The lightning storm mode is vertically aligned from t–15, where the non–lightning storm has a tilt in the mode up to and including t–15.

5.3. Rain lines, Rain and Ice Masses:

Presented are results that were obtained from calculating the rain line for the lightning and non–lightning storms and are shown in Figure 5.26, which are scatter plots of Z_{DP} versus Z_H (rain line) for NPOL at 1 km for the lightning storm, M3, in red (left) and the non–lightning storm, M1, in blue (right) at time t. The solid red (M3) and blue lines (M1) are the least–squares best fit line to the NPOL data which is less sensitive to outliers. For both storm types, the rain line equation (Z_{DP}), the number of points used in the rain line equation and the standard deviation of the data points from the rain line is shown in the plots.

From these plots one can see that the lightning storm has less data points available after the analysis was done than the non–lightning storm, with 82 and 89 particles being obtained, respectively. It should be noted that most of the non–lightning storms had many fewer data points than the lightning storms, due to the fact that so few of the non–lightning storms had Z_H values ≥ 35 dBZ in the mixed–phase layer (refer to chapter 3.2.2 above for the explanation on how this is calculated).

From Figure 5.26, one can also see that the lightning producing storm (M3) had higher Z_H values in the mixed–phase, with up to 49 dBZ being reached, where the non–lightning storm only had Z_H values reaching approximately 47 dBZ at 1 km. In addition, there is more scatter about the non–lightning rain line over all the values, whereas the lightning storm only has large scatter at the lower Z_H values (between 35 dBZ and 40 dBZ). The standard deviation that was calculated is therefore much lower for the lightning storm (0.811 dB) than for the non–lightning storm (1.072 dB), which influences the amount of total water and ice mass that is estimated for these storms (see Table 5.1 and Figure 5.27). This table shows the total water and ice masses (in kg) that were obtained for the lightning, M3 (left) and non–lightning, M1 (right), storms from t–45 to t+30 for the mixed–phase region.

Figure 5.27 is a graphical representation of Table 5.1 with the lightning storm (M3) in red and the non–lightning storm (M1) in blue. The solid red line and dashed red line indicates the water and ice mass for the lightning storm, respectively. The solid blue line and dashed blue line indicates the water and ice mass for the non–lightning storm, respectively (but is barely visible on the scale).

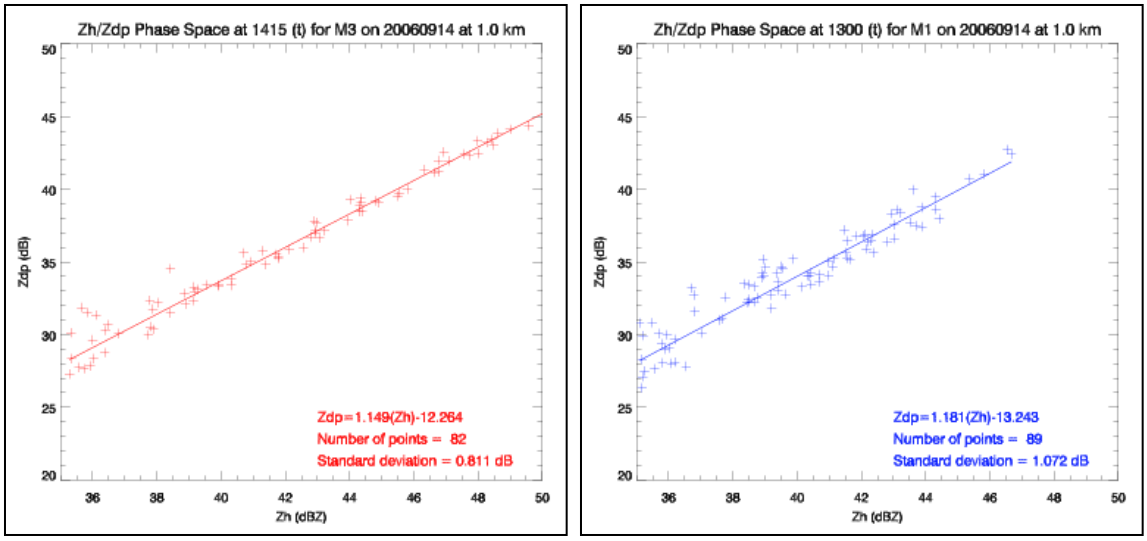

Figure 5.26: Scatter plot of Z_{DP} versus Z_H (rain line) for NPOL at 1 km for the lightning storm, M3, in red (left) and the non–lightning storm, M1, in blue (right) at time t. The solid red and blue lines are the least absolute deviation line to the NPOL data which is less sensitive to outliers. For both storm types, the rain line equation (Z_{DP}), the number of points used in the rain line equation and the standard deviation of the data points from the rain line is shown in the plots.

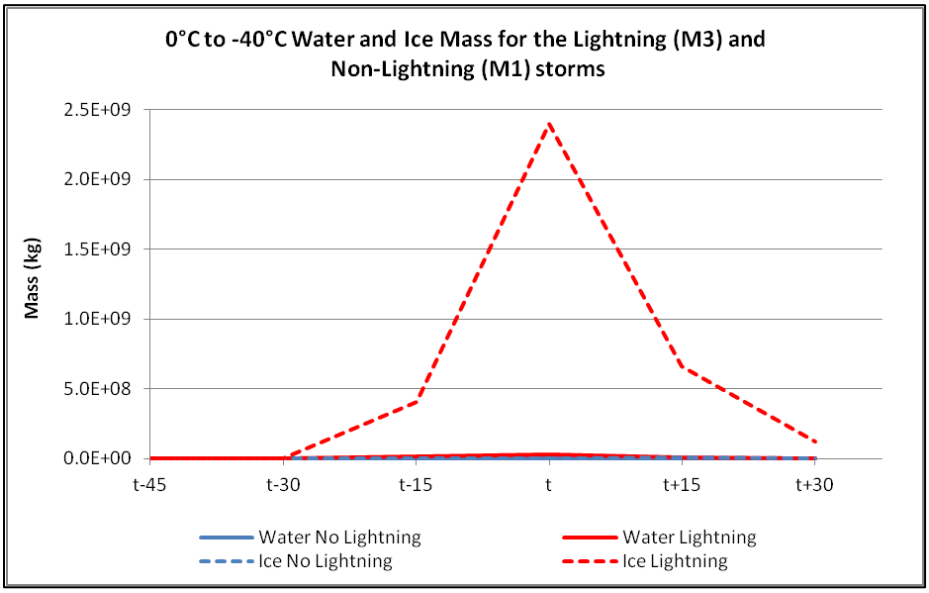

Figure 5.27: Graphical representation of the total water and ice mass in kg obtained for the lightning storm (M3) in red and the non–lightning storm (M1) in blue from t–45 to t+30 for the mixed–phase region. The solid red line and dashed red line indicates the water and ice mass for the lightning storm, respectively. The solid blue line and dashed blue line indicates the water and ice mass for the non–lightning storm, respectively (but is barely visible here).

Table 5.1: Total water and ice mass in kg obtained for the lightning, M3 (left) and non–lightning, M1 (right), storms from t–45 to t+30 for the mixed–phase region.

	Lightning (M3) Storm		**Non–Lightning (M1) Storm**	
	Water (kg)	**Ice (kg)**	**Water (kg)**	**Ice (kg)**
t–45	0	0	0	0
t–30	0	0	0	0
t–15	1.35E+07	4.05E+08	82725	1.85E+06
t	2.77E+07	2.40E+09	0	0
t+15	9.17E+06	6.60E+08	70693.1	5.16E+06
t+30	92927.8	1.20E+08	0	0

It is clear from the table and figure that both the lightning and the non–lightning producing storms have no noticeable water and ice present until t–15 (due to the lack of Z_H values ≥ 35 dBZ in the mixed–phase); the lightning storm have much more water and ice present from t–15 onwards as compared to the non–lightning storm (this is not as evident from Figure 5.27 and is why Table 5.1 was added). There is a sharp increase in the total mass of ice between t–30 and t–15, and the maximum is reached at time t for the lightning storm.

The non–lightning storms also shows a sharp increase in the ice mass between t–30 and t–15 (although much less than for the lightning storm, which is not really noticeable from the figure), with a complete collapse of the ice mass for the non–lightning storm at time t. It is also evident that for both M3 and M1, the ice mass is much larger than the water mass, especially the closer one gets to time t, although M3 has much more ice than M1. This is confirmed by the Z_H and Z_{DR} un–normalized CFADs discussed earlier, with the lightning storm displaying values indicative of large amounts of ice, graupel and hail, with lower amounts being obtained for the non–lightning storm,

especially in the mixed–phase region. However, the presence of supercooled liquid water is very important for the electrification process in thunderstorms, and as can be seen from the table and figure above, storm M3 has much more water available in the mixed–phase region than M1. When these water drops do not freeze, they become supercooled drops. Thus it is clear that a large amount of both water and ice, with more ice than water being needed before and during time t, is essential for the production of lightning.

5.4. MSG Interest Fields:

The MSG satellite interest fields will be discussed here for the individual lightning (M3) and non–lightning (M1) storms. The 10.8 μm T_B field is shown in Figure 5.28, with the lightning storms in red and the non–lightning storms in blue. Here, the 10.8 μm T_B field is indicative of the main updraft strength. These plots clearly show that the main updraft of the lightning storm is much stronger than for the non–lightning storm, with the T_B temperatures being reached at time t being 236.93 K and 261.66 K for the lightning and non–lightning storms respectively. At t–75, 75 minutes before the first CG flash was observed for the lightning storm, this storm is already 10.6 K colder than the non–lightning storm, with 271.86 K and 282.46 K being reached respectively. Although the lightning storm has an increase in the 10.8 μm T_B field between t–75 and t–60, its temperature at t–45 is 12.61 K less than the non–lightning storm at this time. Between time t and t+15, the lightning storm underwent another steep decrease in temperature, with 200.40 K being reached at t+15, where the non–lightning storm only had a decrease to 240.17 K at this time, a total of 39.77 K difference. After t+15, the lightning storm had an increase in the 10.8 μm T_B field, however only with 1.66 K, with a final 10.8 μm

T_B of 202.06 K at t+30, and the non–lightning storm underwent a small decrease of 6.09 K, with a final temperature of 234.08 K at t+30. Thus, it is clear that the main updraft of the lightning storm was much stronger than the non–lightning storm, especially between t–15 and t+30, evident by the large temperature differences between the storms.

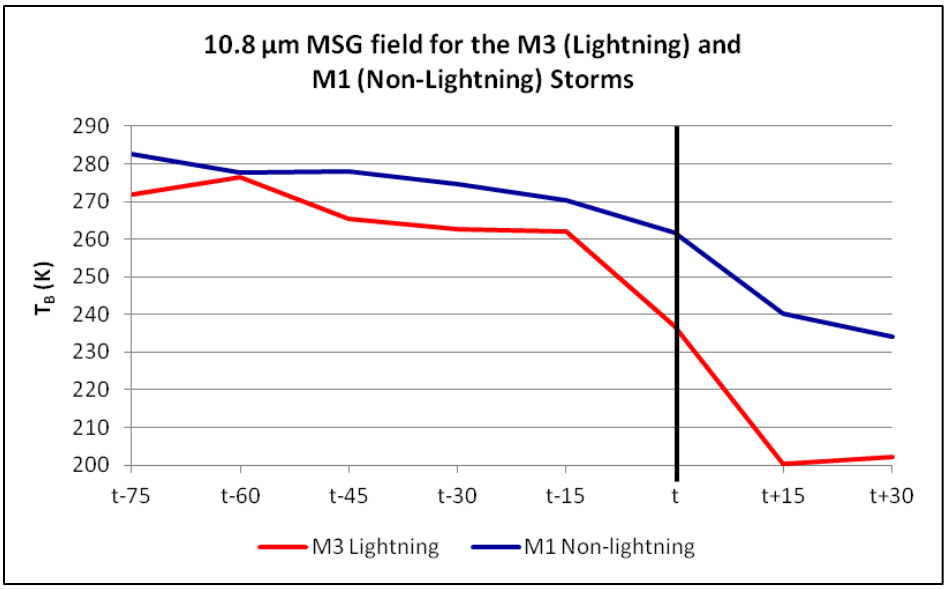

Figure 5.28: Graph of the 10.8 µm T_B field showing the main updraft strength features between the lightning and non–lightning storms from t–75 to t+30. The solid red line shows is the results obtained for the lightning storm, M3 and the solid blue line is the results obtained for the non–lightning storm, M1.

Figure 5.29 through 5.32 show the T_B difference fields used to obtain the updraft strength of the clouds (and is thus closely related to the 10.8 µm T_B field shown in Figure 5.28), which is also important for lightning occurrence. However, in Figures 5.29 and 5.30 there should be a positive trend to show that the updraft strength is increasing, while for Figures 5.31 and 5.32 there should be a negative trend. The 15 minute 6.2 – 7.3 µm T_B time trend is seen in Figure 5.29. Both the lightning and non–lightning storms had a positive trend between t–60 and t–45, however, the lightning storm starts off at –0.97 K and increases to 2.02 K by t–45, where the non–lightning storm has a 6.2 – 7.3 µm T_B

difference of –6.34 K at t–60 and increases to –0.06 K, which leads to a 2.99 K and 6.22 K increase, respectively. Therefore the non–lightning storm actually had a stronger positive trend than the lightning storm during this time period.

Between t–45 and t–15, the lightning storm had a decrease in the 6.2 – 7.3 μm T_B field, with 1.72 K being reached at this time, where the non–lightning storm had a further increase of 0.97 K during this 30–minute period, and thus ending with 0.91 K at t–15. However, within the 15 minutes leading up to the first CG flash, the lightning storm had a very strong positive trend, with a 7.7 K increase, where the non–lightning storm only had a 2.76 K increase, leading to the lightning storm having a 6.2 – 7.3 μm T_B of 9.42 K at time t, and the non–lightning storm only having a channel difference of 3.67 K, 5.75 K less than the lightning storm. Thus, the lightning storm has a stronger updraft at time t as compared to the non–lightning storm at this time, which might be an indication as to why the non–lightning storm did not produce any lightning. However, between time t and t+15, the lightning storm has a strong negative trend, with 5.11 K being reached at t+15, indicating that the updraft strength is weakening during this time, while the non–lightning storm has a further increase in this channel difference to 9.03 K, a 5.36 K increase, although it still does not reach the same 6.2 – 7.3 μm T_B as was reached by the lightning storm before the first CG flash occurred. Both storm types had a negative trend between t+15 and t+30, with the lightning storm 6.2 – 7.3 μm T_B being –1.07 K and the non–lightning storm being 1.54 K at t+30. Although there is a positive trend in this field, thus indicating an increasing updraft, the amount of increase is important; an increase of more than 6.0 K is probably needed in the 15 minute 6.2 – 7.3 μm T_B interest field for CG lightning to initiate.

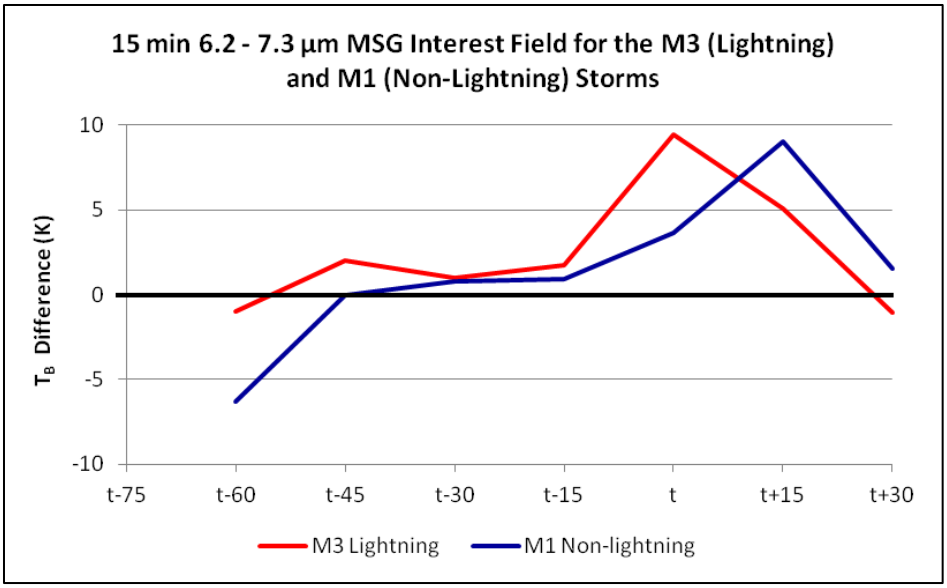

Figure 5.29: Graph of the 15 minute 6.2 – 7.3 µm T_B interest field showing the main updraft strength features between the lightning and non–lightning storms from t–75 to t+30. The red solid line shows is the results obtained for the lightning storm, M3 and the solid blue line is the results obtained for the non–lightning storm, M1.

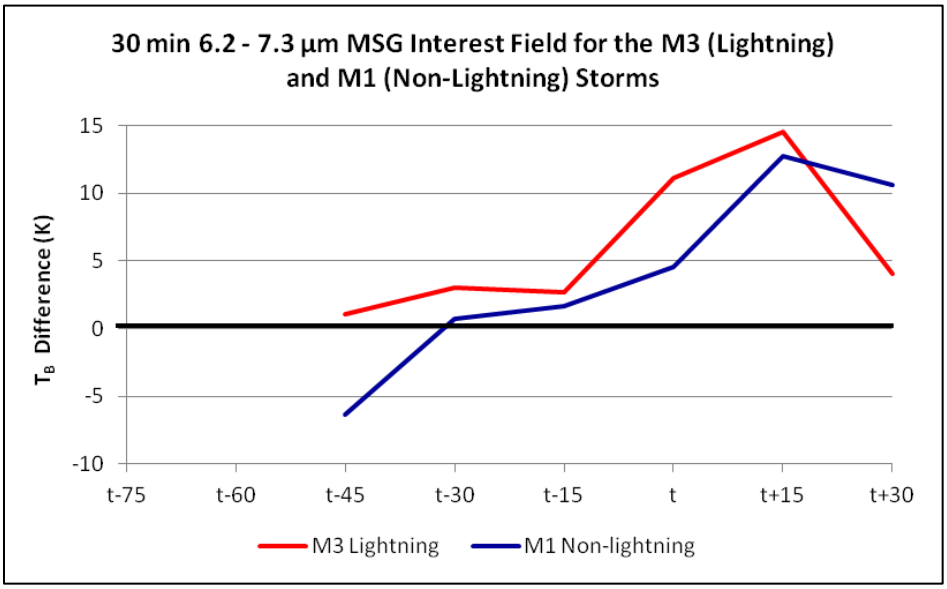

Figure 5.30: Graph of the 30 minute 6.2 – 7.3 µm T_B interest field showing the main updraft strength features between the lightning (M3) and non–lightning (M1) storms from t–75 to t+30. The remainder of the graph is the same as in Figure 5.29.

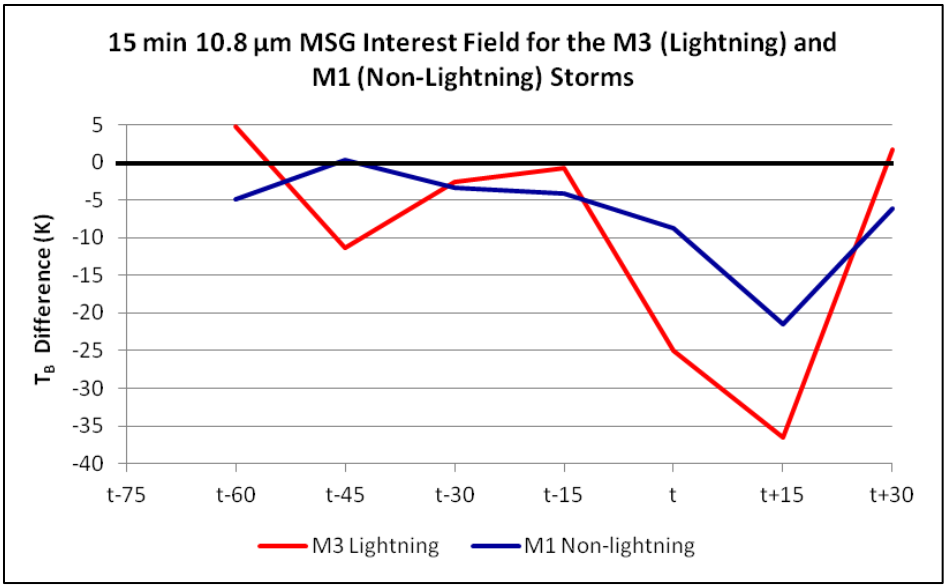

Figure 5.31: Graph of the 15 minute 10.8 µm T_B interest field showing the main updraft strength features between the lightning (M3) and non–lightning (M1) storms from t–75 to t+30. The remainder of the graph is the same as in Figure 5.29.

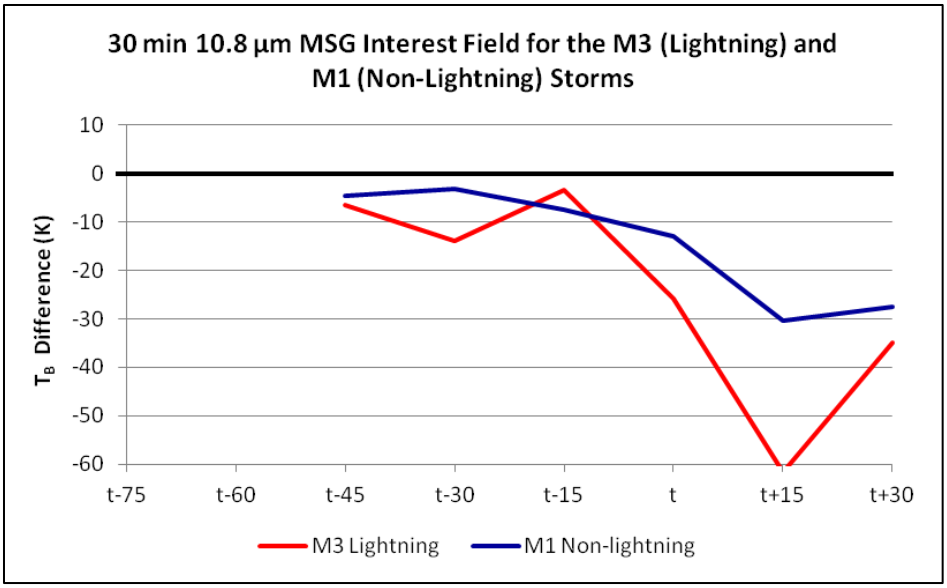

Figure 5.32: Graph of the 30 minute 10.8 µm T_B interest field showing the main updraft strength features between the lightning (M3) and non–lightning (M1) storms from t–75 to t+30. The remainder of the graph is the same as in Figure 5.29.

The 30 minute 6.2 – 7.3 µm T_B time trend for the lightning and non–lightning storms are seen in Figure 5.30. Here there should also be a positive trend to indicate increasing updraft strength, which is seen for both the lightning and non–lightning

storms. At t–45, the lightning storm has a 30 minute 6.2 – 7.3 μm T_B value of 1.04 K, with the non–lightning storm having a value of –6.40 K, which is a 7.44 K difference, however, between t–45 and t–30, the non–lightning storm has a sharp positive increase, with 0.69 K being reached at t–30 (a 7.09 K increase), where the lightning storm only has a 1.96 K increase and thus ending with 3 K at t–30. Between t–30 and t–15, the lightning storm has a small decrease of 0.3 K, where the non–lightning storm is still showing a positive trend, with a 0.97 K increase during this period. However, after t–15, the lightning storm has a very strong positive trend, with an 8.77 K increase between t–15 and t, and a 30 minute 6.2 – 7.3 μm T_B value of 11.14 K at time t.

The non–lightning storm, although also possessing a positive trend, only has an increase of 2.92 K during this period, with a value of 4.58 K at time t. This is a 6.56 K difference from the lightning storm at this time, which might be the reason why the non–lightning storm did not producing any CG lightning after time t. Between time t and t+15, the lightning storm has another increase, although small with a 30 minute 6.2 – 7.3 μm T_B value of 14.54 K being reached at t+15, but the non–lightning storm now has a large increase of 8.12 K, thus having a 30 minute 6.2 – 7.3 μm T_B value of 12.70 K at t+15. Although this is a large positive trend for the non–lightning storm, no CG lightning was observed after t+15, thus pointing towards the fact that a 30 minute 6.2 – 7.3 μm T_B difference of at least 8.5 K is needed for CG lightning to be initiated. After t+15, both the lightning and the non–lightning storms have a negative trend, indicating that the updraft strengths for both storms are now decreasing. At t+30, the lightning storm has a 30 minute 6.2 – 7.3 μm T_B value of 4.05 K and the non–lightning storm has a value of 10.57 K, meaning that the decrease in the updraft strength for the

non–lightning storm is actually much smaller than for the lightning storm. This might be due to gravitational settling, particularly the larger water drops, graupel and hail of the lightning storm, which decreases the updraft magnitude.

Figure 5.31 illustrates the 15 minute 10.8 T_B interest field, which is also indicative of the updraft strength; negative trends indicate increased updraft strength (which is thus opposite of the previous 2 figures). At t–60, the lightning storm has a 15 minute 10.8 T_B value of 4.71 K with the non–lightning storm having a value of –8.43 K, which is 13.14 K lower than the lightning storm value. Between t–60 and t–45, the lightning storm has a strong negative trend, with a 16.0 K decrease and a 15 minute 10.8 T_B value of –11.29 K at t–45. The non–lightning storm however, has an increase in the 15 minute 10.8 T_B field, with a value of 0.25 K being reached at t–45. Between t–45 and t–15, the lightning storm now has a positive trend and the non–lightning storm now has a negative trend, with the lightning storm having a 15 minute 10.8 T_B value of –0.76 K at t–15 and the non–lightning storm having a value of –4.13 K. Therefore, the lightning storm had a decrease in updraft strength during this time period, while the non–lightning storm has an increase in updraft strength. Nevertheless, between t–15 and t, the lightning storm has a very strong negative trend, with a 24.24 K decrease in the 15 minute 10.8 T_B within 15 minutes, and the non–lightning storm only having a 4.65 K decrease. Consequently, the lightning storm had a very strong updraft speed at time t, making it understandable why it initiated CG lightning during this time. From time t to t+15, both storms again display a negative trend, with the lightning storm now reaching –36.54 K (an 11.5 K decrease), and the non–lightning storm now having a value of –21.49 K (a 12.71 K decrease), thus the non–lightning storm has a stronger negative trend than the lightning

storm during this period, but still not enough to increase the updraft strength to such levels as to lead to the production of CG lightning.

Both storms display a strong positive trend after t+15, with 1.66 K and –6.09 K being reached for the lightning and non–lightning storms, respectively. This means that both storm types have a decrease in their updraft strengths, which could again be due to precipitation settling leading to downward friction in the storms. This also implies that the local equilibrium level is being reached, leading to an anvil developing in the lightning storm, with a low–topped "anvil" developing for the non–lightning storm. From the above it is clear that although the 15 minute 10.8 T_B interest field needs a decrease of at least 4 K in 15 minutes to show an increase in updraft strength, a much stronger decrease is needed to develop CG lightning, as seen here. Even with a 12.71 K decrease for the non–lightning storm between time t and t+15, there was still no CG lightning observed, indicating that for CG lightning to be initiated, the 15 minute 10.8 T_B interest field needs to decrease with at least 15 K to 20 K within a 15 minute period.

The 30 minute 10.8 T_B interest field can be seen in Figure 5.32 with the lightning storm (M3) displayed in red and the non–lightning storm (M1) in blue. Here, a negative trend that is larger than the 15 minute 10.8 T_B interest field trend is needed for strong updrafts to be obtained. At t–45, the lightning storm has a 30 minute 10.8 T_B value of –6.59 K, where the non–lightning storm has a value of –4.58 K, thus the two storms were very similar at this time in terms of this interest field. Between t–45 and t–30, the lightning storm shows a negative trend, with –13.83 K being reached, and the non–lightning storm actually has a positive trend, with –3.06 K being reached. Between t–30 and t–15, the lightning storm now has a positive trend, by means of a 10.53 K

increase in the 30 minute 10.8 T_B value, with the non–lightning storm having a negative trend and a decrease of 4.38 K. This brings the lightning and non–lightning storms to –3.30 K and –7.44 K respectively at t–15. For the period from t–15 to time t, the lightning storm has a very strong negative trend, with a 22.5 K decrease in the 30 minute 10.8 T_B field, thus ending with a –25.80 K value at time t. Although this decrease is not much larger than was obtained for the 15 minute 10.8 T_B interest field (Figure 5.31), it was still more than enough to obtain a strong updraft strength, as CG lightning occurred during this time. Although the non–lightning storm has another decrease from t–15 to t, this is only a 5.47 K decrease, which apparently is not enough for CG lightning to occur after this time. Between time t and t+15, both storms have another decrease in the 30 minute 10.8 T_B field, with –61.57 K and –30.27 K being reached for the lightning and non–lightning storms at t+15, respectively. This is a 35.77 K and a 17.36 K decrease for the lightning and non–lightning storm respectively, which for both storms is more than was obtained for the 15 minute 10.8 T_B interest field.

It is clear then that both storms had an increase in updraft strengths as seen in the negative trends obtained in the 30 minute 10.8 T_B interest field; however, since the non–lightning storm did not produce any CG lightning, a stronger negative trend of at least –20 K is possibly needed for CG lightning to occur. Between t+15 and t+30, both storms have an increase in the 30 minute 10.8 T_B field, with the lightning storm having a 26.7 K increase and the non–lightning storm having only a 2.69 K increase, however these storms have a final 30 minute 10.8 T_B value of –34.88 K and –27.58 K at t+30 respectively, thus once again having approximately the same values (as was seen at t–45). This increase in T_B values after t+15, especially for the lightning storm, is indicative of

an anvil forming during this time. It also indicates that after t+15 the updraft strengths decreased for both storms, and due to the anvils that developed during this time, this field (as well as the other interest fields) is no longer useful for predicting CG lightning. Therefore, it is clear from the lightning storm in Figure 5.32 that this 30 minute 10.8 T_B trend confirms the presence of persistent, long–lived updrafts, which is important for the electrification of storms.

Figure 5.33 and 5.34 show the results obtained for the 6.2 – 7.3 μm and 6.2 – 10.8 μm T_B interest fields, respectively, with these two interest fields indicating the cloud depth of the storms. The colder the T_B difference values, the shallower the cloud. Thus for a deep cloud, to occur, the 6.2 – 7.3 μm T_B difference should approach 0 K. From Figure 5.33 one can see that at t–75, the lightning storm has a value of –18.89 K and the non–lightning storm has a value of –13.9 K, with both storms having a decrease between t–75 and t–60. At t–60, the 6.2 – 7.3 μm T_B difference is –19.86 K and –20.23 K for the lightning and non–lightning storms, respectively, thus there is actually a decrease in the cloud depths here (although this is a long time before any CG lightning was observed). Between t–60 and t–15, both the storms have a slow positive trend, with –15.14 K and –18.63 K being reached at t–15 for the lightning and non–lightning storms, respectively. However the lightning storm has a strong positive increase after t–15, with –5.72 K being reached at time t, a 9.42 K increase within 15 minutes. Although the non–lightning storm also has an increase during this time period, the increase is much smaller, with only –14.96 K being reached at time t. This is 9.24 K less than was observed for the lightning storm at the same time, indicating that at time t, the cloud

depth for the lightning storm is much deeper than for the non–lightning storm, which is confirmed by the CG lightning that is observed after time t.

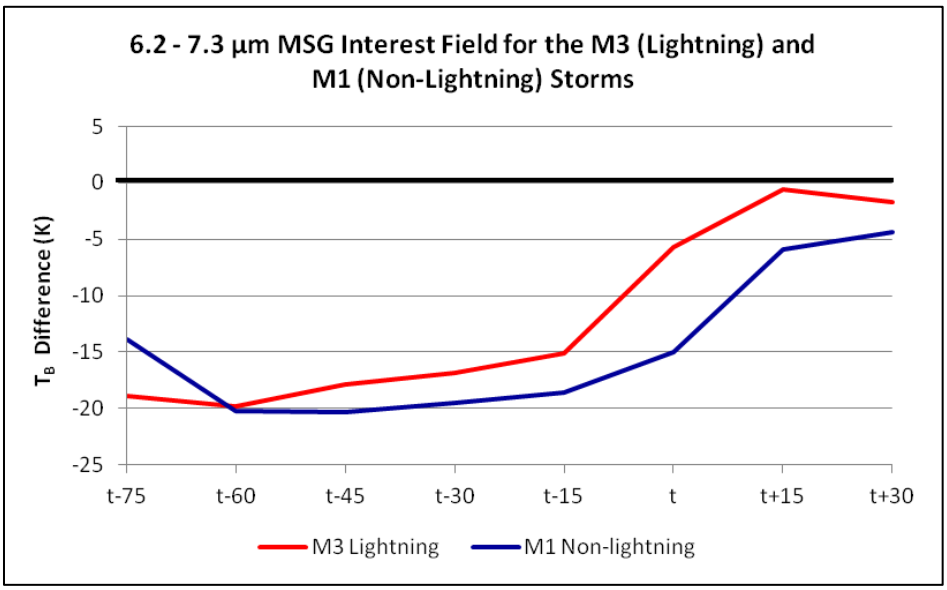

Figure 5.33: Graph of the 6.2 – 7.3 µm T_B interest field showing the cloud–depth features between the lightning (M3) and non–lightning (M1) storms from t–75 to t+30. The remainder of the graph is the same as in Figure 5.29.

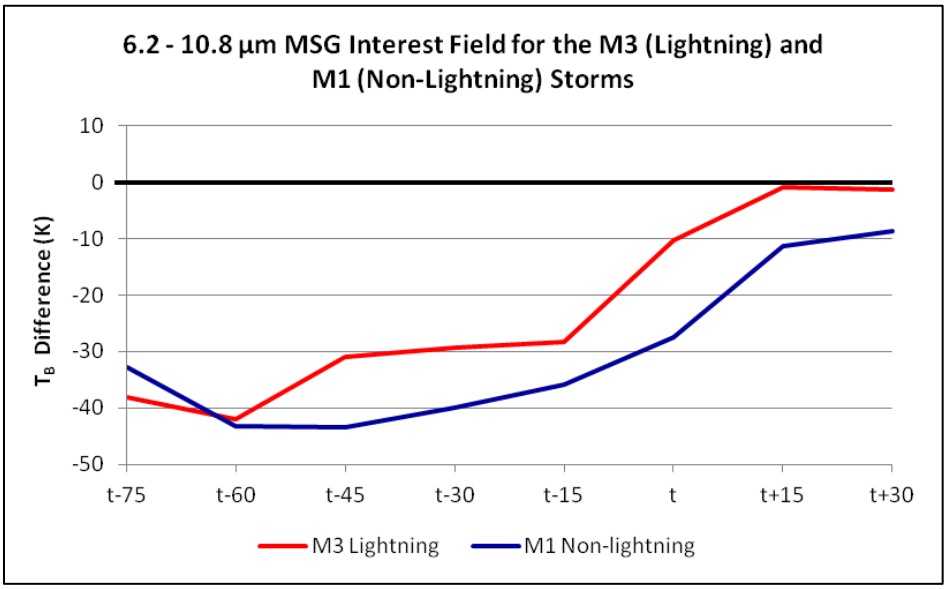

Figure 5.34: Graph of the 6.2 – 10.8 µm T_B interest field showing cloud–depth features between the lightning (M3) and non–lightning (M1) storms from t–75 to t+30. The remainder of the graph is the same as in Figure 5.29.

The 15 minutes after time t shows another positive trend for both storms, with the lightning storm now reaching –0.60 K and the non–lightning storm reaching –5.93 K at t+15. Although the non–lightning storm now has a 6.2 – 7.3 μm T_B difference value very close to the lightning storm before the first CG flashes were observed, the –5.93 K reached here was still not close enough to 0 K to initiate CG lightning. Interestingly, the non–lightning storm has another increase in the 6.2 – 7.3 μm T_B difference field after t+15 with –4.39 K being reached at t+30, and the lightning storm actually has a decrease during this period, with –1.67 K being reached. Therefore, although both storm types show 6.2 – 7.3 μm T_B difference values indicative of deep clouds, the non–lightning storm did not produce any lightning during its entire life, thus even if the cloud depth was deep, the convection in this storm was not strong enough for charge separation to occur to the point of initiating CG lightning. Due to this, it seems as though the 6.2 – 7.3 μm T_B difference should be at least –9.0 K and within –6.0 K of the zero–line in order to indicate the possibility of lightning initiation.

Figure 5.34 shows the results obtained from the 6.2 – 10.8 μm T_B interest field, also indicating the depth of the clouds. This interest field works approximately the same way as the previous interest field, with the closer the values are to 0 K, the deeper the clouds will be; however the critical value for cloud growth to occur is anywhere from –30 K to –10 K. As was the case with the 6.2 – 7.3 μm T_B interest field, both storms have small initial values, with the lightning storm obtaining –38.09 K and the non–lightning storm obtaining –32.73 K at t–75. Both storms see a decrease in values between t–75 and t–60, with –41.96 K and –43.20 K being reached for the lightning and non–lightning storms at t–60, respectively.

At t–45, the lightning storms' 6.2 – 10.8 μm T_B interest field increased to –30.95 K and the non–lightning storms' value decreased again to –43.46 K. Between t–45 and t–15, both storms displayed a positive trend, with –28.33 K and –35.82 K being reached for the lightning and non–lightning storms, respectively. Therefore, although these values are still far from 0 K, it shows that the storm cloud depths are marginally increasing. The lightning storm does have a large increase in the cloud depth between t–15 and time t, with –10.25 K being reached, leading to an 18.08 K increase in the 6.2 – 10.8 μm T_B interest field.

Although the non–lightning storm also displays an increase during this time, this is only an increase of 8.25 K, bringing the 6.2 – 7.3 μm T_B interest field to –27.57 K at time t. Thus, the lightning storm has a deeper cloud at this time as compared to the non–lightning storm, meaning that the cloud–top of the lightning storm is higher, indicating that more ice, graupel and hail will be observed in this storm, as compared to the non–lightning storm. Interestingly, both storms have a further increase between time t and t+15, leading to a 6.2 – 10.8 μm T_B value of –0.84 K and –11.36 K being reached for the lightning and non–lightning storms, respectively. This –11.36 K observed for the non–lightning storm at t+15 is still not enough for CG lightning to be initiated, and is still less than was observed for the lightning storm at time t.

Between t+15 and t+30, the lightning storm now decreases in 6.2 – 10.8 μm T_B value, with –1.32 K being reached, and the non–lightning storm value, reaching –8.63 K. Therefore, one can see that although the 6.2 – 10.8 μm T_B interest field seen here shows values approaching 0 K for both storm types, the lightning storm reaches –10.25 K at time t, indicating a deeper cloud, with higher cloud–tops and thus much more ice, graupel

and possible hail than the non–lightning storm at the same time and at t+15. This signifies that although the cloud–depth is increasing for the non–lightning storm from approximately time t (where the lightning storm already had an increasing cloud depth from t–45), in order for the CG lightning initiation to occur, one needs a 6.2 – 10.8 μm T_B interest field value of at least –10.25 K, or an increase of at least 15 K within a 15–minute period.

Figure 5.35 through 5.38 all show the MSG interest fields that indicate cloud–top glaciation with positive trends and/or a change in sign from negative to positive being needed to signify the glaciation of storm cloud–tops. Figure 5.35 displays the (8.7 – 10.8) – (10.8 – 12.0) μm T_B interest field (also known as the tri–spectral field), Figure 5.36 the 15 minute (8.7 – 10.8) – (10.8 – 12.0) μm T_B interest field (also known as the 15 minute tri–spectral field), Figure 5.37 the 8.7 – 10.8 μm T_B interest field and Figure 5.38 shows the 15 minute μm T_B interest field, with the lightning storm (M3) displayed in red and the non–lightning storm (M1) displayed in blue in each of the plots.

As mentioned earlier, the tri–spectral interest field (Figure 5.35) will change signs as cloud–top glaciation occurs. As seen, at t–75 the lightning storm has a tri–spectral T_B value of –1.98 K and the non–lightning storm has a value of –2.33 K. Between t–75 and t–60, both storms have a decrease with –2.58 K and –3.35 K being reached for the lightning and non–lightning storms, respectively at t–60. However, between t–60 and t–30, both storms have an increase in tri–spectral T_B values, with –0.38 K and –2.12 K being reached for the lightning and non–lightning storms.

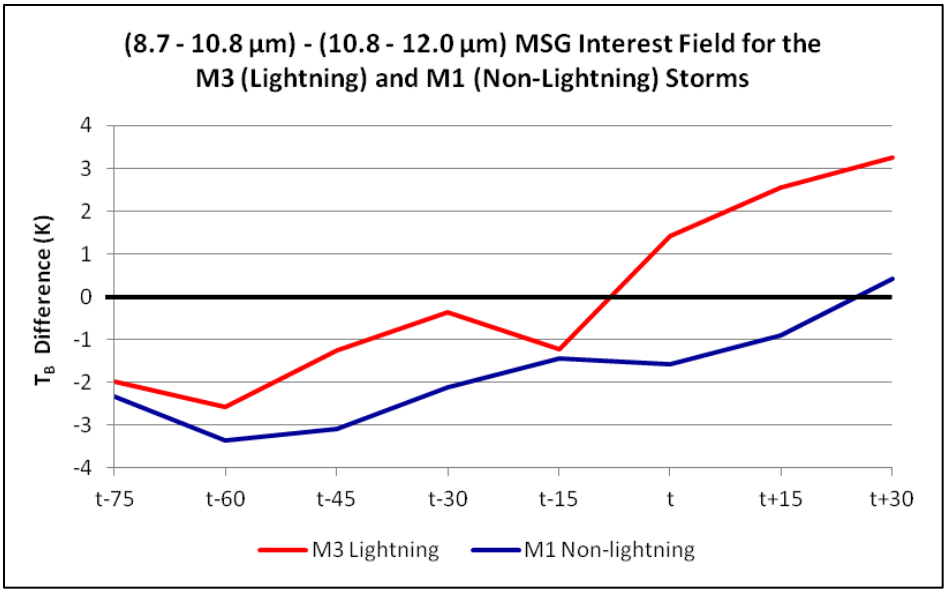

Figure 5.35: Graph of the (8.7 – 10.8) – (10.8 – 12.0) µm T_B interest field showing the cloud–top glaciation features between the lightning (M3) and non–lightning (M1) storms from t–75 to t+30. The remainder of the graph is the same as in Figure 5.29.

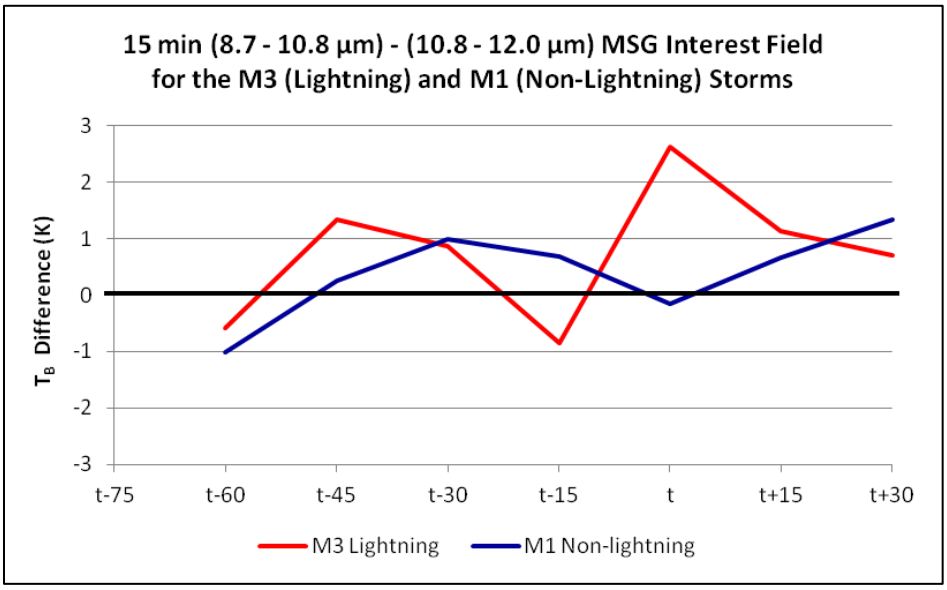

Figure 5.36: Graph of the 15 minute (8.7 – 10.8) – (10.8 – 12.0) µm T_B interest field showing the cloud–top glaciation features between the lightning (M3) and non–lightning (M1) storms from t–75 to t+30. The remainder of the graph is the same as in Figure 5.29.

Between t–30 and t–15, the lightning storm again has a decrease in the tri–spectral T_B field, with –1.23 K being reached, however the non–lightning storm is still increasing

and reaches –1.44 K at t–15. Therefore, even with the increase in the tri–spectral T_B value during this time, the lightning storm still has a value closer to 0 K than the non–lightning storm. During the period from t–15 to time t, the lightning storm has a 2.64 K increase, with 1.41 K being reached at time t, thus changing the tri–spectral T_B sign from negative to positive during this time, which indicates that cloud–top glaciation had occurred before time t was reached.

The non–lightning storms' tri–spectral T_B field, on the other hand, is decreasing during this period, making the value at time t only –1.58 K, not indicative of cloud–top glaciation at this time. Between time t and t+30, the lightning storms' tri–spectral T_B interest field value increases even more, with 3.26 K being reached at t+30. Thus, during this time it is clear that cloud–top glaciation has occurred for at least the previous 30 minutes, which is not seen for the non–lightning storm. In fact, the non–lightning storm only changes signs at t+30, with 0.42 K being reached at this time. Therefore, with the tri–spectral interest field indicating cloud–top glaciation as the T_B value changes from negative to positive, it is clear that the lightning storm has cloud–top glaciation occurring from before time t through t+30, with the non–lightning storm only seeing this at t+30, which is 30 minutes later. Because the non–lightning storm never produced lightning, the transition of the tri–spectral interest field from negative to positive should have an increase of at least 1.5 K while transitioning over 0 K for possible CG lightning initiation.

Figure 5.36 displays the 15 minute tri–spectral field for the lightning (in red) and non–lightning (in blue) storms. Although positive trends are needed for this field to indicate the occurrence of cloud–top glaciation, it is important to know that this field mostly indicates the rate at which cloud–top glaciation is approached. This means that

even though positive trends will be observed, this indicates that cloud–top glaciation is approaching due to the fact that the updrafts are increasing in strength, however, cloud–top glaciation will only occur once the 0 K threshold is crossed. As can be seen from the figure, both the lightning and non–lightning storms show positive trends between t–60 and t–45, with an increase of 1.92 K and 1.27 K being obtained for the storms, respectively. From t–45 to t–15, the lightning storm however shows a negative trend, with a 15 minute tri–spectral T_B value of –0.85 K being reached at t–15. The non–lightning storm on the other hand has an increase from t–45 to t–30, with 0.98 K being reached at t–30, but then also has a decrease after this time, with 0.68 K being reached at t–15. As of t–15, the lightning storm has a strong positive trend, with an increase of 3.49 K during this time, making the 15 minute tri–spectral T_B value at time t, 2.64 K. Thus, for the 15 minutes before CG lightning occurs for M3, there is strong cloud–top glaciation occurring.

The non–lightning storm still has a decreasing trend from t–15 to time t, with –0.14 K being reached, however after time t, the non–lightning storm has a positive trend for the remaining 30 minutes, with 1.34 K being reached at t+30, however, this trend only changes signs from negative to positive after time t, thus indicating that the rate at which cloud–top glaciation is approached, is increasing, however at a much lower rate than was observed for the lightning storm between t–15 and time t. On the other hand, the lightning storm has a sharp decrease in its 15 minute tri–spectral T_B value after time t, with 1.14 K and 0.71 K being reached at t+15 and t+30, respectively.

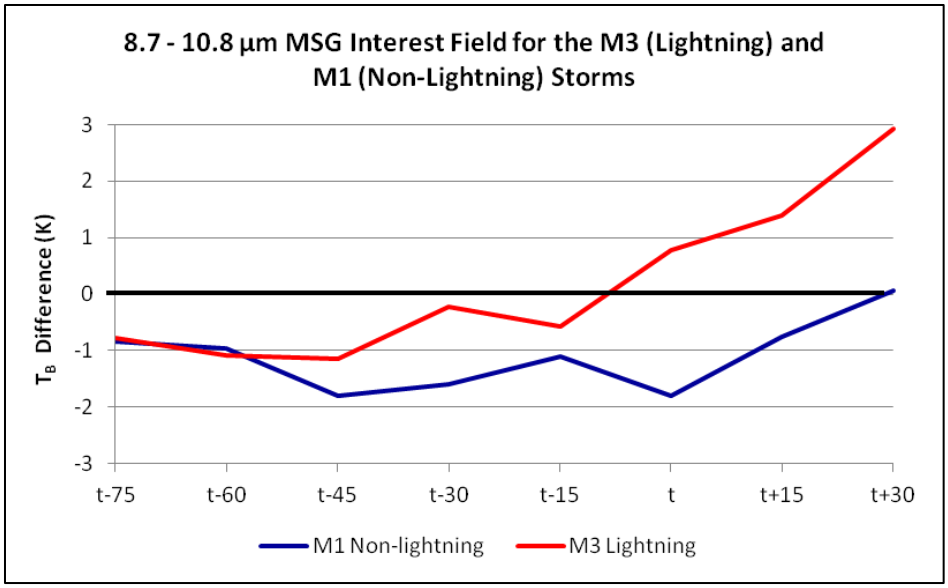

Figure 5.37: Graph of the 8.7 – 10.8 µm T_B interest field showing the cloud–top glaciation features between the lightning (M3) and non–lightning (M1) storms from t–75 to t+30. The remainder of the graph is the same as in Figure 5.29.

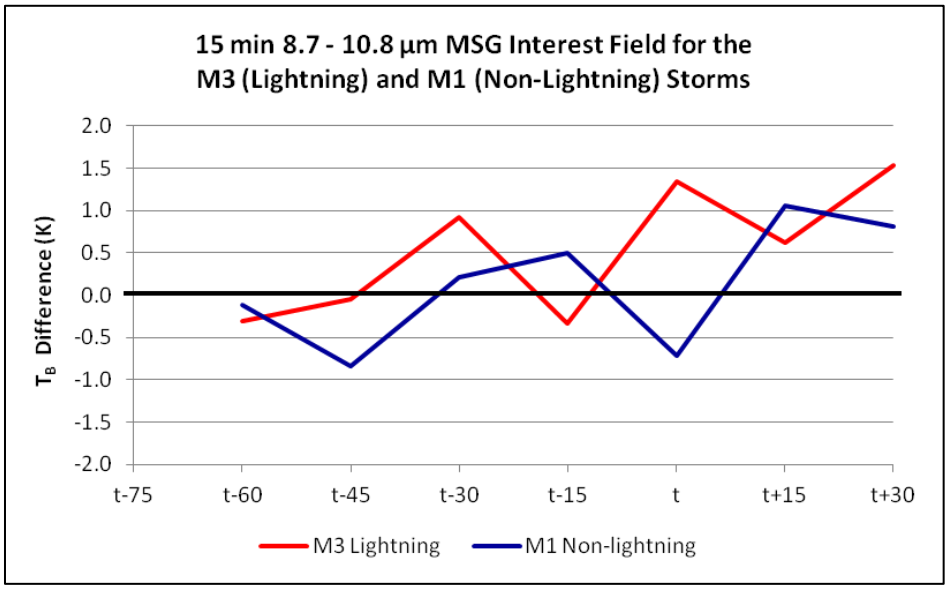

Figure 5.38: Graph of the 15 minute 8.7 – 10.8 µm T_B interest field showing the cloud–top glaciation features between the lightning (M3) and non–lightning (M1) storms from t–45 to t+30. The remainder of the graph is the same as in Figure 5.29.

From the 15 minute tri–spectral T_B field, one can therefore deduce that although both storms had a positive trend between t–60 and t–45 for the lightning storm and t–60

to t–30 for the non–lightning storms, the non–lightning storm only saw a change in signs after time t, with this change in sign already occurring immediately after t–15 for lightning storm. Hence, the lightning storm already had some cloud–top glaciation occurring at time t, whereas this was not the case for the non–lightning storm.

The 8.7 – 10.8 μm T_B interest field is seen in Figure 5.37, with the lightning storm (M3) in red and the non–lightning storm (M1) once again in blue. For cloud–top glaciation to be observed, the trend needs to change signs from negative to positive, and thus also have a positive trend, but with the 0 K level being needed for cloud–top glaciation to occur (which is the same as for the 15 minute tri–spectral field). Once again, there is a lot of variation in the two storms throughout the entire time period. The lightning storm has a 8.7 – 10.8 μm T_B value of –0.79 K at t–75, with this value decreasing to –1.09 K and –1.14 K at t–60 and t–45, respectively. After this time, there is an increase of 0.91 K at t–30, with another decrease between t–30 and t–15. At t–15, the lightning storm has a 8.7 – 10.8 μm T_B value of –0.57 K, after which 0.78 K is reached at time t, indicating that for this interest field, cloud–top glaciation was initiated between t–15 and time t. After time t, the lightning storm has an increase for the next 30 minutes, with a final 8.7 – 10.8 μm T_B value of 2.93 K being reached at t+30. Thus for M3, there is consistent cloud–top glaciation occurring for at least 35 to 45 minutes, although this does include the time after the first CG lightning was observed.

The non–lightning storm on the other hand has a 8.7 – 10.8 μm T_B value of –0.84 K at t–75, with a decrease of 0.12 K at t–60 and –1.14 K being reached at t–45 (which is another decrease). There is a positive trend between t–45 and t–15 for the non–lightning storm, with a 8.7 – 10.8 μm T_B value of –1.1 K being reached at t–15, and

there is another decrease after this, with –1.81 K being reached at time t. From time t, onwards, there is a positive trend that occurs, with the 0 K level only being reached immediately before t+30, with a 0.06 K value reached at this time. This 8.7 – 10.8 μm T_B interest field therefore indicates that the non–lightning storm only displays cloud–top glaciation after t+30, which is at least 30 minutes after the lightning storm. In addition, it is also 30 minutes after the time obtained for the 15 minute tri–spectral field seen in Figure 5.36. Consequently one can infer from the 8.7 – 10.8 μm T_B interest field that although a sign change from negative to positive T_B values are necessary for cloud–top initiation to be observed here, there also needs to be an increase of at least 1.0 K in 8.7 – 10.8 μm T_B values during this sign change for CG lightning to be initiated, which was not seen for the non–lightning storm.

The final MSG interest field is seen in Figure 5.38, which displays the results obtained for the 15 minute 8.7 – 10.8 μm T_B interest field with the trend having to be positive for cloud–top glaciation to occur, similar to the tri–spectral field above. It is important to note that although a positive trend is needed, this positive trend indicates the rate at which cloud–top glaciation is approached. Here it is clear that both the lightning and the non–lightning storms have large variations in the field, with both positive and negative trends occurring throughout the entire period. At t–60, the lightning storms' 15 minute 8.7 – 10.8 μm T_B value is –0.3 K, with an increase to –0.05 K at t–45 and another increase to 0.92 K at t–30, indicating that cloud–top glaciation is already occurring after t–45 when using this interest field. However, after t–30 there is a sharp decrease in the 15 minute 8.7 – 10.8 μm T_B value for the lightning storm, with a –0.34 K being reached at t–15. After t–15, there is once again an increase in the 15 minute

8.7 – 10.8 μm T_B value, with a sharp positive trend and a 1.34 K value being reached at time t. Thus, during this 15–minute timeframe there is a strong signal that cloud–top glaciation is occurring in the lightning storm, which is the 15 minutes leading up to the first CG lightning occurrence. A decrease is once again seen in the 15 minute 8.7 – 10.8 μm T_B field, with 0.62 K being reached at t+15, and a final increase after this time with 1.53 K being reached at t+30. Thus, for the 15 minute 8.7 – 10.8 μm T_B interest field the lightning storm seems to go through various stages of cloud–top glaciation, although the strongest period of glaciation occurs between t–15 and time t.

The non–lightning storm also goes through these variations in the 15 minute 8.7 – 10.8 μm T_B field, with –0.12 K and –0.84 K being reached at t–60 and t–45, respectively. Between t–45 and t–15 there is a positive trend, with a 1.05 K and a 0.29 K increase during this time, thus it seems that cloud–top glaciation is being approached for the non–lightning storm, although this is short–lived. Between t–15 and time t, the non–lightning storm has a strong negative trend, with –0.71 K being reached at time t, after which another positive trend is observed and 1.06 K is reached at t+15. During this time, the positive trend is stronger than before, indicating that the rate at which cloud–top glaciation is approached, is increasing. After t+15, there is another decrease in the 15 minute 8.7 – 10.8 μm T_B value, with 0.81 being reached at t+30. From the above, one can see that although a positive trend is indicative of cloud–top glaciation in the 15 minute 8.7 – 10.8 μm T_B interest field, one needs at least a 1.5 K increase, with at least 1.2 K being reached before CG lightning will occur due to the fact that the non–lightning storm did not produce enough cloud–top glaciation for significant charging and thus CG lightning to occur.

In summary, although a positive trend was seen for both the lightning and non–lightning storms in the 15 minute 6.2 – 7.3 μm T_B interest field, especially between t–15 and time t, with this indicating an increase in the updraft strength, the value of the increase in this interest field seems to be important. This is due to the fact that the lightning storm produced CG lightning after time t, where the non–lightning storm never produced any CG lightning, while both had a positive trend between t–15 and time t, and in fact, the non–lightning storm had a consistent positive trend between t–45 and t+15, which was not seen for the lightning storm. Although there is a positive trend in this field, the amount of increase is more important, with an increase of more than 6.0 K probably being needed in the 15 minute 6.2 – 7.3 μm T_B interest field for CG lightning to initiate.

The 30 minute 6.2 – 7.3 μm T_B interest field, like the 15 minute 6.2 – 7.3 μm T_B interest field, should show a positive trend to imply an increase in the updraft strength. However, here it was shown that in order for CG lightning to occur, one most likely needs a 30 minute 6.2 – 7.3 μm T_B increase (positive trend) of at least 8.5 K over a 15 minute period (due to the non–lightning storm having positive trends while not producing lightning). From the above it is also clear that although the 15 minute 10.8 T_B interest field needs a decrease of at least 4 K in 15 minutes to show an increase in updraft strength, a much stronger decrease is needed to initiate CG lightning, as seen above. Even with a 12.71 K decrease for the non–lightning storm between time t and t+15, there was still no CG lightning observed. This indicates that for CG lightning to occur, the 15 minute 10.8 T_B interest field needs to decrease by at least 20 K within a 15 minute period.

Furthermore, although both storm types show 6.2 – 7.3 μm T_B difference values indicative of deep clouds, the non–lightning storm did not produce any lightning during its entire life, thus even if the cloud depth was deep, the convection in this storm was not strong enough for charge separation to occur to the point of initiating CG lightning. Hence, it seems as though the 6.2 – 7.3 μm T_B difference should be at least –9.0 K and within –6.0 K of the zero–line in order to indicate the possibility of lightning initiation. The 6.2 – 10.8 μm T_B interest field results seen here show values approaching 0 K for both storm types with the lightning storm reaching –10.25 K at time t, indicating a deeper cloud, with higher cloud–tops and thus much more ice, graupel and possible hail than the non–lightning storm at the same time and at t+15. This signifies that although the updraft strength is increasing for the non–lightning storm from approximately time t (where the lightning storm already had strong updrafts occurring from t–45), in order for the CG lightning initiation to occur, one needs a 6.2 – 10.8 μm T_B interest field value of at least –10.25 K, or an increase of at least 15 K within a 15–minute period.

With the tri–spectral interest field indicating cloud–top glaciation is as the T_B value changes from negative to positive, it is clear that the lightning storm has cloud–top glaciation occurring from before time t through t+30, with the non–lightning storm only seeing this at t+30, which is 30 minutes later. Consequently, due to the fact that the non–lightning storm never produced lightning, the transition of the tri–spectral interest field from negative to positive, could be changed to include that this value must increase with at least 1.5 K while transitioning over 0 K for possible CG lightning initiation. The 15 minute tri–spectral interest field indicates the rate at which cloud–top glaciation is approached when positive trends are observed. This field showed positive trends for both

the lighting and non–lightning storms early on in the storms' lives; however, these positive trends were short–lived. Stronger positive trends were observed between t–15 and time t for the lightning storm, making it clear that the majority of cloud–top glaciation occurred here. This is also confirmed by the other fields which indicate an increase in updraft strength and cloud–depths for the lightning storm during this period.

One can infer from the 8.7 – 10.8 μm T_B interest field that although a sign change from negative to positive T_B values are necessary for cloud–top initiation to be observed here, one needs at least a 1.0 K increase in 8.7 – 10.8 μm T_B values during this sign change for CG lightning to be initiated, which was not seen for the non–lightning storm. Finally it was seen that for the 15 minute 8.7 – 10.8 μm T_B interest field the lightning storm seems to go through various stages of cloud–top glaciation, although the strongest period of glaciation occurred between t–15 and time t. Finally, although a positive trend indicates a positive rate at which cloud–top glaciation is approached in the 15 minute 8.7 – 10.8 μm T_B interest field, one a strong positive trend, together with a change in signs (possibly) for cloud–top glaciation to occur, with at least 1.2 K being reached before CG lightning will occur due to the fact that the non–lightning storm did not produce enough cloud–top glaciation for significant charging and thus CG lightning to occur.

CHAPTER 6

RESULTS AFTER STORM AVERAGING

The average results obtained from the NPOL radar, MSG satellite interest fields, and the lightning fields are presented in this chapter. Again, 33 lightning producing and 30 non–lightning convective storms were analyzed as clouds grew from the cumulus to cumulonimbus scale (refer to Appendix A for sounding plots for most of the storm days). Each storm was analyzed separately, with the individual storm results then being averaged to obtain a single variable result to help gain a plot of the most robust physical processes these data have to show.

6.1. Z_H, Z_{DR} and ρ_{HV} CFADs:

Figures 6.1 through 6.6 are average un–normalized Z_H (also called CZ in the plots) CFADs for lightning (left) and non–lightning (right) for all times from t–45 (Figure 6.1) to t+30 (Figure 6.6). As mentioned earlier, the CFADs presented here were not normalized with the bin size at each level, and therefore their units are % dBZ^{-1}.

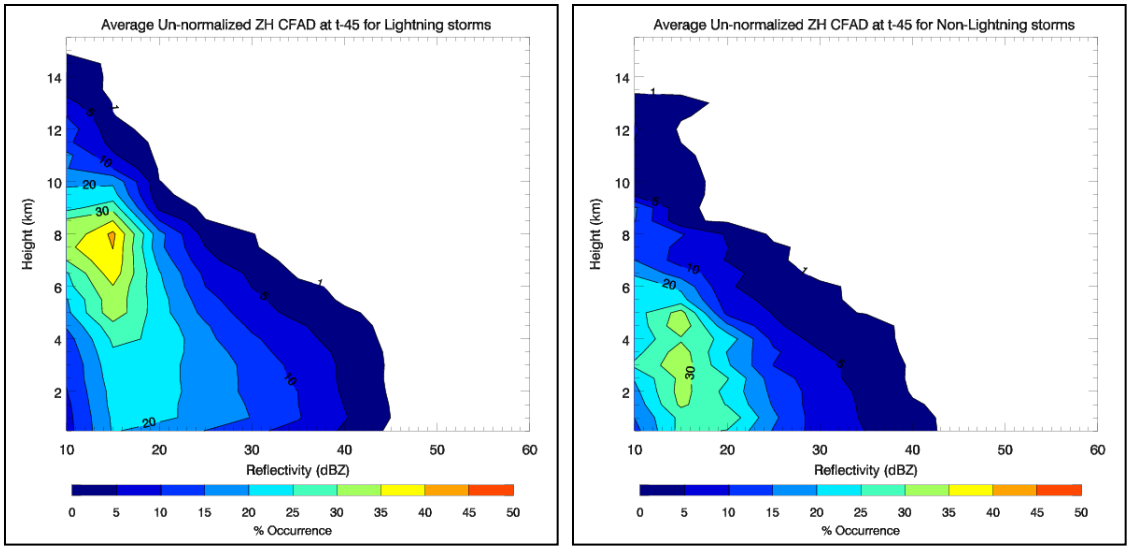

Figure 6.1: Average un–normalized Z_H (called ZH in plot) CFADs for lightning (left) and non–lightning (right) at t–45.

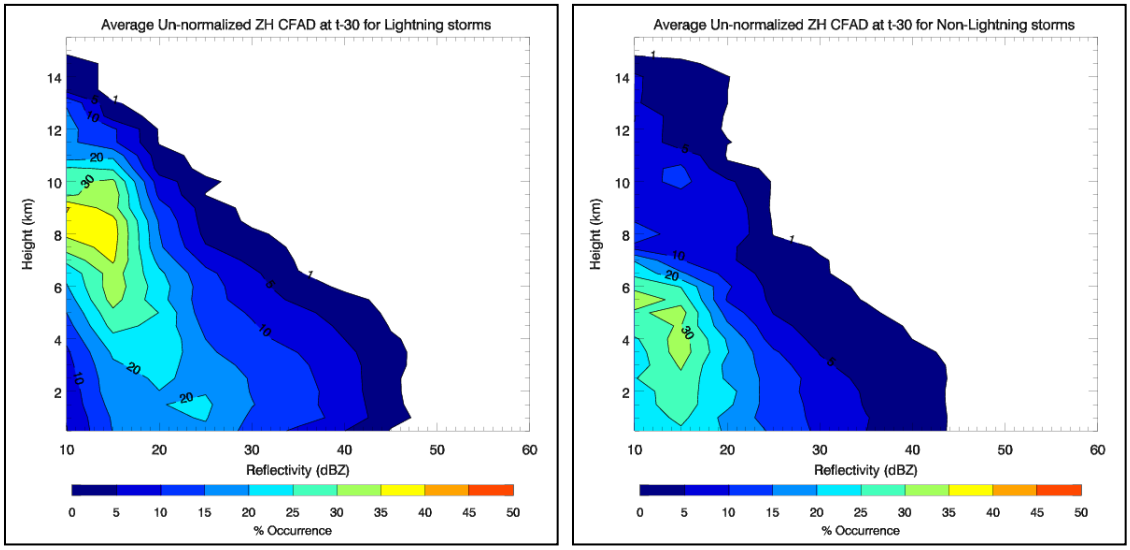

Figure 6.2: Average un–normalized Z_H (called ZH in plot) CFADs for lightning (left) and non–lightning (right) at t–30.

Even at t–45 (Figure 6.1) one can see that there are differences between the lightning and non–lightning producing storms. The lightning producing storms have reflectivity values of 20 dBZ up to a height of 11 km (approximately –40 °C) with an occurrence of 1 % dBZ^{-1}, whereas the non–lightning producing storms have 20 dBZ values only to roughly 8.5 km, also at 1 % dBZ^{-1}. The maximum height reached for the

lightning storms is 15 km (although it should again be noted that some storms had cloud–top heights higher than this, but all analysis were cut off at 15 km), whereas the non–lightning storms reach only about 13.5 km, on average, at t–45. Reflectivity values of up to 45 dBZ were reached to a height of 5 km for the lightning storms, with the non–lightning storms only reaching a maximum reflectivity of 43 dBZ at the ground, with a decrease to 35 dBZ at 5 km at 1% dBZ^{-1}. A maximum mode of reflectivity of between 15 % dBZ^{-1} and 40 % dBZ^{-1} were reached for values between 10 dBZ and 30 dBZ up to 10 km for the lightning storms, while the maximum mode for the non–lightning storms only reached 15 % dBZ^{-1} to 30 % dBZ^{-1} for 10 dBZ to 20 dBZ values up to 4 km. Therefore the lightning producing storms already have many smaller drops, supercooled liquid water and possible ice crystals located in the mixed–phase layer (as can be seen by the lower Z_H values), with large drops, graupel and hail located to at least 5 km (as seen by the higher Z_H values) at t–45 (this is seen more clearly from vertical cross sections as seen in Chapter 5, but is not shown in this chapter due to the results shown here being averages of the lightning and non–lightning storms). The same cannot be said for the non–lightning storms.

Figure 6.2 shows the average un–normalized Z_H CFADs for lightning (left) and non–lightning (right) at t–30. The non–lightning storms now have reflectivity values of up to 20 dBZ to a height of roughly 15 km, while the lightning storms have values of only up to 15 dBZ at this height. However, the lightning storms have maximum reflectivity values at 1 % dBZ^{-1} of up to 46 dBZ below 4.5 km and 44 dBZ up to 5 km; the non–lightning storms obtain 44 dBZ up to 3 km and at 5 km, this value decreases to 36 dBZ at 1 % dBZ^{-1}. In addition, the maximum mode of 15 % dBZ^{-1} to 40 % dBZ^{-1}

occurs up to 13 km for the lightning storms (including reflectivity values up to 30 dBZ at the lowest levels), with the non–lightning storms instead only reaching these percentages up to 7 km. It should also be noted that the core of the lightning storms (30 % dBZ^{-1} to 40 % dBZ^{-1}) is located between 5 km and 10 km, which is in the mixed–phase layer, where electrification occurs. Furthermore, at the lower levels between 0 km and 5 km, the reflectivity mode of the lightning storm is tilted, but above 5 km, this mode is vertically aligned. This means that there is a large variety of drop sizes below the melting layer; larger hydrometeor sizes occur close to the surface and smaller sizes occur close to the melting layer. The non–lightning storms do not show this tilt in the lower levels.

At t–15 (Figure 6.3), the lightning storms now have reflectivity values of 30 dBZ to 15 km at 1 % dBZ^{-1}, with the non–lightning storms only having 15 dBZ values at 14 km, which is the maximum height reached at this time for the non–lightning storms. Maximum reflectivity values of up to 50 dBZ are reached for the lightning storms below 5 km and 44 dBZ below 3.5 km for the non–lightning storms. The mode of the lightning storms between 15 % dBZ^{-1} and 40 % dBZ^{-1} occurs up to 13.5 km. However, the 20 % dBZ^{-1} and 40 % dBZ^{-1} area is now located between 3.5 km and 12.5 km, which is higher than was seen at t–30 (and thus the reflectivity mode at t–15 has lofted to higher levels). For the non–lightning storms, the 15 % dBZ^{-1} and 40 % dBZ^{-1} mode is now located between 0 km and 9 km, with reflectivity values reaching 25 dBZ. Values between 30 % dBZ^{-1} and 40 % dBZ^{-1} are located between 6 km and 9.5 km for 12 dBZ to 17 dBZ for the lightning storms and for the non–lightning storms this occurs between 4.5 km and 7.5 km for Z_H values between 10 dBZ and 17 dBZ. Although both types of

storms show this behavior, the lightning storms' maximum mode occurs at a slightly higher elevation than the non–lightning storms. In addition, the same tilt below 5 km for the lightning storm, with vertical alignment above this level is again present for the lightning storms, and not present for the non–lightning storms. This vertical alignment is indicative of the distribution of particle size being fairly constant with height. The tilt is again showing that the particle sizes vary below the melting level. From the above it can be inferred that the lightning storms have much more ice, graupel, supercooled liquid water and larger drops at t–15 than the non–lightning storms.

Figure 6.4 shows the average un–normalized Z_H CFADs for lightning (left) and non–lightning (right) at time t, which is the 15 minute timeframe in which the lightning storms produced their first CG strokes. Again, one can see that the lightning storms have reflectivity values of up to 20 dBZ at a minimum of 15 % dBZ^{-1} to 15 km, whereas the non–lightning storms only show this up to a height of 12 km. The lightning storms also have reflectivity values of 30 dBZ at 1 % dBZ^{-1} to a height of 15 km, with the non–lightning storm only having reflectivity values of 18 dBZ at 15 km. In addition, the lightning storms have maximum reflectivity values reaching 49 dBZ at 1 % dBZ^{-1} up to 5.5 km, with the non–lightning storms reaching 47 dBZ up to roughly 4 km. The mode of the lightning storm between 20 % dBZ^{-1} and 35 % dBZ^{-1} now occurs between roughly 3 km and 15 km, with the non–lightning storms showing 20 % dBZ^{-1} to 45 % dBZ^{-1} between roughly 2 km and 11 km. Also, at this time, the tilt seen in the previous lightning plots, although remaining below 4 km, is now much less prominent, with most of the values seeming vertically orientated at time t. Again, this vertical alignment is

indicative of the distribution of particle size being fairly constant with height. The tilt is again showing that the particle sizes vary below the melting level.

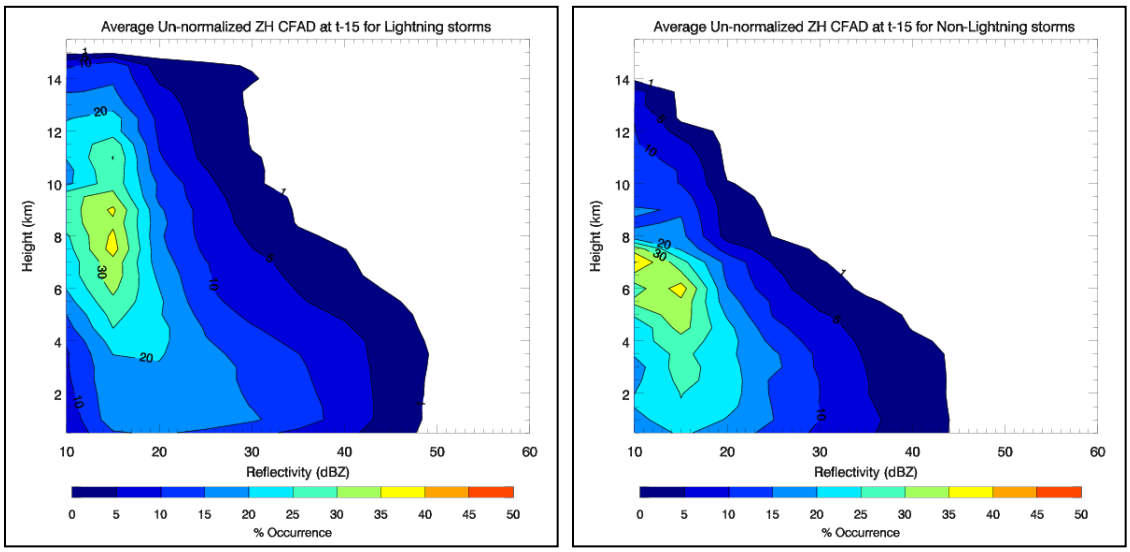

Figure 6.3: Average un–normalized Z_H (called ZH in plot) CFADs for lightning (left) and non–lightning (right) at t–15.

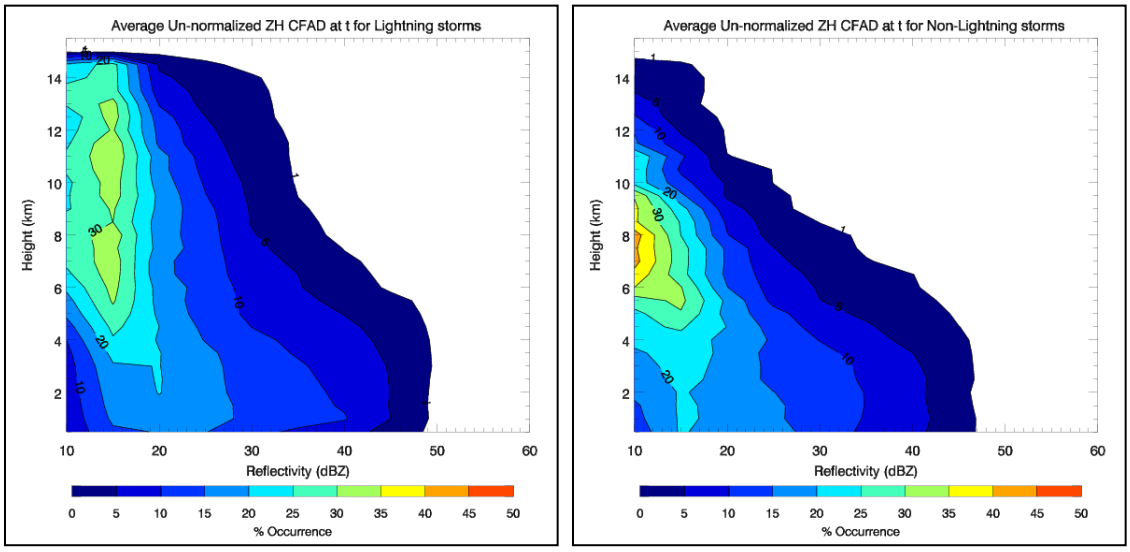

Figure 6.4: Average un–normalized Z_H (called ZH in plot) CFADs for lightning (left) and non–lightning (right) at time t.

At t+15 (Figure 6.5), maximum reflectivity values of 49 dBZ is reached up to 5 km for the lightning storm at 1 % dBZ^{-1} and 46 dBZ up to 4.5 km at 1 % dBZ^{-1} for the

non–lightning storm. Also the non–lightning storms' mode (between 20 % dBZ^{-1} and 45 % dBZ^{-1}) now occurs between 2 and 12 km, therefore, finally reaching the higher levels, which were reached between t–30 and t–15 for the lightning storms. The 20 % dBZ^{-1} to 35 % dBZ^{-1} mode now occurs between 3 km and 14.5 km for the lightning storms. Reflectivity values of up to 30 dBZ are also reached at 15 km for the lightning storms, with only 20 dBZ being reached for the non–lightning storms. Also notable is the tilt in the lower levels (below 5 km) is again present for the lightning storms and now also occurs for the non–lightning storms, with a more vertical alignment occurring above 5 km.

Figure 6.6, which shows the average un–normalized Z_H CFAD for lightning (left) and non–lightning (right) at t+30, indicates that the non–lightning storms' maximum mode of 30 % dBZ^{-1} to 50 % dBZ^{-1} finally occurs at higher levels, between 4 km and 11.5 km, with the 15 % dBZ^{-1} and higher occurring from ground–level to 12 km. At this point, the lightning storms have produced ground flashes for 30 minutes. The lightning storms' mode of 15 % dBZ^{-1} to 45 % dBZ^{-1} now occurs between ground–level up to 14.5 km. Maximum reflectivities of 48 dBZ are reached to 4.5 km and 45 dBZ up to 4 km for the lightning and non–lightning storms, respectively. Also, 30 dBZ values are reached up to 14 km for the lightning storms, with only 22 dBZ up to 13 km for the non–lightning storms. In addition, it seems the tilt is again no longer visible for the lightning storms, with the mode being vertically aligned, but the non–lightning storms now show a slight tilt below 4 km. This vertical alignment is indicative of the distribution of particle size being fairly constant with height. The tilt is again showing that the particle sizes vary below the melting level.

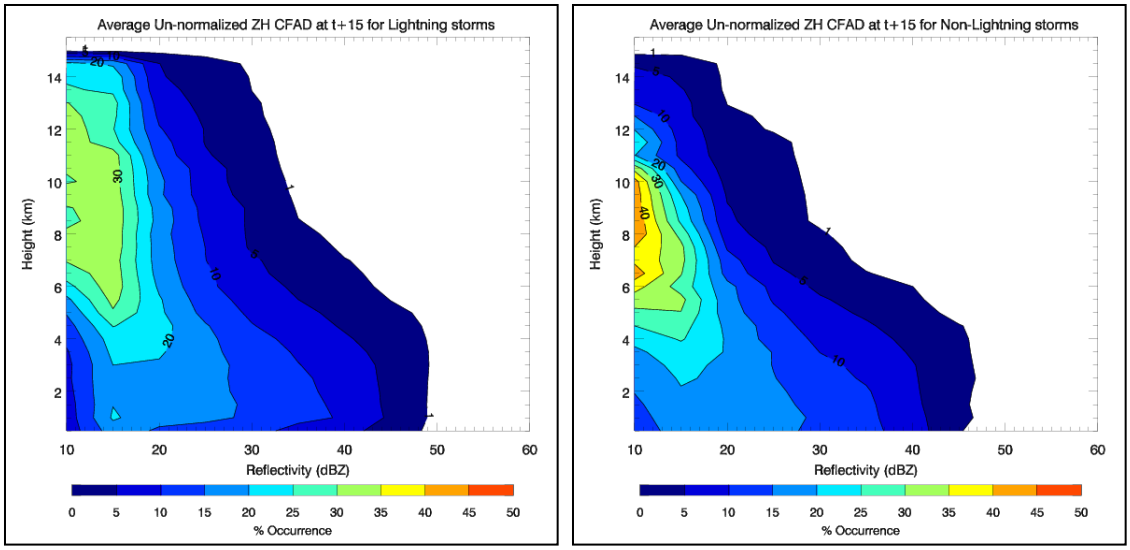

Figure 6.5: Average un–normalized Z_H (called ZH in plot) CFADs for lightning (left) and non–lightning (right) at t+15.

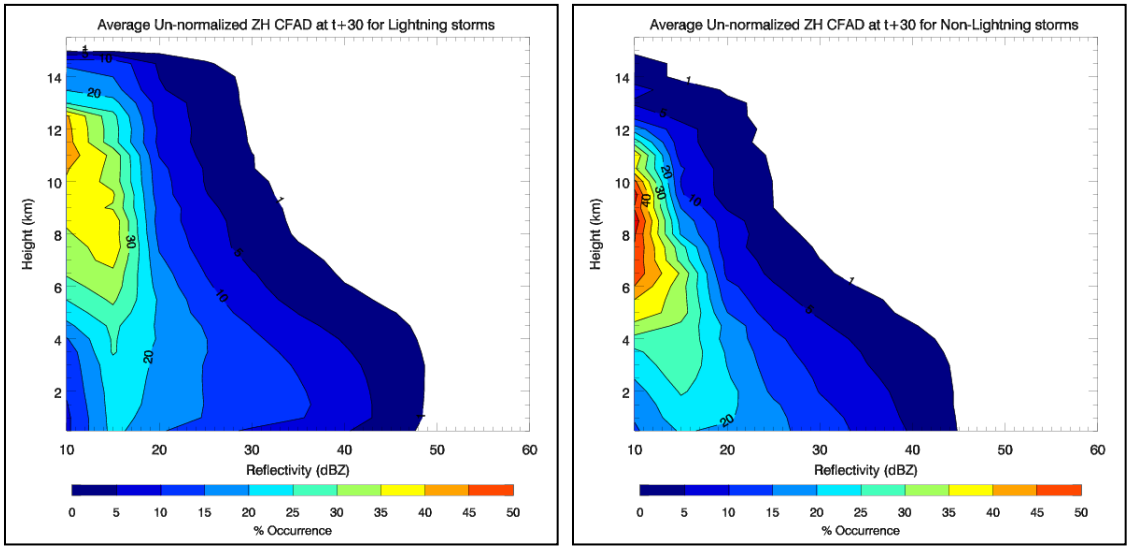

Figure 6.6: Average un–normalized Z_H (called ZH in plot) CFADs for lightning (left) and non–lightning (right) at t+30.

From these average Z_H un–normalized CFAD plots, the non–lightning storms take much too long for larger reflectivities to reach the top of the cloud, with the mode also taking substantially longer to loft to higher levels above 5 km. Due to this, the non–lightning storms do not produce any CG lightning. Furthermore, the non–lightning storms always have lower maximum reflectivity values than the lightning storms, and

these values occur at lower maximum levels than the lightning storms. Another interesting point to note is that the lightning storms show a tilt below and vertical alignment above the melting level (located at approximately 5 km) when one looks at the modes of the storms. This tilting–vertical structure already occurs at t–30 for the lightning producing storms, whereas the non–lightning storms only show this feature at t+15. However, at time t, this tilt is no longer visible for the lightning storms, while the entire mode is now vertically aligned. This tilt is indicative of large particles occurring above ground–level with particle size decreasing as one reaches the melting layer. The vertical alignment is again indicative of the distribution of particle size being fairly constant with height. It is also apparent that the non–lightning storms don't produce enough supercooled liquid water, graupel, and ice for a long enough period, as can be seen with the maximum mode already occurring within the mixed–layer (0 °C to –40 °C) at t–45 for the lightning storms, but only at time t (maximum mode between 5 km and 10 km) for the non–lightning storms, which indicates that this region of maximum mode should occur for at least 30 minutes before lightning will occur.

Figures 6.7 through 6.12 show the average un–normalized Z_{DR} CFADs for lightning (left) and non–lightning (right) from t–45 to t+30. Recall that nearly 0 dB and lower (negative) values (together with high reflectivity values) are indicative of hail and graupel, with Z_{DR} values for water being greater than about 0.5 dB; and larger values as the drop size increases. Ice particles will have Z_{DR} values around 0 dB. Also, the Z_{DR} column, which is a narrow columnar region of positive Z_{DR} values above the 0 °C isotherm, could be supercooled rain drops that are lofted upwards in the cloud due to strong updrafts. Unfortunately, this feature is not clear in the following plots, due to the

fact that the Z_{DR} column is usually seen when viewing vertical cross sections of the Z_{DR} in the clouds, and here, the plots are of CFADs, making this feature difficult to see. In addition, due to the NPOL radar frequency occurring at 10 cm, these supercooled droplets are not seen by the radar.

Figure 6.7 shows the average un–normalized Z_{DR} CFADs for lightning (left) and non–lightning (right) storms at t–45. For the lightning storm, the mode of the Z_{DR} is more positive below 5 km and more negative above this height, indicating that larger drops are located below the melting level, with smaller droplets, ice crystals, and possibly hail and graupel already being present in the storm above 5 km. There is a large amount (20 % dB^{-1} to 25 % dB^{-1}) of Z_{DR} values between –0.1 dB and 0.6 dB present below 5 km, with 10 % dB^{-1} to 20 % dB^{-1} occurrence of –1.5 dB to 0.5 dB between 5 km and 10 km for the lightning storms. Positive Z_{DR} values up to roughly 3 dB occur below 5 km at 1 % dB^{-1}, with –3 dB also being reached for these heights. In the mixed–phase region, the Z_{DR} values become more negative, with up to 5 % dB^{-1} occurring for values between –3 dB and –2 dB, and 0 dB to 1.5 dB for positive Z_{DR} values in this region. The very large negative Z_{DR} values (< –2 dB) could be caused by noise associated with beam filling and side lobe errors. Also, as mentioned earlier, – 0.6 to 0 dB occur 15 % dB^{-1} to 20 % dB^{-1} between 5 km and 8 km. In addition, negative values between 0 dB and –1.4 dB occur up to 15 km for the lightning storms. On the other hand, the non–lightning storms have their Z_{DR} mode between –1 dB and 1 dB, which occur 15 % dB^{-1} to 25 % dB^{-1} of the time, but this is only seen below 4 km. In the mixed–phase region, the Z_{DR} values vary between –3 dB and approximately 1.5 dB at 1 % dB^{-1} to 5 % dB^{-1}, specifically between 5 km and 9 km, with values ranging between –0.8 dB and 0.7 dB

above this region. The % dB^{-1} gradients are tighter for the non–lightning storms, especially for negative Z_{DR} values occurring below 4 km.

At t–30 (Figure 6.8), the lightning storms again show a mostly positive mode below 5 km, and a mostly negative mode above this height, with values ranging between approximately –0.5 dB to 0 dB and 0.5 dB to 1.2 dB between 0 km and 5 km at 15 % dB^{-1} to 25 % dB^{-1} and –1 dB to –0.5 dB and 0 dB to 0.5 dB between 5 km and 10 km occurring at 15 % dB^{-1} to 20 % dB^{-1}. The negative mode of 10 % dB^{-1} to 20 % dB^{-1} above the melting level now occurs up to 11 km, indicating that there is more ice, graupel and possible hail present at this time in the lightning storms as compared to the previous time (Figure 6.7), as well as comparing to the non–lightning storms at both t–45 and t–30. However, up to 2.9 dB is reached between 0 km and 5 km, with values ranging between 1 dB and 2.5 dB for 1 % dB^{-1} between 5 km and 13.5 km. This indicates there is also a lot of larger rain drops and/or melting hail or graupel present below 5 km, and many smaller drops, ice, graupel and hail above 5 km (as mentioned earlier for the negative values). There is also a protrusion that occurs between 8.5 km and 10.5 km, with Z_{DR} values of 1 dB to 2 dB occurring at 1 % dB^{-1}. This feature was also present at t–45, although not as obvious. This might indicate the presence of supercooled rain drops. In addition, a "plateau" is reached at 13 km, with Z_{DR} values ranging between –2 dB and 1.2 dB at 1 % dB^{-1}, which is not evident for the non–lightning storms. This feature might indicate that there are a lot of small ice present at this height.

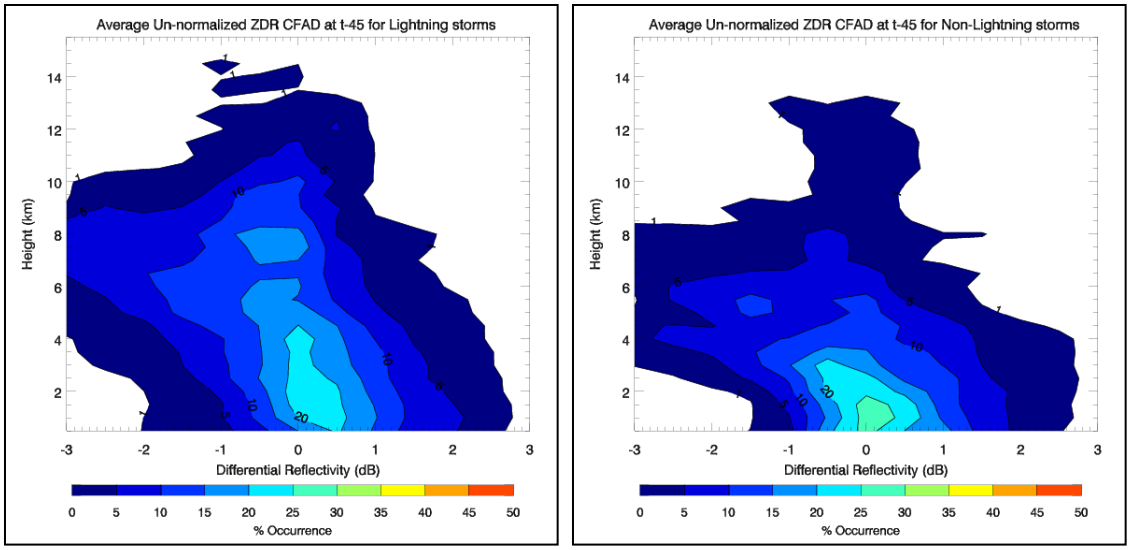

Figure 6.7: Average un–normalized Z_{DR} (called ZDR in plot) CFADs for lightning (left) and non–lightning (right) at t–45.

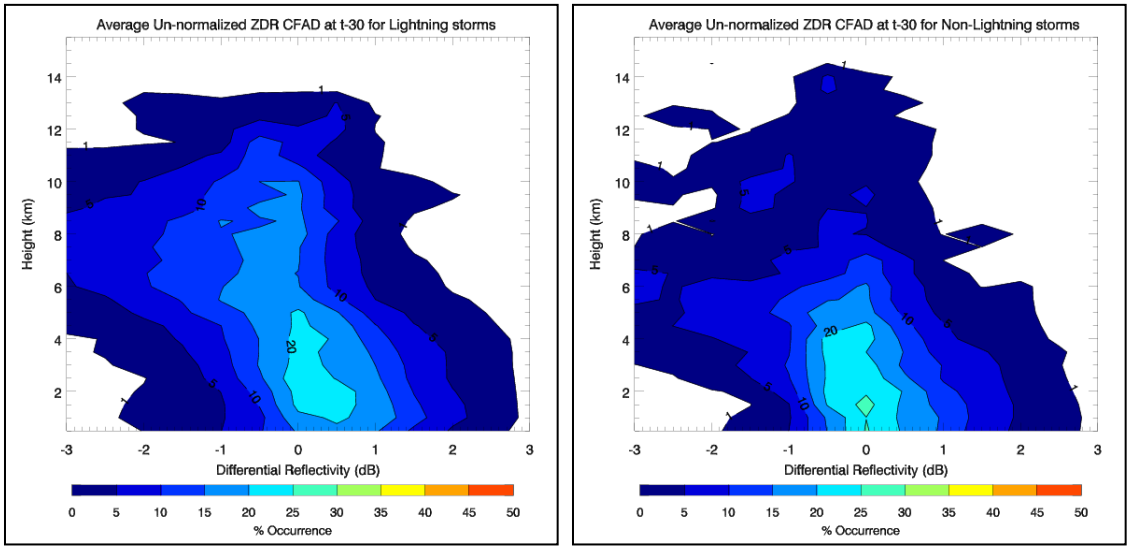

Figure 6.8: Average un–normalized Z_{DR} (called ZDR in plot) CFADs for lightning (left) and non–lightning (right) at t–30.

The non–lightning storms do not show the positive (negative) region below and above the 5 km height, but rather have values ranging from –0.7 dB to 0.9 dB between 0 km and 6 km for up to 25 % dB^{-1}. Although values up to –3 dB is reached in the mixed–phase region; positive values only reach roughly between 1 dB and 2.5 dB for the non–lightning storm, this is only for 1 % dB^{-1} (which is not the same as the positive

(negative) mode values below (above) the melting layer for the lightning storms, which was seen for the Z_{DR} mode with values between 15 % dB^{-1} and 25 % dB^{-1}). Furthermore, although there is also a possible protrusion of Z_{DR} values between 1.3 dB and 2 dB located from 7 km to 8 km at 1 % dB^{-1}, this protrusion is located at temperatures ranging between –10 °C and –20 °C, which is much warmer and less pronounced as for the lightning storms. The gradient of the negative Z_{DR} values below 5 km is tighter than for the lightning storms, as was observed at t–45. Furthermore, as was the case with the lightning storms, the non–lightning storms also have high Z_{DR} values up to 2.8 dB occurring below 5 km at 1 % dB^{-1}, which indicates the presence of large drops and possible melting hail and/or graupel at these heights.

At t–15 (Figure 6.9), which is 15 minutes before the first CG lightning strokes occurred for the lightning producing storms, one can once again see the positive (negative) mode division below (above) the 5 km height for the lightning storms, but not for the non–lightning storms. In fact, this division is becoming more pronounced for the lightning storms as one approaches time t. Up to 25 % dB^{-1} occurs for Z_{DR} values between 0 dB and 1 dB below 5 km and up to 20 % dB^{-1} to 25 % dB^{-1} occurs for values between –1 dB and 0.2 dB above 5 km (up to 12 km). This mode of mostly negative Z_{DR} values between 5 km and 12 km is indicative of ice, graupel and hail, as well as small drops within the mixed–phase region, with the mostly positive values below 5 km indicating larger rain drops or melting ice crystals, graupel and hail. There are also Z_{DR} values of up to 3 dB that is present at ≥ 1 % dB^{-1} that occurs from 0 km to 6.5 km, also indicating larger raindrops or other melting precipitation types. Therefore the height of the presence of these large Z_{DR} values are increasing as one nears the time of first flash.

Although the protrusion of higher Z_{DR} values in the mixed–phase layer that was seen in Figure 6.8 is now smaller in terms of its actual protrusion size, it extends over more heights, with values ranging between 1.3 dB and 2 dB, located between 7.5 km and 11 km, which correspond to approximately –15 °C to –40 °C. Thus, as the actual protrusion lowers as t–time is approached, the whole region of increased Z_{DR} broadens. Also visible here is the increase of negative Z_{DR} values at higher elevations, with –3 dB being reached up to 15 km for at least ≥ 1 % dB^{-1} of the time. However, these large negative Z_{DR} values could be due to noise associated with radar beam filling and side lobe errors. Furthermore, the plateau that started developing at t–30 (Figure 6.8) is now more pronounced, with Z_{DR} values ranging from –3 dB to 1 dB occurring at 1 % dB^{-1}. This, again, might be indicative of large amounts of ice of varying sizes being present at the cloud–tops due to all particles being frozen at temperatures colder than –40 °C. The non–lightning storms' mode finally reaches into the mixed–phase layer, with values ranging between –0.5 dB and 1.2 dB being reached from 0 km to 7 km at ≥ 15 % dB^{-1}. Although there is a slight division in positive (negative) Z_{DR} mode values below (above) the melting layer, this is only comparable to the lightning producing storm division that occurred at t–45, 30–minutes earlier and is thus not as obvious as for the lightning storms at t–15.

The non–lightning storms also have high Z_{DR} values reaching 2.9 dB below 5 km (at 1 % dB^{-1}), but have much less negative values above 5 km, which, if present are important for the indication of ice, graupel and hail at these levels. Also, although the negative Z_{DR} gradient below 5 km is still tighter for the non–lightning storms as compared to the lightning storms, the gradient is becoming weaker, if one compares t–15

to the previous two times for the non–lightning storms. At the top of the non–lightning storm clouds, there are Z_{DR} values ranging from –2.4 dB to 0.7 dB at 1 % dB^{-1}, but this only occurs at a height around 12 km, which does indicate some ice, but not nearly as much as for the lightning storms. There also seems to be some sort of protrusion developing at roughly 7 km, with values up to 2 dB being reached, but this is only comparable to t–45 (Figure 6.7) of the lightning storms, although the non–lightning storms' protrusion here is located at a lower elevation.

Figure 6.10, shows the average un–normalized Z_{DR} CFADs for lightning (left) and non–lightning (right) at time t, where the first CG lightning strokes occurred for the lightning storms within the next 15 minute interval. Comparing these two plots, one can see that there are vast differences between the lightning and non–lightning storms. Here the positive(negative) Z_{DR} mode below(above) the melting level is even more pronounced, with 15 % dB^{-1} to 25 % dB^{-1} occurring between roughly –0.5 dB to 1.2 dB below 5 km and between –1.2 dB to 0.2 dB from 5 km up to 14 km. Therefore, the negative Z_{DR} values now occur up to temperatures colder than –40 °C, which indicate the presence of ice, graupel and hail at temperatures colder than 0 °C. In addition, positive Z_{DR} values also occur above the melting layer, with values ranging from 0 dB to 2.5 dB at 20 % dB^{-1} to 1 % dB^{-1} respectively. The positive values above 0.5 dB and higher indicate larger rain drops in the mixed–phase region.

There is once again a protrusion visible, however, at this time, this feature is located between 11 km and 12 km, with values ranging from 1.4 dB to 1.9 dB, yet, Z_{DR} values of up to 1.4 dB at 1 % dB^{-1} is reached between 7 km and 11 km, which corresponds to approximately –15 °C to –40 °C. At the top of the clouds, the Z_{DR} values

range from –3 dB to 1 dB at 1 % dB^{-1} to 5 % dB^{-1}, which again may indicate large amounts of small ice and frozen drops at the top of the cloud. Interestingly, the gradient of the positive Z_{DR} values between 5 km and 11 km is becoming stronger, but this is not necessarily the case for the negative Z_{DR} values or for values below the 5 km level.

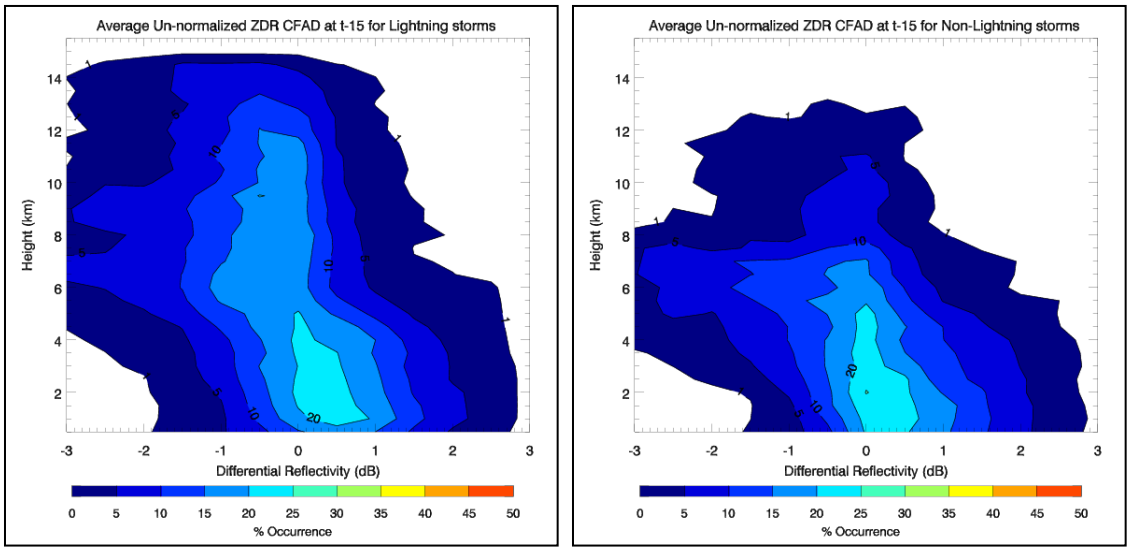

Figure 6.9: Average un–normalized Z_{DR} (called ZDR in plot) CFADs for lightning (left) and non–lightning (right) at t–15.

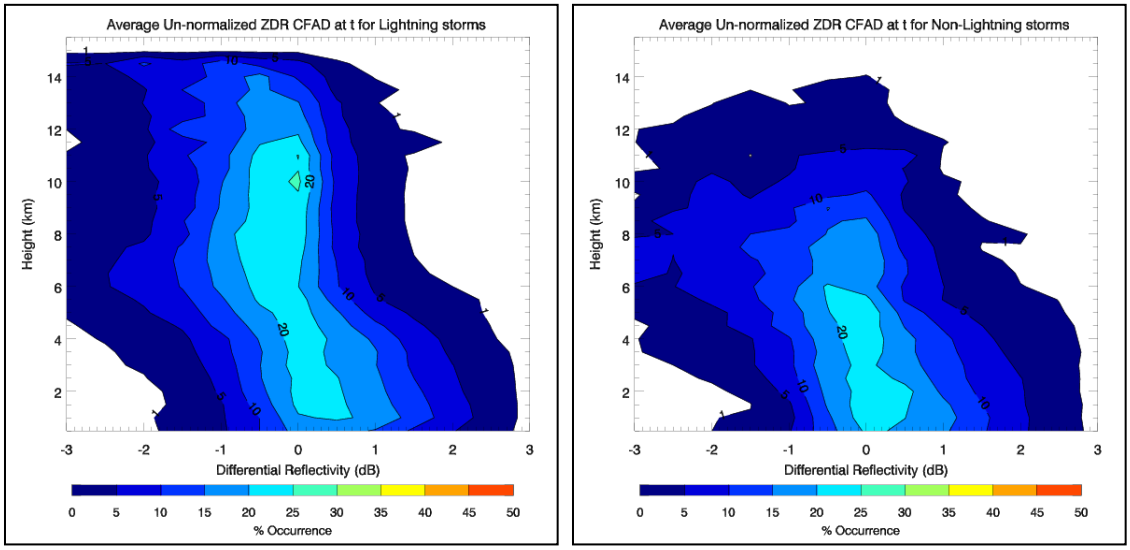

Figure 6.10: Average un–normalized Z_{DR} (called ZDR in plot) CFADs for lightning (left) and non–lightning (right) at time t.

The non–lightning storms in Figure 6.10 show little change from t–15 (Figure 6.9), with the mode of Z_{DR} still being comparable to t–15 for the non–lightning storms and approximately t–45 (Figure 6.7) for the lightning storms. Although the height of the Z_{DR} mode has increased to a maximum of 8 km at ≥ 15 % dBZ^{-1}, this height is much lower than for the lightning storms at time t. However, one can finally start to distinguish the positive (negative) division in the mode below (above) the 5 km level, even if this is just barely visible. Below 5 km, the Z_{DR} values vary between –0.7 dB up to 1 dB at ≥ 15 % dB^{-1}, and above 5 km this is –0.8 dB to 0.5 dB at ≥ 15 % dB^{-1}. Negative Z_{DR} values of to –3 dB occur in the mixed–phase layer (between 5 km and 11 km) at 1 % dB^{-1} to 5 % dB^{-1}, with –3 dB to approximately 0.3 dB being reached at 1 % dB^{-1} at around 13 km, which can be seen as the approximate top of the cloud. Therefore, there are more small ice and small frozen drops present at this time for the non–lightning storms as compared to t–15, however, this is still much less than for the lightning storms at time t. In addition, the large negative Z_{DR} values (Z_{DR} < –2.0 dB) could be due to noise associated with radar beam filling and side lobe errors. In addition, Z_{DR} values to 2.8 dB are present from 0 km to 5 km, which indicates that large drops and melting graupel and/or hail is also present, although this was also the case for lightning storms at t–15. There now also seems to be a protrusion of higher positive Z_{DR} values within the mixed–phase layer, located at roughly 8 km, with values ranging from 1.4 dB to 2 dB at 1 % dB^{-1}. The strong negative Z_{DR} gradient below 5 km that was visible at the previous time, is now weakening to the same approximate gradient strength as the lightning storms. These features all indicate that the non–lightning storms are finally starting to look similar to the lighting storms that occurred at t–30.

Figure 6.11 is 15 minutes after the first lightning flashes occurred for the lightning storms (t+15, left) with the non–lightning storms seen on the right. The positive (negative) Z_{DR} mode below (above) the melting level is still present for the lightning storms, with –0.5 dB to 1.2 dB at ≥ 15 % dB^{-1} below 5 km and –1 dB to 0.4 dB at 15 % dB^{-1} to ≥ 25 % dB^{-1} above 5 km up to 13 km being seen. The gradient of the positive Z_{DR} values are becoming stronger throughout the storms, with 2.2 dB to 2.8 dB being reached below 5 km at 1 % dB^{-1}, indicating that the larger drops below 5 km are now decreasing in numbers as well as size. Also, the amount of negative Z_{DR} values reaching –3 dB above 5 km is decreasing, however these Z_{DR} values still reaches a height of 15 km. The protrusion of positive Z_{DR} values in the mixed–phase region is no longer visible, however, positive values of up to 1.4 dB are reached between 6 km and 15 km at 1 % dB^{-1} and are completely vertical in appearance. The non–lightning storms do not have this vertical appearance.

The non–lightning storms in Figure 6.11 now slightly compare to the lightning storms in Figure 6.9 (t–15), 30 minutes before t+15. The non–lightning storm is showing the positive (negative) Z_{DR} mode below and above the melting layer again, but here it is stronger and more comparable to t–30 (Figure 6.8) for the lightning storms. This is seen with the Z_{DR} values ranging from roughly –0.7 dB to 1 dB at ≥ 15 % dB^{-1} below 5 km and –1 dB to 0.3 dB at ≥ 15 % dB^{-1} above 5 km, although the negative values above 5 km only reaches up to 10.5 km, which was already reached at t–30 for the lightning storms. The positive Z_{DR} values reach up to 2.8 dB below 5 km at 1 % dB^{-1}. Also, the protrusion that was visible at time t (Figure 6.10) is no longer visible, however, Z_{DR} values up to 2.5 dB is reached at 1 % dB^{-1} between 5 km and 7 km, and values between 1 dB and

1.5 dB at 1 % dB^{-1} is observed between 7 km and 13 km. At the top of the cloud, located at 14.5 km, the Z_{DR} values range from –2 dB to 0.4 dB at 1 % dB^{-1}, which again indicates the presence of ice crystals.

At t+30 (Figure 6.12), the lightning storms still show the positive (negative) Z_{DR} mode below (above) the melting level, with Z_{DR} values ranging from roughly –0.7 dB to 0.8 dB at ≥ 15 % dB^{-1} below 5 km and –1.2 dB to 0.3 dB at ≥ 15 % dB^{-1} between 5 km and 13.5 km. Positive Z_{DR} values of up to roughly 2.6 dB is reached below 5 km, with this value decreasing to 1.5 dB between 5 km and 11 km at 1 % dB^{-1}. Negative Z_{DR} values between 5 km and 12 km reaches –3 dB at 1 % dB^{-1}. The Z_{DR} plateau at the top of the cloud (roughly 15 km) now varies between –2.5 dB and 1 dB at 1 % dB^{-1}, which is decreased from t+15. The non–lightning storms seem to be decreasing in height, with the maximum height reached only being 13.5 km at this time. In addition, the positive (negative) Z_{DR} mode below (above) the melting level, although still visible here, is less pronounced than at t+15, with Z_{DR} values roughly reaching –0.5 dB to 0.7 dB below 5 km at 1 % dB^{-1} and –1 dB to 0.4 dB being reached between 5 km and 9.5 km at 1 % dB^{-1}. This negative Z_{DR} mode above the melting layer is reaching a lower altitude as compared to t+15 (Figure 6.11). In addition, the amount of larger rain drops occurring below the melting level is also decreased, with Z_{DR} values of only about 2.6 dB being reached at 1 % dB^{-1}. However, between 5 km and 11 km, the positive Z_{DR} values reach up to 1.4 dB at 1 % dB^{-1}, with a protrusion of 1.8 dB at 1 % dB^{-1} being reached between 11 km and 12 km.

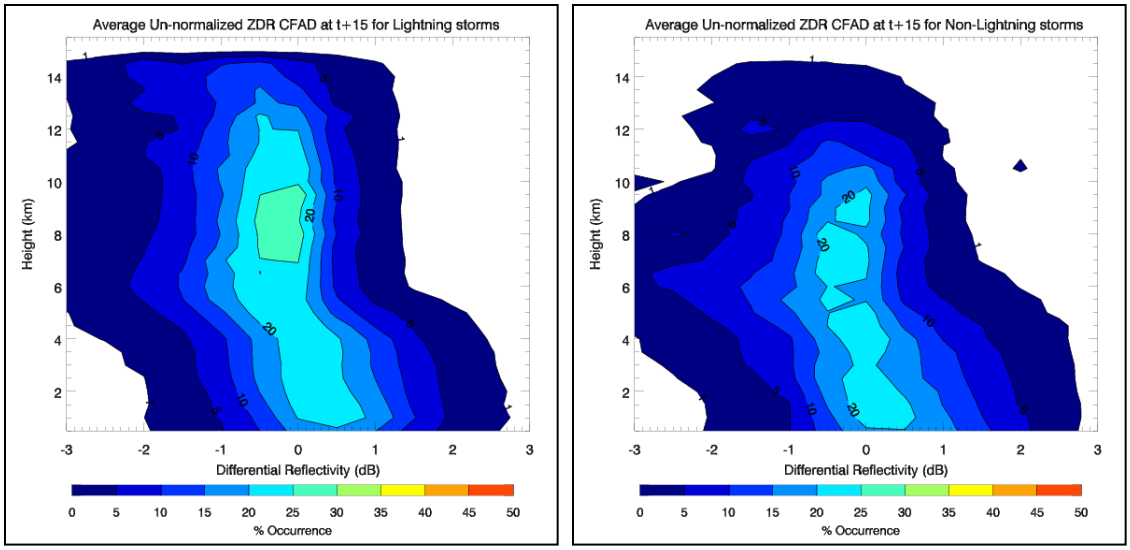

Figure 6.11: Average un–normalized Z_{DR} (called ZDR in plot) CFADs for lightning (left) and non–lightning (right) at t+15.

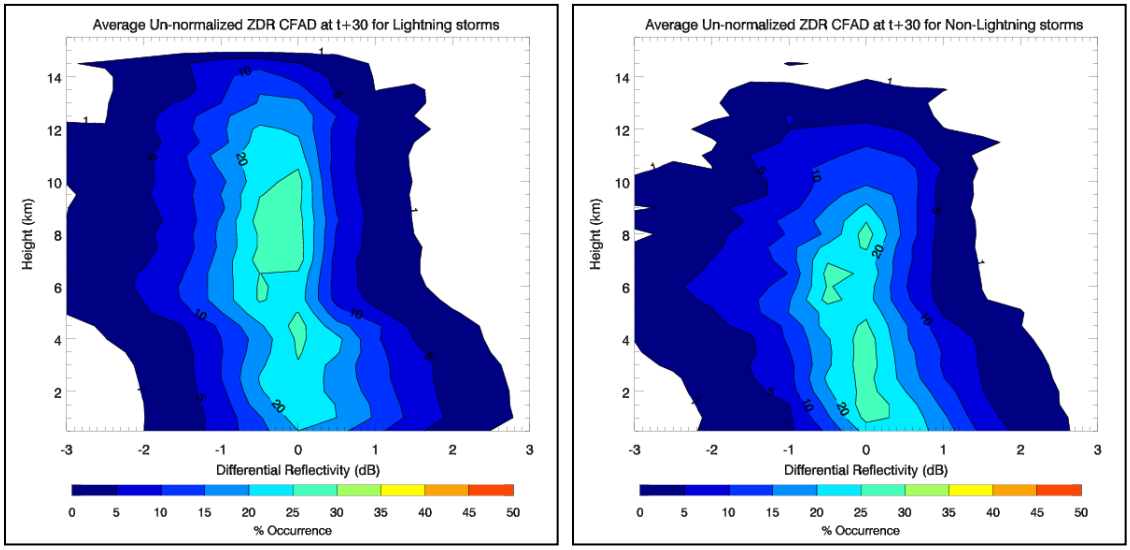

Figure 6.12: Average un–normalized Z_{DR} (also called ZDR in plot) CFADs for lightning (left) and non–lightning (right) at t+30.

From the above, one can see that there are major differences between the lightning and non–lightning storms in terms of the Z_{DR} obtained through CFAD analysis. Most importantly, the lightning storms have a pronounced positive (negative) Z_{DR} mode below (above) the 5 km level from t–30, whereas the non–lightning storms only show this feature from t+15, 45 minutes after the lightning storms. Also interesting, although

not mentioned earlier, is that the lightning storms seem to have a vertical appearance of Z_{DR} % dB^{-1} gradients from t–15 through t+30 (in fact, this vertical appearance becomes more and more apparent after t), with a tilted structure below the melting level at all times. This tilted structure is related to the melting of graupel and hail at temperatures warmer than 0 °C, leading to higher Z_H and Z_{DR} values being obtained due to changes in the dielectric constants of the hydrometeors (water has a higher dielectric constant than ice). The non–lightning storms, however, do not display this vertical structure above the melting level until t+15 (30 minutes after the first occurrence in the lightning storms), but one does observe the tilted structure below the melting level from t–15, although much weaker than was observed for the lightning storms. In addition, the lightning storms have more small ice at earlier times at the top of the clouds as compared to the non–lightning storms, which can be seen by the mostly negative Z_{DR} values at heights above 12 km. Finally, it is clear that the lightning producing storms have higher tops (up to 15 km) which is reached at t–15 through t+30 than the non–lightning storms, which only have cloud–tops reaching 14.5 km at t+15, 15 minutes after the lightning storms first started producing lightning.

For additional information on the differences between lightning and non–lightning producing storms, refer to Figures 6.13 through, 6.17 which shows the average un–normalized ρ_{HV} (also called RH in plot) CFADs for lightning (left) and non–lightning (right) from t–45 through t+30. It is very important to remember here that it was shown that the NPOL radar has a random error for ρ_{HV} of –0.04, which will lead to variations of precipitation values as compared to other radar ρ_{HV} values. This ρ_{HV} error is much more obvious than the previous two variables and is indicative of poor ρ_{HV} quality.

At t–45 (Figure 6.13), the modes of both the lightning and non–lightning storms are at 0.92, with the mode of the lightning storms reaching 9 km and the non–lightning storms only reaching 5.5 km at ≥ 15 %. ρ_{HV} values between 0.8 and 1 are reached for both storm types, however, it seems that for both, the lower ρ_{HV} values are reached below roughly 10 km and the higher ρ_{HV} values are reached above 10 km. The lower correlations (≤ 0.92) could indicate the presence of large, oblate water drops, with the higher correlations indicating graupel and/or hail, as well as smaller drops, especially between 5 km and 11 km, and above this height, the values ≥ 0.95 could indicate the presence of ice crystals, specifically for the lightning storms (however, ρ_{HV} plots is best used in combination with other dual–polarimetric radar variables, especially vertical cross sections of these variables).

At t–30 (Figure 6.14), the mode of the lightning and non–lightning storms are still situated over approximately 0.92, however, the lightning storms' mode of ≥ 15 % is now located up to 10.5 km, and includes values between 0.9 to 0.94, with the non–lightning storms' mode of ≥ 15 % only reaching 6 km. At the top of the lightning storm clouds, it seems that, as was the case with Z_{DR}, the ρ_{HV} values vary between 0.82 to 1 between 12 km and 14.5 km, whereas for the lightning storms, ρ_{HV} values of only 0.87 to 0.96 are reached for the same heights.

Figure 6.15, which shows the average un–normalized ρ_{HV} CFADs for lightning (left) and non–lightning (right) at t–15, illustrates that the maximum height of the modes reached for these two storm types vary a lot, with the lightning storm mode of ≥ 15 %, now reaching up to 13 km, and the non–lightning storm mode of ≥ 15 % only reaching 7 km, which is almost half that of the lightning storms. The lightning storms do however

seem to develop a secondary mode between 6 km and 10 km (approximately –10 °C to –35 °C), which is not seen in the non–lightning storms. However, both storm types now have ρ_{HV} values ranging from 0.82 to 1 at the top of the clouds, where this is located at approximately 14.5 km (1 %) for the lightning storms and 12 km (1 %) for the non–lightning storms. n addition, there is a small area of higher ρ_{HV} values (0.95 to 0.965) located between 7 km and 10 km (–15 °C to –35 °C), with this feature not being that visible in the non–lightning storms.

At time t (Figure 6.16), the mode of ≥ 15 % is still located at 0.92 for both the lightning and non–lightning storms, however, the lightning storms' mode is now visibly divided in two, with the lower mode being located below 6 km and the higher mode being located between 6 km and 14 km. In addition, there now seems to be a small area of ρ_{HV} values between 0.98 and 1 located at 3 km to 4.5 km, which is around the melting level. Finally, at the top of the lightning storm clouds (15 km), the ρ_{HV} values now vary between 0.8 and 1, indicating a large variety of precipitation particles (in terms of size, orientation and shape) at this height, although all particles here will be frozen.

The non–lightning storms' mode of ≥ 15 % now reaches 9 km, which is much lower than the lightning storms' mode, however the ρ_{HV} values are the same as for the lightning storms, with 0.9 to 0.935 being reached. However, for the non–lightning storms, the cloud–top ρ_{HV} values only vary between 0.9 and 0.935, which is the same as the mode of these storms. Furthermore, although all values between 0.8 and 1 are reached for the non–lightning storms, these seem to occur between 11 km and 14.5 km, which is a larger variation in height than the lightning storms. The non–lightning storms

also do not exhibit the same high ρ_{HV} values (≥ 0.98) between 3 km to 5.5 km, which were observed for the lightning storms.

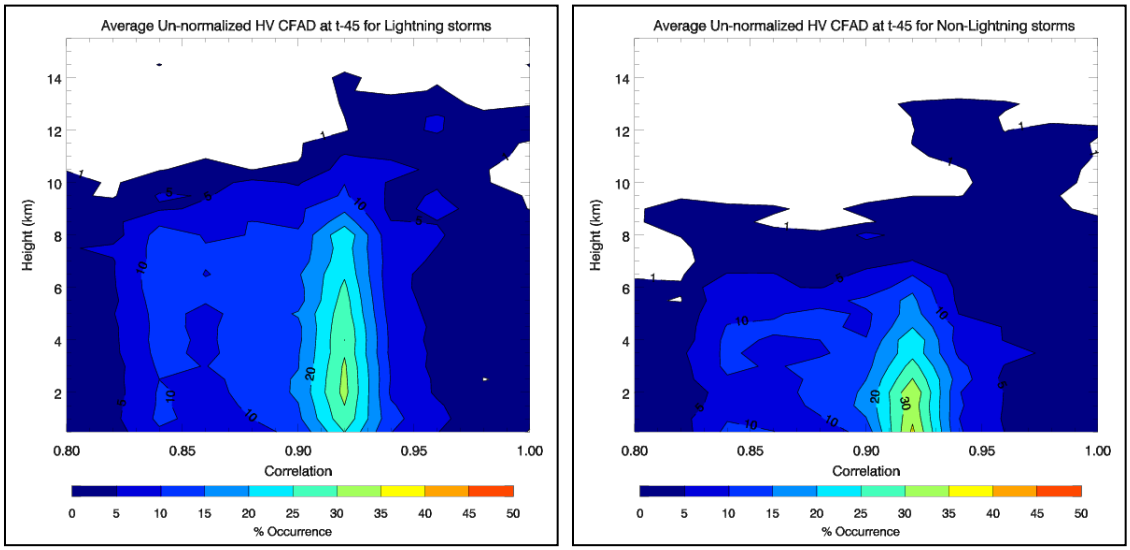

Figure 6.13: Average un–normalized ρ_{HV} (called HV in plot) CFADs for lightning (left) and non–lightning (right) at t–45.

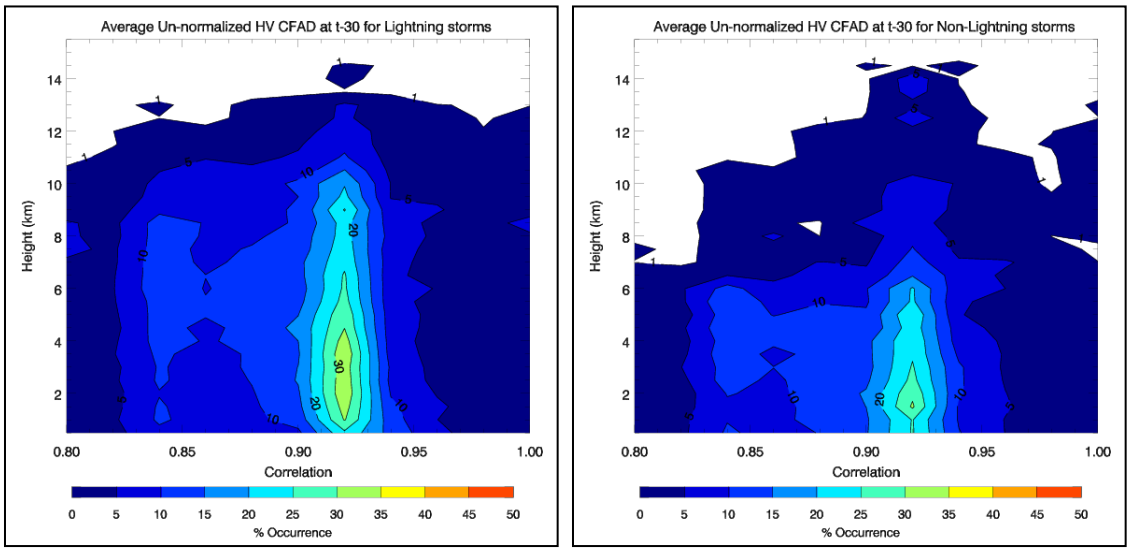

Figure 6.14: Average un–normalized ρ_{HV} (called HV in plot) CFADs for lightning (left) and non–lightning (right) at t–30.

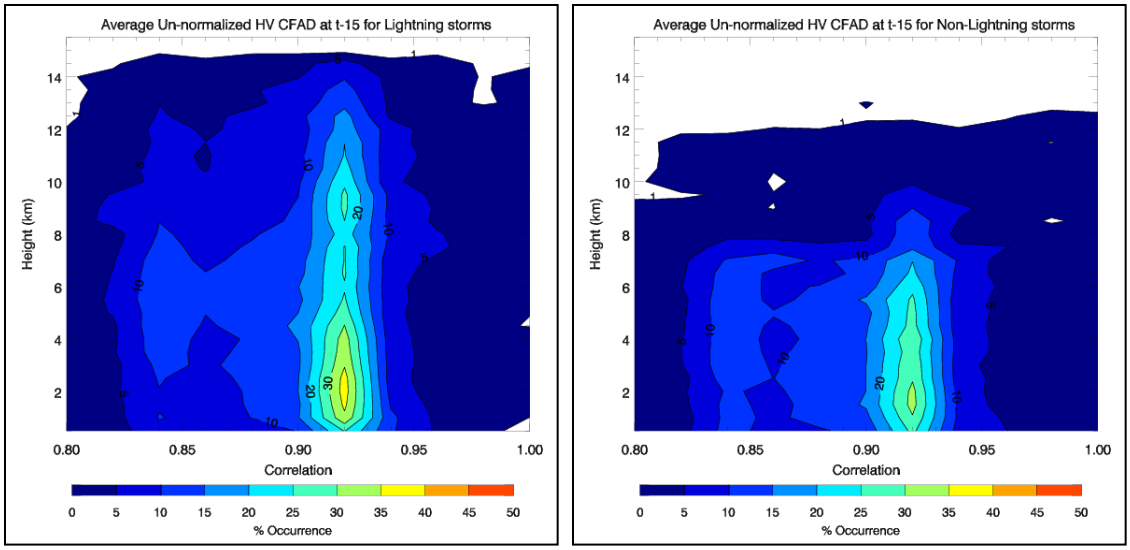

Figure 6.15: Average un–normalized ρ_{HV} (called HV in plot) CFADs for lightning (left) and non–lightning (right) at t–15.

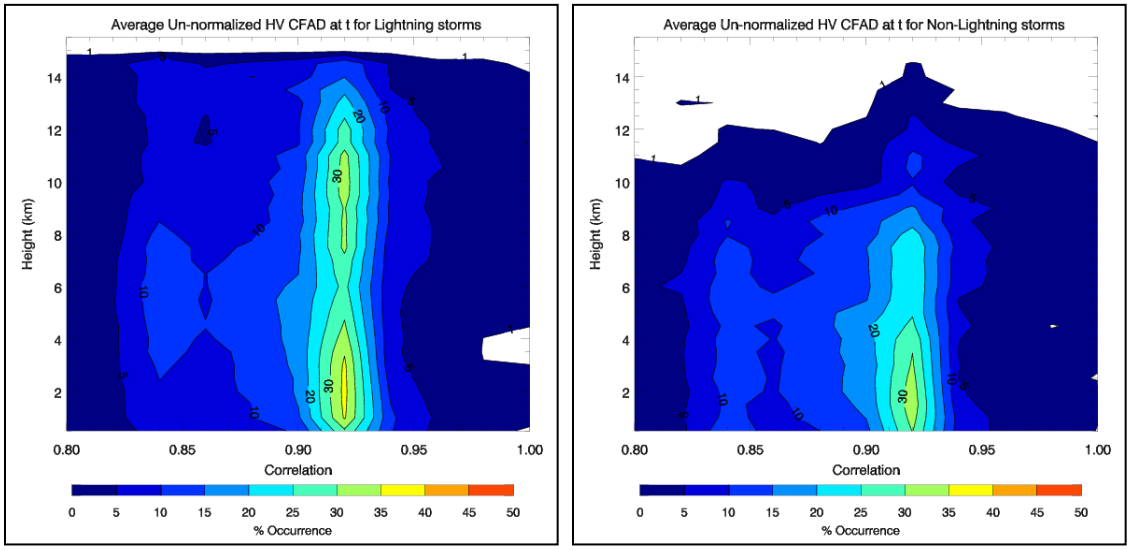

Figure 6.16: Average un–normalized ρ_{HV} (called HV in plot) CFADs for lightning (left) and non–lightning (right) at time t.

From Figure 6.17 (t+15) it is once again clear that the lightning storms' mode is located to higher altitudes than the non–lightning storms, with 14 km being reached for the lightning storms, and only 10.5 km being reached for the non–lightning storms at ≥ 15 %. The lightning storms again also show the division in the mode, with the lower mode being located below 5 km and the higher mode being located between 6. km and

13 km at ≥ 15 %. Also, this mode consists of ρ_{HV} values between 0.88 and 0.94. The area of decreased ρ_{HV} values is now smaller in aerial size and also located at a lower altitude, with only 7 km being reached (as compared to 8 km at time t). Finally, the small area of ρ_{HV} values between 0.98 and 1 is still visible, but is now located between 2 km to 5 km.

The non–lightning storms' mode finally reached higher elevations (10.5 km at ≥ 15 %), and is now comparable to the lightning storms at t–30, 45 minutes earlier. However, the lightning storms' mode reached ≥ 35 % at t–15, whereas the non–lightning storms' mode only barely reaches 35 % at t+15. The non–lightning storms also now seem to develop a division in the mode, with a lower and higher elevation being obtained, but again, this is comparable to the lightning storms at t–15 (30 minutes earlier).

At t+30 (Figure 6.18), the mode of the lightning storms is still located around 0.9 to 0.94, with the elevation reached being 13 km at ≥ 15 %. This mode is again divided into two parts, with a lower mode being located between 0 km and 5 km and the higher mode being found between 5 km and 13 km. ρ_{HV} values of 0.8 to 1 are again reached at the top of the lightning clouds, which occurs at approximately 15 km. The non–lightning storms' mode at t+30 is very comparable to the same storm mode at t+15, with the altitude reached only being 11 km at ≥ 15 %, with the ρ_{HV} values being between 0.89 and 0.935. The non–lightning storms' mode is also again divided into two parts, with a lower mode being located between 0 km and 6 km and the higher mode being found between 6 and 10 km, however, the lower mode reaches 0.89 to 0.935 at 45 %, which is comparable to the lightning storm modes at this time.

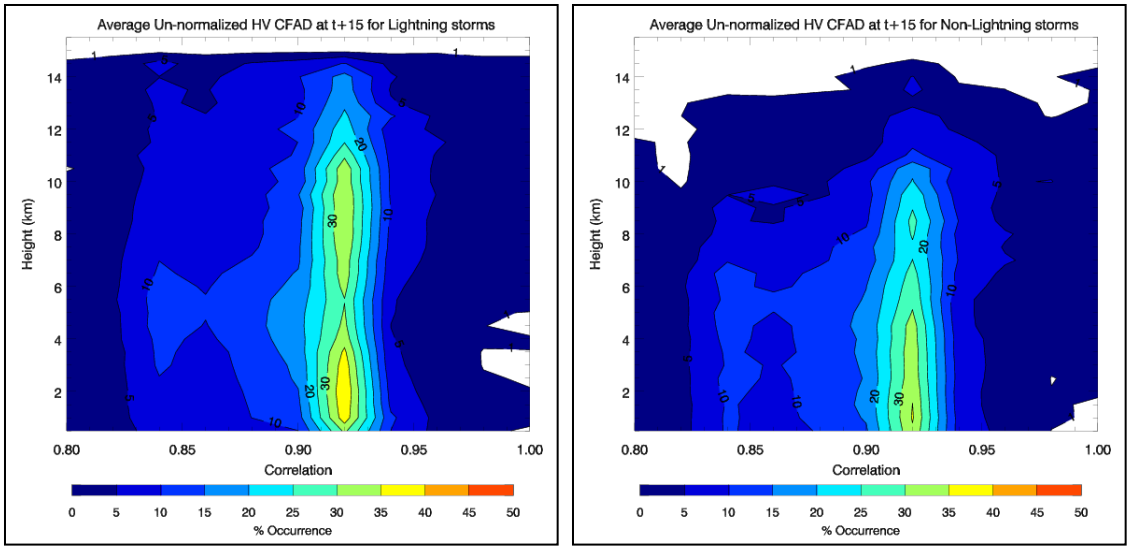

Figure 6.17: Average un–normalized ρ_{HV} (called HV in plot) CFADs for lightning (left) and non–lightning (right) at t+15.

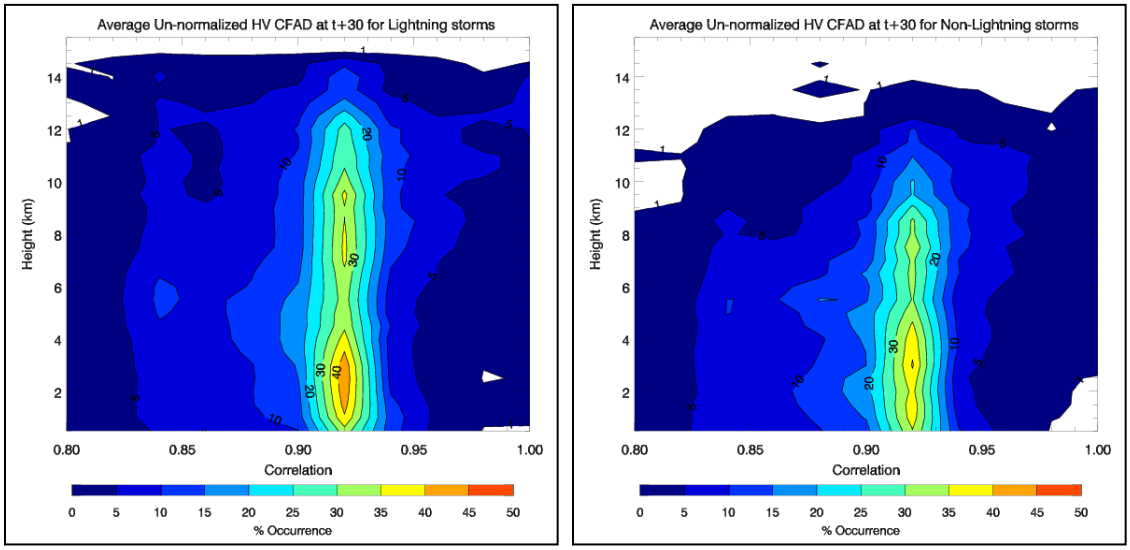

Figure 6.18: Average un–normalized ρ_{HV} (called HV in plot) CFADs for lightning (left) and non–lightning (right) at t+30.

From the above ρ_{HV} un–normalized CFAD plots, one can clearly see that the lightning storms have higher cloud–top heights than the non–lightning storms (as was also the case with the Z_H and Z_{DR} variables), with the mode of ≥ 15 % for values between 0.9 and 0.94 also reaching higher elevations for the lightning storms, as compared to the non–lightning storms. Also seen earlier, is the fact that the non–lightning storms only

seem to reach the same appearance in terms of mode height at t+15, which is comparable to the lightning storms at t–30, 45 minutes earlier. These and other differences between the lightning and non–lightning storms' un–normalized CFADs will be discussed in more detail in the following chapters.

6.2. Rain and Ice Masses:

Figure 6.19 is the graphical representation of Table 6.1 (this table is imperative due to the small amount of water and ice produced by the non–lightning storms), which shows the average total water and ice mass in kg obtained for the lightning and non–lightning storms from t–45 to t+30 for the mixed–phase region (0 °C to –40 °C). The solid red line and dashed red line indicates the water and ice mass for lightning storms, respectively. The solid blue line and dashed blue line indicates the water and ice mass for non–lightning storms, respectively. These masses are calculated only for the mixed–phase region because this region is the most important for charging, and hence lightning production, due to the presence of supercooled liquid water in this temperature range. These rain and ice masses were obtained from the rain and ice fractions, which themselves were obtained from the rain line calculations and scatter from this line, as explained in chapter 3. Due to the constraints used to calculate these variables (such as $Z_H \geq 35$ dBZ and $Z_H > Z_V$), and the fact that the masses were only calculated for 0 °C to –40 °C (5 km to 11 km), many of the non–lightning storms did not have any remaining Z_H values at these heights after the above constraints were applied, which lead to zero rain and ice masses existing for some of these storms, especially for the times during and before t–15. This will be seen more clearly in Figure 6.19.

Table 6.1: Average total water and ice mass in kg obtained for the lightning (left) and non–lightning (right) storms from t–45 to t+30 for the mixed–phase region.

LIGHTNING STORMS		
	AVERAGE TOTAL WATER (KG)	**AVERAGE TOTAL ICE (KG)**
t–45	2.93E+07	2.01E+07
t–30	6.79E+07	5.95E+07
t–15	3.06E+08	8.64E+08
t	4.28E+08	1.08E+09
t+15	6.99E+08	1.21E+09
t+30	4.76E+08	1.87E+09

NON–LIGHTNING STORMS		
	AVERAGE TOTAL WATER (KG)	**AVERAGE TOTAL ICE (KG)**
t–45	8.80E+06	3.63E+07
t–30	2.60E+06	2.11E+07
t–15	1.29E+06	2.43E+07
t	1.05E+08	8.18E+07
t+15	7.38E+07	7.15E+07
t+30	7.11E+07	3.81E+07

From Table 6.1 and Figure 6.19 one can see that the lightning storms produced much more water and ice from t–45 through t+30 than the non–lightning storms. From t–45 to t–30, the lightning storms had more water than ice in the mixed–phase region, with the non–lightning storms actually having more ice than water. In addition, the non–lightning storms' mixed–phase region contained more ice than the lightning storms' mixed–phase region at t–45, but this quickly changes between t–45 and t–30, where the lightning storms now have almost three times more ice and 26 times more water in the mixed–phase region than the non–lightning storms. Further, the lightning storms again have more water than ice in the mixed–phase region at t–30, but this changes in the next 15 minutes (up to t–15), with the ice mass increasing rapidly to 2.88 times more than the mass of water in the lightning storms, and 35.6 times more than the non–lightning storms at t–15.

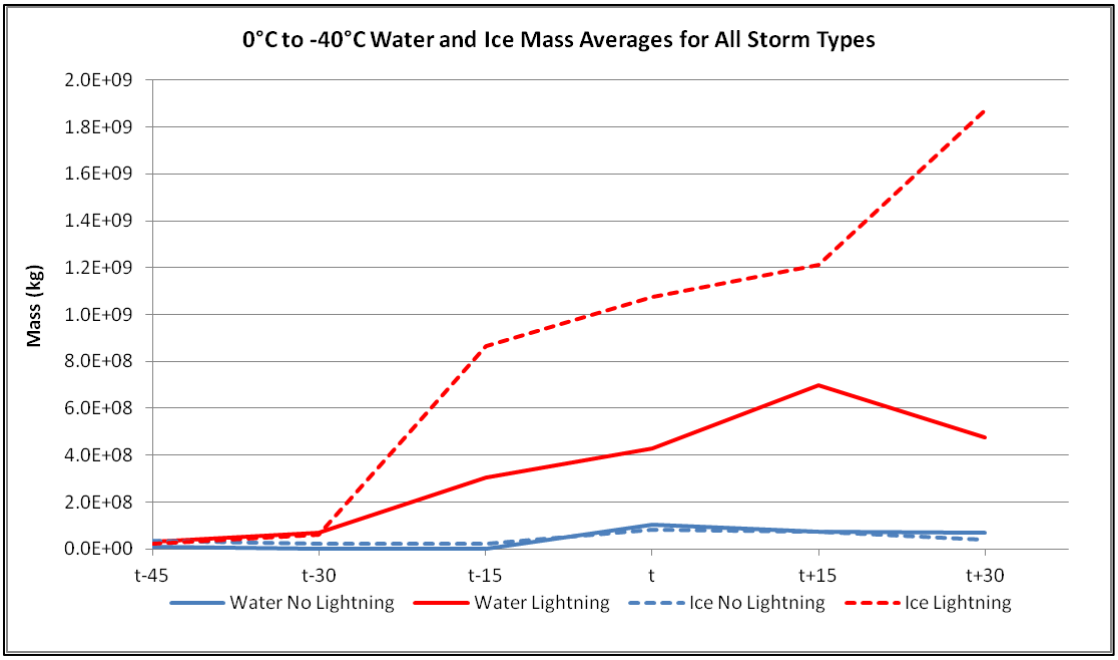

Figure 6.19: Graphical representation of the average total water and ice mass in kg obtained for the lightning and non–lightning storms from t–45 to t+30 for the mixed–phase region. The solid red line and dashed red line indicates the water and ice mass for lightning storms, respectively. The solid blue line and dashed blue line indicates the water and ice mass for non–lightning storms, respectively.

For the remainder of the time (t–15 through t+30), the lightning storms have more ice than water, and much more ice than the non–lightning storms; the non–lightning storms have more water than ice from time t to t+30. At t–15, although the ice and water masses are still increasing for the lightning storms, the increase seems to be less rapid than from t–30 to t–15; however, the ice mass is still 2.8 times more than the water mass for the lightning storms and 36 times more than the non–lightning ice mass at t–15. The first lightning flashes started occurring at time t, indicating that one needs much more ice than water in the mixed–phase region to produce lightning; however, one also needs an abundance of water, especially supercooled rain drops, for lightning to occur. It is thus clear from the table and figure that the non–lightning storms did not contain nearly enough ice or water in the mixed–phase region for charging to occur at significant levels

in order to initiate lightning. Between time t and t+15, there is yet another increase in ice mass for the lightning storms; however, this increase is less than for the previous time frame. Interestingly, although not seen here, the water mass increases more rapidly between time t and t+15 than the ice mass for the lightning storms, and then after t+15 the ice mass increases sharply again, with the amount of water now starting to decrease in the lightning storms. The non–lightning storms show a decrease in both ice and water production from time t onwards.

As is clear from the previous discussion, the lightning producing storms have much more ice and water in the mixed–phase region of the clouds than the non–lightning storms, with an increase in ice and water masses occurring 30 minutes before any CG lightning flashes for the lightning storms. In fact, the ice mass is approximately 2.5 times greater than the water mass for the lightning storms between t–15 to t+15, which is important for charging to occur. This indicates that there are a lot of ice, supercooled water and graupel/hail present in the lightning storms in the mixed–phase region, which is clearly not seen in the non–lightning storms. In addition, very little water and ice was present in the non–lightning storms, with more water than ice being present at time t for these storms.

6.3. MSG Satellite Interest Fields:

The results obtained from the 10 interest fields, as seen in Tables 2.2 and 3.1, will be shown and discussed according to the storms' cloud depth, updraft strength and cloud–top glaciation characteristics. Although not part of the interest fields, the 10.8 μm

T_B trend will also be shown (Figure 6.20), as the coldest pixel from this field is indicative of the strength of the main updraft region.

All MSG interest field plots (Figures 6.20 through 6.30) are shown in a so–called "box and whisker" format. In these figures, the red squares show the maximum value (99^{th} percentile) obtained, the blue squares show the minimum value (1^{st} percentile) obtained, with the see–through rectangle indicating the inner–quartile region (IQR), with the bottom line of this rectangle indicating the 25^{th} percentile of the data and the top line of this rectangle indicating the 75^{th} percentile of the data. The green triangle and connecting lines indicate the median (50^{th} percentile) range of the data (Wilks, 2006). Note that some of the minimum and maximum values were cut off from the plots, as these were outliers, which caused the data to be smoothed to the point where one could not see the differences between the fields. Also note that for these plots, the time period extends from t–75 (and not t–45, as was the case for the radar variables) through t+30. This was done in order to see if the satellite fields could provide additional information before the radar fields. As for the CFADs above, whenever specific MSG field values are mentioned, these will be for the median values obtained for the storms.

The 10.8 μm T_B field is shown in Figure 6.20, with the lightning storms on the left and the non–lightning storms on the right. From these plots it is clear that the main updraft of the lightning storms is much stronger than for the non–lightning storms; the median T_B reached at time t is 223.68 K and 261.21 K for the lightning and non–lightning storms respectively. This is a 37.53 K difference. In addition, between t–75 and t–30, although the lightning storms' T_B values do not decrease by that much, there is still a 10.06 K difference, whereas for the non–lightning storms this decrease is 12.52 K;

however, the T_B at t–30 for the non–lightning storms average 275.75 K, where the lightning storms' T_B at this time is 262.06 K, 13.69 K less. After t–30, the updraft strength of the lightning storms increases tremendously, with a decrease in T_B values of 38.38 K between t–30 and t, while the non–lightning storms only have a decrease of 6.54 K during this time. Note that a 38.38 K decrease over 30 minutes equates to a 3.23 ms^{-1} updraft (following Adler & Fenn, 1981). This value appears low, but it represents an average over a 3 x 3 km pixel. When speaking of updraft strength (related to the 10.8 µm T_B trend field), reference is made to "strong" or "weak" updrafts, and this needs to be qualified given this simple estimation here.

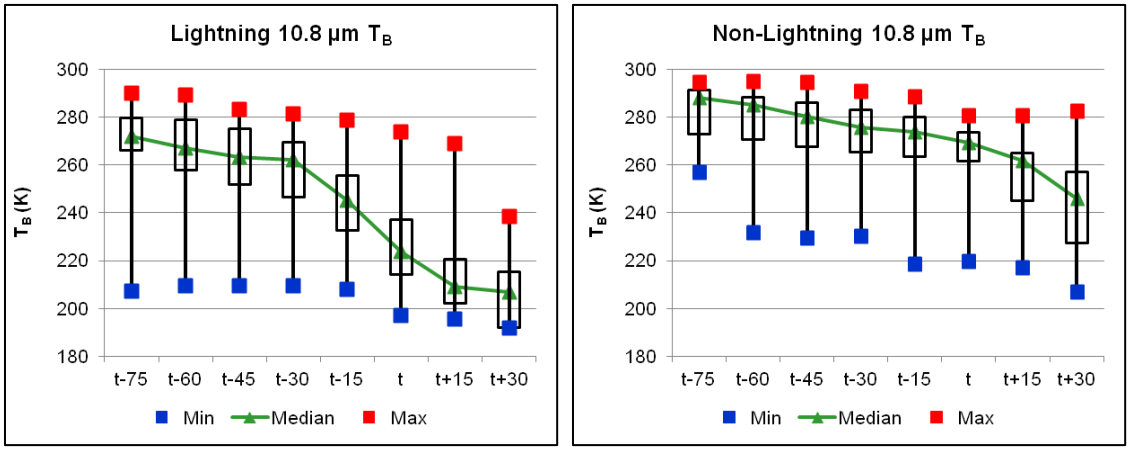

Figure 6.20: Box plots of the 10.8 µm T_B field showing the main updraft strength features between lightning (left) and non–lightning (right) storms from t–75 to t+30. The red squares show the maximum value (99th percentile) obtained, the blue squares show the minimum value (1st percentile) obtained, with the see–through rectangle indicating the inner–quartile region (IQR), with the bottom line of this rectangle indicating the 25th percentile of the data and the top line of this rectangle indicating the 75th percentile of the data. The green triangle and connecting lines indicate the median (50th percentile) range of the data.

By time t, the non–lightning storms did not possess a strong enough updraft to loft larger water and ice particles into the mixed–phase layer, which is vital for electrification

to occur in clouds (due to charging occurring from the rebounding of ice–graupel particles in the presence of supercooled liquid water). On the other hand, the lightning storms had approximately 30 minutes of strong updrafts that lead to these larger water and ice particles being lofted to the mixed–phase, which lead to electrification of these storms to the point of initiating CG lightning. Cloud–top T_B's then relate to the CFAD–estimated storm tops and the soundings shown in Appendix A.

Figures 6.21 through 6.24 show the T_B difference fields used to obtain the updraft strength of the clouds (and is thus closely related to the 10.8 μm T_B field shown in Figure 6.20), which is also important for lightning occurrence. However, with Figures 6.21 and 6.22 a positive trend indicates the updraft strength is increasing and for Figures 6.23 and 6.24 a negative trend implies the updraft strength is increasing. The 15 minute 6.2 – 7.3 μm T_B time trend is seen in Figure 6.21, and one can easily see that the lightning storms show a positive trend between t–60 and t–15, where the non–lightning storms only show a positive trend after time t. Between t–60 and t–15 the lightning storms' 15 minute 6.2 – 7.3 μm T_B values increase from 0.44 K to 3.18 K, which is a 2.74 K increase, with a decrease between t–15 and time t of 0.89 K. Although this decrease in updraft strength is present before time t, the updraft strength is nevertheless strong enough for charge separation to occur in the lightning storms, especially due to the fact that at time t, the 15 minute 6.2 – 7.3 μm T_B time trend is 2.29 K (and therefore still positive).

For the non–lightning storm there is almost no increase before t+15, with values increasing and decreasing toward time t. At t–60, t–45, t–30, t–15 and time t the 15 minute 6.2 – 7.3 μm T_B time trend changes from 0.14 K, 0.25 K, 0.09 K, 0.59 K and 0.38

K respectively, indicating that the updraft strength varies during these times. This might be a reason why the non–lightning storms did not produce lightning, as there was no constant increase in updraft strength during these times. The most increase in updraft strength for the non–lightning storms occur after time t, with a 1.11 K and 1.64 K increase occurring between time t and t+15, and t+15 and t+30, respectively. This is a total increase of 2.75 K, which is approximately the same as for the lightning storms between t–60 and t–15, however it seems that one needs a sustained increase in updraft strength for there to be charge separation in the clouds.

The 30 minute 6.2 – 7.3 μm T_B time trend for the lightning and non–lightning storms are seen in Figure 6.22. There should also be a positive trend to indicate an increasing updraft strength. It is clear that there is a positive trend in the 30 minute 6.2 – 7.3 μm T_B field from t–45 to time t for the lightning storms, but the non–lightning storms only show a positive trend from t–15; in addition, this trend is much weaker than for the lightning storms. Between t–45 and time t, there is a constant positive trend for the lightning storms, with 1.21 K and 6.80 K being reached at t–45 and time t, respectively. This is a 5.59 K increase and positive trend for a total of 45 minutes. After time t there is a negative trend in the 30 minute 6.2 – 7.3 μm T_B field, with a decrease of 5.42 K. Therefore, it seems here that after the initiation of lighting during time t and t+15, the updraft strength started weakening. This could be due to the falling precipitation particles, which will lead to increased friction and thus a decreased updraft strength or it could be related to the varying lifecycle of the storms.

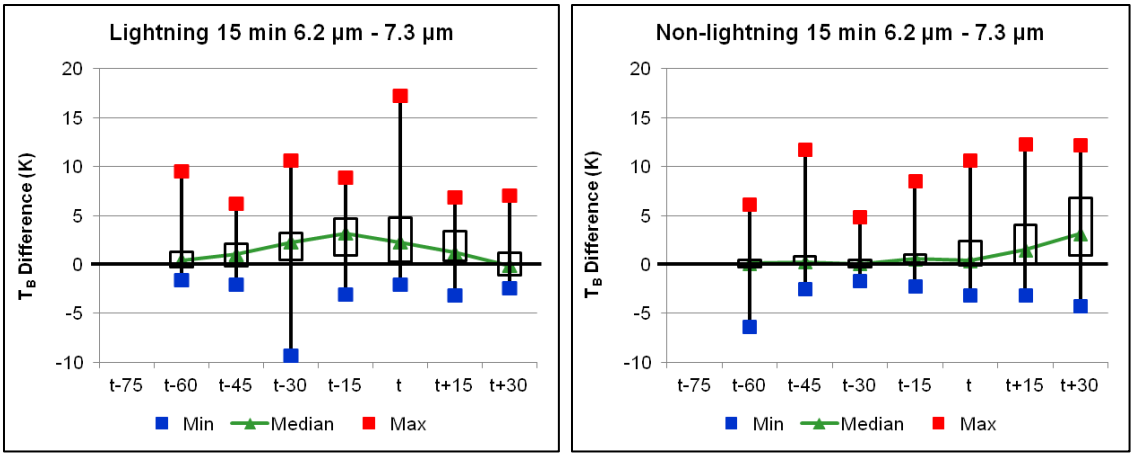

Figure 6.21: Box plots of 15 minute 6.2 – 7.3 µm T_B interest field showing updraft strength features between lightning (left) and non–lightning (right) storms from t–75 to t+30. The features in the plots are the same as in Figure 6.20.

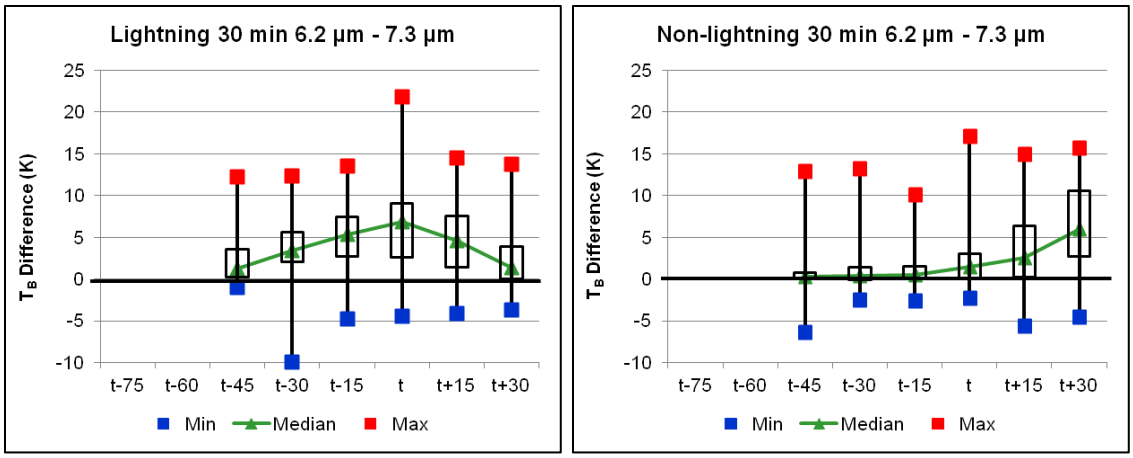

Figure 6.22: Box plots of 30 minute 6.2 – 7.3 µm T_B interest field showing updraft strength features between lightning (left) and non–lightning (right) storms from t–75 to t+30. The features in the plots are the same as in Figure 6.20.

The 30 minute 6.2 – 7.3 µm T_B trend for the non–lightning storms on the other hand, show almost no increase between t–45 and time t, with a decrease actually being observed between t–30 and t–15. Therefore the trend is positive between t–45 and t–30 and negative (with a 0.2 K decrease) between t–30 and t–15 for the non–lightning storms. Furthermore, there is a small positive trend between t–15 and time t, with a 1.1 K increase during this time, and then a 4.12 K increase between time t and t+30. Therefore,

although there is a positive trend between t–15 and t+30 for the non–lightning storms, this trend is small initially and only increases noticeably after time t, which might indicate that for charging to occur in the storms, one needs a sustained positive trend for at least 45 minutes with a constant increase (i.e. linear) being obtained (as seen for the lightning producing storms).

Figure 6.23 illustrates the 15 minute 10.8 μm T_B trend interest field, which is also indicative of the updraft strength and is often simply noted as "cloud–top cooling rates". Negative trends exhibit indicate increased updraft strength (which is opposite from the previous 2 figures). Again, there are clear differences between the lightning and non–lightning storms. The lightning storms display a negative trend from t–60 through time t, with a total decrease during this period being 11.52 K. From t–60 to t–45, the decrease is 1.52 K, with the decrease between t–45 and t–30 being 2.34 K. Between t–30 and t–15 the decrease is 3.36 K and between t–15 and time t this decrease is 4.3 K, the largest decrease throughout the 60–minute period. This constant, approximately linear decrease in the 15 minute 10.8 μm T_B interest field therefore shows an increase in updraft strength for the 60 minutes prior to CG lightning initiation. After time t there is a strong positive trend, with values increasing from –14.42 K to 0.06 K in this 30–minute timeframe, indicating that the updraft strength is decreasing over this time.

The non–lightning storms' 15 minute 10.8 μm T_B trend is much weaker between t–60 and time t as compared to the lightning storm trends; a total decrease of 1.43 K occurs during this time. Actually, there is a small decrease (negative trend) between t–60 and t–45 and then an increase (positive trend) between t–45 and t–30 for the non–lightning storms, followed by another decrease between t–30 and t–15. The

15 minute 10.8 μm T_B interest field again has an increase between t–15 and time t, with a stronger decrease between time t and t+30, although the final 15 minute 10.8 μm T_B at t+30 is only –9.35 K, 5.07 K less than for the lightning storms at time t. Also, the difference between each time from t–60 to time t is as follows: a 0.43 K decrease between t–60 and t–45; a 0.64 K increase between t–45 and t–30; a 1.93 K decrease between t–30 and t–15; and finally a 0.3 K increase between t–15 and time t. Thus one can see that the changes in the 15 minute 10.8 μm T_B interest field are small with varying positive and negative trends. It appears that although there is a consistent negative trend after time t, this trend is nevertheless smaller than for the lightning storms before time t and might occur too late in the storms' development, indicating that the updraft strength was not strong enough before time t, or there was not enough time after time t, for charge separation to occur to cause lightning to occur. In addition it appears that the 15 minute 10.8 T_B value should be at least –10 K before CG lightning will occur.

The 30 minute 10.8 μm T_B interest field can be seen in Figure 6.24 with the lightning storms displayed on the left and the non–lightning storms on the right. Here, a negative trend that is larger than the 15 minute 10.8 μm T_B interest field trend is needed for strong updrafts to be inferred. Not surprisingly, the lightning storms have this negative trend for the entire period before lightning occurs, while the non–lightning storms only obtaining a noticeable negative trend after time t. At t–45 the 30 minute 10.8 μm T_B interest field is already at –7.5 K, with a 5.73 K decrease to t–30 for the lightning storms. At this time, the decrease here is already at least 1.5 larger than was found for the lightning storm at the same time for the 15 minute 10.8 μm T_B interest field.

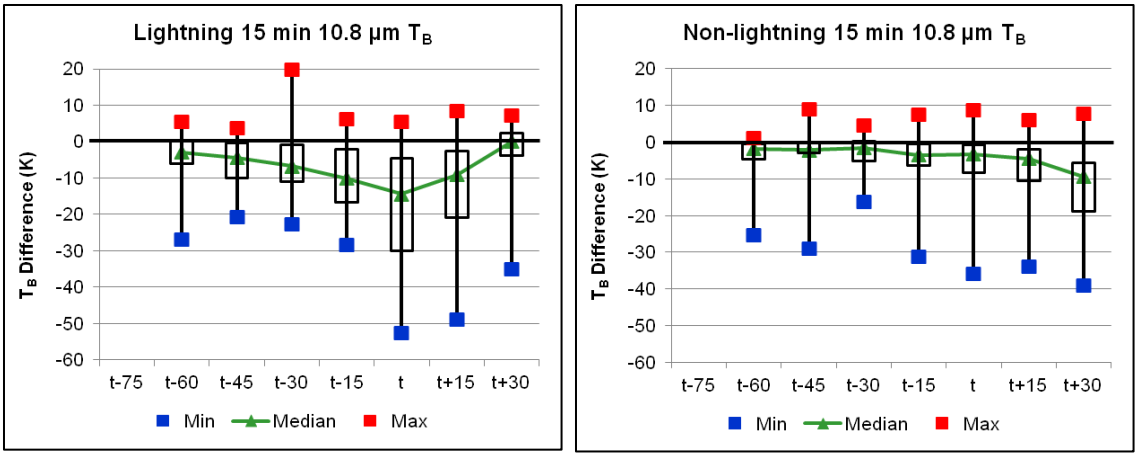

Figure 6.23: Box plots of 15 minute 10.8 μm T_B trend interest field showing updraft strength features between lightning (left) and non–lightning (right) storms from t–75 to t+30. The features in the plots are the same as in Figure 6.20.

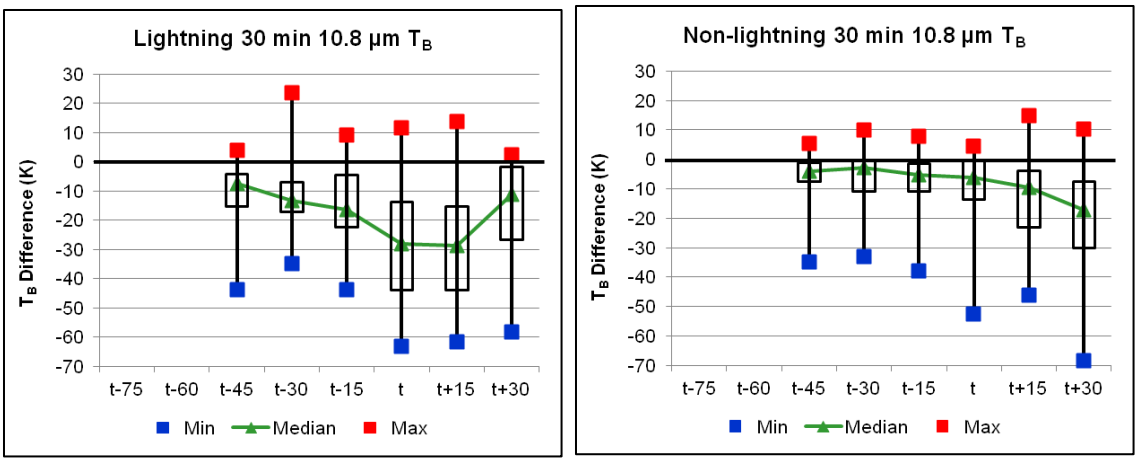

Figure 6.24: Box plots of the 30 minute 10.8 μm T_B interest field showing updraft strength features between lightning (left) and non–lightning (right) storms from t–75 to t+30. The features in the plots are the same as in Figure 6.20.

Between t–30 and time t, the 30 minute 10.8 μm T_B interest field decreases from –13.23 K to –28.11 K, which is a 3 K decrease and a 11.88 K decrease at t–15 and time t, respectively. Therefore, the negative trend more than triples between t–30 and time t, which indicates again that the lightning storms have strong updraft strengths, with a very strong decrease (negative trend) between t–15 and time t. For the 15 minutes after first lightning, the 30 minute 10.8 μm T_B trend stays approximately constant, with a –28.73 K

T_B value being obtained, after which the trend is positive again between t+15 and t+30, with a final value of –11.16 K. Thus after t+15, the updraft strength becomes weaker, again probably due to falling precipitation leading to more friction and consequently causing the storms to start to dissipate.

The non–lightning storms only show a small negative trend between t–30 and time t, with a larger negative trend between time t and t+30. Here, the 30 minute 10.8 μm T_B value at t–45 is only –4.05 K, with a 1.16 K increase to t–30, which indicates that the updraft strength here is very weak. Between t–30 and t–15, the 30 minute 10.8 μm T_B values decrease from –2.89 K to –5.36 K at t–15, and then decreases to –6.04 K at time t, which is 22.07 K more than was obtained at time t for the lightning storms. Between time t and t+30, the values finally start decreasing noticeably, with –9.67 K and –17.28 K being obtained at t+15 and t+30, respectively. Although the difference between t+15 and t+30 is –7.61 K, this is not enough for any lightning to occur and it is clear from the above that the updrafts were much weaker for the non–lightning storms and despite the fact that the updraft strengths did increase after time t, this was not enough for lightning initiation to occur. Therefore, from the above one can see that the lightning storms had stronger updrafts occurring from t–60, with the non–lightning storms only showing an increase in updraft strength comparable to the lightning storms after time t, which is 60 minutes later.

Figures 6.25 and 6.26 show the results obtained for the 6.2 – 7.3 μm and 6.2 – 10.8 μm interest fields, respectively, with these two interest fields indicating the cloud depth of the storms. The more negative the T_B difference values, the shallower the cloud. Thus for a deep cloud to occur, the 6.2 – 7.3 μm T_B difference should approach

0 K. The 6.2 – 7.3 μm T_B difference shows that the lightning storms start at a colder median temperature at t–75 than the non–lightning storms, with the median value being –15.57 K with the minimum and maximum values for the lightning storms being –20.97 K and –2.32 K, respectively. The 6.2 – 7.3 μm T_B values increase slowly towards t–45, indicating that the lightning storms have increasing cloud depths, although this increase is small. Between t–45 and t–30 the lightning storms increase quickly from –13.95 K to –11.31 K, indicating that during this time the cloud depth is growing, which is important for the formation of ice crystals (which is needed for electrification to occur). The most cloud growth occurs between t–30 and time t for the lightning storms, with the T_B difference values changing from –11.31 K to –3.43 K (a 7.88 K increase) during this 30–minute timeframe. Although the first CG lightning occurred after time t, the cloud depths continued growing until t+15, with a T_B difference value of –1.63 K being reached at this time. After t+15, the cloud depth starts to decrease, indicating that the mature phase of the lifecycle has been reached, and therefore the storms will slowly start to decrease in size and dissipate.

As is clear when comparing the non–lightning storms to the lightning storms, the non–lightning storms have much larger negative 6.2 – 7.3 μm T_B differences, indicating that the cloud depths here are smaller than for the lightning storms. At t–75, the median value for the non–lightning storms is –18.42 K, almost 3 K less than for the lightning storms and the minimum and maximum values for the non–lightning storms at t–75 are –21.52 K and –12.19 K, respectively. Between t–75 and time t, the non–lightning storms show some increase in T_B difference values, however, this is much smaller as compared to the lightning storms for the same period. This increase between t–75 and time t for the

non–lightning storms is 2.91 K, which is much less than were observed for the lightning storms, which had a 12.14 K increase during this period. This indicates that the non–lightning storms have a much smaller cloud depth than the lightning storms, which could be one of the reasons why lightning was not present here (deeper clouds have more ice and supercooled water).

Most of the cloud growth for the non–lightning storms only occurs after time t, 45 minutes after the increase in cloud growth for the lightning storms. Between time t and t+30 the 6.2 – 7.3 μm T_B differences are –16.75 K and –7.77 K, respectively, indicating that during this 30–minute timeframe the cloud depth T_B values increased with 8.98 K, with the largest increase occurring between t+15 and t+30. Although these storms had substantial cloud growth between time t and t+30, this growth was still less than the lightning storm growth between t–45 and time t; much colder T_B difference values were reached for the lightning storms by time t than were reached for the non–lightning storms at t+30.

Figure 6.26 shows the results obtained from the 6.2 – 10.8 μm T_B interest field, also indicating the depth of the clouds. This interest field works approximately the same way as the previous interest field, with the closer the values are to 0 K, the deeper the clouds will be. As was the case with the 6.2 – 7.3 μm T_B interest field, there are large differences between the lightning and non–lightning storms in the 6.2 – 10.8 μm T_B interest field. It is clear that the overall tendency of the lightning storms is closer to zero as compared to the non–lightning storms. At t–75, the lightning storms' median 6.2 – 10.8 μm T_B difference is –36.55 K, with a steady increase in T_B difference values occurring from this time to t–30. Between t–75 and t–30, the T_B difference values

increase with 13.09 K, with the T_B value at t–30 being –23.46 K. From t–30 to time t the 6.2 – 10.8 μm T_B difference increases more rapidly, with –7.23 K being reached at time t, which is a total increase of 29.32 K between t–75 and time t, indicating that the cloud growth during this period is considerable, signifying that the cloud–tops were very cold, and thus there are large amounts of ice present in these clouds. Between time t and t+30 there is an additional increase in T_B difference values, with –2.64 K and –2.40 K being reached at t+15 and t+30 respectively.

The non–lightning storms do not show this strong cloud growth, with the 6.2 – 10.8 μm T_B difference between t–75 and time t only being 15.37 K, which is much less than the 29.32 K increase for the lightning storms during this period. In addition, a T_B difference value of only –32.43 K is reached at time t for the non–lightning storms, where this was –7.23 K for the lightning storm. Between time t and t+15, the 6.2 – 10.8 μm T_B difference increased with 5.1 K, thus leading to a –27.33 K T_B difference value being reached. The most cloud growth for the non–lightning storms only occurs between t+15 and t+30, with an increase of 13.12 K, although the T_B difference value is only –14.21 K at t+30, much less than for the lightning storm, which was –2.40 K at t+30. Thus, although the cloud depth increases for the non–lightning storms, this increase is too slow and even with the cloud thickness reaching a maximum at t+30, it is still not enough to produce sufficient amounts of ice to produce CG lightning, due to the fact that the cloud–tops are much lower than the lightning storms' cloud–tops.

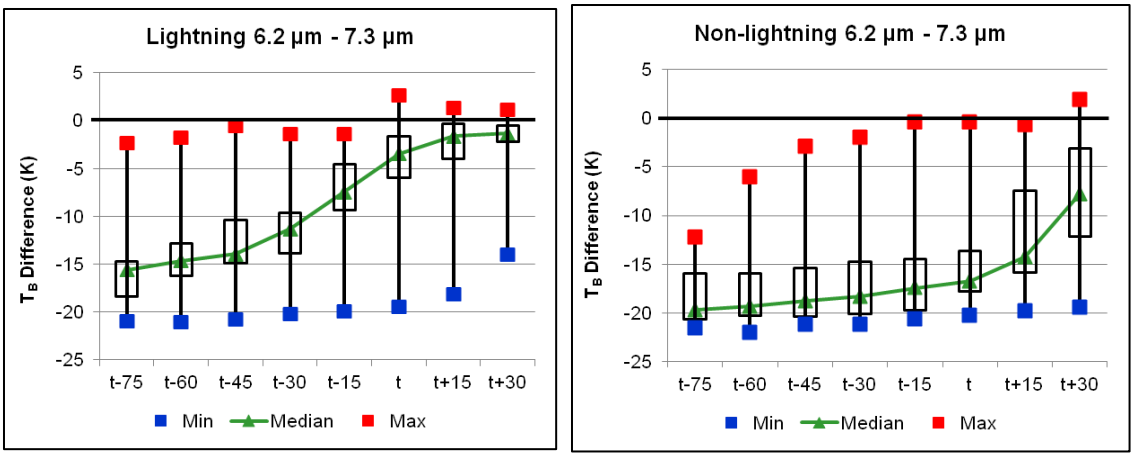

Figure 6.25: Box plots of the 6.2 – 7.3 µm T_B interest field showing cloud depth features between lightning (left) and non–lightning (right) storms from t–75 to t+30. The features in the plots are the same as in Figure 6.20.

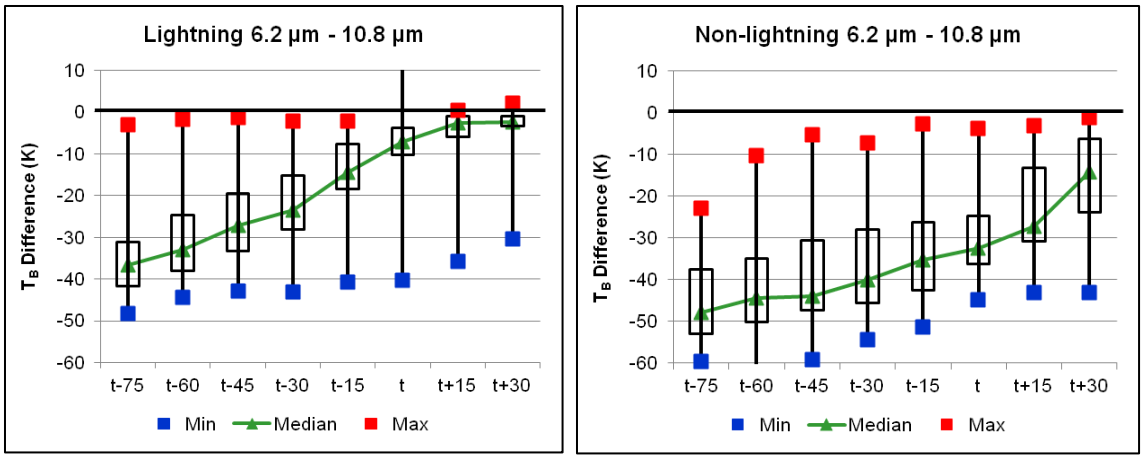

Figure 6.26: Box plots of the 6.2 – 10.8 µm T_B interest field showing cloud depth features between lightning (left) and non–lightning (right) storms from t–75 to t+30. The features in the plots are the same as in Figure 6.20.

From Figures 6.25 and 6.26, one can see that the non–lightning storm tops are much lower, and thus the clouds are shallower than the lightning producing storms and will therefore not be able to produce as much ice in the mixed–phase layer as the lightning storms do. In addition, the lightning producing storms have a faster cloud growth rate as compared with the non–lightning storms, which seems to be important for lightning to occur.

Figures 6.27 through 6.30 all show MSG interest fields that indicate cloud–top glaciation with positive trends and/or a change in sign from negative to positive being needed to signify the glaciation of storm cloud–tops. Figure 6.27 displays the (8.7 – 10.8) – (10.8 – 12.0) μm T_B interest field (also known as the tri–spectral field), Figure 6.28 the 15 minute (8.7 – 10.8) – (10.8 – 12.0) μm T_B interest field (also known as the 15 minute tri–spectral field), Figure 6.29 the 8.7 – 10.8 μm T_B interest field and Figure 6.30 shows the 15 minute 8.7 – 10.8 μm T_B interest field, with the lightning storms displayed on the left and the non–lightning storms displayed on the right of each figure.

For the tri–spectral T_B interest field to show cloud–top glaciation, the values have to change signs from negative to positive. The lightning storms in Figure 6.27 have a clear positive trend and cross the 0 K line at t–15. The lightning tri–spectral μm T_B interest field starts at –2.41 K at t–75 and quickly increases to –1.98 K at t–60. Between t–60 and t–45 and t–45 to t–30, there is a 0.61 K and 0.78 K increase respectively, with –0.58 K being reached at t–30. The trend keeps increasing, with a 0.55 K and a 0.66 K increase between t–30 and t–15, and t–15 to time t, which leads to a positive tri–spectral T_B value of 0.63 at time t. Therefore, between t–15 and time t the tri–spectral μm T_B field changes signs from negative to positive, indicating the start of cloud–top glaciation. Even after time t there is still an increase in values, with 0.63 K and 0.98 K being reached at t+15 and t+30, respectively. Hence, it is clear that there is a large amount of small ice located at the tops of the clouds from t–15 onwards.

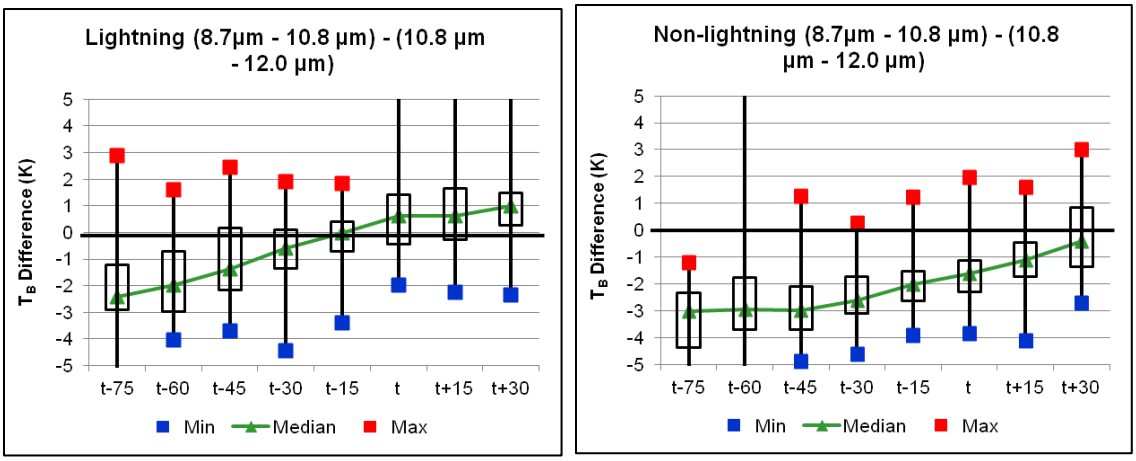

Figure 6.27: Box plots of the (8.7 – 10.8 µm) – (10.8 – 12.0 µm) T_B tri–spectral interest field showing cloud–top glaciation features between lightning (left) and non–lightning (right) storms from t–75 to t+30. The features in the plots are the same as in Figure 6.20.

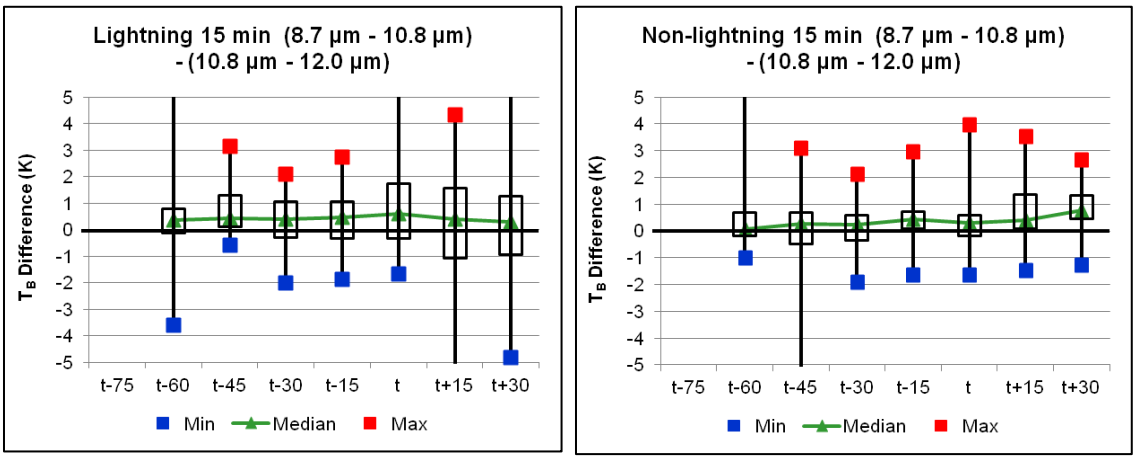

Figure 6.28: Box plots of the 15 minute (8.7 – 10.8 µm) – (10.8 – 12.0 µm) T_B tri–spectral interest field showing cloud–top glaciation features between lightning (left) and non–lightning (right) storms from t–75 to t+30. The features in the plots are the same as in Figure 6.20.

For the non–lightning storms, however, the tri–spectral T_B field does not seem to indicate the presence of cloud–top glaciation, due to the low tri–spectral values, even at t+30. At t–75, the tri–spectral T_B field has a value of –3.01 K, 0.6 K less than for the lightning storms at the same time. Between t–75 and t–60 the tri–spectral T_B field increases to –2.96 K and then decreases again between t–60 and t–45 to –2.98 K. There

is a further increase of 0.36 K between t–45 and t–30, where after the largest increases occur at t–15 and time t, with –2.02 K and –1.63 K being reached, respectively. After time t, the tri–spectral T_B field is still increasing to –1.11 K and –0.42 K at t+15 and t+30, however, these are not enough to lead to a sign–change in the field, indicating that there are little to no cloud–top glaciation for the non–lightning storms, with maybe some development after t+30. These values are consistent with the analyses above, as the non–lightning storms had, on average, lower cloud–top altitudes as compared to the lightning storms, and therefore colder temperatures needed for cloud–top glaciation to occur are not reached by the non–lightning storms.

In the next figure (Figure 6.28) one can see the 15 minute (8.7 – 10.8) – (10.8 – 12.0) μm T_B interest field (also known as the 15 minute tri–spectral field) for the lightning (left) and non–lightning (right) storms. Here there has to be positive trends to indicate cloud–top glaciation, but due to the outliers, one cannot see these trends easily by looking at the plots. However, both the lightning and non–lightning storms have positive trends; the lightning storms have a longer–lasting positive trend before time t. At t–60, the lightning 15 minute tri–spectral field is 0.35 K, with 0.43 K being reached at t–45, indicating a positive trend, however between t–45 and t–30 there is a decrease of 0.04 K, which is small, but nevertheless there. Between t–30 and time t there is a steady positive trend, with 0.48 K and 0.61 K being reached at t–15 and time t, respectively. This indicates that there is a positive trend for at least 30 minutes before the first CG flashes occur, signifying the development of cloud–top glaciation for these times. After time t, there is a steady decrease in the 15 minute tri–spectral field, with 0.39 K and 0.28 K being reached at t+15 and t+30 respectively.

Therefore, although there is not a steady positive trend for the entire 60 minute timeframe before lightning occurs, there is a 30–minute positive trend before time t, indicating that this is a long enough period for cloud–top glaciation and charging to occur in the lightning storms.

The non–lightning storms' 15 minute tri–spectral field varies more than the lightning storms' field, with varying positive and negative trends. At t–60, the 15 minute tri–spectral field value is 0.08 K, much lower than the lightning value at this time, with an increase (positive trend) to t–45 of 0.19 K. Between t–45 and t–30 there is a decrease (negative trend) with 0.23 K being reached. After t–30 there is another increase of 0.21 K and then another decrease of 0.15 K, leading to 0.29 K being reached at time t. Between time t and t+30, there is a steady increase in the 15 minute tri–spectral field, with 0.40 K and 0.77 K being reached at t+15 and t+30 respectively. Therefore, although there is a steady positive trend after time t, this occurs 30 minutes after the lightning storms' positive trend, and due to some of the non–lightning storms dying out by this time, the cloud–top glaciation that occurs here may be very small, and might occur too late for any real charge separation to occur.

The 8.7 – 10.8 μm T_B interest field is seen Figure 6.29, with the lightning storms on the left and the non–lightning storms on the right. Here, for cloud–top glaciation to be observed, the trend needs to change signs from negative to positive. At t–75, the lightning storms have a 8.7 – 10.8 μm T_B value of –0.79 K, with a decrease of 0.15 K, leading to –0.94 K at t–60. After this time, there is a steady increase in 8.7 – 10.8 μm T_B values, with –0.12 K being reached at t–45 and 0.04 K at t–30. Therefore cloud–top glaciation is initiated at t–30 already for the lightning storms for this interest field. After

this time, the 8.7 – 10.8 μm T_B values increase from 0.24 at t–15, to 0.63 at time t, which is when the first CG flashes occurred. Between time t and t+30, these values keep increasing, reaching 1.13 K at t+30. From this, it is clear that the 30 minutes before the first CG flashes occur, positive 8.7 – 10.8 μm T_B values are observed, with this trend continuing until t+30, indicating the presence of large amounts of small ice at the top of the cloud by time t.

Although there is a positive trend for the non–lightning storms seen here, the 8.7 – 10.8 μm T_B trend does not change signs from negative to positive values until t+30. More specifically, 8.7 – 10.8 μm T_B values were –1.41 K, –1.30 K, –1.31 K, –1.16 K and –1.14 K at t–60, t–45, t–30 and t–15 respectively. During t–15 to time t, the values increased with 0.35 K to –0.79 K, which is still below the 0 K level. After time t the 8.7 – 10.8 μm T_B values continue to increase, with –0.42 K and finally 0.14 K being reached at t+15 and t+30. Consequently, the non–lightning storms do not have enough time for cloud–top glaciation to occur and to produce enough ice for charge separation to occur to significant levels and with a positive 8.7 – 10.8 μm T_B value only being reached at t+30. This is 60 minutes after the lightning storms, indicating that the lightning storms have much more time for ice crystals to form at the top of the clouds.

Figure 6.30 is the final figure indicating cloud–top glaciation and displays the 15 minute 8.7 – 10.8 μm T_B interest field for the lightning storms (left) and non–lightning storms (right). Here the trend must be positive for cloud–top glaciation to occur, but once again this is difficult to see in these plots due to the outliers. For the lightning storms, the 15 minute 8.7 – 10.8 μm T_B values at t–60 and t–45 are 0.11 K and 0.03 K, indicating a negative trend during this time. However, there is a positive trend between

t–45 and t–30, with 0.19 K being reached, after which there is another negative trend, with 0.04 K reached at t–15. In spite of this negative trend, there is a strong positive increase between t–15 and time t, with 0.52 K being reached at this time, which is a 0.48 K increase. This indicates that although the trends change, there is some cloud–top glaciation before t–15, although this signal is not very strong, but between t–15 and time t there is a very strong signal, signifying strong cloud–top glaciation at these times. After time t, there is another negative trend, with –0.08 K being reached at t+15 and then there's another positive trend, with 0.47 K reached at t+30, which is another large increase of 0.55 K.

The non–lightning storms, however have a consistent upward trend between t–60 and t–15, with an increase of 0.15 K, though this total 45 minute trend is still less than the 15 minute trends found for the lightning storms. Between t–15 and time t there is a decrease of 0.04 K, leading to 0.06 K being reached at time t, much lower than the 0.52 K for the lightning storms at the same time. Not surprisingly, there is another positive trend for the non–lightning 15 minute 8.7 – 10.8 μm T_B values between time t and t+30, with 0.26 K and 0.55 K being reached at t+15 and t+30, respectively. This positive trend after time t was also seen in Figures 6.27 through 6.29, but this does not seem to be significant enough to cause charge separation to occur at amounts needed for lightning to initiate, because none of the non–lightning storms produced any CG lightning. Therefore it seems that for the 15 minute 8.7 – 10.8 μm T_B trend to be significant enough in terms of signaling cloud–top glaciation, the difference should be more than 0.4 K in a 15 minute timeframe.

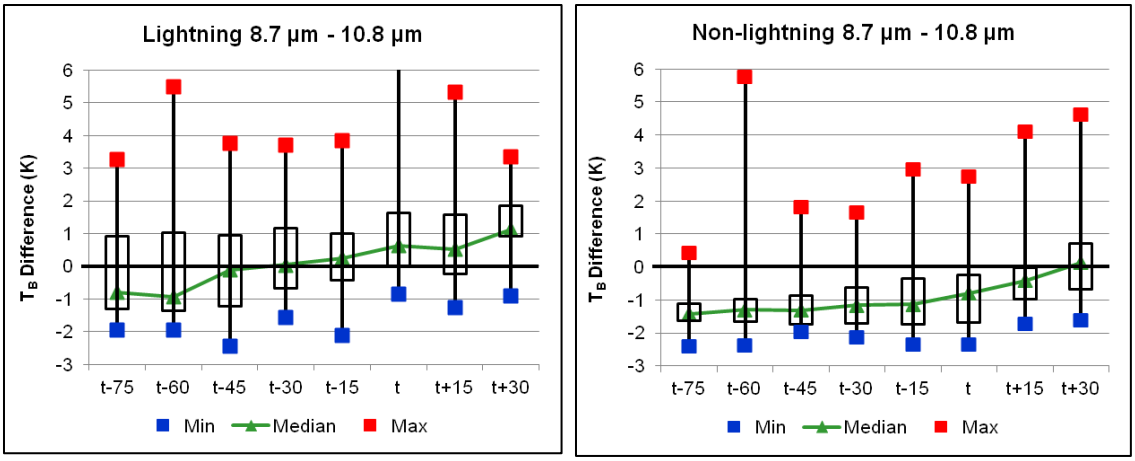

Figure 6.29: Box plots of the 8.7 – 10.8 µm T_B interest field showing cloud–top glaciation features between lightning (left) and non–lightning (right) storms from t–75 to t+30. The features in the plots are the same as in Figure 6.20.

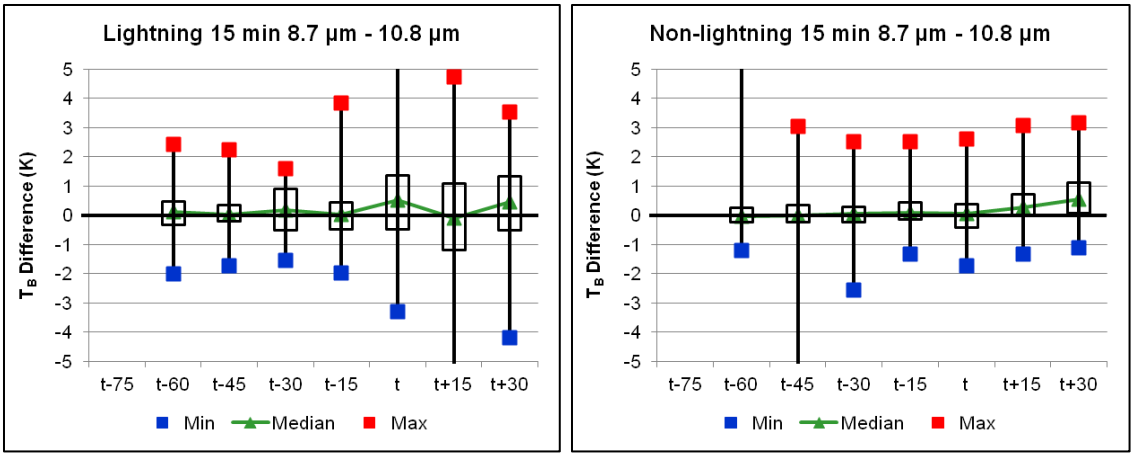

Figure 6.30: Box plots of the 15 minute 8.7 – 10.8 µm T_B interest field showing cloud–top glaciation features between lightning (left) and non–lightning (right) storms from t–75 to t+30. The features in the plots are the same as in Figure 6.20.

The above 10 figures all indicated different characteristics for cloud depth (Figures 6.20 and 6.21), updraft strength (Figures 6.22 through 6.25) and cloud–top glaciation (Figures 6.26 through 6.30). All of these different interest fields have varying critical values and/or trends that signify when the cloud depths are becoming deeper, the updraft strengths are increasing and when cloud–top glaciation will be initiated, as mentioned earlier. Therefore, it was found that the 6.2 – 7.3 µm T_B difference value

found for the lightning storms at time t (–3.43 K) corresponds well to the Mecikalski *et al* (2010a) critical values needed for deep convective clouds to occur to the point where CG lightning is initiated. Also, the 6.2 – 7.3 μm T_B difference value at time t for the non–lightning storms are only –16.75, which is much lower than the critical value needed for increased cloud depths.

The –7.23 K obtained from the 6.2 – 10.8 μm T_B interest field for the lightning storms corresponds well to the critical values needed for deep convective clouds to occur, as found by Ackerman (1996); Schmetz *et al*. (1997) and Mecikalski *et al*. (2010a). However, the –32.43 K 6.2 – 10.8 μm T_B difference at time t for the non–lightning storms are lower than needed for deep convective clouds to occur. The 15 minute 6.2 – 7.3 μm T_B time trend needs to exhibit positive trends over a time period for the critical values to occur in order for strong updraft strengths to occur. This positive trend was seen for the lightning storms for approximately 45 minutes (and up to t–15), where it was only seen for 30 minutes for the non–lightning storms, but here this positive trend was only observed after time t. Although the 30 minute 6.2 – 7.3 μm T_B trend also needs to have a positive trend in order for strong updrafts strengths to be observed, according to Figure 6.24, this positive trend needs to be a linear trend instead of an exponential trend in order to lead to the initiation of CG lightning. In addition, these positive trends (with increasing values of at least 1.48 K per 15 minute time interval) were seen between t–45 and time t for the lightning storms, but was only seen t+15 for the non–lightning storms, which is at least 45 minutes after the lightning storms produced their first CG flashes.

Mecikalski *et al*. (2010a) found that the 15 minute 10.8 T_B interest field needed a decrease of < –4 K per 15–minute interval for strong updraft strengths to occur. This was

found for the lightning storms, with a –4.3 K difference being obtained between t–15 and time t. This critical value was only exceeded between t+15 and t+30 for the non–lightning storms, and with no lightning occurring for these storms. Therefore it seems as though this decrease occurred too late in the non–lightning storms' lifetimes to have a large enough affect on the charge separation within the clouds. The 30 minute 10.8 μm T_B interest field needs to have time trends that are greater than for the 15 minute 10.8 μm T_B interest field in order for strong updraft strengths to be observed (Roberts & Rutledge, 2003; Mecikalski *et al*., 2010a). Although this was found to be true for the lightning storms, it was also found that this decrease should be at least 1.5 times the decrease found in the 15 minute 10.8 T_B interest field; a –20 K time–trend value is required on average before lightning will occur.

The 8.7 – 10.8 μm T_B interest field has its critical value for cloud–top glaciation when this field changes signs from negative to positive values (Ackerman *et al*., 1992; Strabala *et al*., 1994). This was seen for the lightning storms at t–30 already, but was only seen at t+30 for the non–lightning storms. Therefore, it is clear from this field that cloud–top glaciation and charging is initiated no less than 30 minutes before the first CG flash is observed. The 15 minute 8.7 – 10.8 μm T_B is another interest field that signifies the initiation of cloud–top glaciation, with positive trends needed to indicate this (Ackerman *et al*., 1992; Strabala *et al*., 1994; Mecikalski *et al*., 2010a). However, consistent positive trends were seen for the non–lightning storms, especially before t–15. These constant positive trends were not seen for the lightning storms, in fact the trends were varying, but between t–15 and time t there was a very strong positive trend of 0.48 K. Therefore it seems that for the 15 minute 8.7 – 10.8 μm T_B trend to be significant

enough in terms of signaling cloud–top glaciation, the difference should be more than 0.4 K over a 15–minute period instead of just having a positive trend.

When one looks at the (8.7 – 10.8) – (10.8 – 12.0) μm T_B interest field, the critical value that is needed for cloud–top glaciation to occur is a change in signs from negative to positive (Baum *et al*., 2000). Here the lightning storms reached the critical value immediately after t–15, whereas the non–lightning storms never changed signs. Thus, it is clear that the non–lightning storms had very little to no cloud–top glaciation according to this field, where this occurred from t–15 for the lightning storms, leading to enough time for charge separation and CG lightning to occur. In addition, for the 15 minute tri–spectral field to show cloud–top glaciation occurrence, there has to be a positive trend, as found by Mecikalski *et al*. (2010a). Although both the lightning and non–lightning storms have positive trends, the lightning storms had a sustained positive trend for the 30 minutes prior to the first CG flashes, where the non–lightning storms only had a sustained positive trend 30 minutes later, from time t to t+30. Therefore, it seems that this positive trend should occur within 60 minutes of first radar or satellite signature for the cloud–top glaciation to be significant enough. The positive trends in the 15 minute tri–spectral field indicate cloud–top glaciation, yet both the lightning and non–lightning storms display positive trends. Nevertheless, the lightning storms have a steady positive trend from t–30 onwards, with the non–lightning storm only displaying this feature from time t, 30 minutes later and no CG lightning being observed for this storm. It appears then that together with a positive trend, one needs an increase of at least 0.13 K is needed for lightning to initiate, although the non–lightning storm had a larger increase than this between t+15 and t+30.

All of the above illustrated that the lightning storms had stronger updrafts, deeper clouds and cloud–top glaciation occurring at least 15 minutes before the first CG flash occurred, where the non–lightning storms on average either did not display these features or they were only observed 30 to 45 minutes after it was observed in the lightning storms.

CHAPTER 7

STATISTICAL ANALYSIS

Here, the statistical analysis that was done on the lightning and non–lightning storms will be discussed. These statistics were calculated in order to show that even though the ATD VLF network had very low DE and LA, which might lead to misclassification of the non–lightning storms used in this research, these non–lightning storms do indeed possess statistically significant differences compared to the lightning storms. Several statistical methods were considered, including obtaining the probability distribution function (PDF) as well as notched box plots. The PDF plots were done for the radar fields, due to these being a two–dimensional field (the radar variables varies with height), in order to obtain the frequency of occurrence of the different variables for the various timeframes. The notched plots were calculated for both the radar fields as well as the MSG interest fields. These will be explained in more detail in this chapter.

7.1. Statistical Analysis of Radar Variables:

PDF plots are calculated for the radar variables according to the bin–sizes used for the un–normalized CFAD analysis in order to keep the statistics here representative and comparable to the previous results shown in chapters 5 and 6. The methodology for calculating these PDF plots includes dividing the averages of the different radar variables (Z_H, Z_{DR} and ρ_{HV}) obtained for the lightning and non–lightning storms into bin–sizes, then obtaining the frequency of occurrence of each bin at each time frame (i.e., at t–45, t–30, t–15, t, t+15 and t+30). The percentage of occurrence is then calculated for each bin by dividing each bin frequency by the total number of occurrences at each time (the frequency distributions itself, and not the percentage, will be shown as notched box plots, seen later in this chapter). The bin–sizes were as follows: (1) For the Z_H field: 10 dBZ – 15 dBZ, 15 dBZ – 20 dBZ, 20 dBZ – 25 dBZ, 25 dBZ – 30 dBZ, 30 dBZ – 35 dBZ, 35 dBZ – 40 dBZ, 40 dBZ – 45 dBZ and 45 dBZ – 50 dBZ; (2) for the Z_{DR} field: –3.0 dB to –2.5 dB, –2.5 dB to –2.0 dB, –2.0 dB to –1.5 dB, –1.5 dB to –1.0 dB, –1.0 dB to –0.5 dB, –0.5 dB to 0.0 dB, 0.0 dB to 0.5 dB, 0.5 dB to 1.0 dB, 1.0 dB to 1.5 dB, 1.5 dB to 2.0 dB, 2.0 dB to 2.5 dB and 2.5 dB to 3.0 dB and (3) for the ρ_{HV} field: 0.80 – 0.82, 0.82 – 0.84, 0.84 – 0.86, 0.86 – 0.88, 0.88 – 0.90, 0.90 – 0.92, 0.92 – 0.94, 0.94 – 0.96, 0.96 – 0.98 and 0.98 – 1.0.

It is very important to note here that these percentage frequency distributions are done for the mixed–phase region only, which is between 5 km and 11 km (0 °C to –40 °C), as this is the region where the most electrical charging occurs. It was important to do a statistical analysis on this region, because if there are enough variation between the two datasets (lightning versus non–lightning storms) in the mixed–phase region, it is

an additional confirmation that these two datasets are different, and that very little (to no) contamination occurred (i.e., non–lightning storms were not misclassified). A graphical display of the percentage frequency distributions of the average Z_H values obtained for the lightning (red) and non–lightning (blue) storms for the various radar bins from t–45 to t+30 can be seen in Figures 7.1 through 7.6, respectively.

At t–45, which is seen in Figure 7.1, one can see that the non–lightning storms, on average, have higher frequencies of 10 dBZ – 15 dBZ values, with 48.98 % being reached, with the lightning storms only having a 22.94 % of these Z_H values. Therefore, the non–lightning storms on average, have more 10 dBZ – 15 dBZ Z_H values at t–45 than any of the other bin values, with more than double the amount as seen for the lightning storms. In contrast, the lightning storms, on average, have more 15 dBZ – 20 dBZ Z_H values at t–45, with 38.49 % being reached, and the non–lightning storms only have a 30.11 % occurrence at this bin value. Therefore, 79.09 % of the non–lightning storms' precipitation particles fall into the 10 dBZ – 20 dBZ bin, whereas for the lightning storm this is only 61.43%. There is an exponential decrease in the percentage frequency distribution of the remaining Z_H values for both the lightning and non–lightning storms, which is expected, as at t–45 the storms are still developing. For the 20 dBZ – 25 dBZ bin, the lightning storms have an average of 21.17 % and the non–lightning storms an average of 11.64 % frequency, and for the 25 dBZ – 30 dBZ bin, these amounts decreased to 9.9 % and 5.46 % for the lightning and non–lightning storms, respectively. By 30 dBZ – 35 dBZ, the lightning storms have a frequency of 4.95 % as compared to the non–lightning storms' frequency of 2.39 %, less than half of that for the lightning storms. This is due to the fact that at t–45, the non–lightning storms had a smaller mixed–phase

region (as was seen in the un–normalized CFADs) with much fewer higher Z_H values than was observed for the lightning storms. Hence, between 35 dBZ and 50 dBZ, the lightning storms have a frequency of 2.56 % in total, where the non–lightning storm only has a frequency of 1.42 % (in total), once again confirming that at t–45, the lightning storms already had more ice and small graupel in the mixed–phase region, with supercooled liquid water probably also being present.

At t–30 (Figure 7.2), the amount of 10 dBZ – 15 dBZ values observed for the lightning storms is now 25.18 %, which is a 2.24 % increase from t–45, however, the 15 dBZ – 20 dBZ values have decreased with 1.6 % and is now at 36.89 %. These two bins comprise 62.07 % of the entire storm, which is a slight increase from t–45. The 20 dBZ – 25 dBZ, 25 dBZ – 30 dBZ and 30 dBZ – 35 dBZ bins occur at 19.71 %, 9.6 % and 5.3 %, respectively, which is approximately the same as found at t–45. The 35 dBZ to 50 dBZ bins now occur at 3.31 % due to a decrease in the occurrence of 35 dBZ to 45 dBZ values, however there is a slight increase in the 45 dBZ to 50 dBZ bin, indicating that larger graupel and possibly hail is more frequent at t–30.

The amount of 10 dBZ – 15 dBZ values observed for the non–lightning storms has now decreased to 44.8 %, indicating that there are fewer smaller drops, as well as more larger drops in the mixed–phase region (as seen by the higher frequencies of 25 dBZ – 35 dBZ values) for this storm at t–30; however, as can be seen from the figure, these are still at a lower frequency than was observed for the lightning storms. The remainder of the reflectivity values for the non–lightning storms is approximately the same as at t–45, with 31.27 %, 14.81 %, 5.3 % and 2.52 % being reached for the 15 dBZ – 20 dBZ, 20 dBZ – 25 dBZ, 25 dBZ – 30 dBZ and 30 dBZ – 35 dBZ bins, respectively.

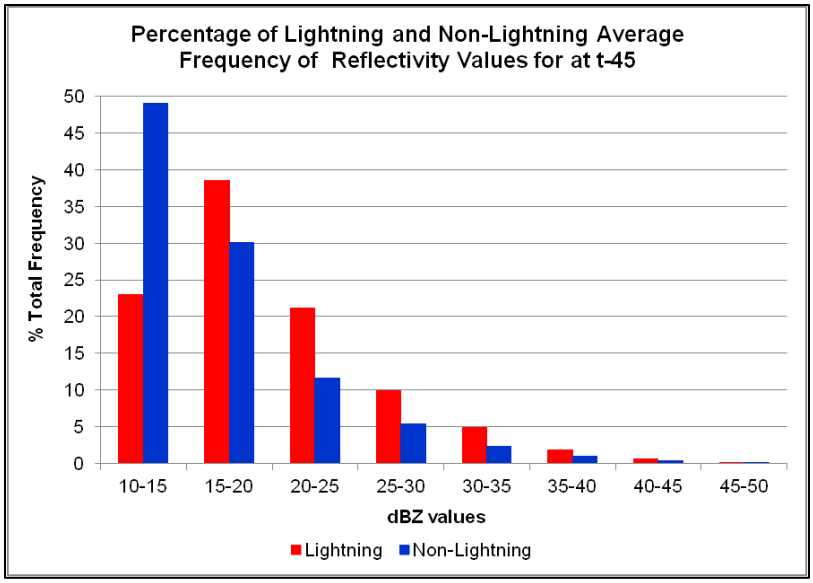

Figure 7.1: A graphical display of the percentage frequency distributions of the average Z_H values obtained for the lightning (red) and non–lightning (blue) storms for the various radar bins in the mixed–phase region at t–45.

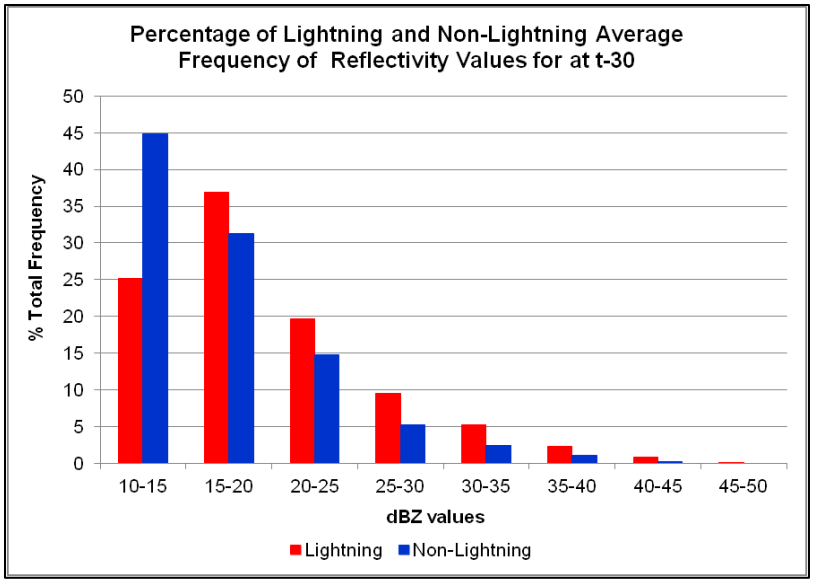

Figure 7.2: A graphical display of the percentage frequency distributions of the average Z_H values obtained for the lightning (red) and non–lightning (blue) storms for the various radar bins at in the mixed–phase region at t–30.

The non–lightning storms now have a 76.09 % and 1.3 % occurrence of bins ranging between 10 dBZ to 20 dBZ and between 35 dBZ and 50 dBZ, respectively and the amount of smaller as well as larger reflectivity values have decreased in the mixed–

phase layer, although the majority of values still occur in the 10 dBZ to 15 dBZ range. It should be noted that the non–lightning storms have an average of 19.62 % more 10 dBZ to 15 dBZ values as compared to the lightning storms, and the lightning storms consistently have higher occurrences of all Z_H values higher than this at t–30.

At t–15 (Figure 7.3), 15 minutes before the lightning storm first produced any CG strokes, the distribution of the non–lightning storms starts to look more like the distribution of the lightning storms. Interestingly, the non–lightning storms now have higher occurrences of 10 dBZ through 25 dBZ Z_H values, as compared to the lightning storms, with the lightning storms having higher occurrences of all Z_H values ≥ 25 dBZ, as compared to the non–lightning storms. Here the lightning storms have 23.1 %, 34.85 %, 19.29 % and 10.75 % percentage of occurrence for the 10 dBZ – 15 dBZ, 15 dBZ – 20 dBZ, 20 dBZ – 25 dBZ and 25 dBZ – 30 dBZ bins, respectively, thus the 10 dBZ to 20 dBZ bins now make up 57.95 % of the lightning storms' volume, which is a 4.12 % decrease from t–30. In addition, the 30 dBZ – 35 dBZ bin now occurs 6.23 % of the time, with the 35 dBZ to 50 dBZ bins now being seen at 5.6 %.

The non–lightning storms have lower frequencies of 10 dBZ to 20 dBZ Z_H values being reached at t–15, as compared to t–45 and t–30, with 64.91 % for these two bins, leading to a 21.13 % decrease in the 10 dBZ – 15 dBZ range from t–30, however the 15 dBZ – 20 dBZ range have now increased by 9.97 %, leading to 41.24 % being reached for this bin at t–15. Thus the lightning and non–lightning storms now have approximately the same 10 dBZ – 15 dBZ occurrence, with the non–lightning storms now having more 15 dBZ – 20 dBZ Z_H values than the lightning storms. The Z_H range

between 20 dBZ and 35 dBZ occurs at 33.46 %, leading to only 1.63 % being reached for Z_H values ≥ 35 dBZ.

Figure 7.4 shows the results obtained for time t. Here it is clear that the 10 dBZ – 15 dBZ percentage of occurrence has decreased again, and now occurs at lower values than for the lightning storms. The lightning storms have 25.59 %, 31.64 %, 18.22 % and 11.9 % percentage of occurrence for the 10 dBZ – 15 dBZ, 15 dBZ – 20 dBZ, 20 dBZ – 25 dBZ and 25 dBZ – 30 dBZ bins, respectively, thus leading to small changes between t–15 and time t. The 30 dBZ – 35 dBZ Z_H bins make up 6.87 % of the storms, with 4.37 % being reached for the 35 dBZ to 50 dBZ range. At the time of first CG lightning, the 10 dBZ – 20 dBZ Z_H range occurs at 57.23 %, which is very much the same as was observed at t–15. The non–lightning storms on the other hand, now have even lower 10 dBZ – 15 dBZ Z_H values, with only 14.49 % being reached, 9.18 % less than was observed at t–15 and 34.49 % less than t–45 as well as now being 11.1 % less than the lightning storms. Value of 15 dBZ – 20 dBZ, 20 dBZ – 25 dBZ and 25 dBZ – 30 dBZ now occur at 40.31 %, 21.99 %, and 11.83 %, thus showing that the 10 dBZ to 20 dBZ range decreased to 54.62 % and surprisingly, the 35 dBZ – 50 dBZ range now occur at 4.96 %, which is more than was observed for the lightning storms.

From the above it seems that the lightning storms have much less variation throughout the storms, as compared to the non–lightning storms, which have large variations for the 10 dBZ through 25 dBZ ranges. One can also see here that the non–lightning storms have higher occurrences of the 15 dBZ through 30 dBZ range,

which is much different than was seen at t–45 and t–30, where the non–lightning storms only had higher occurrences for the 10 dBZ – 15 dBZ bin.

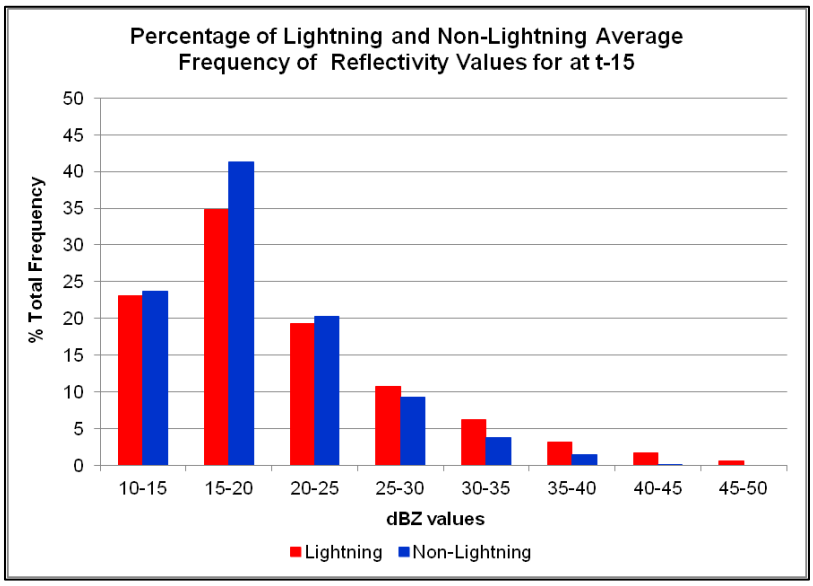

Figure 7.3: A graphical display of the percentage frequency distributions of the average Z_H values obtained for the lightning (red) and non–lightning (blue) storms for the various radar bins in the mixed–phase region at t–15.

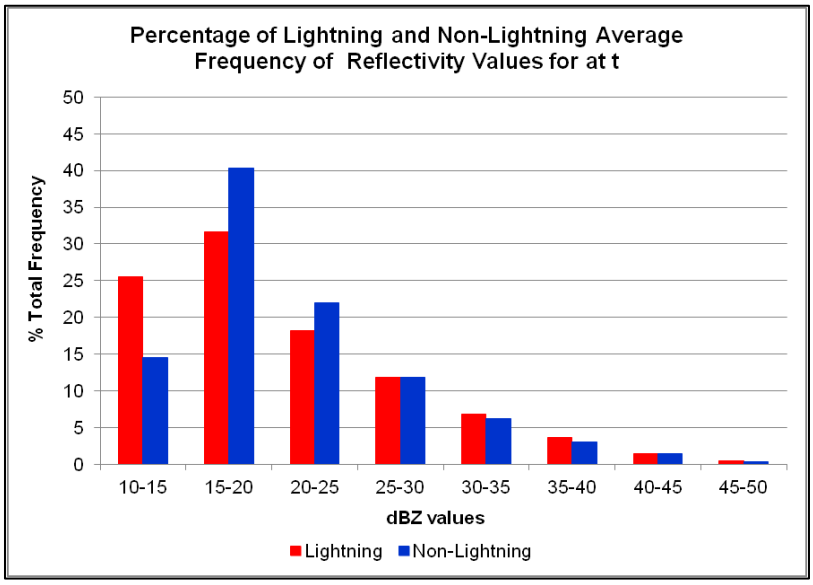

Figure 7.4: A graphical display of the percentage frequency distributions of the average Z_H values obtained for the lightning (red) and non–lightning (blue) storms for the various radar bins in the mixed–phase region at time t.

At t+15 (Figure 7.5), one can see that the lightning storms still display the same distribution as found before, with the 15 dBZ – 20 dBZ bin range occurring the most frequently in the mixed–phase region. Here the lightning storms have 28.52 %, 32.01 %, 18.14 % and 10.66 % percentage of occurrence for the 10 dBZ – 15 dBZ, 15 dBZ – 20 dBZ, 20 dBZ – 25 dBZ and 25 dBZ – 30 dBZ bins, which is again roughly the same as seen at time t. The higher Z_H values of 35 dBZ to 50 dBZ only occurs 4.66 % of the time, with 30 dBZ – 35 dBZ being reached at 5.94 %.

The non–lightning storms again had a large decrease in 10 dBZ – 15 dBZ values, with only 10.53 % being reached here. Thus, it is clear that this bin decreased consistently between t–45 and t+15, with a relatively consistent increase in the 15 dBZ – 20 dBZ bin during this time, with 44.7 % being reached at t+15 for this bin range. The lightning storms, on the other hand did not see large changes in these bins with approximately the same percentage of occurrence being observed for both the 10 dBZ – 15 dBZ and 15 dBZ – 20 dBZ bins from t–45 to t+15. The 35 dBZ to 50 dBZ percentage of occurrence for the non–lightning storms now equals 3.95 %, which is a 0.99 % decrease from time t. Furthermore, the non–lightning storms again seem to have larger percentages for the 15 dBZ to 35 dBZ range as compared to the lightning storms.

Figure 7.6 shows the results obtained for the lighting and non–lightning storms at t+30. Here the 10 dBZ to 20 dBZ range for the lightning storms occur at 65.4 %, which is higher than was obtained for all times before t+30. In addition, the higher Z_H values $\geq$ 35 dBZ now only occur at 3.32 % of the time, which is lower than previously. However, the 20 dBZ – 25 dBZ, 25 dBZ – 30 dBZ and 30 dBZ – 35 dBZ bins occur at

16.53 %, 9.85 % and 4.9 %, respectively, which is again approximately the same as found in the previous figures.

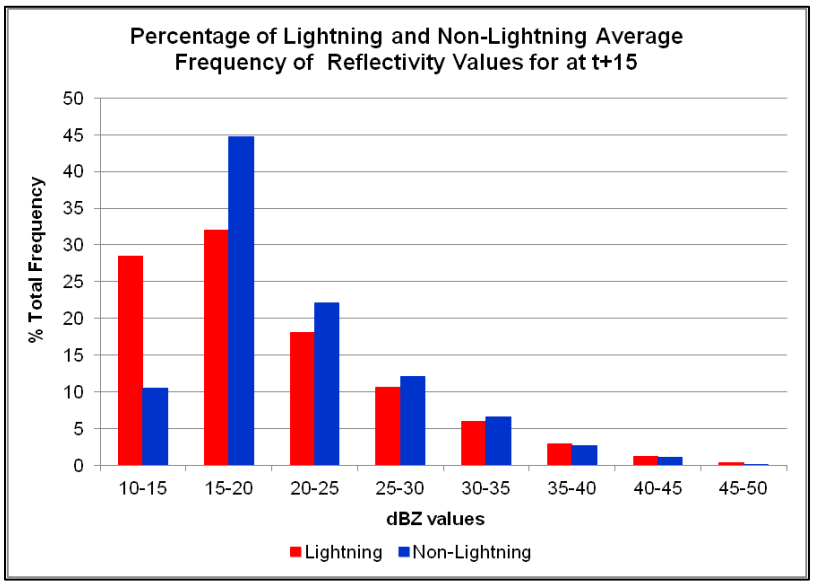

Figure 7.5: A graphical display of the percentage frequency distributions of the average Z_H values obtained for the lightning (red) and non–lightning (blue) storms for the various radar bins in the mixed–phase region at t+15.

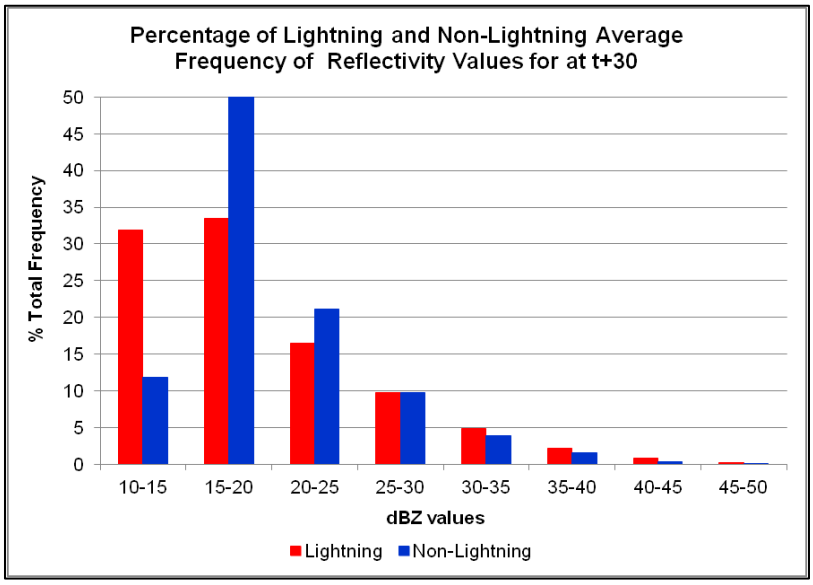

Figure 7.6: A graphical display of the percentage frequency distributions of the average Z_H values obtained for the lightning (red) and non–lightning (blue) storms for the various radar bins in the mixed–phase region at t+30.

It is clear from this figure that the non–lightning storms now have much higher occurrences of the 15 dBZ – 20 dBZ bin range, with 51.3 % being reached, with the 10 dBZ – 15 dBZ bin only occurring at 11.84 %. More than half of all the Z_H values in the non–lightning storms have reflectivities smaller than 20 dBZ. The 20 dBZ – 25 dBZ, 25 dBZ – 30 dBZ and 30 dBZ – 35 dBZ bins occur at 21.11 %, 9.74 % and 3.92 %, respectively, which are all less than was found at t+15. In addition, the Z_H bin ≥ 35 dBZ is now 2.09 %.

From the above six figures, one can see that the non–lightning storms go through more variation in terms of the amount of lower Z_H occurrences, especially for values ≤ 20 dBZ as compared to the lightning storms which seem to have the same approximate distribution from t–45 through t+30. In addition, values of 15 dBZ – 20 dBZ occur the most frequently in the lightning storms for the entire 75 minute period, whereas the same is not seen for non–lightning storms until t–15, but then these Z_H values occur at almost double the amount as seen for the 10 dBZ to 15 dBZ range. These findings could also be important in terms of delineating the lightning and non–lightning storms from each other.

Figures 7.7 through 7.12 are graphical displays of the percentage frequency distributions of the average Z_{DR} values obtained for the lightning (red) and non–lightning (blue) storms for the various radar bins in the mixed–phase region from t–45 through t+30. Here, the bin size was 0.5 dB and included all Z_{DR} values between –3 dB and 3 dB, as mentioned earlier.

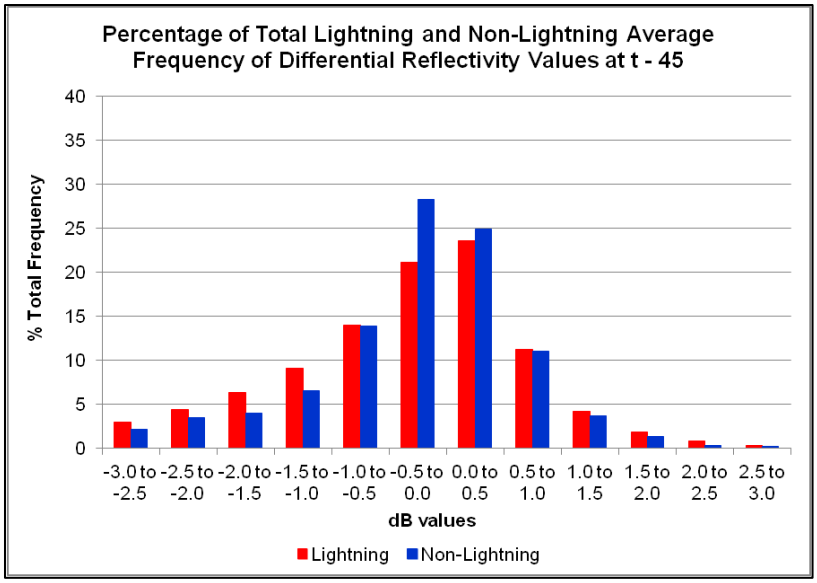

Figure 7.7: A graphical display of the percentage frequency distributions of the average Z_{DR} values obtained for the lightning (red) and non–lightning (blue) storms for the various radar bins in the mixed–phase region at t–45.

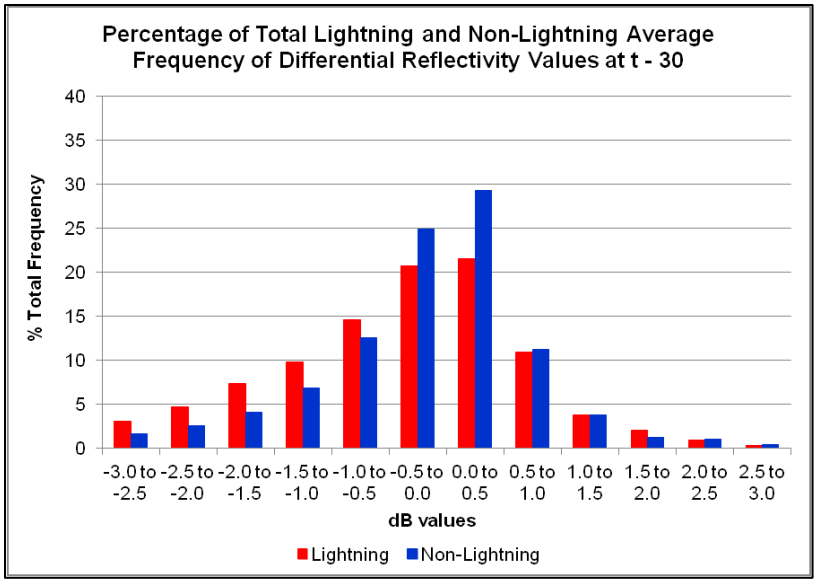

Figure 7.8: A graphical display of the percentage frequency distributions of the average Z_{DR} values obtained for the lightning (red) and non–lightning (blue) storms for the various radar bins in the mixed–phase region at t–30.

At t–45 (Figure 7.7), the lightning storms' Z_{DR} values that occur the most frequently include the –1 dB to –0.5 dB, –0.5 dB to 0 dB, 0 dB to 0.5 dB and 0.5 dB to 1 dB bins, with 13.97 %, 21.17 %, 23.54 % and 11.20 % being reached respectively, thus

showing that the 0 dB to 0.5 dB bin occurs the most frequently, as well as that 58 % of the data are negative. It is clear that large amounts of small water drops, ice, graupel and possible hail are present in the lightning storms during this time. The –3 dB to –1 dB bin ranges occur at 22.86 %, with the 1 dB to 3 dB only occurring at 7.27 %, which also indicates that in the mixed–phase region, the majority of the particles have negative Z_{DR} values, again indicative of ice and graupel particles, although the small percentage of large Z_{DR} values might be indicative of larger water drops as well as supercooled liquid water.

One can also see that the lightning storms have the highest occurrence for all Z_{DR} values between 0.0 dB and 0.5 dB, whereas the non–lightning storms have the highest occurrences for Z_{DR} values between –0.5 dB and 0.0 dB. The non–lightning storms have occurrences of 16.21 %, 78.11 % and 5.68 % for Z_{DR} values of ≤–1 dB, –1 dB to 1 dB and ≥ 1 dB, respectively, with 58.38 % being negative Z_{DR} values. Thus the non–lightning storms have more negative Z_{DR} values than positive Z_{DR} values which also indicates more smaller drops, ice crystals and possible graupel (but not hail, as is deduced from the lower Z_H values seen above).

At t–30 (Figure 7.8), the lightning storms have the same approximate distribution as at t–45, with the 0 dB to 0.5 dB once again having the highest occurrence of Z_{DR} values (with 21.53 % being reached). Also, one can again see that the majority of Z_{DR} values are negative, with 25.03 %, 67.78 % and 7.18 % being reached for the –3 to –1 dB, –1 to 1 dB and ≥ 1 dB bins, respectively, with 60.33 % being negative. The non–lightning storms now also have their maximum occurrence at 0 dB to 0.5 dB with 29.24 % being reached here. The –3 to –1 dB, –1 to 1 dB and ≥ 1 dB bins for the

non–lightning storms occur at 15.24 %, 78.05 % and 6.7 %, respectively, with 52.76 % being negative (7.57 % less than was observed for the lightning storms). One can see that the smaller negative Z_{DR} values occur less often in the non–lightning storms as compared to the lightning storms, with a large decrease in positive Z_{DR} values ≥ 1 dB for both the lightning and non–lightning storms. In addition, at t–30, the lightning storms have a higher percentage of occurrence for Z_{DR} values between –3 dB and –0.5 dB, with the non–lightning storms having higher percentages for –0.5 dB to 1 dB, with both having the exact same percentage of 1 dB to 1.5 dB Z_{DR} values.

Figure 7.9 shows the percentage frequency distributions of the average Z_{DR} values obtained for the lightning (red) and non–lightning (blue) storms for the various radar bins in the mixed–phase region at t–15. Here, once again, the lightning storms have the same relative distribution as was seen earlier, with a maximum percentage being reached for Z_{DR} values between 0 dB and 0.5 dB (which occur at 23 %). As was the case for the previous two times, the majority of Z_{DR} values are negative, with 21.5 %, 71.5 % and 7 % being reached for the –3 to –1 dB, –1 to 1 dB and ≥ 1 dB bins, respectively, with 57.97 % being negative. At this time, the lightning storm again has higher percentage bins for Z_{DR} values ≤ –0.5 dB, as well as for 1 dB to 1.5 dB and ≥ 2 dB, with the non–lightning storms having higher occurrences for the remaining four bins, including the 0 to 0.5 dB bin. The non–lightning storms have an occurrence of 18.58 %, 75.11 % and 6.31 % for the –3 to –1 dB, –1 to 1 dB and ≥ 1 dB Z_{DR} bins (with 52.36 % of these being negative), and one can see that the –1 dB to 1 dB bin is decreasing in percentage, although only by a little.

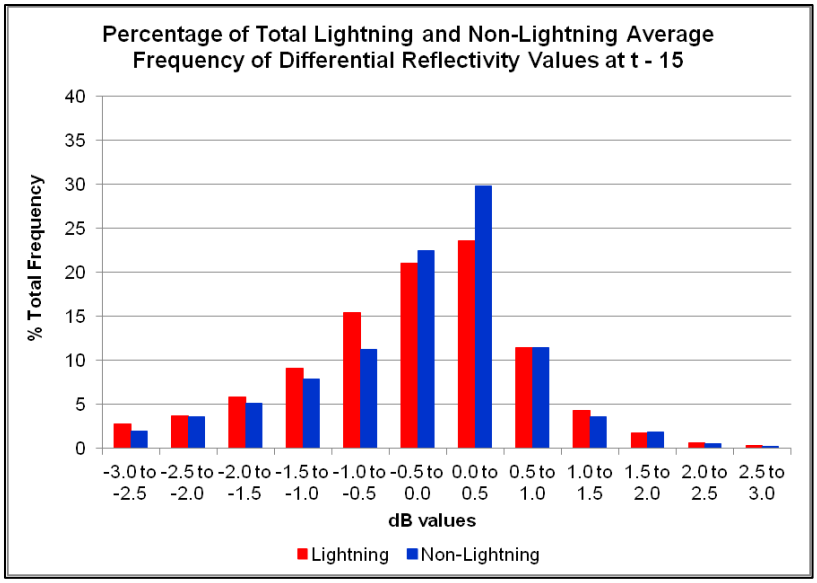

Figure 7.9: A graphical display of the percentage frequency distributions of the average Z_{DR} values obtained for the lightning (red) and non–lightning (blue) storms for the various radar bins in the mixed–phase region at t–15.

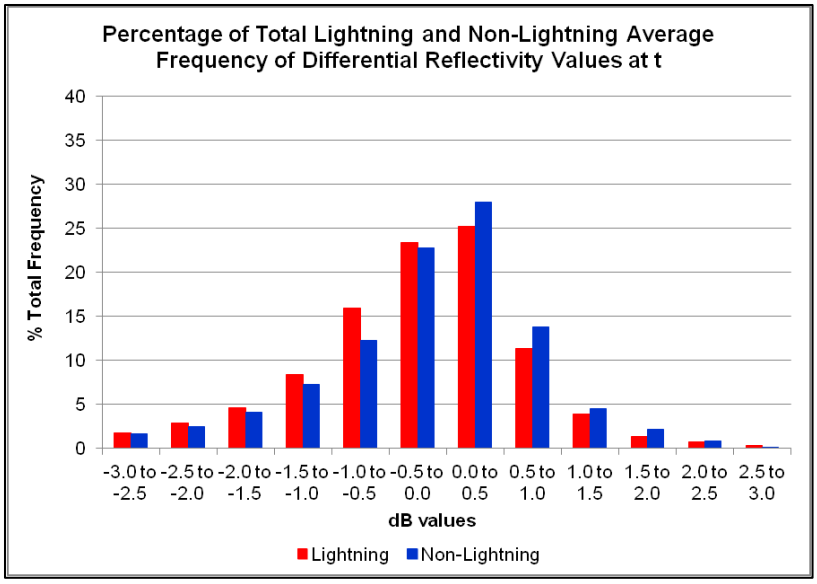

Figure 7.10: A graphical display of the percentage frequency distributions of the average Z_{DR} values obtained for the lightning (red) and non–lightning (blue) storms for the various radar bins in the mixed–phase region at time t.

At time t (Figure 7.10), the lightning storms have a maximum percentage being reached for Z_{DR} values between 0 dB and 0.5 dB, with 25.16 % being reached as compared to 23.6 % that was reached at t–15. Once again, the majority of Z_{DR} values for

the lightning storms are negative, with 17.69 %, 75.88 % and 6.43 % being reached for the –3 to –1 dB, –1 to 1 dB and ≥ 1 dB bins, respectively, with 57.03 % of the values being negative. The distribution of the non–lightning storms are finally starting to look more like the distribution of the lightning storms, with a maximum percentage of 27.98 % now also occurring at 0 dB to 0.5 dB, as was the case earlier. Half (50.55 %, 6.48 % less than for the lightning storms) of the non–lightning storms Z_{DR} values are also negative, with 15.56 %, 76.73 % and 7.72 % being reached for the –3 to –1 dB, –1 to 1 dB and ≥ 1 dB bins, respectively. What is interesting at this time, is that the lightning storms have higher percentages of negative Z_{DR} values (–3 dB to 0 dB) than the non–lightning storms, but the non–lightning storms have higher percentages of positive Z_{DR} values (0 dB to 3 dB). This could be an important difference between lightning and non–lightning convective storms.

By t+15 (Figure 7.11) both storms again have the same approximate distribution, with both having a maximum percentage of occurrence for 0 dB to 0.5 dB, the lightning with 27.63 % and the non–lightning with 29.82 %. The majority of Z_{DR} values for the lightning storms are negative, with 16.12 %, 78.37 % and 5.51 % being reached for the –3 to –1 dB, –1 to 1 dB and ≥ 1 dB bins, respectively, with 54.84 % of the values being negative, which is a 2.19 % decrease from time t. The majority of Z_{DR} values for the non–lightning storms are also negative here, with 16.20 %, 77.57 % and 6.23 % being reached for the –3 to –1 dB, –1 to 1 dB and ≥ 1 dB bins, respectively, with 53.31 % of the values being negative. However, at t+15, the non–lightning storms have a higher percentage of occurrence for Z_{DR} values between –3 dB and –1.5 dB, between –0.5 dB and 0.5 dB and all values larger than 1 dB.

Figure 7.12 shows the results for the lightning and non–lightning storms at t+30, and as seen, both the lightning and non–lightning storms again have their maximum percentages between 0 dB and 0.5 dB, with 29.16 % and 29.92 % being reached respectively. As was the case previously, the majority of Z_{DR} values for the lightning storms are negative, with 14.92 %, 79.24 % and 5.84 % being reached for the –3 to –1 dB, –1 to 1 dB and ≥ 1 dB bins, respectively, with 54.05 % of the values being negative. The non–lightning storms however, now seem to have the majority of Z_{DR} values located in the positive region, with 14.21 %, 79.70 % and 6.09 % being reached for the –3 to –1 dB, –1 to 1 dB and ≥ 1 dB bins, respectively, with 50.92 % of the values now being positive. Also different at t+30, is the fact that the lightning storms have higher percentages for the –3 to –2.5 dB, –1.5 to 0 dB, as well as 1.5 dB to 3 dB Z_{DR} bins as compared to the non–lightning storms.

From these six figures, one can see that the majority of the lightning storms' Z_{DR} values in the mixed–phase region is negative for the entire 75 minute period, whereas for the non–lightning storms, this is also true for all the times, except at t+30, when the majority of the values are positive. In addition, the lightning storms had the highest percentages for the 0 dB to 0.5 dB bin throughout, while the non–lightning storms' highest percentage occurred for the –0.5 dB to 0 dB bin at t–45 and 0 dB to 0.5 dB bin from t–30 through t+30. For most of the times, the lightning storms have higher percentages for the –3 dB to –0.5 dB bins, with the non–lightning storms having higher percentages for the –0.5 dB to 1 dB bin. The remaining bins had varying results.

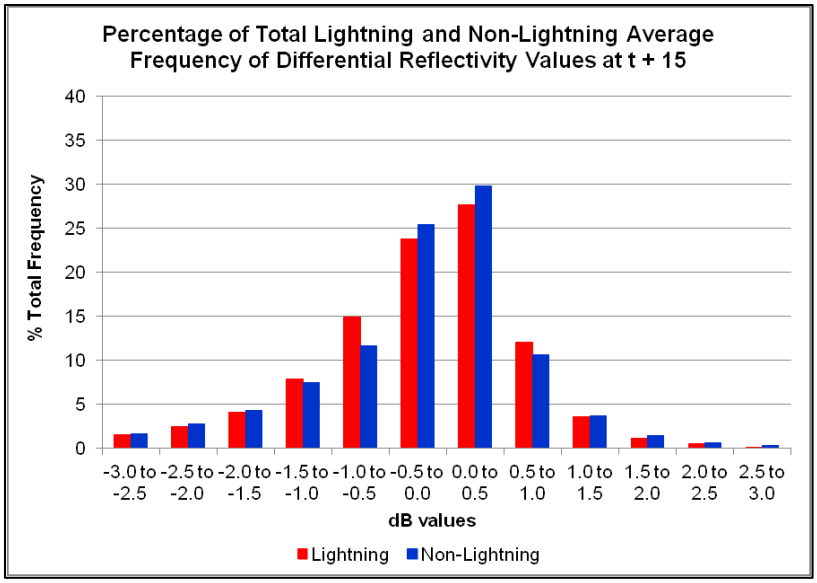

Figure 7.11: A graphical display of the percentage frequency distributions of the average Z_{DR} values obtained for the lightning (red) and non–lightning (blue) storms for the various radar bins in the mixed–phase region at t+15.

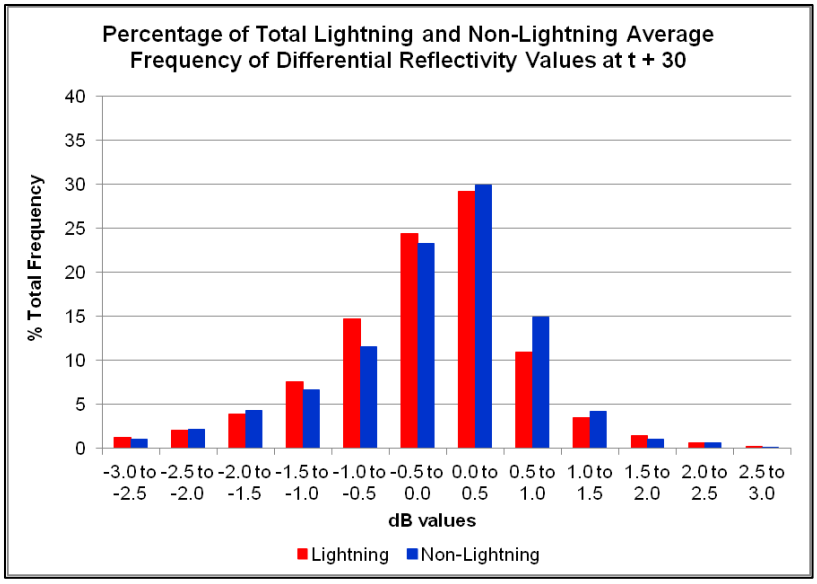

Figure 7.12: A graphical display of the percentage frequency distributions of the average Z_{DR} values obtained for the lightning (red) and non–lightning (blue) storms for the various radar bins in the mixed–phase region at t+30.

Figures 7.13 through 7.18 are graphical displays of the percentage frequency distributions of the average ρ_{HV} values obtained for the lightning (red) and non–lightning (blue) storms for the various radar bins in the mixed–phase region from t–45 through

t+30, respectively. For these plots it is no surprise that the 0.92 to 0.94 bin obtained the highest percentages for all the times, because the ρ_{HV} modes in the un–normalized CFADS plots were obtained around these values. At t–45 (Figure 7.13), this maximum for the lightning and non–lightning storms is 28.18 % and 29.64 % respectively. The lightning storms have a higher percentage of occurrences for ρ_{HV} values between 0.8 and 0.92, as compared to the non–lightning storms for these bins.

In contrast, the non–lightning storms have higher percentages for all ρ_{HV} values ≥ 0.92. The smaller ρ_{HV} values indicate that the lightning storms have many more larger water drops, as well as graupel that do not have vertical and horizontal dimensions that are equal, with the larger ρ_{HV} values showing that the non–lightning storms have more smaller drops that have the same vertical and horizontal dimensions. It is also clear that there is a peak in the 0.84 – 0.86 bin size of 12.04 % and 5.89 % for the lightning and non–lightning storms, respectively. In addition, the non–lightning storms also display another difference in the trend, where instead of there being an exponential decrease in the ρ_{HV} values after 0.94 (as seen for the lightning storms), there is a final increase in the 0.98 – 1 bin, with 13.62 % being reached here. This once again indicates that the non–lightning storms have more smaller–sized precipitation particles, with equal vertical and horizontal dimensions as compared to the lightning storms at this time.

At t–30 (Figure 7.14), the distribution of the lightning and non–lightning storms appears similar, although there are some small changes. As was the case at t–45, the 0.92 – 0.94 bin had the highest percentages, with 30.96 % and 31.60 % being reached for the lightning and non–lightning storms, respectively. The exponential increase of ρ_{HV} values between the 0.8 to 0.94 bins, with the additional peak in the 0.84 – 0.86 bin is

again observed here for both the lightning and non–lightning storms, with 10.66 % and 6.2 % being obtained, respectively. However, only the lightning storms have an increase in the 0.98 – 1 bin, with 4.43 % being obtained here. Also, the lightning storms have a higher percentage of occurrences for ρ_{HV} values between 0.8 and 0.92, as compared to the non–lightning storms for these bins, whereas the non–lightning storms have higher percentages for all ρ_{HV} values ≥ 0.92, as compared to the lightning storms.

From Figure 7.15 (t–15), the results again look similar as previously, with the 0.92 – 0.94 ρ_{HV} bin yet again having the highest percentages, with the lightning storms obtaining 31.61 % and the non–lightning storms obtaining 31.69 %. The same features in terms of the peak in the 0.84 – 0.86 ρ_{HV} bin, as seen in the previous two figures, are again observed here with 11.21 % and 7.08 % being reached for the lightning and non–lightning storms respectively, as well as the peak in the 0.98 – 1 bins, with 4.01 % and 9.44 % being reached, respectively. Furthermore, the lightning storms again have higher percentages of the lower ρ_{HV} values, with the non–lightning storms having higher percentages for all bins ≥ 0.92.

At time t (Figure 7.16), one again sees the same approximate features as was observed in the previous times, however, here the lightning storms have higher percentages of the 0.92 – 0.94 ρ_{HV} than the non–lightning storm, with 34.89 % and 32.54 % being reached, respectively, which is the first time this occurred for the ρ_{HV} values. In addition, the total percentage of ρ_{HV} values ≤ 0.92 is now decreased as compared to the previous times, with only 44.88 % (as compared to 52.78 % at t–15) being observed for the lightning storms at time t.

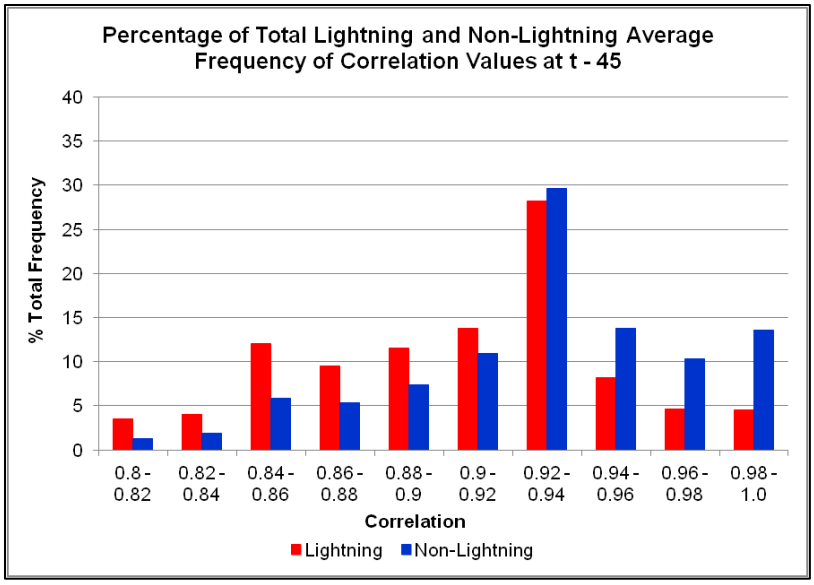

Figure 7.13: A graphical display of the percentage frequency distributions of the average ρ_{HV} values obtained for the lightning (red) and non–lightning (blue) storms for the various radar bins in the mixed–phase region at t–45.

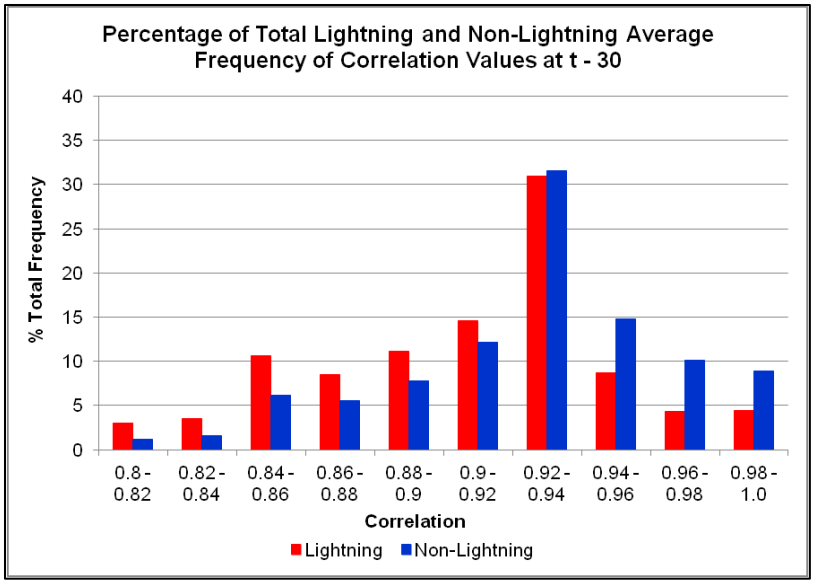

Figure 7.14: A graphical display of the percentage frequency distributions of the average ρ_{HV} values obtained for the lightning (red) and non–lightning (blue) storms for the various radar bins in the mixed–phase region at t–30.

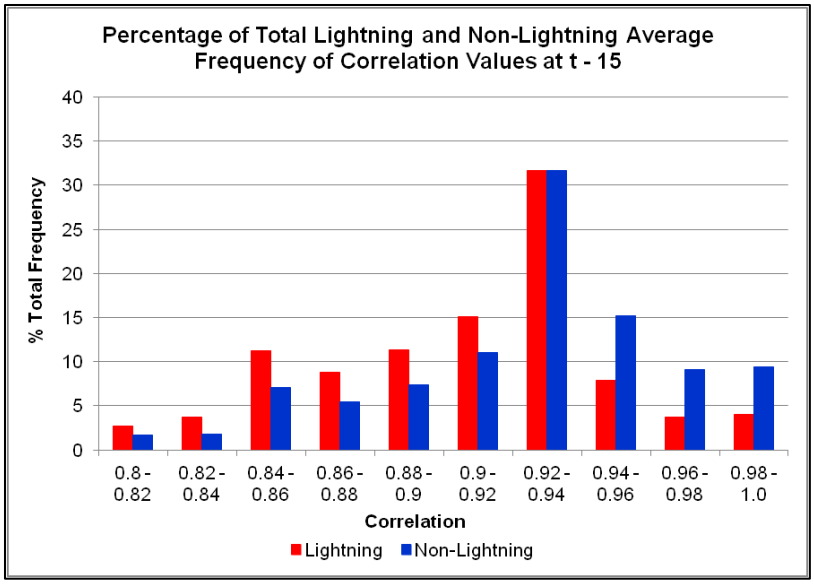

Figure 7.15: A graphical display of the percentage frequency distributions of the average ρ_{HV} values obtained for the lightning (red) and non–lightning (blue) storms for the various radar bins in the mixed–phase region at t–15.

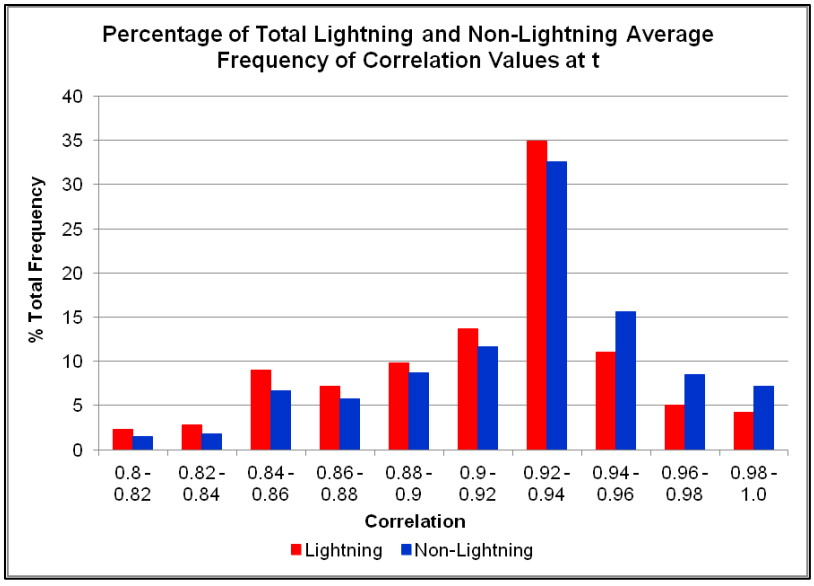

Figure 7.16: A graphical display of the percentage frequency distributions of the average ρ_{HV} values obtained for the lightning (red) and non–lightning (blue) storms for the various radar bins in the mixed–phase region at time t.

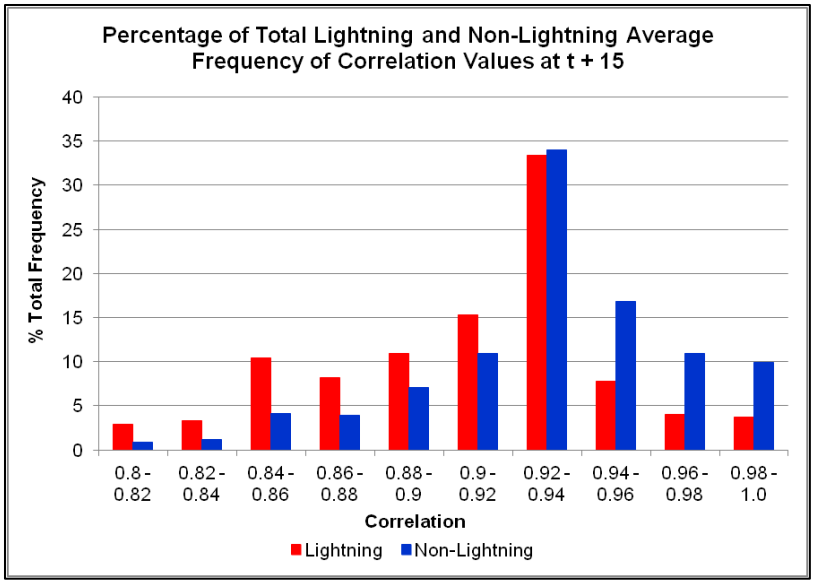

Figure 7.17: A graphical display of the percentage frequency distributions of the average ρ_{HV} values obtained for the lightning (red) and non–lightning (blue) storms for the various radar bins in the mixed–phase region at t+15.

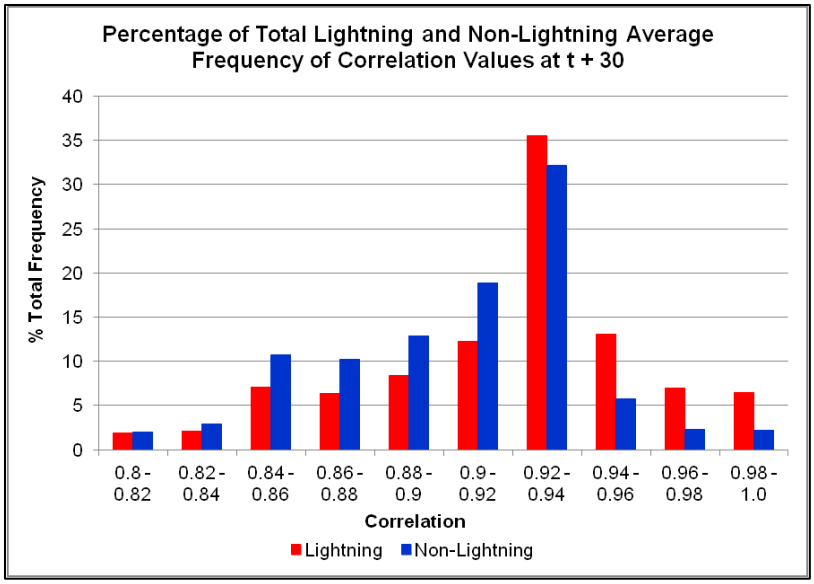

Figure 7.18: A graphical display of the percentage frequency distributions of the average ρ_{HV} values obtained for the lightning (red) and non–lightning (blue) storms for the various radar bins in the mixed–phase region at t+30.

For the non–lightning storms there is a small increase in ρ_{HV} values ≤ 0.92 here, with 36.1 % being reached (with 34.55 % at t–15). Both storm types again have the exponential increase between 0.8 and 0.94, with the peak in 0.84 – 0.86, with 9 % and

6.68 % being reached for the lightning and non–lightning storms respectively. In addition, the lightning storms have higher percentages for the 0.8 – 0.94 bins, with the non–lightning storms only having higher percentages for the 0.94 – 1 bins. Therefore at time t, one can see that the 0.92 – 0.94 peak is larger for the lightning storms as compared to the non–lightning storms. The peak in the ρ_{HV} values ≥ 0.94 is no longer visible for either of the storm types.

Figure 7.17 displays the results for t+15, with approximately the same distribution being observed once again, however it is clear there are fewer ρ_{HV} values ≥ 0.94 for the lightning storms than were observed at time t, thus indicating that the lower ρ_{HV} values are increasing. The non–lightning storms again have the highest percentage for the 0.92 – 0.94 bin (as was seen at t–45 and t–30), with 33.98 % being reached for the non–lightning storms and 33.42 % being reached for the lightning storms. The peak in the 0.84 – 0.86 bin is still visible, however the peak is much larger for the lightning storms than for the non–lightning storms, with 10.47 % and 4.18 % being obtained, respectively. Both storms have a decrease in ρ_{HV} values ≥ 0.94. Finally, the lightning storms have more ρ_{HV} values between 0.8 and 0.92 than the non–lightning storms, with 50.99 % and 28.34 % being reached respectively. Thus the lightning storms have almost double the percentage of ρ_{HV} values between 0.8 – 0.92 than the non–lightning storms have at this time.

At t+30, there is an unexpected change in the distribution of the data, with the non–lightning storms now having more ρ_{HV} values between 0.8 and 0.92, with 57.57 % being obtained (which is a 29.23 % increase) and the lightning storms now only obtaining 38.02 % (a 12.97 % decrease). The lightning storms now have more 0.92 – 0.94 ρ_{HV}

values than the non–lightning storms, with 35.5 % and 32.19 % being obtained, respectively, and the non–lightning storms now have a larger peak for the 0.84 – 0.86 bin size, which is less prominent (although still observed) for the lightning storms. The lightning storms now seem to have more precipitation particles that have equal vertical and horizontal dimensions as can be seen with the higher percentages of ρ_{HV} values close to 1, and the non–lightning storms now have more particles that do not have equal dimensions, as seen by the 0.8 to 0.90 ρ_{HV} values.

From these six figures, there is an overall exponential increase in ρ_{HV} values between 0.8 and 0.92. The maximum percentages are reached for the 0.92 – 0.94 ρ_{HV} bin, after which there is an approximate exponential decrease in values for both the lightning and non–lightning storms. Before time t, the non–lightning storms consistently obtained lower percentages for the 0.92 – 0.94 bin, but at time t and t+30, the lightning storms had higher percentages for this bin as compared to the non–lightning storms. The lightning storms had larger total percentages of ρ_{HV} values $\leq$ 0.92 from t–45 through t+15, with the non–lightning storms having larger total percentages for ρ_{HV} values $\geq$ 0.94 during this time frame, but between t+15 and t+30, these two fields changing around, with the lightning storm now having larger percentages for ρ_{HV} values $\geq$ 0.94 and the non–lightning storms having larger percentages for ρ_{HV} values $\leq$ 0.92.

The remainder of this chapter will be focused on the notched box plots, which are variations on the usual box and whisker plots shown for the MSG interest fields, and is a way of indicating whether two data sets are statistically significantly different. These notched box plots will be shown for both the radar fields (as seen above, however for the following plots, the time trends of the frequency of occurrence will be seen, instead of the

percentage of occurrence) as well as for the satellite interest fields. Therefore, due to the fact that the above statistics for the radar fields have already been discussed, the notched plots will not be discussed in much detail, and because the box plots of the MSG interest fields were seen in chapter 5, this will also not be discussed in much detail. Thus these plots will only be shown here in order to illustrate that the lightning and non–lightning storms were statistically different.

An example of how a notched–box plot is analyzed, is shown in Figure 7.19. Here, the box represents the IQR (25 % to 75 %) of the data, with the horizontal lines that divides the box into two sections being the median value obtained for the data set (McGill *et al*., 1978; Wilks, 2006). The larger these IQR boxes are, the higher the spread in the data are. The upper whisker is the 75^{th} percentile + 1.5 x IQR and the lower whisker is the 25^{th} percentile – 1.5 x IQR, thus these will be longer the more spread (and accordingly the larger the IQR) there is. Any values larger than the upper whisker and smaller than the lower whisker are seen as "outliers" and shown as a circle (although in Figure 7.19, these outliers are shown as crosses). The biggest difference between these notched box plots and "normal" box plots is the notch found in the IQR. The notches extend to $+/-1.58\ IQR/\sqrt{N}$ (N is the number of data points). If these notches do not overlap for different datasets, then the data sets are significantly different at the 95^{th} percent confidence level (McGill *et al*., 1978). In addition, these notches will be smaller if the spread (and thus the IQR) is smaller and vice versa. It should be noted here that the blue diamond that signifies the mean of the data set seen in Figure 7.19, is not displayed in the results shown below.

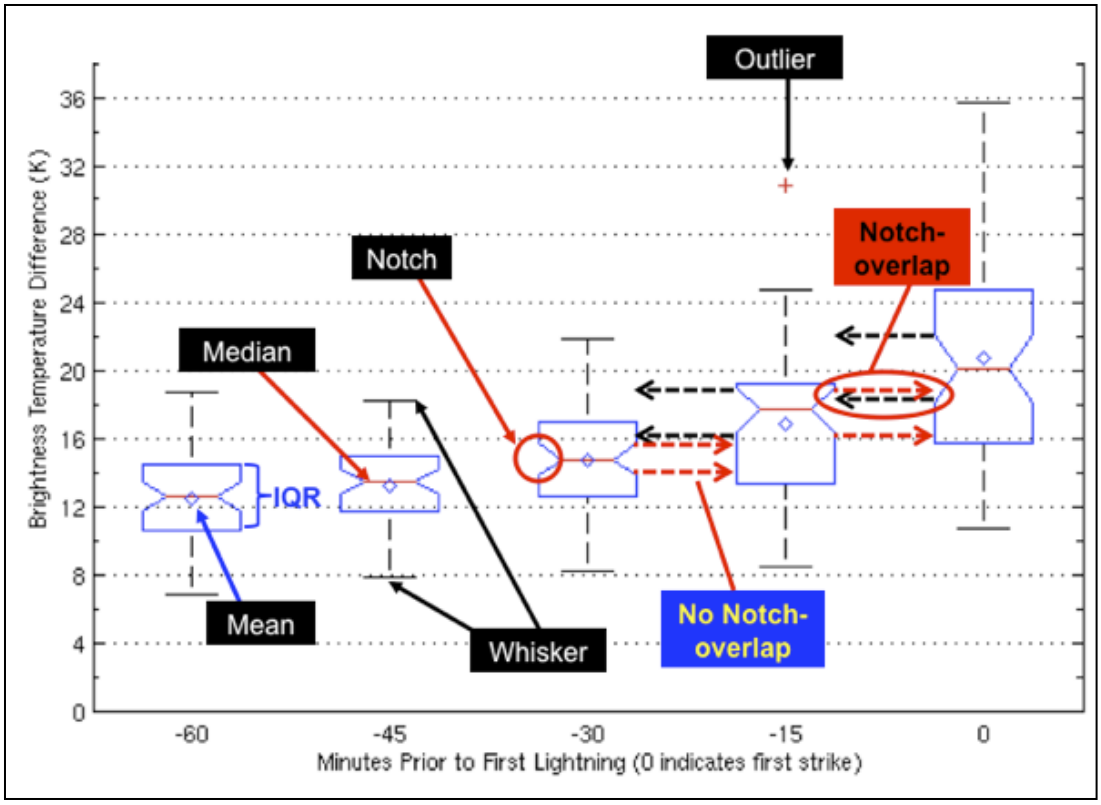

Figure 7.19: Notched box plot explanation (from Harris *et al*., 2010). Refer to text for an explanation on how the plot is interpreted.

The following Figures 7.20 through 7.23 show the notched box plots obtained for the Z_H radar variable, but shows the number of occurrences of the various bin sizes (and not the percentage of occurrence) for the lightning (red) and non–lightning (blue) for t–45 through t+30 for the mixed–phase region. Please note the different y–axis labels here. The figures are for the following bin sizes: Figure 7.20 shows the 10 dBZ – 15 dBZ bin on the left and the 15 dBZ – 20 dBZ bin on the right; Figure 7.21 shows the 20 dBZ – 25 dBZ bin on the left and the 25 dBZ – 30 dBZ bin on the right; Figure 7.22 shows the 30 dBZ – 35 dBZ bin on the left and the 35 dBZ – 40 dBZ bin on the right and Figure 7.23 shows the 40 dBZ – 45 dBZ bin on the left and the 45 dBZ – 50 dBZ bin on the right.

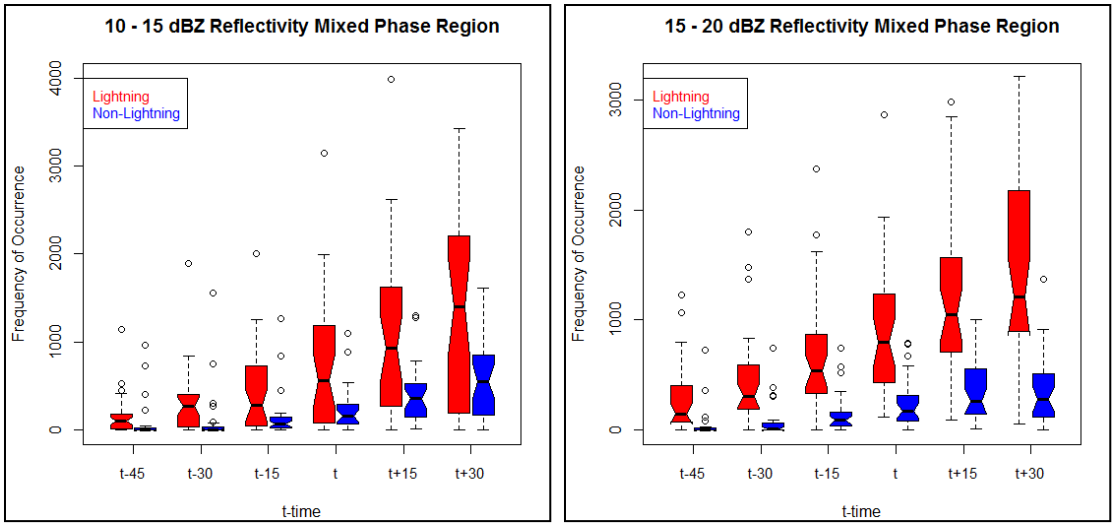

Figure 7.20: Notched box plots of the 10 – 15 dBZ (left) and 15 – 20 dBZ (right) Z_H values obtained for the lightning (red) and non–lightning (blue) storms from t–45 through t+30.

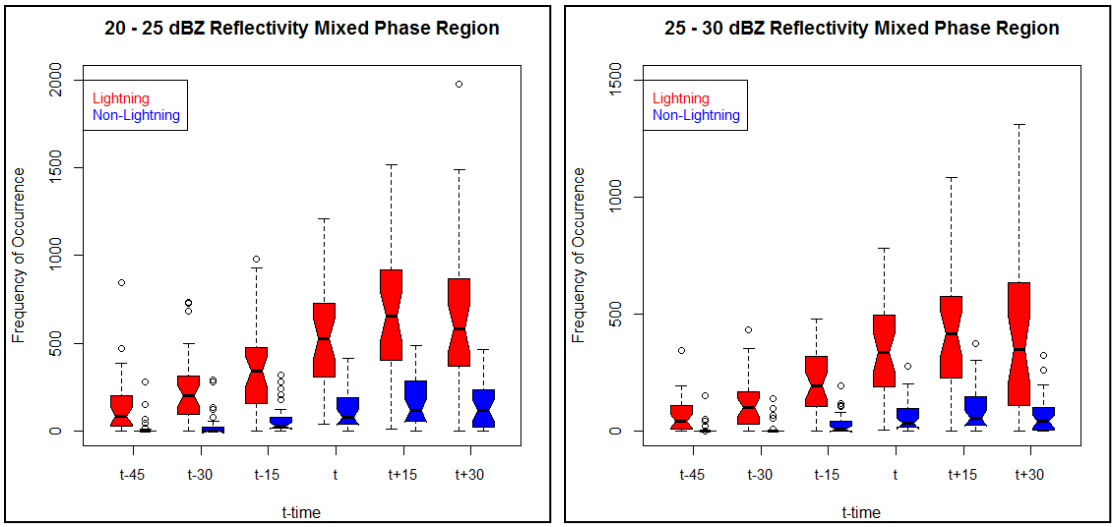

Figure 7.21: Notched box plots of the 20 – 25 dBZ (left) and 25 – 30 dBZ (right) Z_H values obtained for the lightning (red) and non–lightning (blue) storms from t–45 through t+30.

These plots are similar to Figures 7.1 through 7.6, however here it is the actual number of occurrences that is shown instead of the percentage, as well as the fact that here each plot has the entire time trend in one plot. Again, the main reason for doing this is to show that the lightning and non–lightning storms are significantly different, with

higher occurrences consistently being obtained for the lightning storms, due to these storms having higher cloud–tops, and thus more data points, than the non–lightning storms. This is important, as one needs more ice, graupel and supercooled liquid water in the mixed–phase region for electrification and CG lightning to occur.

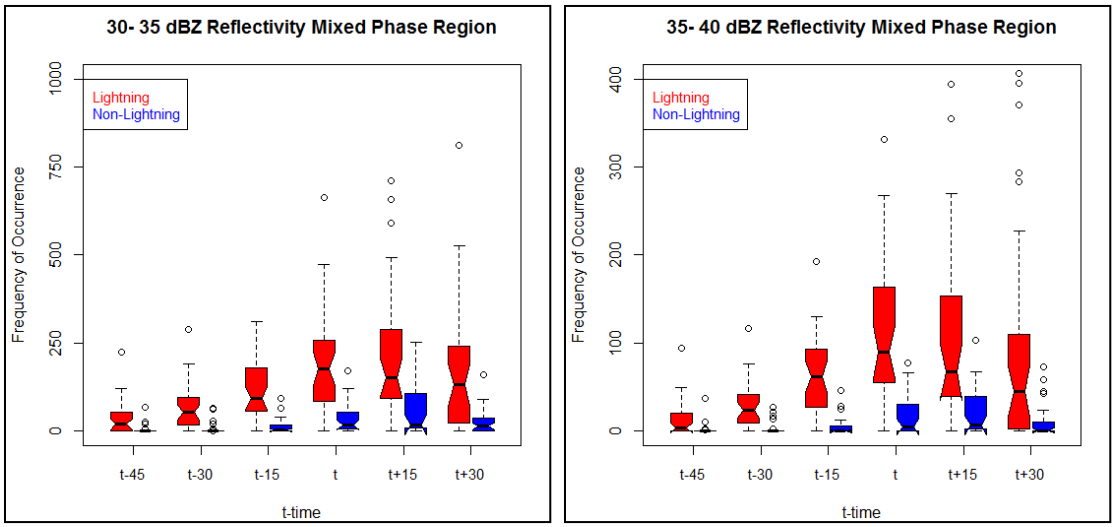

Figure 7.22: Notched box plots of the 30 – 35 dBZ (left) and 35 – 40 dBZ (right) Z_H values obtained for the lightning (red) and non–lightning (blue) storms from t–45 through t+30.

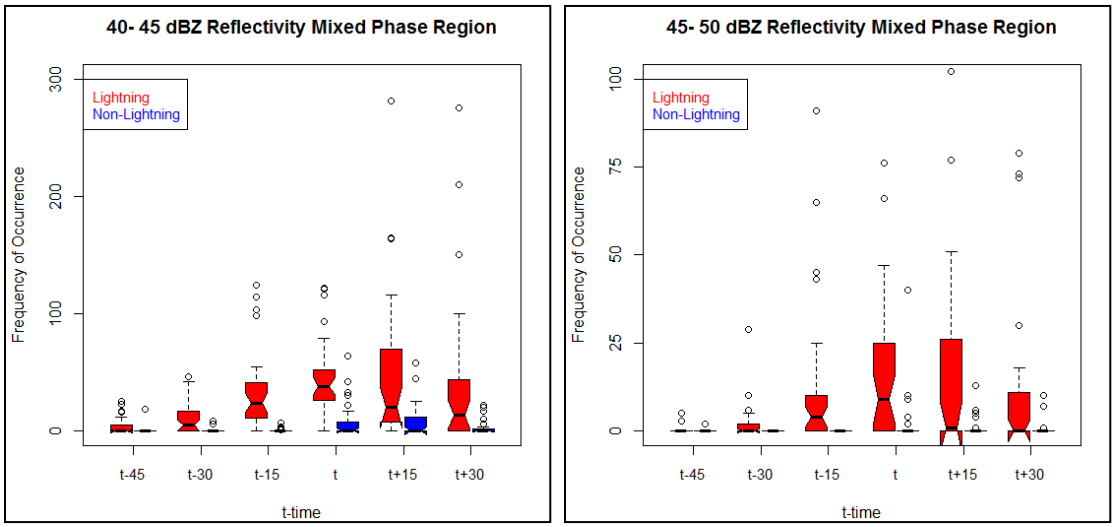

Figure 7.23: Notched box plots of the 40 – 45 dBZ (left) and 45 – 50 dBZ (right) Z_H values obtained for the lightning (red) and non–lightning (blue) storms from t–45 through t+30.

These four figures show that none of the lightning and non–lightning storms notches overlap, even though the lightning storms consistently have larger spread (indicated by the longer IQRs). It is clear that both the lightning and non–lightning storms have outliers, but this does not seem to influence the results much. It is interesting to note that the IQR of the lightning storms are consistently located at higher frequencies as compared to the non–lightning storms, with the separation between the notches increasing with every 15 minutes that pass from t–45 to time t. It is also clear from Figure 7.23 that the non–lightning storms have very few 40 dBZ to 50 dBZ Z_H values in the mixed–phase region, which indicates that the non–lightning storms did not have enough large water drops, graupel and/or hail present for electrification to occur to the point of initiating CG lightning. The spread increases as one approaches time t, through t+30, for both the lightning and non–lightning storms and that the lightning storms consistently have much higher frequencies for all the Z_H bins, particularly for the lower Z_H values. Moreover, the lower Z_H values of 10 dBZ to 20 dBZ occur the most frequently of all the bins, which is not surprising. From these plots, it is clear that the Z_H values of the lightning and non–lightning storms were statistically different at the 95^{th} percent confidence level.

Figures 7.24 through 7.29 display the notched box plots obtained for the Z_{DR} radar variable and show the frequency of occurrence of the various bin sizes for the lightning (red) and non–lightning (blue) for t–45 through t+30 for the mixed–phase region. Please note the different y–axis labels for these figures. The figures are for the following bin sizes: Figure 7.24 shows the –3 dB to –2.5 dB bin on the left and the –2.5 dB to –2 dB bin on the right; Figure 7.25 shows the –2 dB to –1.5 dB bin on the left

and the –1.5 dB to –1 dB bin on the right; Figure 7.26 shows the –1 dB to –0.5 dB bin on the left and the –0.5 dB to 0 dB bin on the right; Figure 7.27 shows the 0 dB to 0.5 dB bin on the left and the 0.5 dB to 1 dB bin on the right; Figure 7.28 shows the 1 dB to 1.5 dB bin on the left and the 1.5 dB to 2 dB bin on the right and Figure 7.29 shows the 2 dB to 2.5 dB bin on the left and the 2.5 dB to 3 dB bin on the right.

For these figures one can see that although the notches do not overlap at any point, the variation between the lightning and non–lightning storms' Z_{DR} values are less than was observed for the Z_H fields. It is interesting that the –3 dB to –2 dB bins show a slow increase up to t–15, where after there is a decrease in the spread for the lightning storms, which is not necessarily seen for the non–lightning storms. In addition, the –1 dB to 1 dB fields have much higher frequencies than the other fields for both the lightning and non–lightning storms, with the highest frequencies occurring for the 0 dB to 0.5 dB bin. However, it is important to note that the large negative Z_{DR} values ($Z_{DR} < –2.0$ dB) could be due to radar beam filling and side lobe errors, as well as due to random noise.

The 1.5 dB to 2.5 dB bins have more variation than the other fields, especially for the lightning storms, where there is an increase in the occurrence of 1.5 dB to 2 dB values between t–45 and time t, where after there's a decrease to t+15 and then another increase in values at t+30 in terms of the 75^{th} percentile level as well as for the median values, being reached. The 2 dB to 2.5 dB bin has an increase between t–45 and t–30, with a decrease between t–30 and t–15, with another increase before time t is reached, followed by a decrease after this time. These higher frequencies of Z_{DR} values greater than

approximately 1 dB could be indicative of supercooled liquid water being present in these storms, which is important for electrification of the storms.

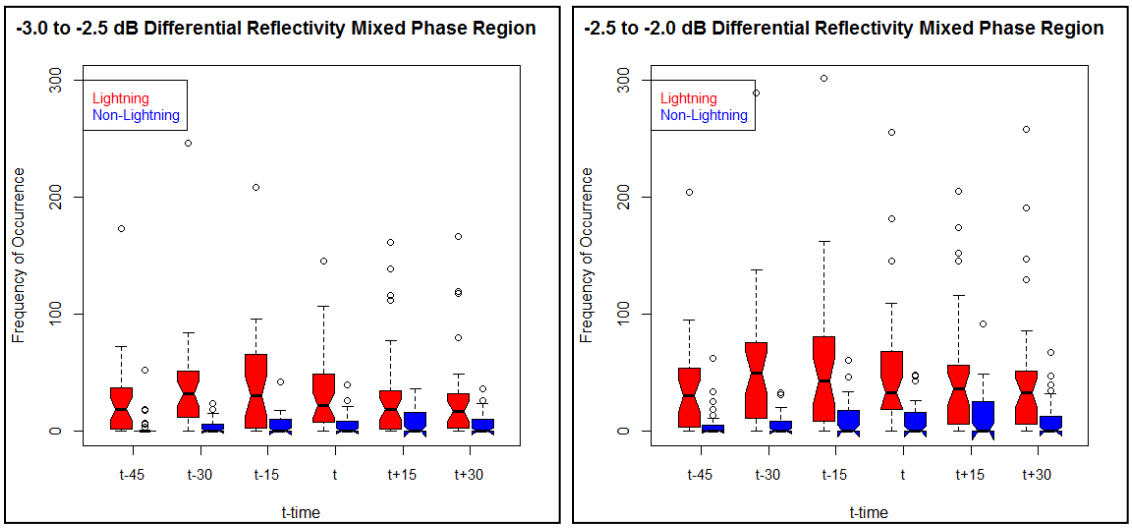

Figure 7.24: Notched box plots of the –3 to –2.5 dB (left) and –2.5 to –2 dB (right) Z_{DR} values obtained for the lightning (red) and non–lightning (blue) storms from t–45 through t+30.

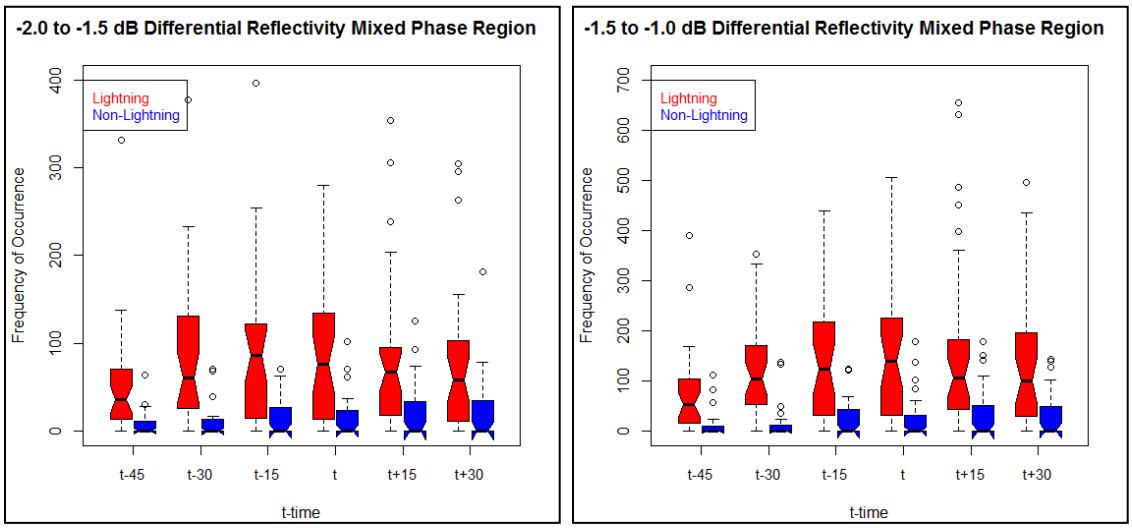

Figure 7.25: Notched box plots of the –2 to –1.5 dB (left) and –1.5 to –1 dB (right) Z_{DR} values obtained for the lightning (red) and non–lightning (blue) storms from t–45 through t+30.

Finally, the non–lightning storms had very low frequencies of Z_{DR} values ≥ 2 dB, as compared to the lightning storms indicating that there are fewer supercooled rain drops for these storms. From these figures it is clear that in terms of the Z_{DR} field, the lightning and non–lightning storms were statistically different at the 95th percent confidence level.

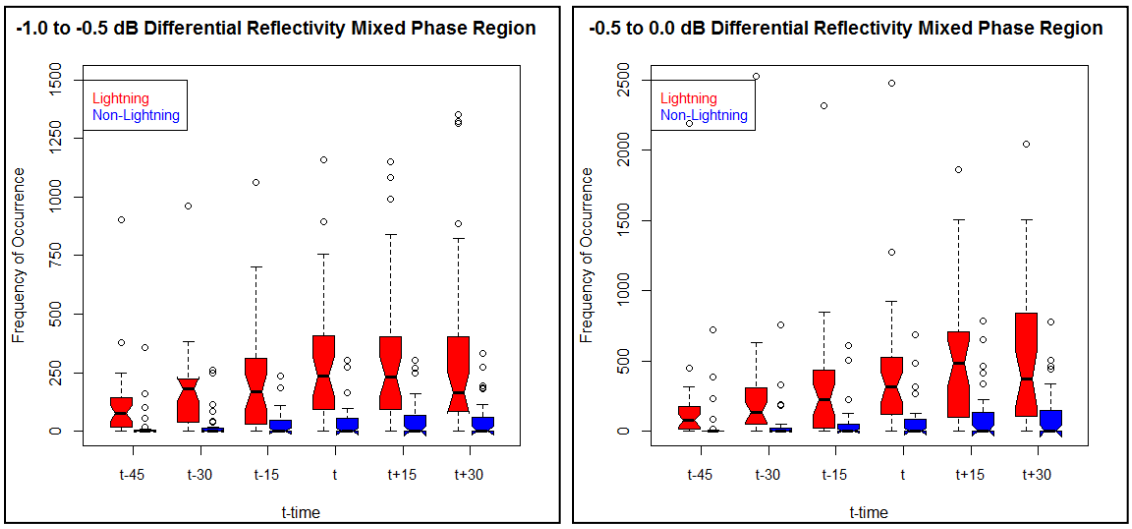

Figure 7.26: Notched box plots of the –1 to –0.5 dB (left) and –0.5 to 0 dB (right) Z_{DR} values obtained for the lightning (red) and non–lightning (blue) storms from t–45 through t+30.

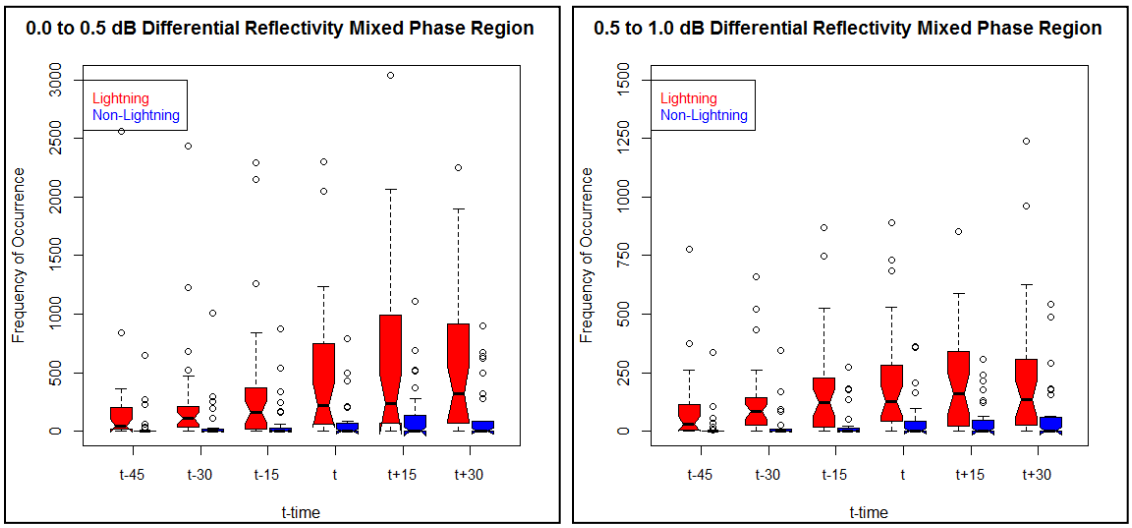

Figure 7.27: Notched box plots of the 0 to 0.5 dB (left) and 0.5 to 1 dB (right) Z_{DR} values obtained for the lightning (red) and non–lightning (blue) storms from t–45 through t+30.

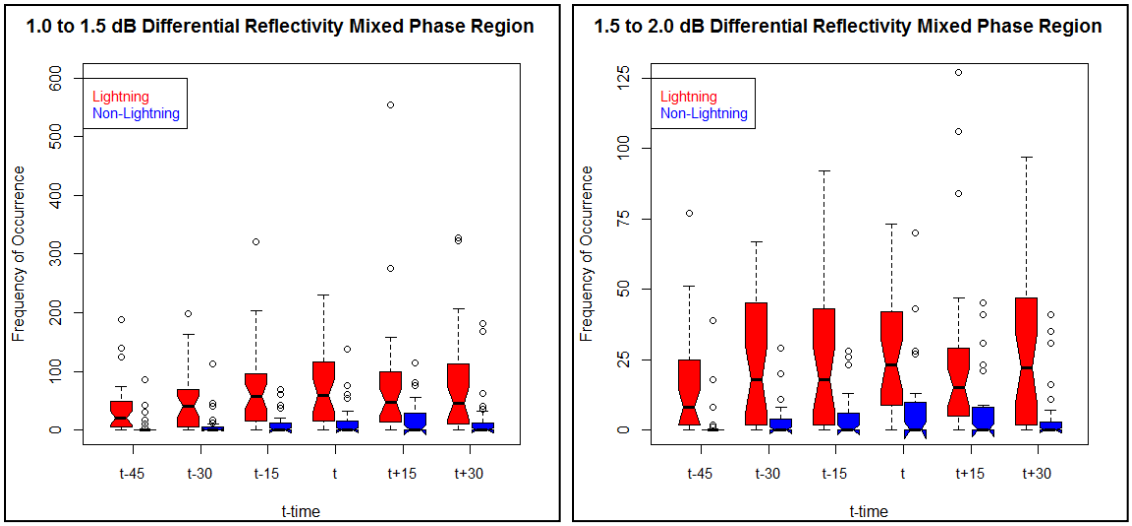

Figure 7.28: Notched box plots of the 1 to 1.5 dB (left) and 1.5 to 2 dB (right) Z_{DR} values obtained for the lightning (red) and non–lightning (blue) storms from t–45 through t+30.

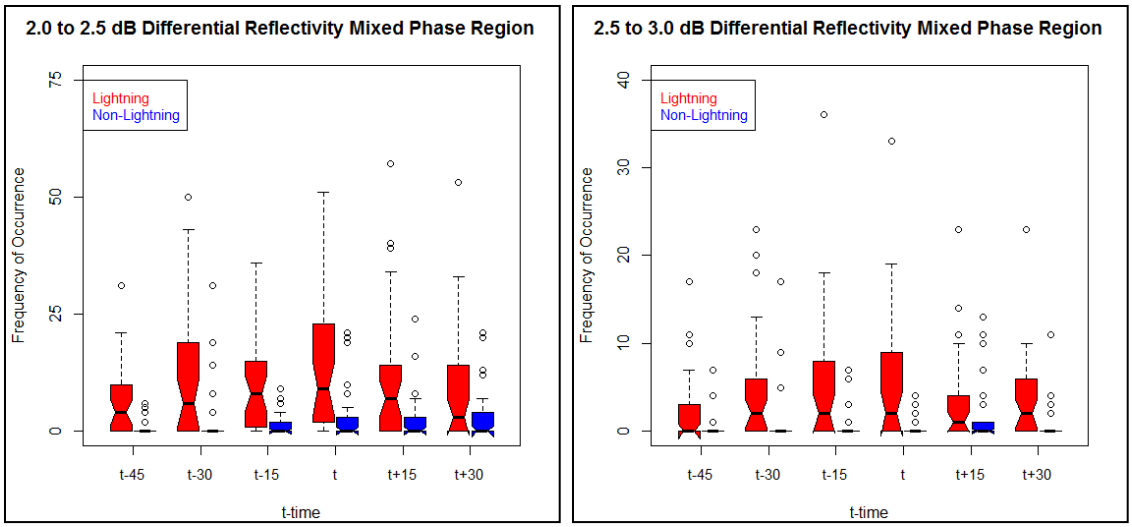

Figure 7.29: Notched box plots of the 2 to 2.5 dB (left) and 2.5 to 3 dB (right) Z_{DR} values obtained for the lightning (red) and non–lightning (blue) storms from t–45 through t+30.

Figures 7.30 through 7.34 display the notched box plots of the ρ_{HV} values obtained for the lightning (red) and non–lightning (blue) storms from t–45 through t+30. Note the different y–axis labels for these figures. The figures are for the following bin sizes: Figure 7.30 shows the 0.8 to 0.82 bin on the left and the 0.82 to 0.84 bin on the

right; Figure 7.31 shows the 0.84 to 0.86 bin on the left and the 0.86 to 0.88 bin on the right; Figure 7.32 shows the 0.88 to 0.9 bin on the left and the 0.9 to 0.92 bin on the right; Figure 7.33 shows the 0.92 to 0.94 bin on the left and the 0.94 to 0.96 bin on the right; and Figure 7.34 shows the 0.96 to 0.98 bin on the left and the 0.98 to 1 bin on the right.

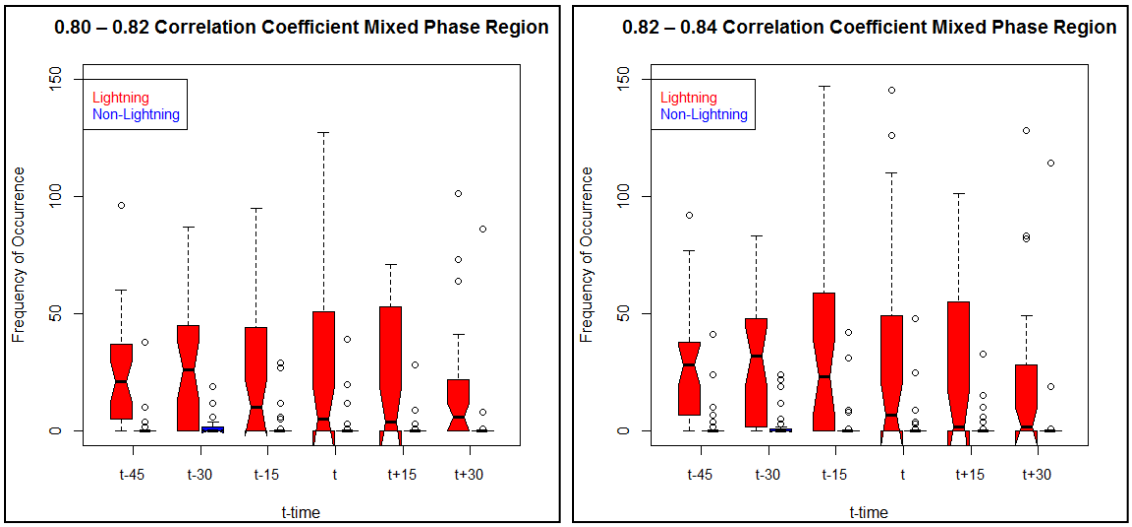

Figure 7.30: Notched box plots of the 0.8 – 0.82 (left) and 0.82 to 0.84 (right) ρ_{HV} values obtained for the lightning (red) and non–lightning (blue) storms from t–45 through t+30.

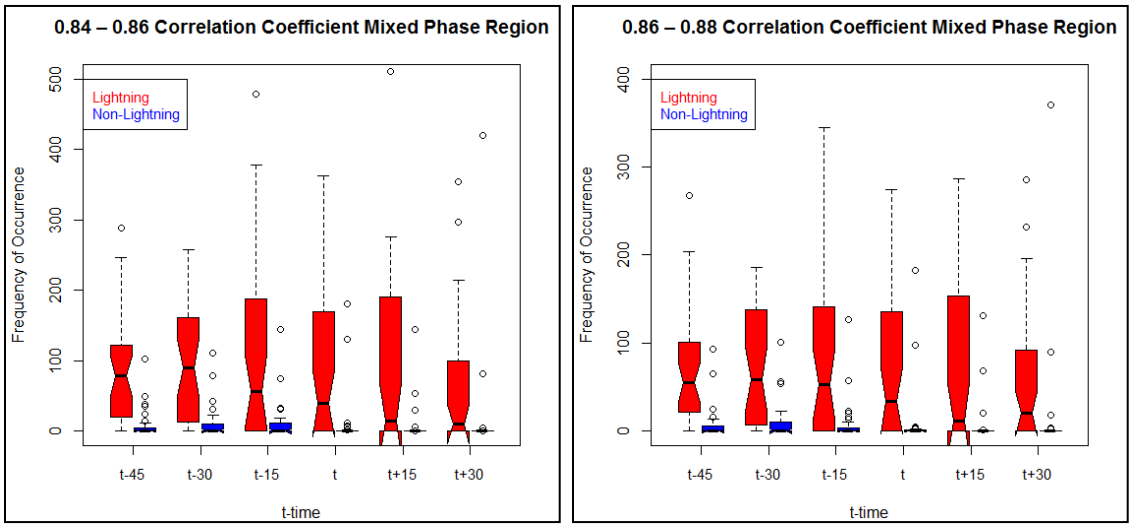

Figure 7.31: Notched box plots of the 0.84 – 0.86 (left) and 0.86 to 0.88 (right) ρ_{HV} values obtained for the lightning (red) and non–lightning (blue) storms from t–45 through t+30.

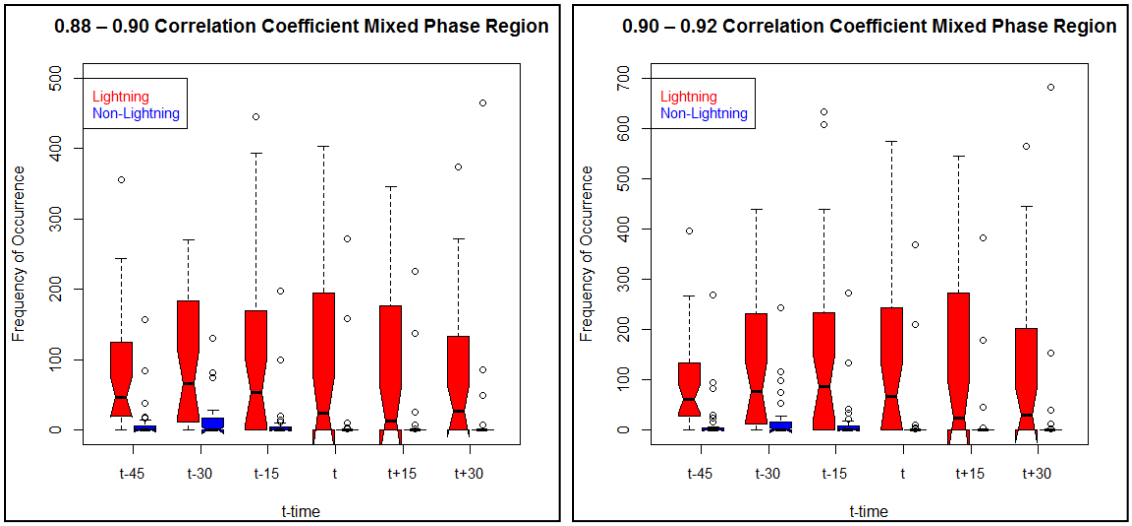

Figure 7.32: Notched box plots of the 0.88 – 0.9 (left) and 0.9 to 0.92 (right) ρ_{HV} values obtained for the lightning (red) and non–lightning (blue) storms from t–45 through t+30.

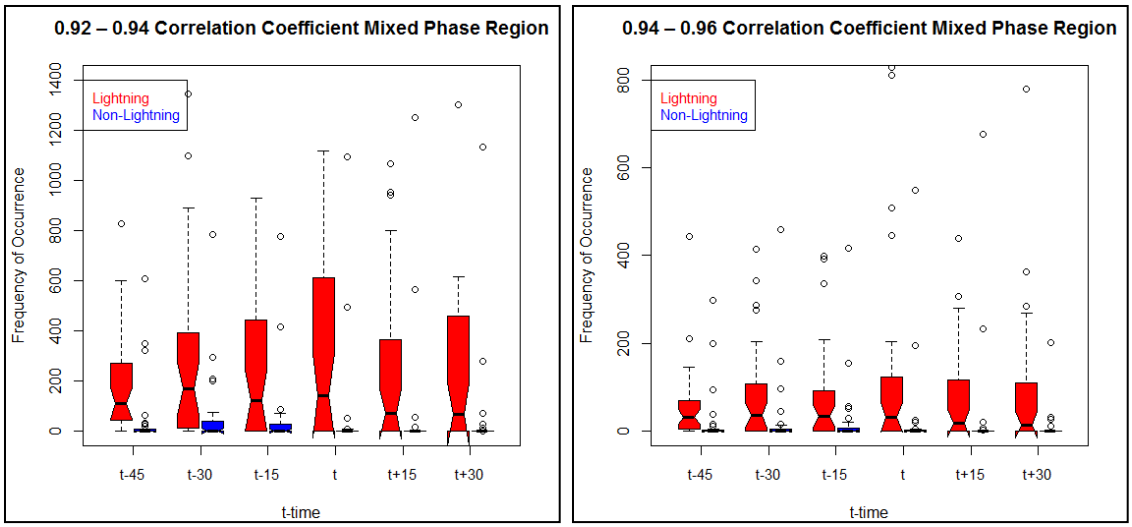

Figure 7.33: Notched box plots of the 0.92 – 0.94 (left) and 0.94 to 0.96 (right) ρ_{HV} values obtained for the lightning (red) and non–lightning (blue) storms from t–45 through t+30.

These figures are interesting in the sense that for all the ρ_{HV} values, the lightning storms have a much higher occurrence than the non–lightning storms, especially for the ρ_{HV} values ≤ 0.94. This indicates that the lightning storms have much more larger water

drops, as well as graupel and hail. Furthermore, the spread of the lightning storms is smaller for all ρ_{HV} values ≥ 0.94.

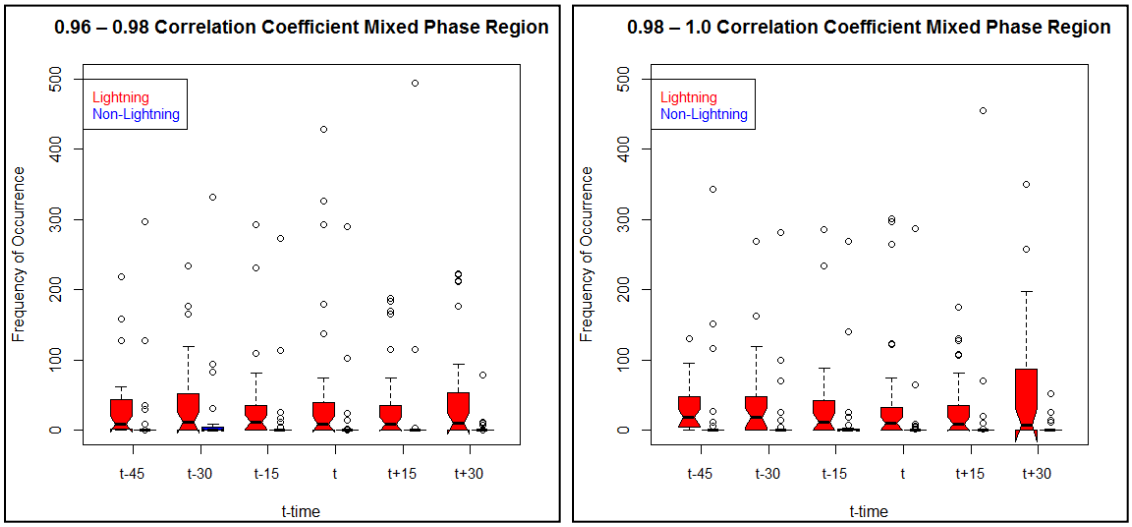

Figure 7.34: Notched box plots of the 0.96 – 0.98 (left) and 0.98 to 1 (right) ρ_{HV} values obtained for the lightning (red) and non–lightning (blue) storms from t–45 through t+30.

In contrast, the largest spread seems to occur at t–15 and time t for the lightning storms for all ρ_{HV} values. Note the non–lightning storms' ρ_{HV} values ≥ 0.94 occur at much lower frequencies than for the lightning storms, implying that the non–lightning storms had very few particles with equal horizontal and vertical dimensions, such as graupel, hail and/or smaller liquid drops. Both of these are important for the electrification of storms, and thus this is an additional confirmation that if electrification occurred in the non–lightning storms, it was not enough to produce CG lightning.

In addition, it seems as though for all values ≥ 0.94, there are more outliers for both the lightning and non–lightning storms, indicating that although both storm types had lower frequencies of these ρ_{HV} values, some of the storms had higher frequencies, leading to these outliers being obtained. Finally, as is clear, none of the notches of the

lightning and non–lightning storms overlap, indicating that the ρ_{HV} fields for these two storm types are statistically different at the 95th percent confidence level.

7.2. Statistical Analysis of MSG Satellite Interest Fields:

The remainder of this chapter will focus on the MSG 10.8 μm T_B and the interest fields discussed earlier. Here, approximately the same results as in chapter 5 will be shown, but displayed as notched box plots in order to verify whether these fields are statistically significantly different for the lightning and non–lightning storms. Due to the fact that these fields were discussed in detail in chapter 5, the discussion here will be brief, although where necessary, more detail will be given. The interpretation of the notched box plots are similar to .Figure 7.19.

Figures 7.35 through 7.37 display the notched box plot results for the 10.8 μm T_B field, the 15 minute 6.2 – 7.3 μm T_B interest field (left) and the 30 minute 6.2 – 7.3 μm T_B interest field (right) as well as the 15 minute 6.2 – 7.3 μm T_B interest field (left) and 30 minute 6.2 – 7.3 μm T_B interest field (right), respectively, all indicating the change in updraft strengths, with the 10.8 μm T_B field indicating the main updraft strengths for the lightning (red) and non–lightning (blue) storms. Figures 7.38 displays the notched box plot results for the 6.2 – 7.3 μm T_B interest field (left) and the 6.2 – 10.8 μm T_B interest field (right), with both plots indicating the change in cloud depth for the lightning (red) and non–lightning (blue) storms. Finally, Figures 7.39 and 7.40 display the notched box plot results for the (8.7 – 10.8 μm) – (10.8 – 12.0 μm) T_B tri–spectral interest field (left) and the 15 minute (8.7 – 10.8 μm) – (10.8 – 12.0 μm) T_B tri–spectral interest field (right) as well as the 8.7 – 10.8 μm T_B interest field (left) and the 15 minute 8.7 – 10.8 μm T_B

interest field (right), respectively, with all indicating the initiation of cloud–top glaciation for the lightning (red) and non–lightning (blue) storms. The same trends and critical values mentioned in chapters 3 and 5 will be applicable here.

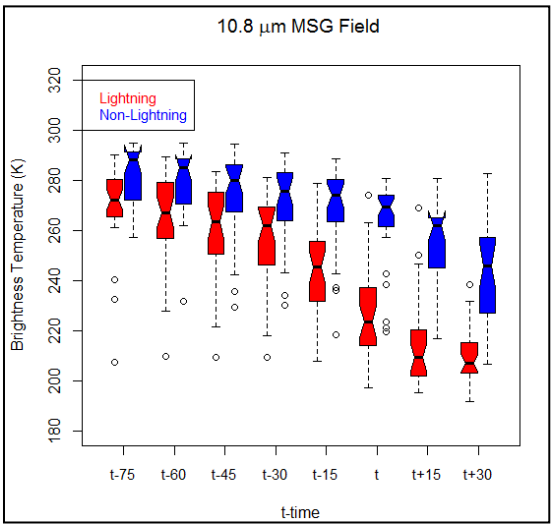

Figure 7.35: Notched box plots of the 10.8 μm T_B field showing the main updraft strength features between lightning (red) and non–lightning (blue) storms from t–75 to t+30.

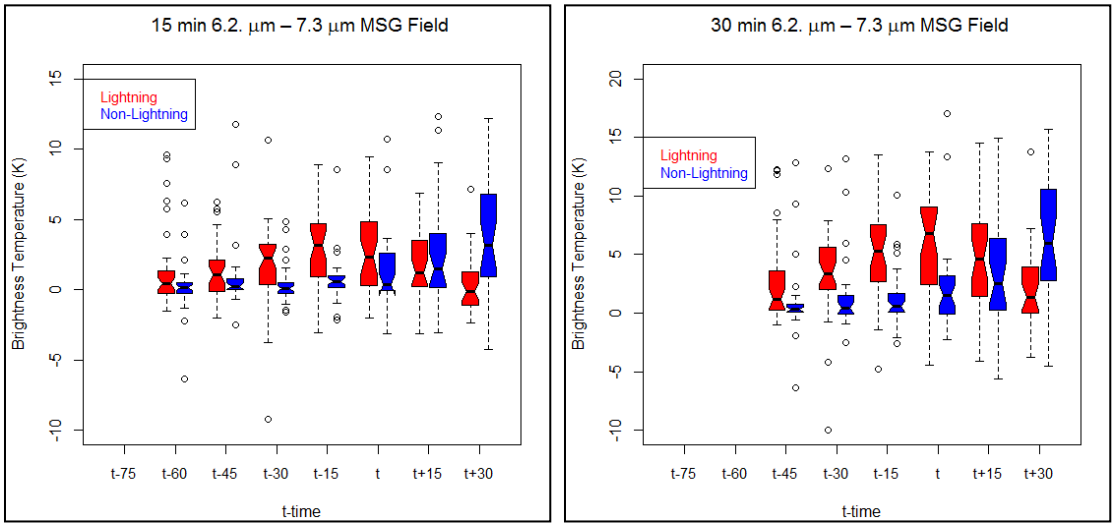

Figure 7.36: Notched box plots of the 15 minute 6.2 – 7.3 μm T_B interest field (left) and the 30 minute 6.2 – 7.3 μm T_B interest field (right) showing updraft strength features between lightning (red) and non–lightning (blue) storms from t–75 to t+30.

The 10.8 μm T_B notched box plot (Figure 7.35) shows that the lightning storms' T_B values decrease faster as compared to the non–lightning storms which means that the lightning storms' updraft strength is increasing much faster, especially from t–45 onwards. As is clear from this figure, the lightning and non–lightning storms' notches do not overlap at any time from t–75 through t+30, although there is some overlap of the IQR from t–75 to t–30. However, the spread of both storm types is relatively small, with the non–lightning storms having a smaller spread compared to the lightning storms, especially as time t is approached. Furthermore, as time t is approached, the lightning and non–lightning storm results diverge, with a large separation occurring at time t. Thus, the 10.8 μm T_B field for the lightning and non–lightning storms is statistically significantly different at the 95th percentile level because the notches to not overlap. This indicates that this field is important to use if one wants to obtain differences between these two storm types.

In Figure 7.36 it is evident that some of the notches do overlap. The 15 minute 6.2 – 7.3 μm T_B interest field (left in the figure) have notches that overlap at t–60 and t+15, implying that for these two times, the two groups of storm types are not statistically different. However, for the t–45 through time t, as well as t+30, the storms' notches do not overlap, indicating that for these periods, the storms are statistically significantly different at the 95th percentile level. One can also see here that the lightning storms show an increase in spread from t–60 through time t, with a decrease in spread after this time. The non–lightning storms on the other hand only show an increase in spread after t–15, with no decrease being visible after this time. There are also more outliers visible for the earlier times, up to t–30 for the lightning storms, with more outliers being visible for the

non–lightning storms for the entire period. The 30 minute 6.2 – 7.3 μm T_B interest field (right) seen in Figure 7.36, also show some overlap between the storms, but only at t+15, implying that for all times except t+15, the lightning and non–lightning storms' 30 minute 6.2 – 7.3 μm T_B interest fields are statistically independent at the 95th percentile level. Here the lightning storms again have a larger spread than was obtained for the non–lightning storms, except for t+15, where both storm types seem to have the approximate same spread, with this spread increasing as time t is approached. In addition, the separation between the two storm types increases between t–45 and time t, where after this separation decreases.

The spread in the distribution for the fields in Figures 7.36, as well as others, is the result of a larger distribution of values. Increased spread, especially after time t also implies very limited cloud development for some of the 30 non–lightning events, and hence increased variability in the interest field values. In contrast, when the distributions are small, a large fraction of the events possessed similar characteristics.

The 15 minute 10.8 μm T_B interest field seen in Figure 7.37 shows that the spread of the lightning storms once again increases from t–60 through time t, where after this spread decreases with this spread consistently being larger than the spread obtained for the non–lightning storms. The non–lightning storms however have an increasing spread from t–45 through t+30. One can see that there is notch–overlap at t–60, t–45 and t+15, but for all other times, the notches do not overlap. For all times then from t–30 through time t, as well as at t+30, the 15 minute 10.8 μm T_B interest fields for the lightning and non–lightning storms are significantly different at the 95th percentile level. For the 30 minute 10.8 μm T_B interest field (seen on the right in Figure 7.37), the lightning

storms again have more spread than the non–lightning storms for all times, however the lightning storms have fewer outliers. In addition, between t–30 and t+15 there is no overlap of notches, however overlap is observed at t–45 and t+30. Thus, for the period between t–30 and t+15, the two storm types are once again statistically significantly different at the 95th percentile level.

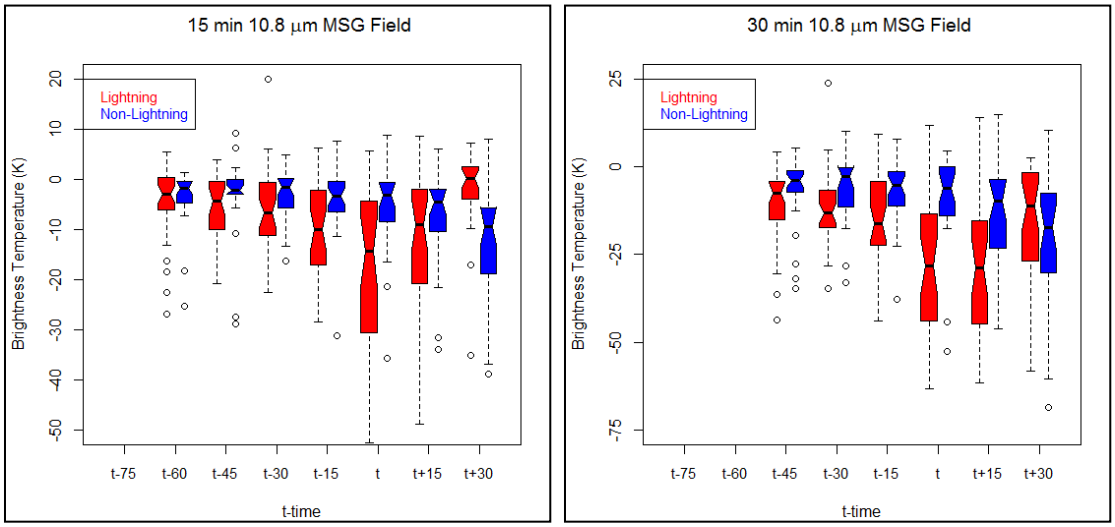

Figure 7.37: Notched box plots of the 15 minute 10.8 μm T_B interest field (left) and the 30 minute 10.8 μm T_B interest field (right) showing updraft strength features between lightning (red) and non–lightning (blue) storms from t–75 to t+30.

These three figures imply the MSG interest fields showing an increase in updraft strength, the T_B values and T_B difference values of the lightning and non–lightning storms are significantly different for all times between t–30 and time t, especially for the time–trend fields. This means that there is a 30 minute period where these interest fields can show important differences between the lightning and non–lightning storms discussed here, and be used in a predictive sense for the occurrence of CG lightning.

The 6.2 – 7.3 μm T_B interest field (left) and the 6.2 – 10.8 μm T_B interest field (right) seen in Figure 7.38 both indicate vertical cloud growth. For both these interest

fields it is clear that no overlap occurs between the lightning and non–lightning storms at any time, thus signifying that these two storm types are different at the 95th percentile level. For the 6.2 – 7.3 μm T_B interest field, one can see that the two storms diverge from t–75, with the lightning storms having more spread at t–30 and t–15 as compared to the non–lightning storms, but the non–lightning storms have more spread at t+15 and t+30. The separation between the two storm types' IQR are also increased between t–15 and t+15. In addition, the non–lightning storms' results look approximately the same for all times between t–75 and t–15, with an increase in 6.2 – 7.3 μm T_B values only occurring at time t, as seen by the IQR being located at the same T_B value range before t–15.

The 6.2 – 10.8 μm T_B interest field also shows a diverging trend between the lightning and non–lightning storms, with a large separation between the IQR being observed from t–15 through t+15. The lightning storms seem to have a decreasing spread as time t is approached, whereas the non–lightning storms' spread varies more. By time t, the lightning storms have a very small IQR (and decreasing up to t+30), indicating that most of the lightning storms have approximately the same T_B values, in contrast to the non–lightning storms.

From the two plots seen in Figure 7.38, both the 6.2 – 7.3 μm T_B interest field and the 6.2 – 10.8 μm T_B interest field can be used to obtain differences in cloud–depths for the storms presented here, as there is no notch overlap present at all times. Therefore, one can say with 95 % confidence that the lightning storms had deeper clouds, i.e., cloud–tops are located at higher altitudes, making the formation of ice crystals easier in these storms (as compared to the non–lightning storms).

The tri–spectral field as well as its time trend is seen in Figure 7.39, with varying results being obtained here. As seen for the tri–spectral field (on the left in the figure), the t–75 and t–60 lightning and non–lightning storms' notches overlap, but after this time, no overlaps are present. Furthermore, although small, there is an increase in the separation between the IQR regions of the two storm types, with both storm types showing decreased spread as time t is approached. The tri–spectral field results seen here show that from t–45, the lightning and non–lightning storms' are significantly different at the 95^{th} percent confidence level.

On the other hand, the 15 minute tri–spectral time trend shows notch overlap for the entire period, from t–60 through t+30, with median values also overlapping during some of these times. This could be due to the very small difference values obtained for this field, and suggesting that this field is not as usable as the tri–spectral field itself for delineating or predicting CG lightning, due to the results for the lightning and non–lightning storms not being significantly different. However, different results for the lightning and non–lightning storms are still obtained for this field, as was seen in chapter 5, although these differences are not as strong as in some of the other interest fields.

The notched box plots of the 8.7 – 10.8 μm T_B interest field, as seen in Figure 7.40 (left), show some small overlap between the lightning and non–lightning storms for t–75 and t–60; however, no overlap is observed for the remaining times. Therefore, for all times from t–45 onwards, the results obtained here are statistically different at the 95^{th} percentile level. Interestingly, the IQR spread in the lightning storms decrease as time t is approached, but increases for the non–lightning storms during these

times. Also seen for this interest field is the fact that both storm types have more positive outliers than negative outliers.

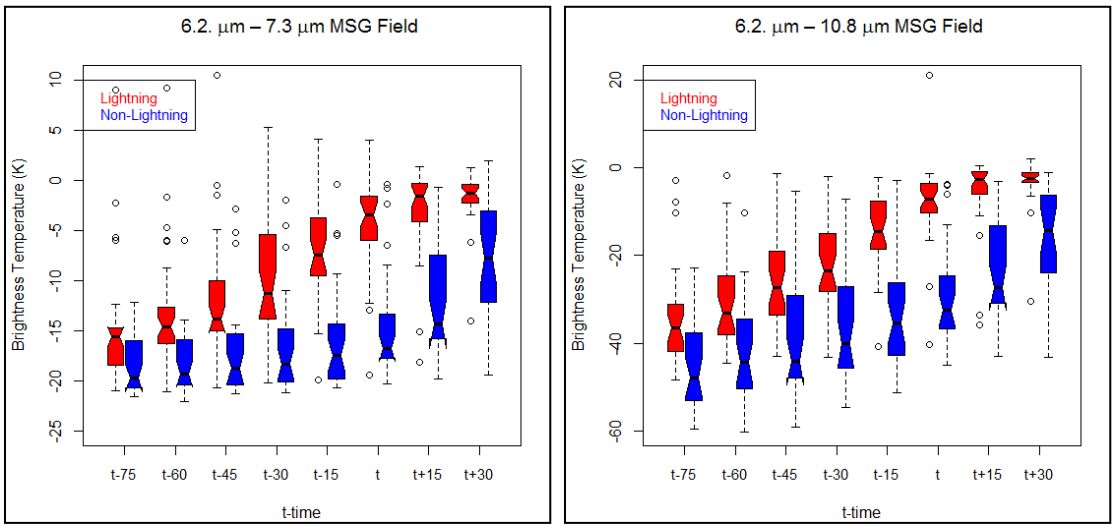

Figure 7.38: Notched box plots of the 6.2 – 7.3 μm T_B interest field (left) and the 6.2 – 10.8 μm T_B interest field (right) showing cloud depth features between lightning (red) and non–lightning (blue) storms from t–75 to t+30.

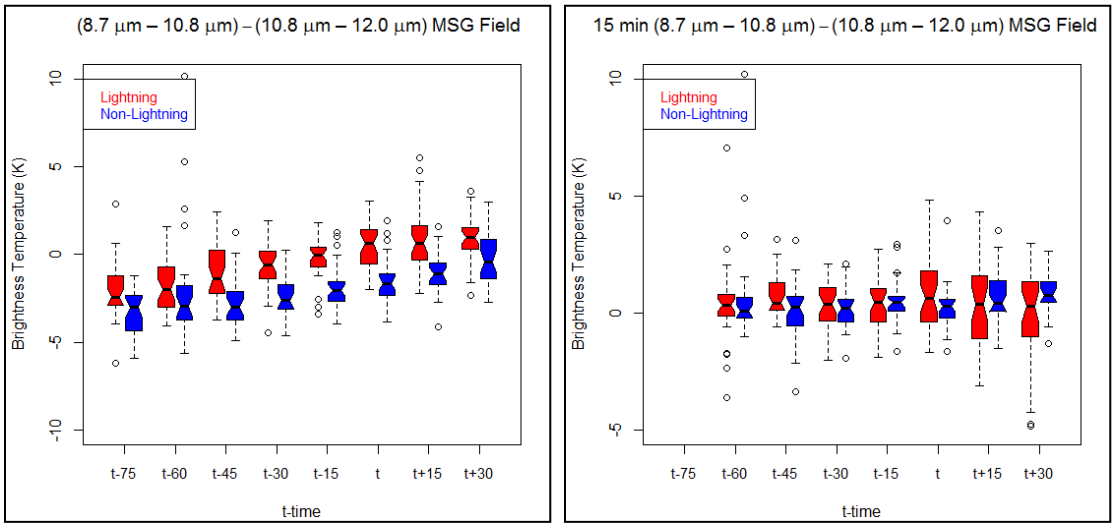

Figure 7.39: Notched box plots of the (8.7 – 10.8 μm) – (10.8 – 12.0 μm) T_B tri–spectral interest field (left) and the 15 minute (8.7 – 10.8 μm) – (10.8 – 12.0 μm) T_B tri–spectral interest field (right) showing cloud–top glaciation features between lightning (red) and non–lightning (blue) storms from t–75 to t+30.

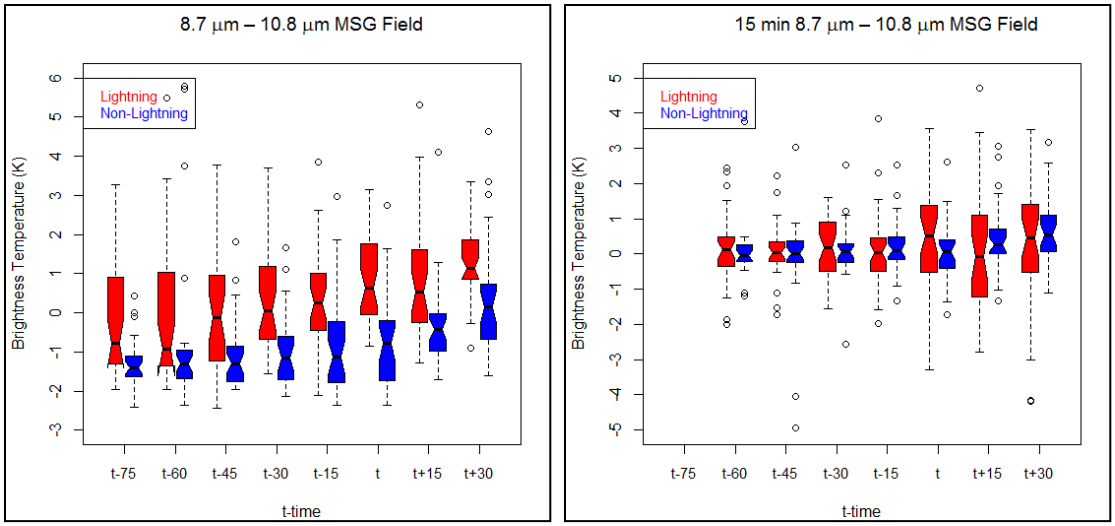

Figure 7.40: Notched box plots of the 8.7 – 10.8 μm T_B interest field (left) and the 15 minute 8.7 – 10.8 μm T_B interest field (right) showing cloud–top glaciation features between lightning (red) and non–lightning (blue) storms from t–75 to t+30.

The 15 minute 8.7 – 10.8 μm T_B interest field is seen on the right of Figure 7.40, which shows that the lightning and non–lightning storms' notches overlap for all times shown here, with the median values between t–45 and t–15 almost overlapping. For both the lightning and non–lightning storms, the IQR varies, with the largest spread being obtained at time t and t+15 for both storm types. Thus the 15 minute 8.7 – 10.8 μm T_B interest field does not show that the lightning and non–lightning storms are statistically not unique; thus it is probably best to use some of the other interest fields instead of this field when identifying lightning from non–lightning storms.

The results from these two figures are used to indicate the initiation of cloud–top glaciation, which shows the presence of ice crystals at the top of the cloud (i.e., possible cirrus and anvil formation). Here it was shown that the 15 minute tri–spectral T_B interest field and the 15 minute 8.7 – 10.8 μm T_B interest field do not show that the results obtained are statistically different at the 95th percent confidence level, and the tri–spectral

T_B interest field as well as the 8.7 – 10.8 μm T_B interest field do show that these two storm types are statistically significantly different at the 95th percentile level. As noted, it is probably best to use the latter two interest fields in describing cloud–top glaciation for these two storm types. It is important to note that even though some of these interest fields show notch overlap, it does not mean that these fields are not useable, as these results are only applicable to the storms analyzed here (in a tropical environment), and not on storms in midlatitudes, for example. Therefore, of the 10 interest fields used here (not including the 10.8 μm T_B field), eight of the fields indicated that for each specific interest field T_B value, the lightning and non–lightning storms are statistically significantly different at the 95th percent confidence level, especially for all times between t–30 and t+15. Hence the possibility of the non–lightning storms actually producing CG lightning is very small. Even though the VLF ATD network had very poor LA and DE, this did not have as much of an influence on the results as expected.

CHAPTER 8

SUMMARY AND DISCUSSION

In order to increase understanding on the relationships between lightning and non–lightning convective storms, radar and lightning observations from the NAMMA campaign were analyzed in concert with satellite data. The focus of this research was on establishing and documenting the relationships observed between lightning and non–lightning producing convective storms over the Equatorial Africa region by analyzing the time–evolution of infrared satellite fields, ground–based dual–polarimetric radar and lightning fields of 33 lightning and 30 non–lightning producing convective storms during August and September 2006. Using the S–band NPOL radar, VLF ATD lightning data and MSG SEVIRI data, the physical attributes of growing cumulus clouds, including water and ice mass production, updraft strength, cloud depth and cloud–top glaciation were illustrated and explained in this research. In addition to documenting storms in a remote region of the Earth, a main outcome of this study is to enhance predictability and identification of CG lightning initiation events by quantifying radar CFAD patterns and defining MSG interest field thresholds.

Dual–polarimetric variables of Z_H, Z_{DR}, ρ_{HV}, as well as Z_{DP} are often used to distinguish various hydrometeors from each other due to the fact that water drops have a different shape and dielectric constant than ice crystals and small or large hail. Thus, the combination of varying oblateness of hydrometeors for the same particle size distribution (small droplets versus large drops, ice crystals, supercooled drops, graupel and hail), lower dielectric constants of ice particles (including hail and graupel), possible canting as well as variations in vertical and horizontal dimensions for certain hydrometeors, make it possible to distinguish water droplets, large drops, ice crystals and graupel/hail from each other. This is again important, especially in the mixed–phase region, due to electrification be triggered when convective clouds have enough ice particles and graupel to collide and rebound in the presence of supercooled liquid water (which is only present in the mixed–phase region) and thus eventually lead to the occurrence of CG lightning (Balakrishnan & Zrnić, 1990; Meischner *et al*., 1991; Doviak & Zrnić, 1993; Yuter & Houze, 1995; Carey & Rutledge, 1996; Vivekanandan *et al*., 1999; Straka *et al*., 2000; Bringi & Chandrasekar, 2001.

As radar polarimetric variables are important when separating various precipitation particles, information from satellites, such as cloud–top temperature, updraft strength, cloud–top glaciation, and texture, are also important and can help distinguish storms that have large amounts of ice and thus may develop into lightning–producing convective storms, and convective storms that will not produce lightning. These fields can be obtained due to satellite channels being located at various wavelengths, which all have a somewhat distinct weighting function, and thus lead to different temperatures being reached at these different heights. To this end, 10 interest fields were used in the

research here to obtain the variation in cloud–top temperature, updraft strength and cloud–top glaciation between lightning and non–lightning storms. These interest fields included the following channel differences and time trends: 6.2 μm – 7.3 μm, 6.2 μm – 10.8 μm (indicating cloud–depth increase), 15 minute 6.2 μm – 7.3 μm, 30 minute 6.2 μm – 7.3 μm, 15 minute 10.8 μm, 30 minute 10.8 μm (indicating increase in updraft strengths), 8.7 μm – 10.8 μm, 15 minute 8.7 μm – 10.8 μm, tri–spectral field and the 15 minute tri–spectral field (indicating cloud–top glaciation).

It was found that for the average lightning and non–lightning storms, a T_B of 223.68 K and 261.21 K was reached, respectively, at time t for the 10.8 μm MSG field. This is a 37.53 K difference at the time of first CG lightning between these two storm tops. Between t–30 and time t, the lightning storm had a decrease in T_B of approximately 40 K, indicating that the main updraft strength increased a great deal during this time, where the non–lightning storm only saw a decrease of 6.5 K during this time. This field is often used to obtain the main updraft and is thus used in many of the interest fields seen here (Strabala *et al*., 1994; Ackerman, 1996; Schmetz *et al*., 1997; Setvák *et al*., 2003; Mecikalski & Bedka, 2006; Mecikalski *et al*., 2008; Rosenfeld *et al*., 2008; Harris *et al*., 2010; Mecikalski *et al*., 2010a,b). The other interest fields that were used to indicate an increase in the updraft strength include 15 minute 6.2 μm – 7.3 μm, 30 minute 6.2 μm – 7.3 μm, 15 minute 10.8 μm, 30 minute 10.8 μm, as mentioned above with the various critical values needed for this increase being listed in Table 3.1. The first two fields (15 minute 6.2 μm – 7.3 μm and 30 minute 6.2 μm – 7.3 μm) showed that the lightning storms, on average, had positive trends between t–60 and t+15 for the lightning storms, where the non–lightning storms only had positive trends from time t. These

positive trends indicate an increase in the updraft strength for the mentioned interest fields. In addition, the 15 minute 10.8 μm interest field had negative trends between t–60 and time t, with less than –4 K being reached from t–45 for the lightning storms, where the non–lightning storms displaying only a slight negative trend between t–30 and t–15, with –4 K only being reached at t+30. These negative trends here indicate an increase in the updraft strength, with the –4 K T_B representing the critical value for this increase in updraft strength. The T_B values obtained from the 30 minute 10.8 μm interest field has to be less than was obtained for the 15 minute 10.8 μm interest field in order to see an increase in updraft strength. This was seen from t–45 through time t for the lightning storm, with a weaker negative trend being observed for the non–lightning storm. Thus, from this, it is clear that the lightning storms had stronger updrafts than the non–lightning storms at time t, as the lightning storms had an increase in updraft strength for at least 45 minutes before the first CG lightning was recorded. The non–lightning storms, however, had much weaker updraft strengths, with an increase only being obtained after time t for most of these interest fields. This corresponds well to the increase in Z_H values in the lightning storms, with 45 dBZ already being reached at ≥ 1 % dBZ^{-1} at t–45 up to a height of 5 km, and cloud–tops already being located at 15 km at this time, whereas lower Z_H values were reached for the non–lightning storms, together with lower cloud–top heights being obtained for these storms at t–45. At t–15, the lightning storms had Z_H values up to 50 dBZ at ≥ 1 % dBZ^{-1} that reaches up to 5 km, and 30 dBZ at ≥ 1 % dBZ^{-1} up to 15 km. The non–lightning storms only obtained 44 dBZ at ≥ 1 % dBZ^{-1} below 3.5 km and 15 dBZ being reached at 14 km, which was the cloud–top here. This same trend, with higher Z_H values being observed for the lightning storms as well as higher

cloud–tops were seen for the remainder of the storms' lifetimes presented here. Thus, these increasing updraft strengths for the lightning storms will lead to the graupel and hail colliding and rebounding with the ice crystals found in the mixed–phase region of the lightning storms, in the presence of supercooled liquid water. Without these increasing updrafts, the ice crystals and supercooled drops will not have been lofted to higher elevations, and the graupel and hail particles will have fallen to the ground earlier, to due gravitational sorting.

The 6.2 μm – 7.3 μm, 6.2 μm – 10.8 μm interest fields are used to indicate an increase in cloud–depths, as mentioned earlier. Here, the lightning storms showed a weak positive trend from t–75 through t–45, with a strong positive trend after this. The non–lightning storms on the other hand, only showed a very weak positive trend up to time t, with a stronger trend being observed after this. However, for the cloud–depth to increase in the 6.2 μm – 7.3 μm interest field mentioned here, one needs an increase to 0 K, which is not seen for the non–lightning storms, but is seen for the lightning storms. 6.2 μm – 10.8 μm interest field for the lightning storms indicated a strong positive trend for the entire period up to t+15, with roughly –8 K being reached at time t. The non–lightning storms also displayed a positive trend, especially between t–45 and t+30, however at t+30, a T_B of only –15 K is reached. Thus although both storms showed an increase in cloud–depths, the lightning storms had a longer period of vertical growth, with much higher cloud–tops being reached on average. This was also seen from the radar variables, especially for times between t–45 and time t. These increased cloud–tops for the lightning storms will mean more ice, graupel and possible hail in the clouds, especially at colder temperatures. This was seen in the Z_{DR} fields, with negative Z_{DR}

values being reached more often and at much colder temperatures for the lightning storms than were observed for the non–lightning storms.

The remaining four interest fields were used to indicate the initiation of cloud–top glaciation, with a change in signs from negative to positive being needed for the tri–spectral, 8.7 μm – 10.8 μm and 15 minute 8.7 μm – 10.8 μm interest fields, and a positive trend being needed in the 15 minute tri–spectral field. Here, positive trends were seen from at least t–60, with a change in signs being observed from t–30 for the lightning storms, and although the non–lightning storms also displayed positive trends, these were much weaker than for the lightning storms, with positive T_B values only being reached after t+15. Thus, cloud–top glaciation already started occurring from at least t–30 for the lightning storms, leading to a lot of ice particles in the cloud–tops in the lightning storms, as seen by the lower Z_{DR} values at these heights, as well as higher ρ_{HV} values. Although the non–lightning storms also seem to indicate the initiation of cloud–top glaciation, this is only seen from t+15, and at much lower rates than for the lightning storms. Thus, as seen from the higher Z_{DR} values obtained for the non–lightning storms, and the fact that the cloud–tops here were lower than for the lightning storms, the non–lightning storms had much less ice at the top.

Outward of the CFAD analyses, other interesting features that were observed includes the fact that the lightning storms' core (≥ 20 % dBZ^{-1}) were located between 0 km and 10 km at t–45, with a steady increase in height being observed up to time t, thus indicating that this core lifted to higher elevations as the t–time for CG lightning was approached (which have been seen in previous studies from vertical Z_H cross sections). The lightning storms' core was located between 2 km and 15 km at time t, with this

lofting not being observed for the non–lightning storms. The mode (≥ 15 % dBZ^{-1}) of the lightning storms was tilted below the 5 km melting level and vertically aligned above this level from t–30 until t, where after the tilt below the 5 km level seemed to become more vertically aligned. This tilt indicates that there is a higher occurrence of larger drops present close to the ground, with smaller drops being observed closer to the melting level. Due to the fact that the non–lightning storms' mode were located at much lower altitudes than the lightning storms, especially up to t+15, where the mode reached 12.5 km, this tilt below the melting level was only seen from t+15.

The Z_{DR} values obtained for the lightning storms were consistently more positive below the melting layer and more negative above this layer, which is indicative of larger water drops, as well as melting graupel and hail below this layer and more ice particles, smaller liquid drops, graupel and possible hail above this layer. This negative Z_{DR} mode was located to 14 km altitude from t–15 through t+30, which corresponds well to the MSG interest fields showing that cloud–top glaciation, updraft strengths and cloud depths were increasing for these storms. Due to the fact that the non–lightning storms' Z_{DR} mode only really reached the mixed phase at t–15, this positive (negative) feature below (above) the melting layer was only comparable to the lightning storms at t–45 (and was thus scarcely visible), with this feature only becoming more pronounced after t+15. However, even though this feature is visible for the non–lightning storms at these times, the mode only reaches to 9 km at t+30, which is the highest elevation reached throughout, thus indicating that much less ice (as well as graupel and/or hail) is present in these clouds, especially at the cloud–tops, as confirmed by the MSG interest fields. In addition, as was the case with the Z_H mode for the lightning storms, these storms again

displayed a tilt below 5 km, with vertical alignment above this level for the entire 75 minute period, whereas this tilt below and vertical alignment above the 5 km level was only seen from t+15 for the non–lightning storms, with these storms starting to die out at this time, and thus no CG lightning will be initiated after this time. This tilt again indicates that there is a higher occurrence of larger drops (with $Z_H \neq Z_V$) and/or melting hail and graupel present close to the ground, with smaller drops and possible ice crystals ($Z_H = Z_V$) being observed closer to the melting level.

As seen from the water and ice masses calculated from the rain lines, the lightning storms had more ice than water between t–30 and onwards, as well as much more ice and water than was observed in the non–lightning storms throughout the entire 75 minute period. The non–lightning storms seem to have more water than ice from time t onwards, which would explain why no CG lightning was observed for these storms. One needs to remember that these water and ice masses were calculated for the mixed–phase region only, and corroborate the MSG interest field and other radar field results.

Finally, from the above analysis, it is possible to obtain a set of critical values for CG lightning initiation for the MSG interest fields that may be applicable in forecast applications. One needs to be cautious when using these values, as they have not been validated with any other storms except the 63 events discussed here. In addition, these values were obtained using the median results of the storms presented here, and do not necessarily include any outlier storm values. These results can be seen in Table 8.1, showing the critical values for CG initiation the 6.2 μm – 7.3 μm, 6.2 μm – 10.8 μm (indicating cloud–depth increase), 15 minute 6.2 μm – 7.3 μm, 30 minute 6.2 μm – 7.3 μm, 15 minute 10.8 μm, 30 minute 10.8 μm (indicating increase in updraft

strengths), 8.7 μm – 10.8 μm, 15 minute 8.7 μm – 10.8 μm, tri–spectral field and the 15 minute tri–spectral field (indicating cloud–top glaciation). As seen here, the critical values for CG initiation are different as compared to the critical values found by Strabala *et al*. (1994); Ackerman (1996); Baum *et al*. (2000); Mecikalski *et al*. (2010a), which it should be, as the critical values found from the previous research was for the actual occurrence of increasing updraft strength, increasing cloud–depth and initiation of cloud–top glaciation.

Table 8.1: MSG interest fields used here that indicates updraft strength, glaciation and cloud depth, as well as the critical values that indicate the possible initiation of CG lightning.

Channel differencing and time trends	**Category**	**Critical value for CG lightning initiation**
15 minute 6.2 μm – 7.3 μm	Updraft strength	Positive trends for ≥ 30 minutes with ≥ 2 °C increase during this time
30 minute 6.2 μm – 7.3 μm	Updraft strength	Positive trends for ≥ 30 minutes with ≥ 4 °C increase during this time
15 minute 10.8 μm	Updraft strength	≤ –10 °C
30 minute 10.8 μm	Updraft strength	≤ –20 °C
6.2 μm – 7.3 μm	Cloud depth	≥ –5 °C
6.2 μm – 10.8 μm	Cloud depth	≥ –10 °C
8.7 μm – 10.8 μm	Cloud–top glaciation	≥ 0.5 °C
15 minute 8.7 μm – 10.8 μm	Cloud–top glaciation	N/A*
(8.7 μm – 10.8 μm) – (10.8 μm – 12.0 μm)	Cloud–top glaciation	≥ 0.5 °C
15 minute (8.7 μm – 10.8 μm) – (10.8 μm – 12.0 μm)	Cloud–top glaciation	N/A*

* Due to results from these interest fields not being significantly different at the 95 % confidence level, no critical value was obtained.

CHAPTER 9

CONCLUSIONS AND FUTURE WORK

After analyzing the time–evolution of infrared satellite fields, ground–based dual–polarimetric radar and lightning fields of 33 lightning and 30 non–lightning producing convective storms that occurred during August and September 2006 over the NAMMA region, various differences were found between the lightning and non–lightning storms. More specifically it was found that, on average, the lightning storms had much higher cloud–top heights, larger maximum Z_H values, with the un–normalized CFAD mode as located at higher elevations and lofted even higher as time t was approached with the non–lightning storms having lower maximum Z_H values and lower elevations for the Z_H mode. The lightning storms' mode also had a tilt in the Z_H field below 5 km and a vertical alignment above this level until time t, with this tilt only being observed for the non–lightning storms at t+30. In addition, the lightning storms' Z_{DR} mode was mostly negative above 5 km and mostly positive below this level throughout the storms' lifetime (from t–45 to t+30), with this feature being extremely weak and only occurring after t–15 for the non–lightning storms. Furthermore, the lightning storms again displayed a tilt in the mode below the 5 km level, with a vertical

alignment above this level with this feature only being evident, although very weakly so, from t+15 for the non–lightning storms. The ρ_{HV} fields showed that the lightning and non–lightning storms had approximately the same characteristics, with the mode being consistently centered around 0.92 for both storm types, however, the lightning storms' mode was located to higher altitudes than the non–lightning storms throughout the period.

From the MSG interest fields, it was found that the lightning storms had stronger updraft strengths, higher cloud–tops and cloud–top glaciation occurring much sooner than the non–lightning storms. In addition, from the water and ice masses obtained from the rain line equation, it was found that the lightning storms had more ice and water in the mixed–phase region than the non–lightning storms, with more ice than water being observed in this layer for the lightning storms.

Future work will entail expanding these results to the United States, where better radars and lightning detection networks are more easily available, in the hopes that the same features found here will be obtained over the United States as well as testing the critical values for the interest fields. In addition, the Optimal Cloud Analysis (OCA) will be performed on the data here, as these fields provide unique information about unique information about the microphysical processes that occur at or near the cloud top, to a depth of approximately 100 m. These retrieved fields include cloud optical thickness (τ), cloud–top particle effective radius (r_e) and cloud–top pressure (p_c).

APPENDIX A

Here the atmospheric radiosondes that were representative of the storms presented in this paper, are shown as an additional measure. All radiosonde data presented were recorded at Dakar, Senegal, which is located approximately 20 km from the NPOL radar at the time of the research. Storms formed part of a specific radiosonde if the storm had its t–time within less than 6 hours of that radiosonde, otherwise the next available radiosonde was presented. The storms that are represented by each radiosonde are mentioned in the figure captions. It should be noted here that radiosondes were not available for the 26th of August 2006, which represents three non–lightning storms; M1, S1 and S2. As can be seen, the 0 °C level occurred between approximately 4.5 km and 5.5 km, with the –40 °C level being located at roughly 11 km.

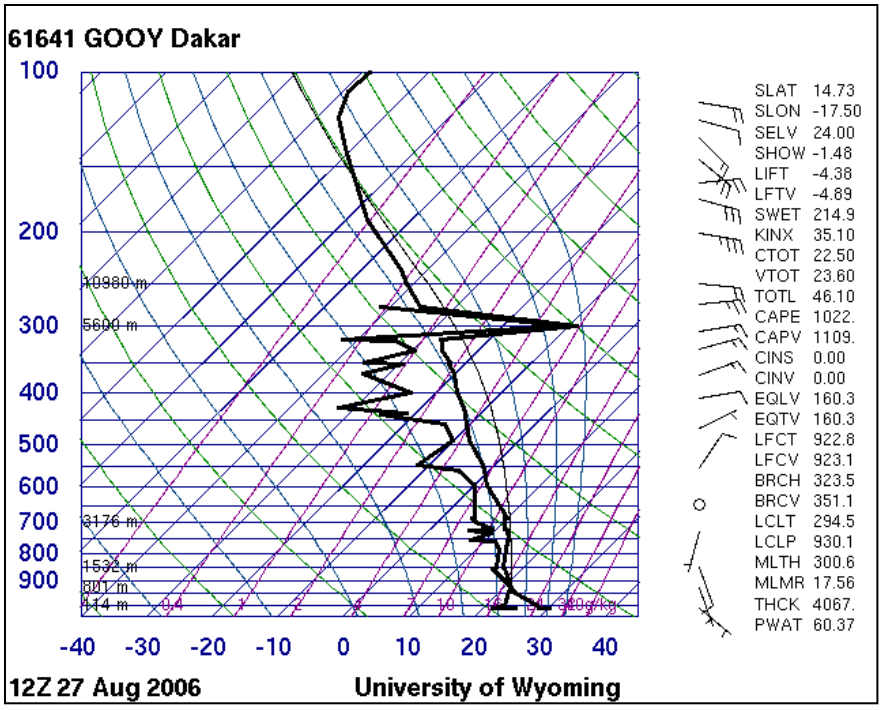

Figure A1: Skew–T for 1200 UTC on 27 August 2006; representative of non–lightning storms M1 and M2.

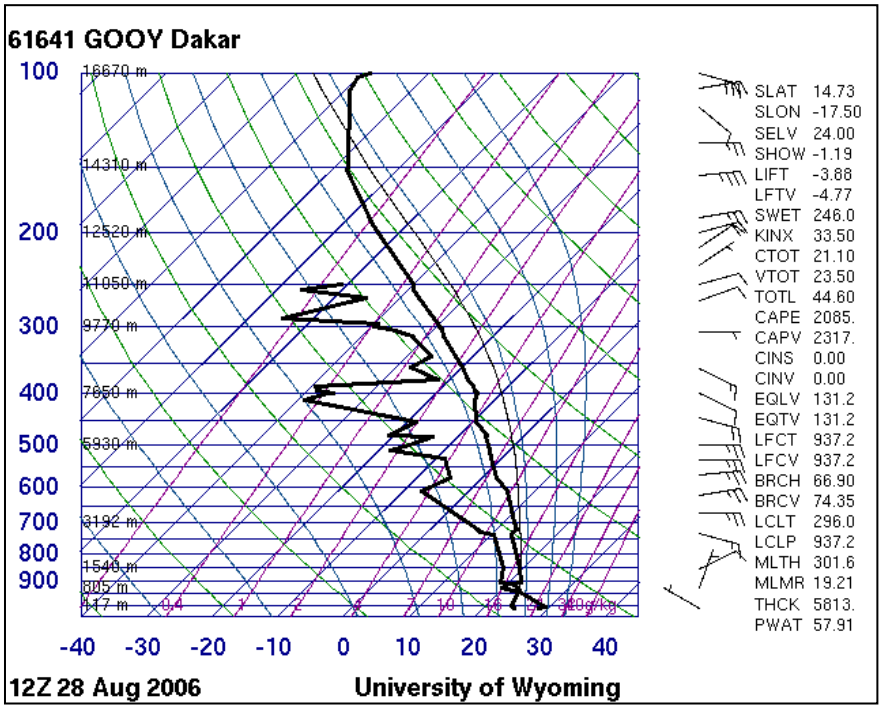

Figure A2: Skew–T for 1200 UTC on 28 August 2006; representative of non–lightning storm S1.

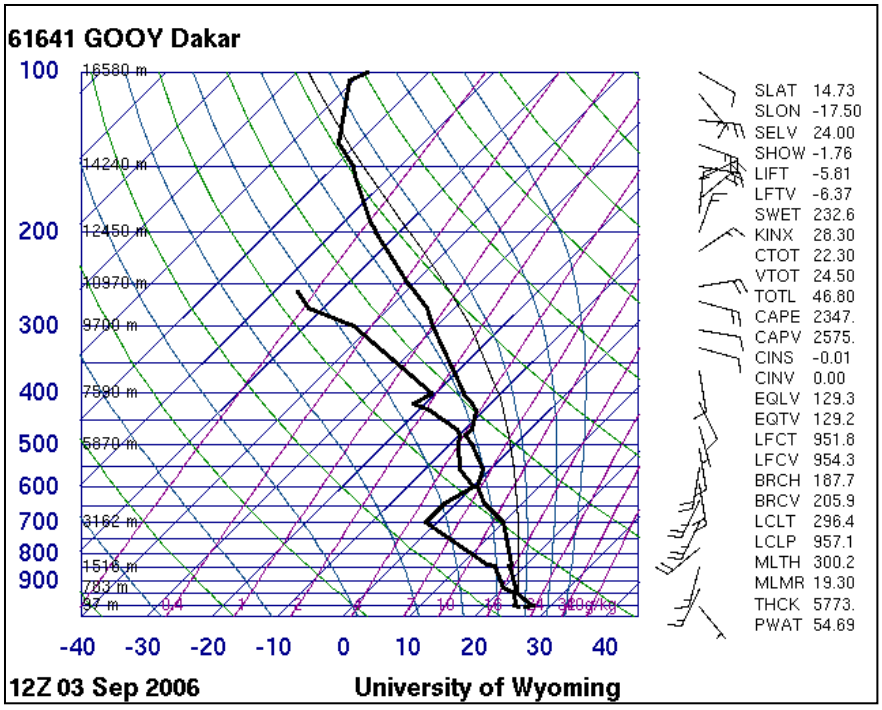

Figure A3: Skew–T for 1200 UTC on 03 September 2006; representative of non–lightning storms M4, S3, S6, S13 and S14 and lightning storms M1, M2, M3 and M6.

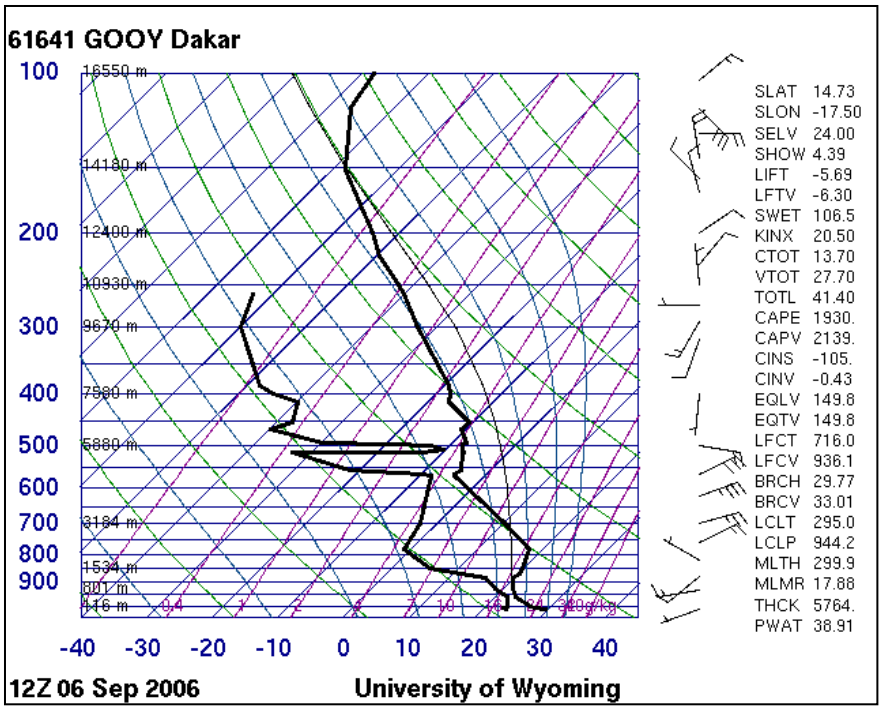

Figure A4: Skew–T for 1200 UTC on 06 September 2006; representative of non–lightning storms S2 and S3 and lightning storms M4, M5, S1, S6 and S7.

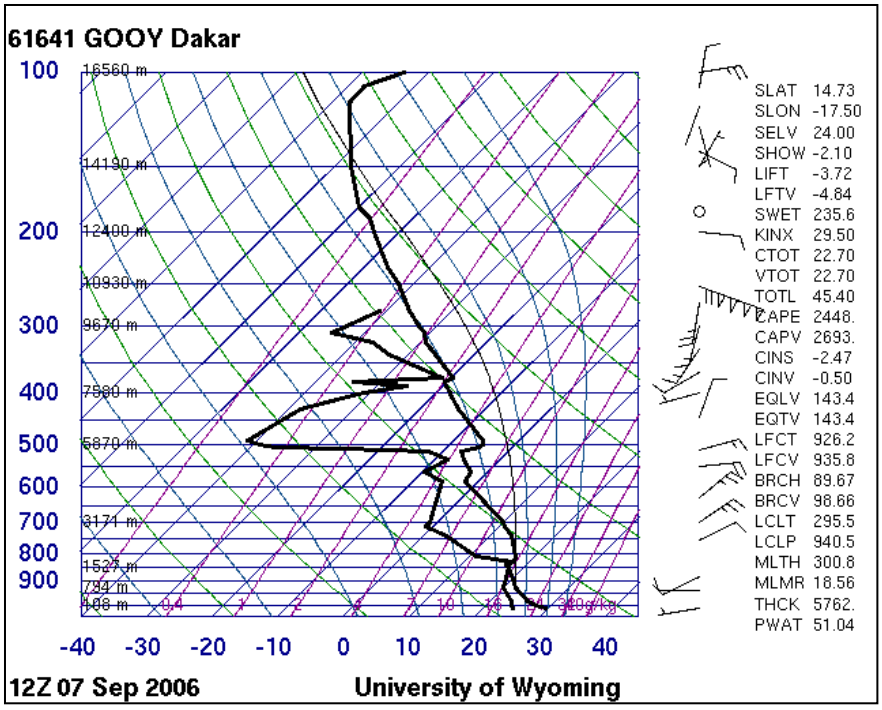

Figure A5: Skew–T for 1200 UTC on 07 September 2006; representative of the lightning storm M1.

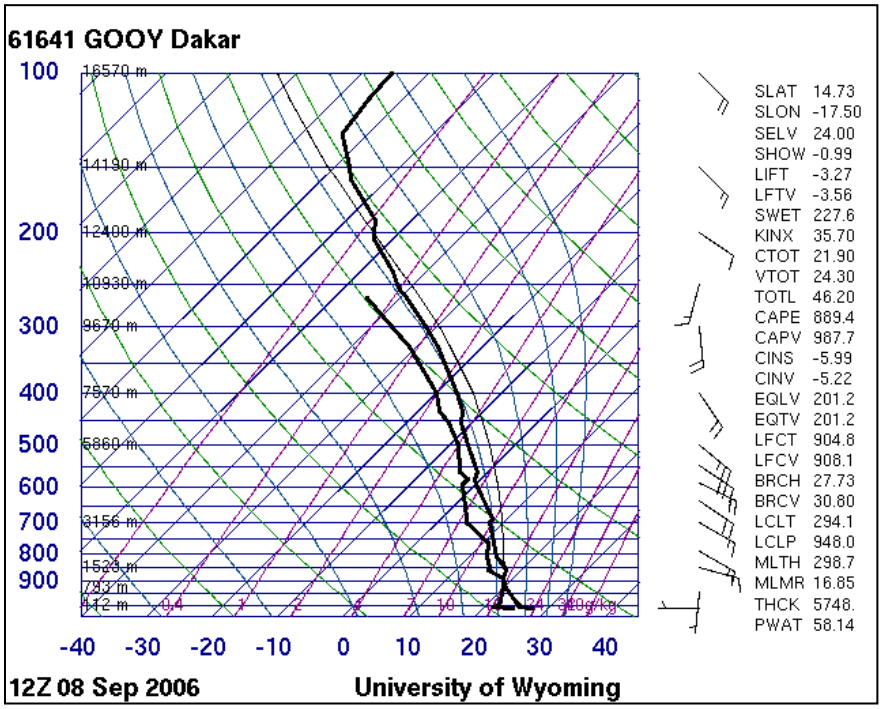

Figure A6: Skew–T for 1200 UTC on 08 September 2006; representative of non–lightning storms S1, S2, S3 and S4.

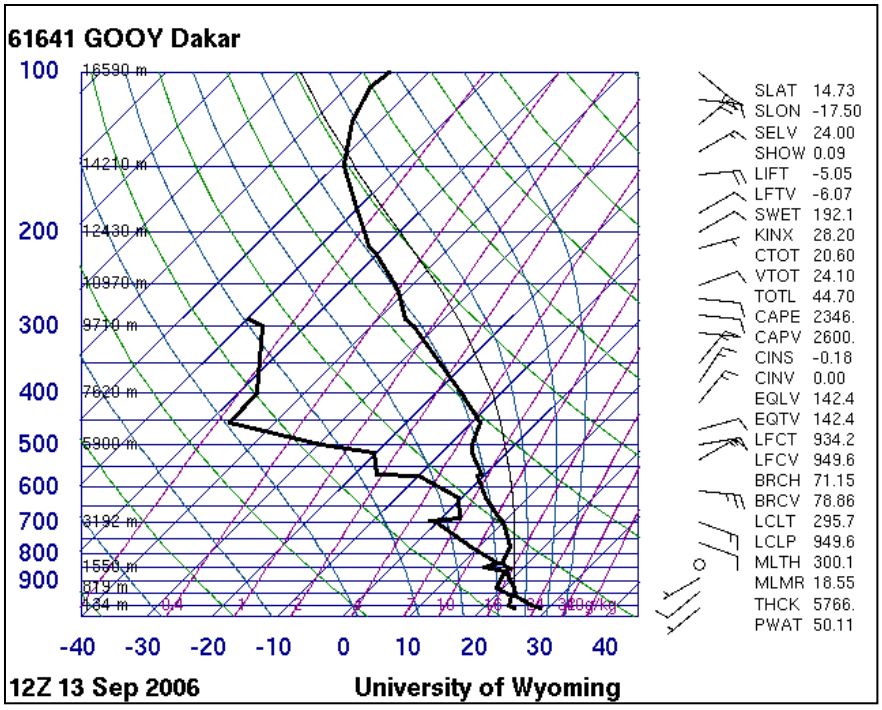

Figure A7: Skew–T for 1200 UTC on 13 September 2006; representative of lightning storm M1.

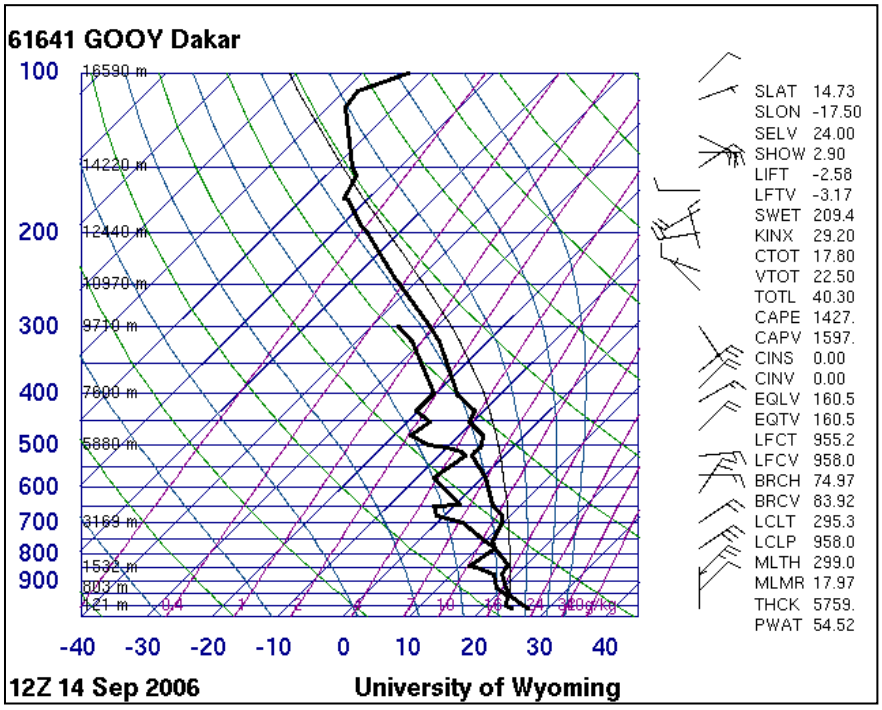

Figure A8: Skew–T for 1200 UTC on 14 September 2006; representative of non–lightning storms M1, M2, S6, S7, S8 and S10 and lightning storms M3, M4 and M8.

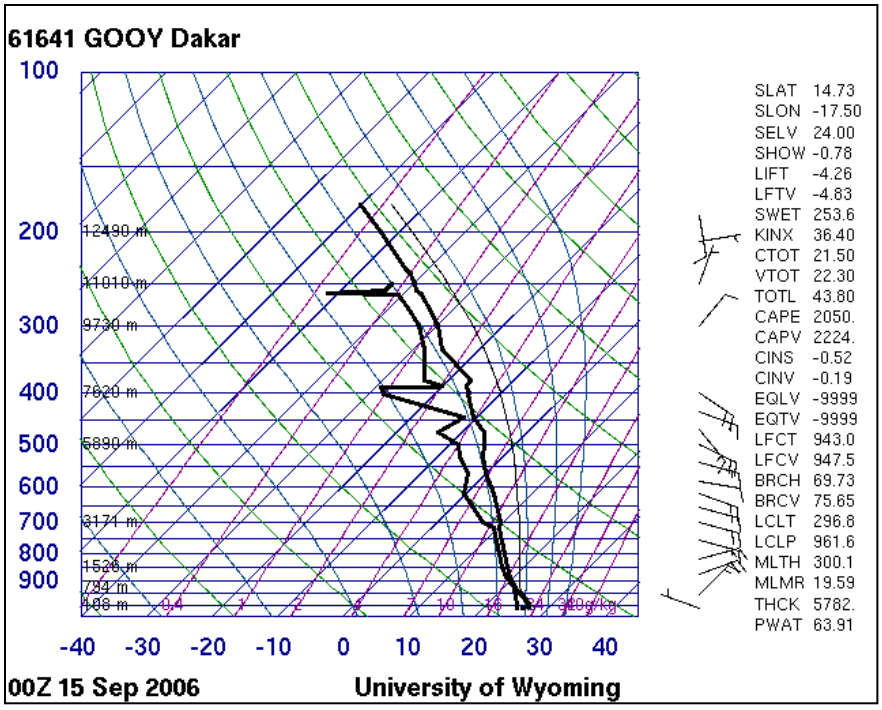

Figure A9: Skew–T for 0000 UTC on 15 September 2006; representative of non–lightning storm S14 and lightning storms M12, S11 and S13.

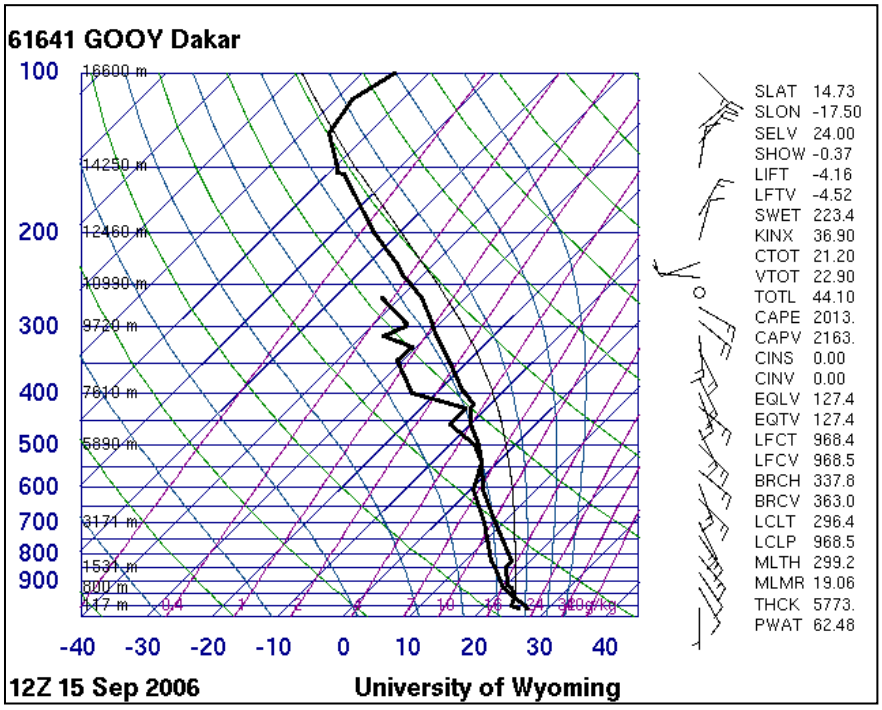

Figure A10: Skew–T for 1200 UTC on 15 September 2006; representative of lightning storms M1 and S2.

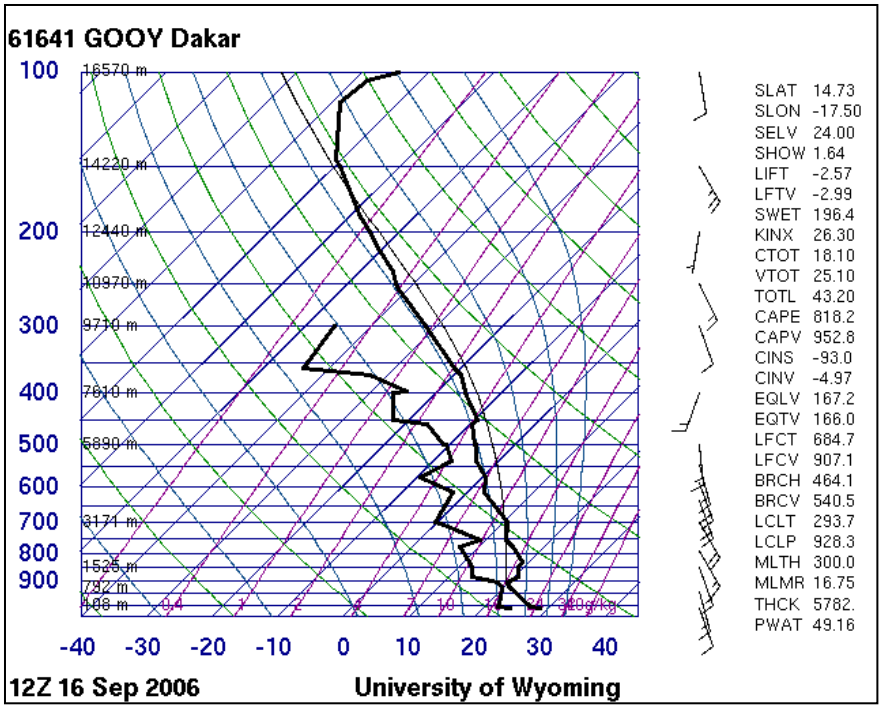

Figure A11: Skew–T for 1200 UTC on 16 September 2006; representative of non–lightning storm M2 and lightning storm M1.

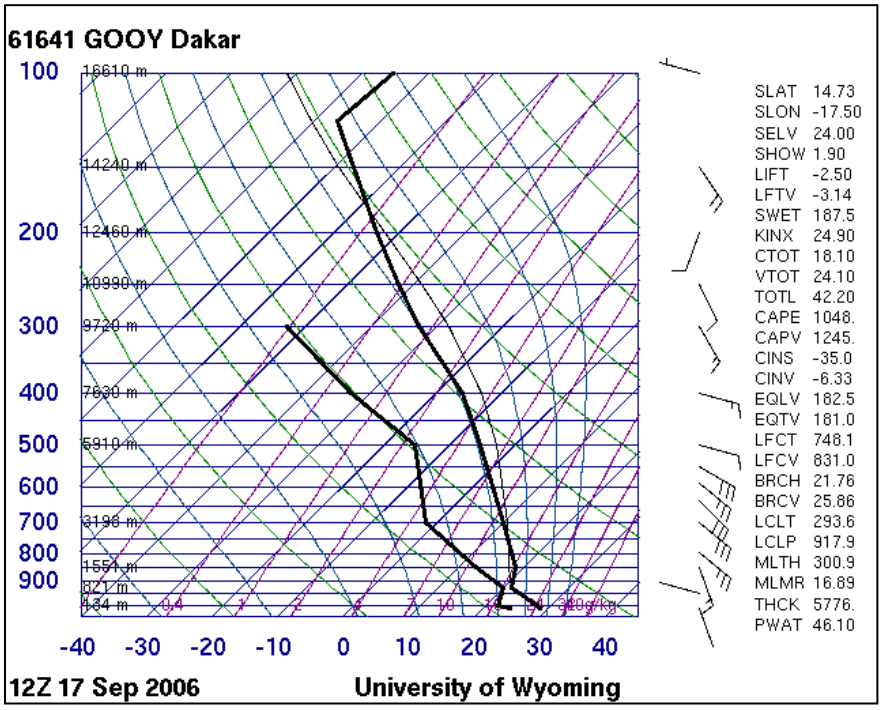

Figure A12: Skew–T for 1200 UTC on 17 September 2006; representative of non–lightning storms S1, S3, S4, S5 and S6.

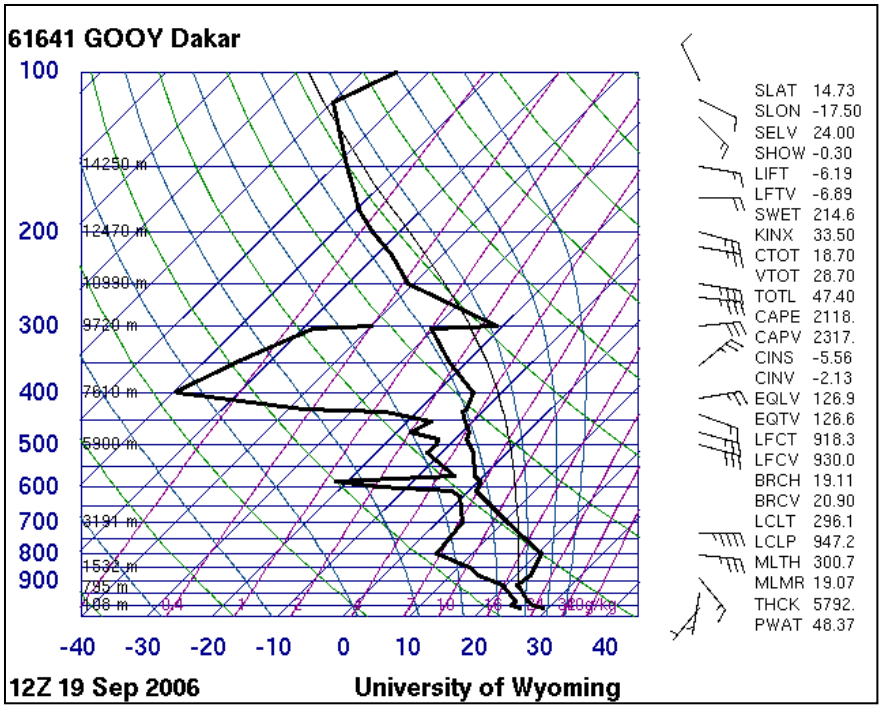

Figure A13: Skew–T for 1200 UTC on 19 September 2006; representative of non–lightning storm S5 and lightning storms M2, M3, M4, M5, M6, M7, M8, M9, M10, M11, S1 and S3.

REFERENCES:

Ackerman, S.A., 1996: Global satellite observations of negative brightness temperature differences between 11 and 6.7 μm, *Journal of Atmospheric Sciences*, **53**, 2803 – 2812.

Adler, R.F., and Fenn, D.D., 1981: Satellite–observed cloud–top height changes in tornadic thunderstorms. *Journal of Applied Meteorology*, **20**, 1369–1375.

Adler, R.F., Markus, M.J., and Fenn, D.D., 1985: Detection of severe Midwest thunderstorms using geosynchronous satellite data, *Monthly Weather Review*, **113**, 769 – 781.

Arnault, J., and Roux, F., 2009: Case study of a developing African easterly wave during NAMMA: An energetic point of view, *Journal of Atmospheric Sciences*, **66**, 2991 – 3020.

Aydin, K., and Giridhar, V., 1992: C–band dual–polarization radar observables in rain, *Journal of Atmospheric and Oceanic Technology*, **9**, 383 – 390.

Balakrishnan, N., and Zrnić, D.S., 1990: Use of polarization to characterize precipitation and discriminate large hail, *Journal of Atmospheric Sciences*, **47** (13), 1525 – 1540.

Baum, B.A., Soulen, P.F., Strabala, K.I., King, M.D., Ackerman, S.A., Menzel, W.P. and Yang, P., 2000: Remote sensing of cloud properties using MODIS airborne simulator imagery during SUCCESS 2, Cloud thermodynamic phase, *Journal of Geophysical Research*, **105** (D5), 11781 – 11792.

Boccippio, D.J., Goodman, S.J., and Heckman, S., 2000: Regional differences in tropical lightning distributions, *Journal of Applied Meteorology*, **39**, 2231 – 2248.

Bringi, V.N. and Chandrasekar, V., 2001: *Polarimetric Doppler Weather Radar – Principles and Applications*, Cambridge University Press, United Kingdom, pp 636.

Browning, K.A., and Atlas, D., 1965: Initiation of precipitation in vigorous convective clouds. *Journal of Atmospheric Sciences*, **22**, 678–683.

Bruning, E.C., Rust, W.D., Schuur, T.J., MacGorman, D.R., Krehbiel, P.R., and Rison, W., 2007: Electrical and polarimetric radar observations of a multicell storm in TELEX, *Monthly Weather Review*, **135**, 2525 – 2544.

Carey, L.D. and Rutledge, S.A., 1996: A multiparameter radar case study of the microphysical and kinematic evolution of a lightning producing storm, *Meteorology and Atmospheric Physics*, **59**, 33 – 64.

Carey, L.D. and Rutledge, S.A., 2000: The relationship between precipitation and lightning in tropical island convection: a c–band polarimetric radar study, *Monthly Weather Review*, **128**, 2687 – 2710.

Carey, L.D., Peterson, W.A. and Rutledge, S.A., 2003: Evolution of cloud–to–ground lightning and storm structure in the Spencer, South Dakota, tornadic supercell of 30 May 1998, *Monthly Weather Review*, **131**, 1811 – 1831.

Carey, L.D., 2007: Rain maps inferred from polarimetric radar observations over costal locales, *Unpublished Report*, Texas A&M University Project, pp 15.

Cecil, D. J., 2011: Relating Passive 37–GHz scattering to radar profiles in strong convection. *Journal of Applied Meteorology and Climatology*, **50**, 233 – 240.

Cecil, D.J., Goodman, S.J., Boccippio, D.J., Zipser, E.J., and Nesbitt, S.W., 2005: Three years of TRMM precipitation features. Part I: Radar, radiometric, and lightning characteristics, *Monthly Weather Review*, **133**, 543 – 566.

Cecil, D.J., and Zipser, E.J., 2002: Reflectivity, ice scattering, and lightning characteristics of hurricane eyewalls and rainbands. Part II: Intercomparison of observations, *Monthly Weather Review*, **130**, 785 – 801.

Cifelli, R., Peterson, W.A., Carey, L.D., Rutledge, S.A and Da Silva Dias, M.A.F., 2002: Radar observations of the kinematic, microphysical and precipitation characteristics of two MCSs in TRMM LBA, *Journal of Geophysical Research*, **107** (D20), 44–1 – 44–16.

Cifelli, R., Carey, L.D., Petersen, W.A., and Rutledge, S.A., 2004: An ensemble study of wet season convection in Southwest Amazonia: Kinematics and implications for diabatic heating, *Journal of Climate*, **17**, 4692 – 4707.

Cifelli, R., Lang, T., Rutledge, S.A., Guy, N., Zipser, E.J., Zawislak, J., and Holzworth, R., 2010: Characteristics of an African easterly wave observed during NAMMA, *Journal of Atmospheric Sciences*, **67**, 3 – 25.

Deierling, W., Petersen, W.A., Latham, J., Ellis, S., and Christian Jr., H.J., 2005: On the relationship of thunderstorm ice hydrometeor characteristics and total lightning measurements, *Atmospheric Research*, **76**, 114 – 126.

Deierling, W., Petersen, W.A., Latham, J., Ellis, S., and Christian, H.J., 2008: The relationship between lightning activity and ice fluxes in thunderstorms, *Journal of Geophysical Research*, **113** (D15210), 1 – 20.

De Leonibus, L., Biron, D., Giorgi, C., Mäkelä, A., Tuomi, T., Pylkkö, P., and Haapalainen, J., 2007: Study on the present status and future capabilities of ground–based lightning location networks, *Unpublished Report*, EUMETSAT, Germany, EUM/CO/06/1584/KJG.

DeMott, P.J., Sassen, K., Poellot, M.R., Baumgardner, D., Rogers, D.C., Brooks, S.D., Prenni, A.J., and Kreidenweis, S.M., 2003: African dust aerosols as atmospheric ice nuclei, *Geophysical Research Letters*, **30** (14), 1 – 4.

Doviak, R.,J. and Zrnić, D.S., 1993: *Doppler Radar and Weather Observations*, 2nd edition, Dover Publications, United States of America, pp 562.

Donovan, M.F., Williams, E.R., Kessinger, C., Blackburn, G., Herzegh, P.H., Bankert, R.L., Miller, S., and Mosher, F.R., 2008: The identification and verification of hazardous convective cells over oceans using visible and infrared satellite observations, *Journal of Applied Meteorology and Climatology*, **47**, 164 – 184.

EUMETSAT, 2007: Typical Radiometric Accuracy and Noise for MSG–1/2, *Unpublished Report*, EUMETSAT, Germany, EUM/OPS/TEN/07/0314, pp. 4.

Ferreira, R.N., Rickenbach, T., Guy, N., and Williams, E., 2009: Radar observations of convective system variability in relationship to African easterly waves during the 2006 AMMA special observing period, *Monthly Weather Review*, **137**, 4136 – 4150.

Gaffard, C., Nash, J., Atkinson, N., Benett, A., Callaghan, G., Hibbett, E., Taylor, P., Turp, M., and Schulz, W., 2008: Observing lightning around the globe from the surface, *20th International Lightning Detection Conference; 2nd International Lightning Meteorology Conference*, Tucsan, Arizona, USA, 21 – 25 April 2008.

Golestani, Y., Chandrasekar, V., and Bringi, V.N., 1989: Inter–comparison of multiparameter radar measurements, Proceedings of the 24th Conference on Radar Meteorology, Tallahassee, Florida, *American Meteorological Society*, 309 – 314.

Gumley, L.E., 2002: *Practical IDL Programming: Creating Effective Data Analysis and Visualization Applications*, Morgan Kaufmann Publishers, USA, pp. 508.

Harris, R.J., Mecikalski, J.R., MacKenzie Jr., W.M., Durkee, P.A., and Nielsen, K.E., 2010: The definition of GOES infrared lightning initiation interest fields, *Journal of Applied Meteorology and Climatology*, **49,** 2527 – 2543.

Harrison, S.J., Mecikalski, J.R., and Knupp, K.R., 2009: Analysis of outflow boundary collisions in North–Central Alabama, *Weather and Forecasting*, **24**, 1680 – 1690.

Hondl, K.D. and Eilts, M.D., 1994: Doppler radar signatures of developing thunderstorms and their potential to indicate the onset of cloud–to–ground lightning, *Monthly Weather Review*, **122**, 1818 – 1836.

Jenkins, G.S., and Pratt, A.S., 2008: Saharan dust, lightning and tropical cyclones in the eastern tropical Atlantic during NAMMA–06, *Geophysical Research Letters*, **35** (L12804), 1 – 6.

Jenkins, G.S., Pratt, A.S., and Heymsfield, A., 2008: Possible linkages between Saharan dust and tropical cyclone rain band invigoration in the eastern Atlantic during NAMMA–06, *Geophysical Research Letters*, **35** (L08815), 1 – 7.

Keogh, S., Hibbett, E., Nash, J., and Eyre, J., The Met Office arrival time difference (ATD) system for thunderstorm detection and lightning location, *Unpublished Report*, UK Met Office, United Kingdom, Numerical Weather Prediction: Forecasting Research Technical Report No. 488.

Khain, A.P., Rosenfeld, D., and Pokrovsky, A., 2005: Aerosol impact on the dynamics and microphysics of convective clouds, *Quarterly Journal of the Royal Meteorological Society*, **131**, 2639 – 2663.

King, MD., Tsay, S.–C., Platnick, S.E., Wang, M., and Liou, K.–N., 1998: Cloud retrieval algorithms for MODIS: optical thickness, effective particle radius, and thermodynamic phase. MODIS Algorithm Theoretical Basis Document No. ATBD–MOD–05 (version 5, December 1997), pp. 79.

Koren, I., Kaufman, Y.J., Rosenfeld, D., Remer, L.A., and Rudich, Y., 2005: Aerosol invigoration and restructuring of Atlantic convective clouds, *Geophysical Research Letters*, **32** (L14828), 1 – 4.

Krehbiel, P.R., 1986: The electrical structure of thunderstorms, In *The Earth's Electrical Environment*, eds. E.P. Krider and R.G. Roble, National Academy Press, Washington DC, pp. 90 – 113.

Kucera, P.A., 2006: Overview of NASA polarimetric Doppler weather radar (NPOL) data collected during NAMMA, Global Hydrology Resource Center (GHRC) at the Global Hydrology and Climate Center, Huntsville, Alabama. pp. 11.
ftp://ghrc.nsstc.nasa.gov/pub/doc/namma/namnpol/NPOL_NAMMA_Product_Documentation.pdf

Lang, S., Tao, W.–K., Simpson, J., and Ferrier, B., 2003: Modeling of convective–stratiform precipitation processes: Sensitivity to partitioning methods, *Journal of Applied Meteorology*, **42**, 505 – 527.

Leap, R.M., 1986: Evaluation of cloud–to–ground lightning data from the Western United States for the 1983 – 84 summer seasons, *Journal of Climate and Applied Meteorology*, **25**, 785 – 799.

Lee, A.C.L., 1986: An operational system for the remote location of lightning flashes using a VLF arrival time difference technique, *Journal of Atmospheric and Oceanic Technology*, **3**, 630 – 642.

Lee, A.C.L., 1990: Bias elimination and scatter in lightning location by the VLF arrival time difference technique, *Journal of Atmospheric and Oceanic Technology*, **7**, 719 – 733.

Lee, W., Walther, C. and Oye, R., 1994: Doppler Radar Data Exchange format DORADE, *Unpublished report*, NCAR Tech. Note, NCAR/TN–4031IA.

Lee, T.F., Turk, F.J., and Richardson, K., 1997: Stratus and fog products using GOES–8–9 3.9– μm data, *Weather and Forecasting*, **12**, 664 – 677.

Levi, Y., and Rosenfeld, D., 1996: Ice nuclei, rainwater chemical composition, and static cloud seeding effects in Israel, *Journal of Applied Meteorology*, **35**, 1494 – 1501.

Lindsey, D.T., Hillger, D.W., Grasso, L., Knaff, J.A., and Dostalek, J.F., 2006: Goes climatology and analysis of thunderstorms with enhanced 3.9–μm reflectivity, *Monthly Weather Review*, **134** (9), 2342 – 2353.

Lund, N.R., MacGorman, D.R., Schuur, T.J., Biggerstaff, M.I. and Rust, W.D., 2009: Relationship between lightning location and polarimetric radar signatures in a small mesoscale convective system, *Monthly Weather Review*, **137**, 4151 – 4170.

MacGorman, D.R., and Rust, W.D., 1998: *The Electrical Nature of Storms*, Oxford University Press, New York, pp 422.

Marshall, J.S., and Radhakant, S., 1978: Radar precipitation maps as lightning indicators. *Journal of Applied Meteorology.*, **17**, 206–212.

Marshall, J.S. and Palmer, W.Mc K., 1948: The distribution of raindrops with size, *Journal of Meteorology*, **5**, 165 – 166.

McGill, R., Tukey, J.W., and Larsen, W., 1978: Variations of box plots, *The American Statistician*, **32**, 12 – 16.

Mecikalski, J.R., and Bedka, K.M., 2006: Forecasting convective initiation by monitoring the evolution of moving cumulus in daytime GOES imagery, *Monthly Weather Review*, **134**, 49 – 78.

Mecikalski, J.R., Bedka, K.M., Paech, S.J., and Litten, L.A., 2008: A statistical evaluation of GOES cloud–top properties for Nowcasting convective initiation, *Monthly Weather Review*, **136**, 4899 – 1914.

Mecikalski, J.R., MacKenzie Jr., W.M., Koenig, M., and Muller, S., 2010a: Cloud–top properties of growing cumulus prior to convective initiation as measured by Meteosat Second Generation. Part I: Infrared fields, *Journal of Applied Meteorology and Climatology*, **49**, 521 – 534.

Mecikalski, J.R., MacKenzie Jr., W.M., Koenig, M., and Muller, S., 2010b: Cloud–top properties of growing cumulus prior to convective initiation as measured by Meteosat Second Generation. Part II: Use of visible reflectance, *Journal of Applied Meteorology and Climatology*, **49**, 2544 – 2558.

Mecikalski, J.R., Watts, P.D., and Koenig, M., 2011: Use of Meteosat Second Generation optimal cloud analysis fields for understanding physical attributes of growing cumulus clouds, *Atmospheric Research*, **102**, 175 – 190.

Meischner, P.F., Bringi, V.N., Heimann, D., and Höller, 1991: A squall line in Southern Germany: Kinematics and precipitation formation as deduced by advanced polarimetric and Doppler radar measurements, *Monthly Weather Review*, **119**, 678 – 701.

Menzel, W.P., Frey, R.A., and Baum, B.A., 2010: Cloud top properties and cloud phase – MODIS algorithm theoretical basis document (version 8, October 2010), pp. 62.

Mohr, C.G., Miller, L.J., Vaughn, R.L., and Frank, H.W., 1986: The merger of mesoscale datasets into a common Cartesian format for efficient and systematic analysis, *Journal of Atmospheric and Oceanic Technology*, **3**, 143 – 161.

Mosier, R.M., Schumacher, C., Orville, R.E., and Carey, L.D., 2011: Radar nowcasting of cloud–to–ground lightning over Houston, Texas. *Weather and Forecasting*, **26**, 199–212.

Mueller, C., Saxen, T., Roberts, R., Wilson, J., Betancourt, T., Dettling, S., Oien, N., and Yee, J., 2003: NCAR Auto–Nowcast system, *Weather and Forecasting*, **18**, 545–561.

Nakajima, T., and King, M.D., 1990: Determination of the optical thickness and effective particle radius of clouds from reflected solar radiation measurements: Part 1: Theory, *Journal of Atmospheric Sciences*, **47**, 1878 – 1893.

Otkin, J.A., Greenwald, T.J., Sieglaff, J., and Huang, H.–L., 2009: Validation of a large–scale simulated brightness temperature dataset using SEVIRI satellite observations, *Journal of Applied Meteorology and Climatology*, **48**, 1613 – 1626.

Oye, R.C., Mueller, C., and Smith, C., 1995: Software for radar translation, visualization, editing, and interpretation, *Preprints, 27th Conf. on Radar Meteorology*, Vail, CO, American Meteorological Society.

Pessi, A.T., and Businger, S., 2009: Relationships among lightning, precipitation, and hydrometeor characteristics over the North Pacific Ocean, *Journal of Applied Meteorology and Climatology*, **48**, 833 – 848.

Petersen, W.A., and Rutledge, S.A., 2001: Regional variability in tropical convection: Observations from TRMM, *Journal of Climate*, **14**, 3566 – 3586.

Petersen, W.A., Christian, H.J., and Rutledge, S.A., 2005: TRMM observations of the global relationship between ice water content and lightning, *Geophysical Research Letters*, **32**, L14819.

Poelman, D.R., 2010: On the science of lightning, *Unpublished report*, Royal Meteorological Institute of Belgium, Brussels.

Poulsen, C.A., Watts, P.D., Thomas, G.E., Sayer, A.M., Siddans, R., Grainger, R.G., Lawrence, B.N., Campmany, E., Dean, S.M., and Arnold, C., 2011: Cloud retrievals from satellite data using optimal estimation: Evaluation and application to ATSR, *Atmospheric Measurement Technical Discussion*, **4**, 2389 – 2431.

Rakov, V.A., and Uman, M.A., 2003: *Lightning Physics and Effects*, Cambridge University Press, New York, pp 687.

Reale, O., Lau, W.K., Kim, K.–M., and Brin, E., 2009: Atlantic tropical cyclogenetic processes during SOP–3 NAMMA in the GEOS–5 global data assimilation and forecast system, *Journal of Atmospheric Sciences*, **66**, 3563 – 3578.

Redelsperger, J.–L., Thorncroft, C.D., Diedhiou, A., Lebel, T., Parker, D.J., and Polcher, J., 2006: African monsoon multidisciplinary analysis: An international research project and field campaign, *Bulletin of the American Meteorological Society*, **87**, 1739 – 1746.

Rew, R.K., and Davis G.P., 1990: NetCDF: An interface to scientific data access, *Computer Graphics and Applications, IEEE*, 76 – 82.

Roberts, R.D., and Rutledge, S., 2003: Nowcasting storm initiation and growth using GOES–8 and WSR–88D data, *Weather and Forecasting*, **18**, 562 – 584.

Rodger, C.J., Brundell, J.B., Dowden, R.L., and Thomson, N.R., 2004: Location accuracy of long distance VLF lightning location network, *Annales Geophysicae*, **22**, 747 – 758.

Rogers, R.F., Black, M.L., Chen, S.S., and Black, R.A., 2007: An evaluation of microphysics fields from mesoscale model simulations of tropical cyclones. Part I: Comparisons with observations, *Journal of the Atmospheric Sciences*, **64**, 1811 – 1834.

Rogers, R.R. and Yau, M.K., 1989: *A Short Course in Cloud Microphysics*, Third edition, Elsevier Publisher (Butterworth–Heinemann), Oxford, United Kingdom, pp 290.

Rosenfeld, D., and Nirel, R., 1996: Seeding effectiveness – The interaction of desert dust and the southern margins of rain cloud systems in Israel, *Journal of Applied Meteorology*, **35**, 1502 – 1510.

Rosenfeld, D., Woodley, W.L., Lerner, A., Kelman, G., and Lindsey, 2008: Satellite detection of severe convective storms by their retrieved vertical profiles of cloud particle effective radius and thermodynamic phase, *Journal of Geosphysical research*, **113** (D04208), 1 – 22.

Ross, R.S., and Krishnamurti, T.N., 2009: Energy transformation and diabatic processes in developing and non–developing African easterly waves observed during the NAMMA project of 2006, *Weather and Forecasting*, **24**, 1524 – 1548.

Rowe, A.K., Rutledge, S.A., and Lang, T.J., 2011: Investigation of microphysical processes occurring in isolated convection during NAME, *Monthly Weather Review*, **139**, 424 – 443.

Rutledge, S.A., Williams, E.R., and Keenan, T.D., 1992: The down under Doppler and electricity experiment (DUNDEE): Overview and preliminary results, *Bulletin of the American Meteorological Society*, **73** (1), 3 – 16.

Saunders, C.P.R., 1993: A review of thunderstorm electrification processes, *Journal of Applied Meteorology*, **32**, 642 – 655.

Saunders, C.P.R., Keith, W.D., and Mitzeva, R.P., 1991: The effect of liquid water on thunderstorm charging, *Journal of Geophysical Research*, **96**, 11007 – 11017.

Schultz, C.J., Petersen, W.A., and Carey, D.L., 2009: Preliminary development and evaluation of lightning jump algorithms for the real–time detection of severe weather, Journal of *Applied Meteorology and Climatology*, **48**, 2543 – 2563.

Schmetz, J, Tjemkes, S.A., Gube, M., and van de Berg, L., 1997: Monitoring deep convection and convective overshooting with METEOSAT, Advances *in Space Research*, **19**, 433 – 441.

Schmetz, J., Pili, P., Tjemkes, S., Just, D., Kerkmann, J., Rota, S., and Ratier, A., 2002: An Introduction to Meteosat Second Generation (MSG), *Bulletin of the American Meteorological Society*, 977 – 992.

Setvák, M., Rabin, R.M., Doswell III, C.A., and Levizzani, V., 2003: Satellite observations of convective storm top features in the 1.6 and 3.7/3.9 μm spectral bands, *Atmospheric Research*, **67** – 68C, 589 – 605.

Steiger, S.M., Orville, R.E., and Carey, L.D., 2007: Total lightning signatures of thunderstorm intensity over North Texas, Part I: Supercells, *Monthly Weather Review*, **135**, 3281 – 3302.

Stolzenburg, M., and Marshall, T.C., 1998: Charged precipitation and electric field in two thunderstorms, *Journal for Geophysical Research*, **103** (D16), 19777 – 19790.

Strabala, K.I., Ackerman, S.A., and Menzel, W.P., 1994: Cloud properties inferred from 8 – 12 μm data, *Journal of Applied Meteorology*, **33**, 212 – 229.

Straka, J., M., Zrnić, D.S. and Ryzhkov, A.V., 2000: Bulk hydrometeor classification and quantification using polarimetric radar data: synthesis of relations, *Journal of Applied Meteorology*, **39**, 1341 – 1372.

Takahashi, T., 1978: Riming electrification as a charge generation mechanism in thunderstorms, *Journal of Atmospheric Sciences*, **35**, 1536 – 1548.

Tong, H., Chandrasekar, V., Knupp, K.R., and Stalker, J., 1998: Multiparameter radar observations of time evolution of convective storms: Evaluation of water budgets and latent heating rates, *Journal of Atmospheric and Oceanic Technology*, **15**, 1097 – 1109.

Toracinta, E.R., Cecil, D.J., Zipser, E.J., and Nesbitt, S.W., 2002: Radar, passive microwave, and lightning characteristics of precipitating systems in the Tropics, *Monthly Weather Review*, **130**, 802 – 824.

Vincent, B.R., Carey, L.D., Dchneider, D., Keeter, K., and Gonski, R., 2003: Using WSR–88D reflectivity data for the prediction of cloud–to–ground lightning: a Central North Carolina study, *National Weather Digest*, **27**, 35 – 44.

Vivekanandan, J., Turk, J., and Bringi, V.N., 1991: Ice water path estimation and characterization using passive microwave radiometry, *Journal of Applied Meteorology*, **30**, 1407 – 1421.

Vivekanandan, J., Zrnic, D.S., Ellis, S.M., Oye, R., Ryzhkov, A.V. and Straka, J., 1999: Cloud microphysical retrieval using S–band dual–polarization radar measurements, *Bulletin of the American Meteorological Society*, **80** (3), 381 – 388.

Wang, J.–J., and Carey, L.D., 2005: The development and structure of an oceanic squall–line system during the South China sea monsoon experiment, *Monthly Weather Review*, **133**, 1544 – 1561.

Wang, J.–J., Li, X., and Carey, L.D., 2007: Evolution, structure, cloud microphysical, and surface rainfall processes of monsoon convection during the South China sea monsoon experiment, *Journal of Atmospheric Sciences*, **64**, 360 – 380.

Watts, P.D., Mutlow, C.T., Baran, A.J., and Zavody, A.M., 1998: Study on cloud properties derived from Meteosat Second Generation Observations, *Unpublished Report*, EUMETSAT ITT no. 97/181. Final Report, pp. 334.

Wilks, D.S., 2006: *Statistical Methods in the Atmospheric Sciences*, 2nd Edition, Academic Press, Oxford, pp. 627.

Williams, E.R., Lyons, W.A., Hobara, Y., Mushtak, V.C., Asencio, N., Boldi, R., Bór, J., Cummer, S.A., Greenberg, E., Hayakawa, M., Holzworth, R.H., Kotroni, V., Li, J., Morales, C., Nelson, T.E., Price, C., Russel, B., Sato, M., Sátori, G., Shirahata, K., Takahashi, Y., and Yamashita, K., 2009: Ground–based detection of sprites and their parent lightning flashes over Africa during the 2006 AMMA campaign, *Quarterly Journal of the Royal Meteorological Society*, 1 – 15.

Wilson, J.W., Foote, G.B., Crook, N.A., Fankhauser, J.C., Wade, C.G., Tuttle, J.D., Mueller, C.K., and Kruger, S.K., 1992: The role of boundary–layer convergence zones and horizontal rolls in the initiation of thunderstorms. A case study. *Monthly Weather Review*, **120**, 1785–1815.

World Meteorological Society (WMO), 2006, UK Met Office long range lightning detection network summary, *Unpublished report*, Geneva, Switzerland, CIMO–XIV/INF.4

Yayaratne, E.R., Saunders, C.P.R., and Hallet, J., 1983: Laboratory studies of the charging of soft–hail during ice crystal interactions, *Quarterly Journal of Royal Meteorological Society*, **109**, 609 – 630.

Yuter, S.E., and Houze Jr., R.A., 1995: Three–dimensional kinematic and microphysical evolution of Florida cumulonimbus. Part II: Frequency distributions of vertical velocity, reflectivity, and differential reflectivity, *Monthly Weather Review*, **123**, 1941 – 1963.

Zawislak, J., and Zipser, E.J., 2010: Observations of seven African easterly waves in the east Atlantic during 2006, *Journal of Atmospheric Sciences*, **67**, 26 – 43.

Zeng, Z., Yuter, S.E., Houze Jr., R.A., and Kingsmill, D.E., 2001: Microphysics of the rapid development of heavy convective precipitation, *Monthly Weather Review*, **129**, 1882 – 1904.

Zipser, E.J., Twohy, C.H., Tsay, S.–C., Thornhill, K.L., Tanelli, S., Ross, R., Krishnamurti, T.N., Ji, Q., Jenkins, G., Ismail, S., Hsu, N.C., Hood, R., Heymsfield, G.M., Heymsfield, A., Halverson, J., Goodman, H.M., Ferrare, R., Dunion, J.P., Douglas, M., Cifelli, R., Chen, G., Browell, E.V., and Anderson, B., 2009: The Saharan air layer and the fate of African easterly waves, *Bulletin of the American Meteorological Society*, 1137 – 1156.

Zrnić, D.S., Balakrishnan, N., Ziegler, C.L., Bringi, V.N., Aydin, K., and Matejka, T., 1993: Polarimetric signatures in the stratiform region of mesoscale convective systems, *Journal of Applied Meteorology*, **33**, 45 – 52.